

CHARACTERISATION OF THE STRUCTURAL PROPERTIES OF ECNF EMBEDDED PAN NANOMAT REINFORCED GLASS FIBER HYBRID COMPOSITES

Philip Bradley

A thesis submitted to the Faculty of Engineering and the Built Environment, University of the Witwatersrand, Johannesburg, in fulfilment of the requirements for the degree of Master of Science in Engineering.

Johannesburg, May 2016

DECLARATION

I declare that this dissertation is my own unaided work, except where otherwise acknowledged. It is being submitted for the Degree of Master of Science in Engineering to the University of the Witwatersrand, Johannesburg. It has not been submitted before for any degree or examination to any other University.

Signed this 16th day of May 2016

Philip Bradley

ABSTRACT

In this study, hybrid multiscale epoxy composites were developed from woven glass fabrics and PAN nanofibers embedded with short ECNFs (diameters of $\sim 200\text{nm}$) produced via electrospinning. Unlike VGCNFs or CNTs which are prepared through bottom-up methods, ECNFs were produced through a top-down approach; hence, ECNFs are much more cost-effective than VGCNFs or CNTs. Impact absorption energy, tensile strength, and flexural strength of the hybrid multiscale reinforced GFRP composites were investigated. The control sample was the conventional GFRP composite prepared from the neat epoxy resin. With the increase of ECNFs fiber volume fraction up to 1.0%, the impact absorption energy, tensile strength, and flexural strength increased. The incorporation of ECNFs embedded in the PAN nanofibers resulted in improvements on impact absorption energy, tensile strength, and flexural properties (strength and modulus) of the GFPC. Compared to the PAN reinforced GRPC, the incorporation of 1.0% ECNFs resulted in the improvements of impact absorption energy by roughly 9%, tensile strength by 37% and flexural strength by 29%, respectively. Interfacial debonding of matrix from the fiber was shown to be the dominant mechanism for shear failure of composites without ECNFs. PAN/ECNFs networks acted as microcrack arresters enhancing the composites toughness through the bridging mechanism in matrix rich zones. More energy absorption of the laminate specimens subjected to shear failure was attributed to the fracture and fiber pull out of more ECNFs from the epoxy matrix.

This study suggests that, the developed hybrid multiscale ECNF/PAN epoxy composite could replace conventional GRPC as low-cost and high-performance structural composites with improved out of plane as well as in plane mechanical properties. The strengthening/ toughening strategy formulated in this study indicates the feasibility of using the nano-scale reinforcements to further improve the mechanical properties of currently structured high-performance composites in the coming years. In addition, the present study will significantly stimulate the long-term development of high-strength high-toughness bulk structural nanocomposites for broad applications.

ACKNOWLEDGEMENTS

I would like to thank the Centre of Excellence in Strong Materials at the University of the Witwatersrand as well as the NRF and DST for sponsoring my research and study which lead to the completion of this dissertation. Thanks to my parents, partner and brothers for their unconditional love, encouragement and support throughout the most challenging times.

I would like to thank my supervisor, Prof. Jacob Muthu, for his guidance and unwavering support throughout this study. Without his encouraging presence and insightful knowledge this work would not have been possible.

I would also like to thank Dr. Shane Durbach and Prof. Ratnam Paskaramoorthy for their financial support, advice and encouragement during my research. I would also like to thank Mr. Shaun Riekert and Ms. Nomso Hintsho for their advice and help during the experimental setup and design analysis.

Lastly, I would like to thank my lab partner and good friend Mr. Isuru Jinasena for making this journey an adventure.

TABLE OF CONTENTS

DECLARATION	ii
ABSTRACT.....	iii
ACKNOWLEDGEMENTS	iv
LIST OF FIGURES	vi
LIST OF TABLES.....	xi
NOMENCLATURE	xii
1 INTRODUCTION	1
1.1 Background and Motivation.....	1
1.2 The Research Problem	3
1.3 The Purpose of the Study	4
1.4 Objectives	4
2 LITERATURE REVIEW	5
2.1 Introduction to Composite Materials	5
2.2 Polymer Composites	5
3 METHODOLOGY	22
3.1 Materials	22
3.2 Experimental Process Design.....	23
3.3 Mechanical Testing.....	40
3.4 Morphological Characterisation.....	50
4 PAN NANOMAT & ECNF: PRODUCTION, OPTIMISATION & MORPHOLOGICAL CHARACTERISATION	53
4.1 Design & Development of Electrospinning Setup.....	53
4.2 PAN Nanomats	59
4.3 ECNFs.....	69
5 RESULTS AND DISCUSSION	79
5.1 Glass Reinforced Epoxy Composite	79
5.2 PAN Nanomat Reinforced GRPC.....	90
5.3 ECNF doped PAN Reinforced GFR Hybrid Composite.....	102

6	CONCLUSIONS.....	119
7	BIBLIOGRAPHY	121
	APPENDIX A (Raw Testing Data and Samples)	133
	A.1 Tensile and Flexural Testing Results	133
	A.2 Impact Testing.....	159
	APPENDIX B (Sample Calculations).....	166
	B.1 Tensile Data.....	166
	B.2 Flexural Data	168
	B.3 Impact Data	170

LIST OF FIGURES

Figure 2.1: Chemical structure of bisphenol-A diglycidyl ether epoxy resin showing the repeatable epoxide group [23].....	6
Figure 2.2: Chemical structure of Triethylenetetramine [24].	7
Figure 2.3: Plain woven glass fibers supplied in a rolled up mat.	8
Figure 2.4: TEM image showing a typical untreated nanofiber structure [39]......	11
Figure 2.5: Graphical representation of the stabilisation and carbonisation procedure in order to achieve carbon fibers from PAN fibers (Figure has been reproduced from reference [74]).....	18
Figure 3.1: Simplified manufacturing process of the neat glass fiber composites.....	25
Figure 3.2: Schematic drawing of the VARTM setup used to cast all composite plates.	25
Figure 3.3: VARTM setup during operation.....	26
Figure 3.4: Image of the DoALL band saw which was used to cut composite plates.	27
Figure 3.5: Stainless steel template used to hold the rectangular tensile specimen during shaping.	28
Figure 3.6: TensilKut diamond shaping tool used to shape the tensile dog-bone specimens.	28
Figure 3.7: Visual comparison between the neat epoxy samples (A) and the glass reinforced samples (B).	29
Figure 3.8: Manufacturing process of the PAN mat reinforced glass fiber composites.	30
Figure 3.9: Loaded Syringes in NE-1600 syringe pump.....	32
Figure 3.10: High voltage power supply used to supply the electric field for the electrospinning process.	33
Figure 3.11: Fiber mat layup placed into the VARTM.....	34
Figure 3.12: Time lapsed images of a VARTM casting process showing the remnants of an un-wetted fiber zone of a sample with high PAN fiber volume fraction reinforcement.....	35
Figure 3.13: Full process schematic showing the experimental procedures performed.	36
Figure 3.14: Sonicated ECNF/DMF solution.	38
Figure 3.15: Good dispersion of PAN nanofibers on a woven glass mat.	39
Figure 3.16: Macro-agglomerations of ECNFs imbedded in the PAN fibers electrospun onto the woven glass mats.	40
Figure 3.17: Tensile testing sample dimensions as per ASTM D638:2010.....	41
Figure 3.18: The Shimadzu testing equipment in operation.	42
Figure 3.19: Tensile grip attachments for the Shimadzu testing machine.	43
Figure 3.20: Laser extensometer used to measure the jaw displacement under tensile loading.	44
Figure 3.21: 3 point bending sample dimensions as per ASTM D790:2010.	46
Figure 3.22: Close up image of the 3-point flexural test attachment during a test	47
Figure 3.23: Impact testing sample dimensions as per ASTM D256:2010.	48
Figure 3.24: Avery pendulum impact testing machine used to test the impact specimen.	49

Figure 3.25: Simplified diagram showing the working method of the Raman Effect.	51
Figure 3.26: Fundamental concept behind the Raman Effect	52
Figure 4.1: Syringe pump designed and built by author using an Arduino uno.	53
Figure 4.2: Electrospinning capillary network from the syringes (A) to the needles (B) using PTFE tubing with luer lock connectors.	54
Figure 4.3: Images showing the three collectors experimented with in order to collect quality nanofibers; (A) parallel plate, (B) fixed plate and (C) rotating drum.	56
Figure 4.4: Electrospinning Setup designed and built at the University of the Witwatersrand.	59
Figure 4.5: Graph showing nanofiber diameter vs. PAN concentration.	60
Figure 4.6: Images showing the phenomenon of beading of PAN fibers caused by poor electrospinning processing.	60
Figure 4.7: TEM image showing diameter and structural homogeneity of PAN nanofibers.....	61
Figure 4.8: SEM images showing ribbon like structure (A) and poor surface morphology (B) of PAN nanofibers electrospun with high PAN concentrations.	61
Figure 4.9: Image showing poor dispersion of PAN nanofibers collected on the woven glass fiber mats.	63
Figure 4.10: Electrospun PAN nanofibrous mat collected using the rotating drum collector.	63
Figure 4.11: Comparison between droplet formation of a 90° end tip (A) and a 30° angled tip (B). ...	64
Figure 4.12: Images showing glass syringe (A) and disposable plastic syringes (B).’	64
Figure 4.13: Graphical representation of the 3-dimensional experimental matrix.....	65
Figure 4.14: Microscopic images showing the beading phenomenon caused by poor electrospinning parameter control.	67
Figure 4.15: SEM images showing the optimized PAN nanofiber diameters and the quality of the morphological structures.....	68
Figure 4.16: Images of the box furnace (A) and the muffle furnace (B) experimented with in order to achieve well graphitized carbon nanofibers.	69
Figure 4.17: Carbonisation furnace used to convert PAN fibers into carbon nanofibers.	70
Figure 4.18: TEM image of the final ECNFs as produced by electrospinning and carbonisation of the PAN nanofibers.....	71
Figure 4.19: TEM image of the disordered graphitic structure of the nanofiber surface.....	72
Figure 4.20: TEM image of CNT showing thin skin-core structure [44].	73
Figure 4.21: Turbostratic carbon crystallite thickness of skin-core structure of PAN carbonized at 1300°C.	73
Figure 4.22: TEM images of ECNFs used to characterise fiber diameter and quality of fiber structures.	74
Figure 4.23: Raman spectrograph for the ECNF sample prepared at carbonisation temperature of 800°C for one hour.....	75

Figure 4.24: Amorphization trajectory, showing a schematic variation of the G position and $I(D)/I(G)$ ratio.	76
Figure 4.25: TG graph comparing the thermal degradation of both the neat PAN and the ECNFs in terms of weight loss as a percentage.	77
Figure 4.26: DSC thermogram which was used to further characterize the cyclization temperature of the PAN polymer during the oxidative exothermic stabilisation process.	78
Figure 4.27: Elemental analysis of the sample prepared at the holding carbonisation temperature of 800°C.	78
Figure 5.1: Triangular unit cell in hexagonal close packing arrangement [127].	80
Figure 5.2: Tensile strengths of varying glass fiber volume fractions.	82
Figure 5.3: SEM image of a 16% volume fraction GRPC sample showing poor interfacial bonding as shown by the fiber pullout of the glass fiber after tensile failure.	82
Figure 5.4: SEM image of a 24% volume fraction GRPC sample showing a mixture of both fiber pullout and breakage which is indicative of improved interfacial bonding between fibers and matrix over that of the 16% fiber volume fraction samples.	83
Figure 5.5: SEM image of a 32% volume fraction GRPC sample showing the lack of fiber pullout which is indicative of good interfacial bonding between fibers and matrix.	84
Figure 5.6: Tensile moduli of varying glass fiber volume fractions.	85
Figure 5.7: Flexural strengths of varying glass fiber volume fractions.	86
Figure 5.8: SEM image showing good interfacial bonding between fibers and matrix characterised by the uneven surfaces of the glass fibers, as well as reduced matrix rich zones.	87
Figure 5.9: Flexural moduli of varying glass fiber volume fractions.	88
Figure 5.10: Impact resistance of varying glass fiber volume fractions.	89
Figure 5.11: SEM image of a 32% volume fraction GRPC sample showing the debris of glass fibers left after failure whereby the glass fibers accommodated for the shearing load and showed fiber breakage.	89
Figure 5.12: Tensile strengths of varying PAN nanofiber volume fraction GRPC.	92
Figure 5.13: SEM image showing a PAN nanofiber aligned along the glass fiber axis.	93
Figure 5.14: SEM image of the fracture surface for a 0.5% PAN/ GRPC whereby the good interfacial bonds between the PAN and epoxy are shown.	94
Figure 5.15: SEM image showing stretched PAN nanofibers which allowed the tensile loads to be transferred to the stronger glass fibers.	95
Figure 5.16: Tensile moduli of varying PAN nanofiber volume fraction GRPC.	95
Figure 5.17: Flexural strengths of varying PAN nanofiber volume fraction GRPC.	96
Figure 5.18: Flexural moduli of varying PAN nanofiber volume fraction GRPC.	97
Figure 5.19: SEM image of 0.5% PAN reinforced GRPCs failed three point bending test sample showing good adhesion between nanofibers and matrix.	98

Figure 5.20: SEM image of 0.2% PAN reinforced GRPCs failed three point bending test sample showing the large surface areas and interconnected porosity of the PAN nanofibers which improved interfacial interaction with the epoxy matrix and the glass fibers.	98
Figure 5.21: Impact resistance of varying PAN nanofiber volume fraction GRPC.....	99
Figure 5.22: Distribution network of a PAN nanofiber mat which resulted in decreased distances between fibers.	100
Figure 5.23: SEM image of the failure surface of a 0.5% PAN/GRPC impact sample showing the nano fibrous layer after impact failure whereby crack propagation was restricted.....	100
Figure 5.24: SEM image of the failure surface of a 0.5% PAN/GRPC impact sample showing nanofiber bridging.....	101
Figure 5.25: SEM image of the failure surface of a 0.5% PAN/GRPC impact sample showing the debris of glass fiber after failure.	102
Figure 5.26: SEM image of fibrous mat showing alignment of ECNFs along the PAN nanofiber length.	103
Figure 5.27: Tensile strengths of varying ECNF reinforced PAN nanofiber volume fraction GRPC.	105
Figure 5.28: Tensile moduli of varying ECNF reinforced PAN nanofiber volume fraction GRPC... ..	106
Figure 5.29: Fracture surface of a 1.0% ECNF reinforced PAN/GRPC sample.	106
Figure 5.30: SEM images showing the cracking behaviour of the individual composite fibers under tension.....	107
Figure 5.31: SEM images showing the polymeric crazing effect under tension.....	107
Figure 5.32: Fracture surface of a GFRP composite sample with 0.5% ECNFs added.....	108
Figure 5.33: Fracture surface of a GFRP composite sample with 0.5% ECNFs added.....	109
Figure 5.34: Fracture surfaces of GFRP composites with 1.0% ECNFs added.....	110
Figure 5.35: Fracture surfaces of GFRP composites with 0.5% ECNFs added.....	110
Figure 5.36: Flexural strengths of varying ECNF reinforced PAN nanofiber volume fraction GRPC.	111
Figure 5.37: Flexural moduli of varying ECNF reinforced PAN nanofiber volume fraction GRPC.	112
Figure 5.38: SEM image of the 0.5% ECNF sample showing the mechanism of failure.	113
Figure 5.39: SEM image of failed 1.0% ECNF sample showing the pitted fracture feature.	114
Figure 5.40: SEM image of the 1.0% ECNF sample showing the presence of closely arranged broken glass fibers.	114
Figure 5.41: Impact resistance of varying ECNF reinforced PAN nanofiber volume fraction GRPC.	115
Figure 5.42: Fracture surface of the 1.0% ECNF embedded PAN nanofiber reinforced GRPC showing short, jagged and multi-plane fracture lines.....	117

Figure 5.43: Fracture surface of a 1.0% ECNF embedded PAN nanofiber reinforced GRPC sample.
..... 118

LIST OF TABLES

Table 2.1: Mechanical properties of commonly used microfiber reinforces for composite materials [25].....	8
Table 2.2: The effects of increasing the operating parameters on the diameter and formation of beads of the fibers.	14
Table 2.3: Ideal electrospinning operating parameters for the production of PAN nanofibers.	16
Table 3.1: Mix ratio of hardener to resin for Ampreg 21[104].....	22
Table 3.2: Physical & mechanical properties of AMPREG 21 and hardener at 25°C	22
Table 3.3: Physical & Mechanical properties of E-glass woven fibers.	23
Table 3.4: Parameters and conditions for Tensile Test.....	41
Table 4.1: Gamma HVPS specifications.....	55
Table 4.2: Table showing the drum collector’s motor specifications.	58
Table 4.3: Experimental observations made regarding the electrospinning process.	66
Table 5.1: Typical values for fiber volume fractions in polymer composites [127].	80
Table 5.2: Optimum nanofiber volume fractions from a variety of researchers in the field of polymeric nanofiber reinforcement for composites.	91

NOMENCLATURE

Symbol	Description	Units
A_{avg}	Average cross-sectional area	mm^2
w_{avg}	Average width	mm
T_{avg}	Average Thickness	mm
σ_{ult}	Ultimate tensile strength of specimen	MPa
F_{max}	Maximum load	N
ϵ	Tensile strain	mm/mm
Δl	Extensometer displacement	mm
l	Extensometer gauge length	mm
E	Tensile modulus of elasticity of the specimen	GPa
$\Delta\sigma$	Difference in tensile stress between two data points	MPa
$\Delta\epsilon$	Difference in tensile strain between two data points	mm/mm
σ_f	Flexural stress	MPa
b	Width of flexural test specimen	mm
h	Thickness of flexural test specimen	mm
L	Distance between supports for flexural test	mm
ϵ_f	Flexural strain	mm/mm
D	Vertical deflection in flexural testing	mm
E_f	Flexural Modulus of Elasticity	GPa
K_I	Impact Resistance	J/m^2
Δe_I	Absorbed impact energy	J
A_I	Cross-sectional area of impact specimen	m^2
PAN	Polyacrylonitrile	-
ECNF	Electrospun Carbon Nanofibers	-
GRPC	Glass Reinforced Polymer Composites	-
VGCNF	Vapour Grown Carbon Nanofiber	-
CNT	Carbon Nanotube	-

1 INTRODUCTION

1.1 Background and Motivation

Throughout history, engineering materials have had an immense influence on technological development and have been fundamental in the evolution of the human race. During the industrial era of the 19th century, metals such as steel and iron were the predominant engineering materials. Over time, the use of alloying metals improved their properties which led to superior materials with a wider range of functionality. However, there were still many applications where metals were not ideally suited such as in the aerospace industry where stronger and lighter weight materials were required. Modern technology requires materials that possess remarkable combinations of properties that cannot be provided by conventional metal alloys, ceramics or polymeric materials. It was with the introduction of composite materials prior to the First World War where the development of these superior polymeric composite materials began. However, it was only until the 1970's when the major growth of polymeric composites took place, with the development of plastic resins such as epoxy and the introduction of stronger reinforcing fibers such as carbon fiber [1].

Epoxy resins are possibly the most significant polymers used in structural engineering applications due to their much higher modulus compared with other polymeric materials [2]. However, epoxy resins are highly cross-linked by nature which affects the material's properties such as lack of durability and increased brittleness. Consequently, reinforcement has been developed to improve these problems by principally changing the morphologies of the system by adding reinforcing fibers.

Commercially, glass fiber reinforced polymeric composites (GRPC) are widely used in a variety of engineering industries such as aviation, aerospace, automobile and ship construction, because the composites are extremely strong, stiff, lightweight, cheap and less brittle than carbon fiber reinforced polymeric composites (CRPC). However, a common problem with GRPCs is the failure in matrix-rich inter-laminar regions where the poor stress transfer between load-bearing fibers and the weaker matrix occurs. This is a common cause of catastrophic interlaminar failure in GRPCs and is of critical concern in commercial applications.

As a result, researchers both in industry and in academia have focused a great deal of attention on improving the stress transfer between fiber and matrix by reinforcing polymers with nano-sized fillers, which can represent an additional secondary reinforcement, and is expected to improve both the interlaminar regions and the mechanical in-plane properties of fiber reinforced polymeric composites. This secondary reinforcement of nanofibers is believed to improve the mechanical in-plane properties by improving the homogeneity of the composite in that the distance between weak matrix rich zones and that of the cross-sectional plies is reduced. A composite such as this with two or more different reinforcements, with different scales, incorporated into the same system is termed a multiscale hybrid composite, where the nanoparticles are incorporated into the matrix system to

increase the stiffness, strength, and toughness. According to Kickelbick *et al.* [3], a reduction in the size of the inorganic fillers to the same level as the organic building blocks of the matrix could lead to more homogeneous materials that have improved performance and process ability of materials on a macroscopic scale. Additionally, hybrid composites are cheap to manufacture and allow engineers to design and uniquely tailor them for a wide variety of applications by combining key characteristics of different fillers to compensate each of their flaws. Furthermore, research into the use of multiscale fillers to reinforce polymer matrices has also shown more controllable designs of the mechanical properties of polymer nanocomposites [4,5,6,7,8,9].

The majority of current research on nanofiber reinforced composites is primarily concerned with the use of vapour grown carbon nanofiber (VGCNF) or carbon nanotube (CNT) fillers commonly produced via Chemical Vapour Deposition (CVD) or laser ablation methods. These resultant fillers when impregnated in polymer matrices do provide toughening however do not provide expected strengthening because of their discontinuous and irregular entangled forms which cause fiber agglomerations resulting in stress concentration sites and improper dispersion that lead to poor mechanical properties. Additionally, other factors affecting the strengthening of polymers using discontinuous fillers are the poor interfacial adhesion between the fillers and the polymer matrix and the difficulties in producing a homogenous spread of fillers within the polymeric matrix. The interfacial adhesion is vital in allowing for load transfer from the matrix to nanofillers and is imperative for the utilization of the nanofillers potential as a secondary reinforcement for hybrid composites. Alternatively, electrospun polymer nanofibers made from electrospinning polymers such as polyacrylonitrile (PAN) are of particular interest because they are continuous and possess fiber diameters on a nano-scale.

Electrospinning is a promising method that can be used to produce random nonwoven mats of nanofibers suitable for interlaminar reinforcement and toughening to form hybrid multiscale composites, which can be made in a relatively efficient way while maintaining the relatively high strength and reducing the effects of discontinuous fillers. The major advantage of these fibrous mats is the fact that they can be easily inserted between conventional fabrics, thus the addition of them does not lead to a substantial increase in processing costs. They are also very thin, thus the addition of them does not add significant weight increase to the final composite material. The electrospun fibers in the mats are randomly oriented, thus the distribution of these fibers between adjacent laminas in the composites are relatively homogeneous. Moreover, the excellent porous characteristics of the polymeric nanofibers and the highly porous nature of the collected nonwoven mats with excellent pore-interconnectivity and extremely large surface to volume ratio can lead to an interpenetrated structure when dispersed in the matrix caused by the remarkable permeability to facilitate resin flow, therefore ensuring complete impregnation of reinforcements [10]. These characteristic features of nanofibers enable the transfer of applied loads to the fiber–matrix interface in a better manner than most of the commonly used filler materials. Also, the relatively low cost and uncomplicated

production of nanofiber mats make them ideal substitutes for CNTs or VGCNFs as reinforcing fillers for polymeric materials. However, the individual fiber strengths of these fibers produced via electrospinning are not yet comparable to that of VGCNFs or CNTs.

Therefore, improvements of such mats, with more suitable fibers to be used in structural enhancement, are continuous electrospun nanofibers doped with nanofillers. PAN is the most commonly used precursor for both microscale and nano-scale carbon fiber production with 90% of the carbon fibers produced worldwide being synthesised from PAN [11]. This is as a result of its high yield, good fiber strength and high elastic modulus. The nanofillers are mixed into the PAN/solvent solution and electrospun using the electrospinning method. Electrospun carbon nanofibers (ECNFs) that can be developed through heat treatments (i.e., stabilisation followed by carbonisation) of their electrospun precursor polymers such as polyacrylonitrile (PAN) nanofibers [12,13,14] are of particular interest as the electrospun PAN nanofibers possess an extremely high degree of macromolecular orientation and a significantly reduced amount of structural imperfections. In addition, the diameter of nanofibers is approximately 100 times smaller than that of conventional carbon fibers used for reinforcement. As a result, the ECNFs possess superior mechanical properties that would unlikely be achieved through conventional drawing techniques. Also, the relatively low cost and uncomplicated production of ECNFs also make them ideal substitutes for CNTs or VGCNFs as reinforcing fillers in PAN nanofibrous mats.

1.2 The Research Problem

There has and always will be an increased need for strong and lightweight materials as mankind's technological requirements increase. Research in the field of polymer nanocomposites has exploded in recent years due to the fact that it is providing for a new era in material sciences. It is for this reason that the research problem is to discover improved material properties by optimizing both manufacturing processes and hybridization of a new hybrid material.

In theory, the high aspect ratio of ECNF's makes them ideal for the use as fillers in high performance composite materials. However, the use of ECNFs as functional fillers for hybrid composites is still in research infancy. Outcomes of improved materials for the use in the aerospace industry will result in more effective and safer aircraft structures that will ultimately advance the aerospace industry.

1.3 The Purpose of the Study

The purpose of this study is to investigate the potential use of ECNFs as functional fillers for engineering polymeric materials. In particular, this study focuses on the investigation of a hybrid multiscale composite consisting of both ECNF embedded PAN nanofibers and micro glass fibers used as functional fillers with the polymeric matrix, epoxy. Even though electrospun fiber reinforced polymer composites have a great future prospective for the improvement of stronger and tougher engineering materials, there still remains few studies that have investigated the use of ECNFs as

reinforcing fibers in composites. Information regarding the fabrication and characterisation of the structural properties of such composites is still believed to be useful, even though little research has been performed.

1.4 Objectives

1. Design and manufacture a functional electrospinning setup capable of fabricating electrospun PAN nanofibers with diameters of less than $500nm$.
2. Fabricate smooth carbon nanofibers from PAN nanofiber precursors by optimizing the heat treatment parameters for high strength carbon nanofibers.
3. Design and fabricate a multidirectional hybrid multiscale epoxy composite consisting of both PAN based ECNFs embedded in PAN nanofibers and woven glass fiber mats.
4. Obtain the mechanical properties, such as the strength and stiffness of the composite by means of destructive tensile, flexural and impact tests of test specimens.
5. Perform morphological characterisation techniques to determine the true nature of the dispersion and adhesion of the nanofillers and the overall quality of the nanocomposites.

1.5 Overview

In closing, the objective of this study has been defined as the mechanical characterisation of a GRPC hybridized with ECNF embedded PAN nanofiber interplies. Firstly, the optimum glass fiber volume fraction for the GRPC will need to be established. Secondly, the optimum PAN nanofiber volume fraction for the multiscale PAN reinforced GRPC will need to be established. Finally, the fabrication of the multiscale hybrid ECNF embedded PAN reinforced GRPC using the optimum glass fiber mass fraction along with the different weight fraction of ECNFs/PAN and the characterisation results will be presented.

2 LITERATURE REVIEW

2.1 Introduction to Composite Materials

A composite material is that which consists of two or more physically and/or chemically distinct phases containing characteristics that are not evident in any of the components in separation [15]. One of the phases is called the filler which is generally discontinuous and provides reinforcement by means of increased strength and stiffness to the composite, whereas the other phase is generally a continuous matrix that holds the filler together. The concept of composites is not new by any means, as nature itself illustrates many examples of composite materials. Wood is probably the most well-known natural composite which is a fibrous composite consisting of cellulose fibers embedded in a lignin matrix. The cellulose fibers possess high tensile strength but low stiffness, while the lignin matrix joins the fibers and provides the increased stiffness.

Modern, man-made, composites have advanced with the development of polymers, such as polystyrene, phenolic, vinyl, polyester and epoxy; also with ceramics, such as silicon carbide and tungsten carbide; and with metals, such as aluminium, titanium and steel alloys. These types of composite materials can be classified as polymer composites (PCs), ceramic composites (CCs), and metal composites (MCs). Unlike CCs and MCs, in which the reinforcement is used primarily to improve the fracture toughness, the reinforcement in PCs provides strength and stiffness that are lacking in the matrix. The composite is designed so that the mechanical loads to which the structure is subjected in service are supported by the reinforcement and the function of the relatively weak matrix is to bond the fibers together and to transfer loads between them [17]. Currently, the major disadvantage for MCs and CCs are the higher costs of fabrication as opposed to PCs, and lower ductility and toughness as opposed to metals.

2.2 Polymer Composites

A great deal of research has been performed in recent years in discovering the effects of impregnating polymer matrices with conventional macro sized fibers, such as glass fibers, on the mechanical properties of the composites. Composite theory and common practice has shown that the mechanical properties of these composites increase significantly due to the added reinforcement offered by the fibers.

PCs make use of polymeric matrices, commonly called polymers or resins, which are materials, composed of long molecular chains with repeating atomic units. The properties of any polymer are defined by the make-up of these repeating atomic units as well as the method in which they are bonded. All polymers will either fit into one of two categories, namely thermosetting or thermoplastic polymers. Thermosetting polymers are materials that when cured by thermal processes undergo an irreversible chemical change and as such, the original characteristics change and cannot be returned to

the same state prior to curing. Thermoplastic polymers differ to thermosetting polymers in that they do not undergo an irreversible chemical change and thus the process can be reversed. Thermoplastic polymers would seem to be the better choice as the material can be recycled and reused, however thermosetting polymers are of particular interest for reinforcement as they form the basis of many important advanced materials, ranging from computer chips to aerospace composite materials [18]. This is due to their improved strength, process ability, higher temperature stability and better chemical resistance compared with thermoplastic polymers.

Epoxy resins are possibly the most significant thermosetting polymers used in structural applications, such as in automobile body work [19] or aircraft ailerons [20], because of their much higher modulus compared with other thermosetting polymers. Epoxy resins are also extensively used in the electronics industry as moulding compounds because of their excellent insulating characteristics, good adhesive properties, outstanding chemical resistance, retention of properties under severe operating conditions and low moisture absorption [21].

The molecular structure of epoxy resins, which contains at least one epoxide functional group, consisting of an oxygen atom joined by single bonds to two adjacent carbon atoms, can be altered to vary the molecular weight and viscosity of the overall resin. Figure 2.1 shows this feature of the resin where the number “ n ” of the repeatable unit, also called degree of polymerisation, can be increased to increase the molecular weight of the resin. There are two major types of epoxy resins namely; glycidyl epoxy and non-glycidyl epoxy. The most commonly used epoxy resin type is Glycidyl epoxy which can further be defined as an amine, ester or ether type which depends solely on the reaction type [22]. Bisphenol A is reacted with epichlorohydrin in the presence of a catalyst to produce possibly the most common glycidyl amine epoxy resin [22].

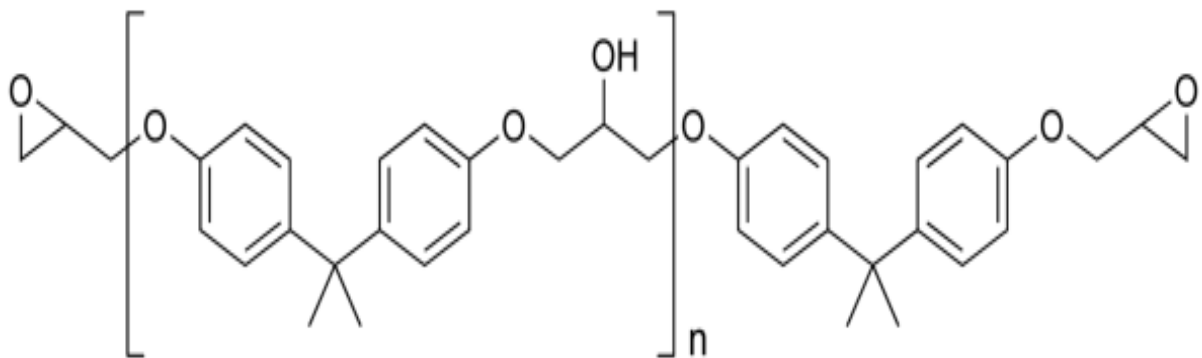


Figure 2.1: Chemical structure of bisphenol-A diglycidyl ether epoxy resin showing the repeatable epoxide group [23]

As mentioned before, thermoset resins undergo chemical reactions that crosslink the polymer chains, called curing, and thus bond the matrix together in a three-dimensional network. This curing reaction is accelerated using a catalyst commonly called a hardener. In general, amine based curing agents are used such as Triethylenetetramine (TETA) as shown in Figure 2.2. In contrast to polyester or vinyl ester resins where the resin is catalysed with a small addition (< 3%) of a hardener, epoxy resins need a great deal more hardener (>40%)[22].

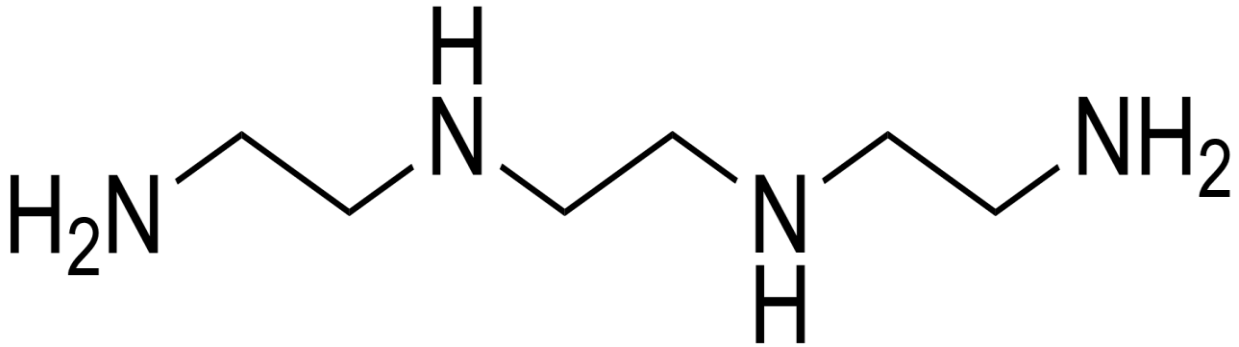


Figure 2.2: Chemical structure of Triethylenetetramine [24]

Thermosetting polymers tend to have a high dimensional stability, high-temperature resistance, and good resistance to solvents because of their three-dimensional crosslinked structure [16]. However, because of the highly cross-linked nature of the cured polymer, there are major limitations in the materials properties such as lack of durability and increased brittleness, resulting in poor mechanical properties, making them less used as engineering materials. Consequently, PCs have been developed to rectify these problems by principally changing the structure and morphologies of the system by adding reinforcing fillers in order to improve the poor engineering properties of these materials. PCs show these improved mechanical properties over and above the neat matrix because of the high (axial, longitudinal) strength values and high (axial, longitudinal) stiffness values of the fillers incorporated in the matrix.

Commercially, there is a wide variety of possible reinforcing fillers, ranging from continuous woven fibrous mats to particulates and whiskers, all used in the manufacturing of PCs, and all with differing properties used for a variety of engineering purposes. Table 2.1 shows a few examples of commonly used microfiber reinforcing fibers and their respective mechanical and physical properties. Of all the reinforcing fibers, glass fiber is typically the most commonly used fiber in fiber reinforced composites (FRC) and is likely to remain the most widely used reinforcement filler for high-volume commercial FRC applications because it is an extremely strong and lightweight material, which is generally cheaper and much less brittle than that of carbon fiber. More specifically, the major advantage of GRPCs is the very low price of glass fibers compared with other fibers, making it the most abundant fiber used in low cost projects ranging from recreational sporting goods to aircraft fuselages.

Table 2.1: Mechanical properties of commonly used microfiber reinforcements for composite materials [25]

Materials	Density (g/cm³)	Tensile Strength (MPa)	Young's Modulus (GPa)
E-Glass	2.55	2000	80
S-Glass	2.49	4750	89
Carbon	2.0	2900	525
Kevlar 29	1.44	2860	64
Kevlar 49	1.44	3750	136

Glass fiber is made from extremely fine fibers of glass and has been manufactured since the early 1930s. In general, glass fibers contain quartz, soda, sodium sulphate, potash, feldspar and a variety of additives [26]. Glass fiber is formed by an extrusion process whereby fine strands of glass are extruded into many fibers with small diameters suitable for textile processing such as weaved rovings, as shown in Figure 2.3. The technique of heating and extruding glass into fine fibers has been commonly used for years; however, the use of these fibers for mechanical reinforcement applications is more recent. Also, woven glass fibers are preferred over randomly orientated glass fibers because of the more ordered structure of the woven strands of fibers which lends itself to improved strength characteristics as compared with the randomly orientated non-woven fibers.

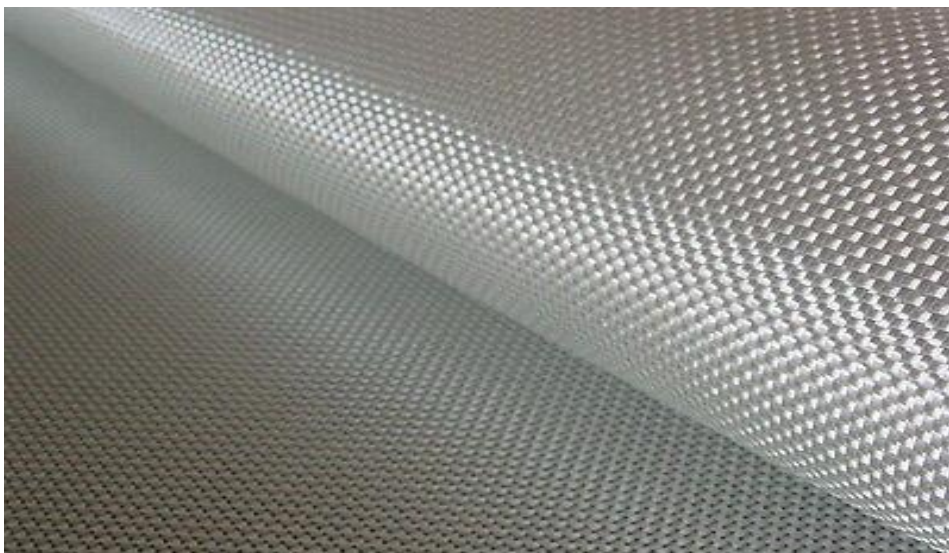


Figure 2.3: Plain woven glass fibers supplied in a rolled up mat

The characteristics of the different types of glass fibers are defined by the combination of raw materials and their chemical composition. There are four main types of glass used in the formation of glass fibers, namely [25]:

1. A-glass: Alkaline resistant.
2. C-glass: More resistant to chemical impact.
3. E-glass: Combines the properties of C-glass with improved insulation to electricity.
4. R,S or T-glass: Trade named by manufacturer's for equivalent fibers having higher tensile strength and modulus than E-glass.

Of these types, E-glass is the most common form of reinforcing fiber used in polymer matrix composites because of its superior strength properties at a very low cost. In many industries it represents over 90% of the reinforcements used [27]. The main advantages of using E-glass fibers include low cost, high strength, light weight and high chemical resistance. However, humidity is an important factor in affecting the tensile strength as moisture is easily absorbed into the fibers and can weaken the fiber structure by inducing microscopic cracks and surface defects.

In order to test the mechanical properties of polymeric nanocomposites requires the transformation of the mixed material into standard test sections related to the mechanical properties that are being tested for. There are two major processes that are commonly employed in the polymer industry, namely compression moulding and injection moulding.

Compression moulding is the most common process used with thermosetting resins [28], which involves filling a female and male counterpart mould of the desired dimensions with the required material. The mould with the material inside is then heated to a temperature above the materials' melting point and thus causing the material to melt. Pressure is then applied to the mould for a period of time which then results in the molten material assuming the shape of the mould cavity. The material is then left to cool for a short period of time before being removed from the mould as a solid material in the desired shape. However, the major disadvantage of the compression moulding process is that the orientation of the fibers may be affected by the movement of the molten polymer under the large pressures.

In the case of thermosetting resins, there is one particular injection method of manufacturing that has been extensively used in past research; namely, vacuum assisted resin transfer moulding [29,30,31,32]. This process makes use of a similar mould to the compression mould but instead of filling the mould prior to melting of the material; the material is introduced into the mould in a much less viscous phase. The resultant material is similar to that of compression moulding, although problems can arise with the viscosity of the material when introduced into the mould, which generally leads to the formation of voids and gas bubbles unless the inlet flow rate is carefully controlled [33].

Also the viscosity of every material blend will behave differently and as such a specific process for each blend must be designed.

Singh *et al.* [34] presented their investigations of mechanical behaviour of glass fiber reinforced epoxy composites and revealed that the tensile strength and flexural strength was greatly influenced by the fiber content of reinforcement in the matrix. The reinforced glass fiber composite showed improved tensile and flexural strength as compared with unreinforced epoxy. A 20% weight fraction of glass fibers resulted in the tensile strength and flexural strength increase of 14.5% and 123.65% respectively. The overwhelming contribution to flexural strength over tensile strength was due to presence of glass fibers which increased the overall stiffness of the composites. The value of Young's modulus of elasticity also increased with an increase in weight fraction of material, which is as a result of the increased strength and reduced strain.

Chalwa *et al.* [35] presented their findings on the development and mechanical characterisation of new polymer composites consisting of glass fiber reinforcement, epoxy resin and hybridized filler materials such as TiO₂ and ZnS. They performed tensile testing, three point bending and impact testing to discover the influence of filler materials on the mechanical characteristics of GFRP composites. Their results have shown that the higher the filler material volume percentage is, the greater the strength for both TiO₂ and ZnS filled glass epoxy composites.

The improved mechanical properties of incorporating reinforcing fibers, such as glass fiber, into polymeric materials, such as epoxy resin, coupled with the low weight and improved electrical properties of the composite make such materials ideal for the use in high strength, low weight applications. However, there still exist fundamental challenges in incorporating conventional macro fibers within the matrix to achieve such desirable properties of PCs.

The major challenge is in the bonding of the materials which takes place in the interfacial region between the two materials. This interfacial region is the region in which loads are transmitted between the reinforcement fibers and the matrix. The extent of interaction between the reinforcement fibers and the matrix may vary from strong chemical bonding to weak frictional forces, which can often be controlled by using an appropriate surface treatment on the reinforcing fibers [17]. Generally, a strong interfacial bond makes the PC more rigid, but simultaneously more brittle, whereas a weak bond decreases stiffness, but enhances toughness. If the interfacial bond is not at least as strong as the matrix, debonding and fiber pull-out can occur at the interfacial region under certain loading conditions, causing premature failure of the composite [17]. Therefore, it is important for the interfacial bonds between the fibers and the matrix to be controlled such that the fibers are able to transfer the loads more adequately between fibers and matrix; and prevent further crack propagation by increasing the amount of energy required to promote this. Optimal control can be attained by careful selection of filler surface treatments called functionalization techniques [10]. However, when

the adhesion is too strong, the composite material becomes more brittle and reduces fracture toughness.

Aside from this issue, there exist methods to further improve the mechanical properties of conventional PCs, which are of particular interest to engineers in the field of composite materials, these being; the use of nanofillers as opposed to macro fillers for reinforcement, and the use of hybrid materials to further tailor the properties of the final PC to suit the application.

2.2.1 *Nano-PCs*

The use of nanofillers as high performance reinforcement of engineering materials is based on two significant characteristics; the smaller the size of the filler particulate, the lower the probability of having imperfections in the material and the higher the aspect ratio (L/d), the higher the portion of the applied load that can be transferred via the matrix to the stiffer and stronger fibers. Cylindrical materials such as carbon nanofibers demonstrate this large aspect ratio which improves the efficiency of the nanocomposite by insuring that only a low mass fraction is required to gain large increases in physical properties [36]. This coupled with the reduction in mass and cost, makes CNFs ideal for applications including structural laminates and woven composites with improved matrix toughness for the aerospace and automotive sectors [37].

The history of CNFs dates back to over a century ago in which a patent was published describing the fabrication of carbon filaments grown from carbon containing gases using a metal catalyst [38]. Figure 2.4 below shows a TEM image of a carbon nanofiber, showing the amorphous nature of the fiber.

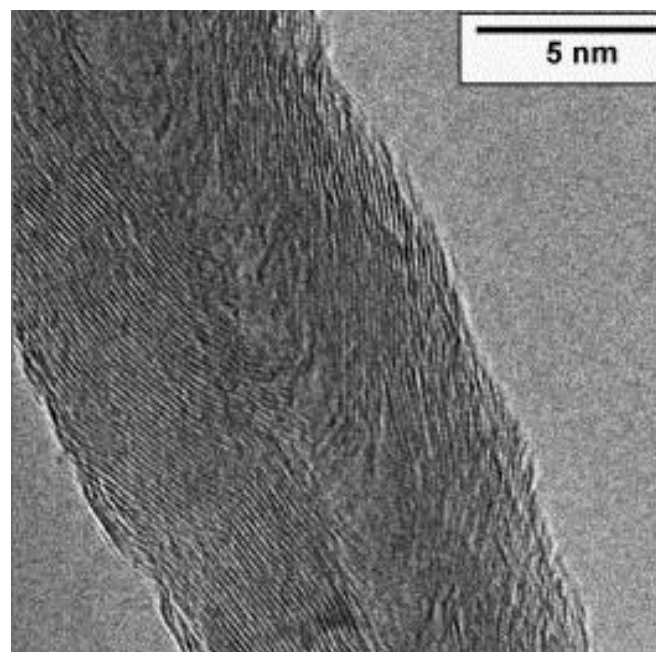


Figure 2.4: TEM image showing a typical untreated nanofiber structure [39]

Since this discovery, plenty of research was undertaken by laboratories and large corporations alike, as the interest in CNFs began to grow. Research by Bacon *et al.* [40] in the early 1960's has shown that CNFs with diameters of about 200nm could be synthesised by the electric arc technique. More research in the 1970's by Oberlin *et al.* [41] showed that CNFs of around 7nm in diameter could be produced with the chemical vapour deposition (CVD) technique. Research by Iijima in 1991 [42] showed that CNTs and CNFs could be formed during the arc discharge synthesis of C₆₀ and other fullerenes which once again ignited an even larger interest in both CNFs and CNTs. It was soon realized however, that the arc discharge and laser ablation techniques lead to mixtures of carbon materials and thus required troublesome purification processes to separate the CNFs and CNTs from the mixtures. There was still however a desire to control the properties of the fibers, such as; the surface structure, aspect ratio, texture, mechanical properties and the degree of agglomeration of the fibers in order to produce stronger macroscopic materials. This type of controllability was achieved with the recent carbon fiber production process whereby continuous and aligned CNFs were produced by carbonizing electrospun nanofibers from PAN and from pitch with diameters in the nano-scale and up to several microns, respectively [37,43,12,44].

Zussman *et al.* [44] were among the first to report on PAN derived CNFs. They found that the tensile strength of as-spun PAN derived CNFs had values ranging from between 0.32 - 0.9GPa and an average Young's modulus of $63 \pm 7GPa$. These results show that these values are roughly 6 times lower than those attained with microscale carbon fibers. The authors identified that the fiber skin-core cross-sectional structure was the cause of the low mechanical properties. Similarly, Zhou *et al.* [43] reported on PAN derived CNF bundles with tensile strength of between 0.3 – 0.6GPa and an average Young's modulus of $50 \pm 10GPa$. The authors acknowledged in their report that the quality of processing and further optimization of the precursor PAN could improve the physical properties further.

Chae *et al.* [46] were among the few to produce PAN derived carbon fibers with higher strengths and moduli produced from electro-gel-spun PAN and PAN-CNT composites, however the fibers produced were not on the nano-scale. Their experiments on carbon fiber bundles resulted in tensile strength and modulus of 3.2GPa and 337GPa, respectively. While experiments performed on CNT reinforced carbon fibers resulted in tensile strength and modulus of 4.5GPa and 463GPa, respectively, which are comparable to high quality commercial carbon fibers [47].

The majority of work in current literature on polymeric nanocomposites is concerned primarily with CNT or VGCNF reinforcements [48,49,50]. Thus far, VGCNFs are the only CNFs with diameters in the nano-scale that possess high tensile strengths, between 2.7 - 3.3GPa, and average Young's modulus between 180 - 250GPa [51]. However, they are discontinuous, only 100µm in length, and are significantly wavy in structure. The waviness of the structure is of particular importance because it is the limiting factor that prevents composite stiffening for strains as high as 1 - 2% [52]. Also the

discontinuity of the fibers can produce stress concentration sites due to their irregular shapes; and cracks can propagate by cutting through the fillers or between them.

In addition, lack of fiber dispersion caused by the formation of agglomerates and the entanglement of discontinuous nanofibers at higher concentrations, cause matrix rich zones, which act as stress concentration sites, leading to premature failure [36]. The alignment or orientation of the fibers is also critical in providing for the uniaxial mechanical properties of such composites. Current available experimental data [53] shows that a uniform distribution and structured orientation of the short length nanofillers is generally difficult to achieve with the current mixing techniques and hence the enhancement in the mechanical and physical properties is limited to some extent.

Therefore, although CNTs and VGCNFs can provide matrix toughening, their discontinuous and wavy form does not support strengthening and can reduce the overall strength of the polymeric matrix; and the need for adequate dispersion and fiber alignment of the discontinuous nanofibers is required in order to improve the mechanical properties [37].

Electrospinning is a promising method to manufacture high performance polymer composites by rather using continuous carbon or polymer nanofibers, which can be made in a relatively efficient way while maintaining the relatively high strength and reducing the negative effects of discontinuous fillers mentioned above, such as fiber waviness, fiber agglomeration formation and irregularities causing stress concentrations. Moreover, the high percentage of porosity and irregular pores between the fibers can lead to an interpenetrated structure when dispersed in the matrix, which also enhances the mechanical strength due to an interlocking mechanism [10]. These characteristic features of nanofibers enable the transfer of applied loads to the fiber–matrix interface in a better manner than most of the commonly used filler materials.

The electrospinning process was first developed by Formhals *et al.* [56] nearly 80 years ago where their goal was to continuously produce small diameter fibers from polymer solutions and melts. Until recently, little research using electrospinning was undertaken. However, today hundreds of various polymer fiber blends have been electrospun with thanks to the renewed popularity of electrospinning by Reneker's research team. In principle, they succeeded in producing low density, porous membranes by continuously electrospinning fibers onto a stationary electrode in which it was possible to collect an arrangement of fibers forming a multilayered membrane several hundreds of microns thick.

Electrospinning is the process in which a high electric voltage, between 10-30 kV, is applied between a fine needle containing a polymeric solution and a metallic collector, to produce small diameter micro and nanofibers [57]. The electric field produced by a high electric voltage power supply produces a force that overcomes the surface tension of the polymeric solution at the needle tip. As the electric field increases, the surface of the solution at the tip of the polymeric solution begins to deform

and elongates to form a Taylor cone [58]. As the electric field increases further, it reaches a critical value where the forces overcome the surface tension of the polymeric solution droplet. When this occurs, the charged jet is then expelled from the tip of the cone towards the grounded collector [59]. As the jet travels to the grounded collector, a whipping of the fine jet occurs caused by a bending instability coupled with the electrified jet [60]. A thinning of the jet also occurs as most of the solvent evaporates in travelling to the grounded collector. The polymer nanofibers gathered on the collector are continuous and can be aligned depending on the collector type. The major parameters concerning the final diameter and quality of the electrospun fibers are namely;

1. The relevant fluid properties, such as density, viscosity, surface tension, permittivity, conductivity and viscoelasticity [61].
2. The relevant operating parameters such as flow rate, electric field strength, and electric current flow between the electrode and collector. The volumetric flow rate is closely controlled with the use of a syringe pump and the field strength may be varied by changing either the applied voltage or the distance between the electrodes [61].

The most crucial property in electrospinning is the fiber diameter which determines the mechanical properties of the fibers. Since nanofibers are attained from evaporation of the solvent and solidification of the polymer fluid jet, the fiber diameters will depend mainly on the jet diameter as well as on the polymer concentration in the jet. Another important issue with regards to electrospinning is the problem encountered with defects such as beads and pores. Therefore, in order to improve the overall properties of the electrospun fibers, the diameter of fibers as well as reduction in beading is essential. Table 2.2 below shows the effects of increasing the operating parameters on the diameter and formation of beads of the fibers.

Table 2.2: The effects of increasing the operating parameters on the diameter and formation of beads of the fibers.

Parameter Increase	Diameter	Beads
Electric Field Strength (<i>kV</i>)	Increase	Decrease
Collector Distance (<i>cm</i>)	Decrease	Decrease
Flow Rate (<i>l/h</i>)	Increase	Increase
Nozzle Diameter (<i>mm</i>)	Decrease	Increase
Polymer Concentration (%)	Increase	Decrease

Electric Field Strength – An increase in electric field strength, voltage, would be expected to reduce the diameter of fibers because of the increased stretching of the jet. However, Yarin *et al.* [62] have

shown that the diameter of fibers in fact increases due to increased whipping instability and increased flow rate. However this increase in diameter is only slight and Gu *et al.* [63] has shown that increased voltage is an insignificant factor when the concentration levels are high. It has also been found that increasing the electric field strength will create more uniform fibers with less beads [54]. This is due to electrostatic forces acting on the suspended droplet being greater than the surface tension of the droplet which induces a jet that originates from the Taylor cone.

Collector Distance – When the distance from the needle tip to the collector is increased, the fiber diameters slightly decrease. The longer distance, >15cm, enables greater stretching of the solution jet and allows the polymeric solution time to dry before being collected. Furthermore, Salman *et al.* [37] have shown that nanofibers spun with a rather large distance had the highest modulus and tensile strength, which is a result of the improved molecular orientation that is crucial for high mechanical properties. Also, shorter distances seem to increase the dripping tendency and wet fiber collection which thus increases the occurrence of beads.

Flow Rate – In general, it has been found that lowering flow rates yields fibers with smaller diameters. This is due to the fact that higher flow rates >5ml/hr do not promote the jet stability required in order to obtain a Taylor cone and thus ultimately produce nanofibers. Also, an increase in flow rate can result in beading since the polymeric solution does not have the time to dry prior to reaching the collector [54].

Nozzle Diameter – The nozzle diameter is heavily dependent on the polymer concentration of the solution and thus the viscosity of the polymeric solution. The higher the viscosity of the polymeric solution is, the larger the nozzle diameter size required. Heikkilä *et al.* [64] found that the fiber diameters produced from larger nozzle diameters, >0.5mm, were often smaller than those produced from smaller nozzles and there was less variation in fiber diameter. They suggested that this could be as a result of the more stable spinning process obtained with larger nozzle diameters which could promote a continuous solution flow.

Polymer Concentration – Solution viscosity has been found to most strongly affect fiber diameter size, with fiber diameter increasing with increasing solution viscosity according to a power law relationship [12]. The solution viscosity mainly depends on the polymer concentration and as a result the higher solution concentration results in fibers with a larger diameter. This is as expected as the molecular weight directly affects the entanglement of the polymer chains and thus reduces the stretching of the polymer solution that is required to form a continuous solution jet. Furthermore, Zong *et al.* [65] documented that increasing the polymer concentrations results in less formation of beads. At lower polymer concentrations, beading is generally observed due to the occurrence of looping bundles which is a result of wet fibers being collected.

In Summary, there exists a combination of the parameters that results in an ideal domain of potential uniform nanofibers. The fiber diameter can effectively be reduced by either decreasing the electric field strength, flow rate and polymer concentration or by increasing the collector distance and nozzle diameter. The beads can also be effectively minimized either by increasing the solution concentration, distance and applied electric voltage to a certain level or by decreasing the flow rate. According to present research this potential domain for PAN/DMF is predicted in Table 2.3 [37,54,62,63,64,65].

Table 2.3: Ideal electrospinning operating parameters for the production of PAN nanofibers

Electric Field Strength (<i>kV</i>)	10 - 20
Collector Distance (<i>cm</i>)	>15
Flow Rate (<i>l/h</i>)	1 - 3
Nozzle Diameter (<i>mm</i>)	0.5 – 1.5
Polymer Concentration (%)	8 – 10

CVD, Laser ablation and plasma techniques are still commonly used in synthesising CNFs; however electrospinning has been shown to be quite promising as the most feasible solution for industrial level fabrication, mainly due to the following reasons:

- The cheap and very simple fabrication process, using little required raw materials and treatment processes. This ultimately lends itself to a good price to unit ratio.
- Nanofibers can be spun directly on a desired substrate and the results are almost always repeatable.
- Continuous and aligned fibers can be spun up to meters in length which make for ideal reinforcing fillers.

Electrospinning has received more and more attention in recent years, with which obtained fibers have been found to have diameters as low as $3nm$ [54]. This method can be used to produce random nonwoven mats of nanofibers suitable for interface reinforcement to form hybrid multiscale composites [55]. The advantages of using these mats include:

1. They can be easily inserted between conventional fabrics, thus the addition of them does not lead to a considerable increase in processing costs.
2. They are very thin, thus the addition of them does not add significant weight increases to the final composite material.

3. The electrospun fibers in the mats are randomly oriented, thus the distribution of these fibers between adjacent laminas in the composites are relatively homogeneous.

Dzenis and Reneker [66,67] have demonstrated that a composite laminate with nanofiber mats placed at ply interfaces provides improved interlaminar toughness, strength and delamination resistance without a significant decrease of in-plane properties and an increase in weight. They found that by increasing the fiber content, the bending modulus and the toughness of the epoxy nanocomposite were slightly improved whereas the fracture energy increased quite significantly. Bergshoef and Vancso [68] also fabricated electrospun reinforced nanocomposites, using electrospun Nylon-4,6 nanofiber non-woven membranes in epoxy. They reported that both the stiffness and strength of the composite were significantly higher than those of the neat matrix, even though the fiber content was low.

Several reasons can be attributed to the lesser development of electrospun polymer nanofiber reinforced composites. Firstly, not a sufficient quantity of uniaxial and continuous nanofibers has been obtained that can be used as fiber reinforcement in composite materials. Secondly, composite theory shows that improvements of the structural properties of composites can only be attained when fibers provide homogeneous reinforcement. And lastly, electrospun PAN nanofibers possess poorly developed crystalline structures as a result of the quick solidification of the spinning polymer jet. Therefore, post-treatments are required for improving the crystalline structure and mechanical strength of the fibers by converting these polymers in to CNFs.

Therefore, more suitable fibers for the use in structural enhancement would rather be continuous electrospun CNFs that can be developed through heat treatments (i.e., stabilisation followed by carbonisation) of their electrospun precursor polymers such as PAN nanofibers [12,13,14]. These ECNFs possess an extremely high degree of macromolecular orientation and a significantly reduced amount of structural imperfections; in addition, the diameter of nanofibers is approximately 100 times smaller than that of conventional carbon fibers. As a result, the ECNFs possess superior mechanical properties that would unlikely be achieved through conventional drawing techniques. Only a few research efforts have been made to develop and evaluate composites reinforced with electrospun nanofibers [4,5,6,69,70,71,72,73].

In general, carbon fibers are known to be brittle and as such their strength is governed by both the size and distribution of flaws. In order to prepare carbon nanofibers from electrospun PAN fibers, the electrospun PAN nanofibers need to undergo a series of heat treatments as shown in Figure 2.5. The first step in the process is oxidization of the PAN precursor nanofibers commonly called stabilisation. Stabilisation is used to retain the PAN fibrous structures during subsequent high temperature carbonisation which is achieved by forming a non-meltable ladder polymer structure [37]. Stabilisation is an exothermic process and occurs in air at temperatures between 250-300°C whereby the PAN undergoes cyclization and partial dehydrogenation [16]. This process results in the formation

of carbon-nitrogen double bond ring structures forming a ladder polymer which results in denser and more stable fibers.

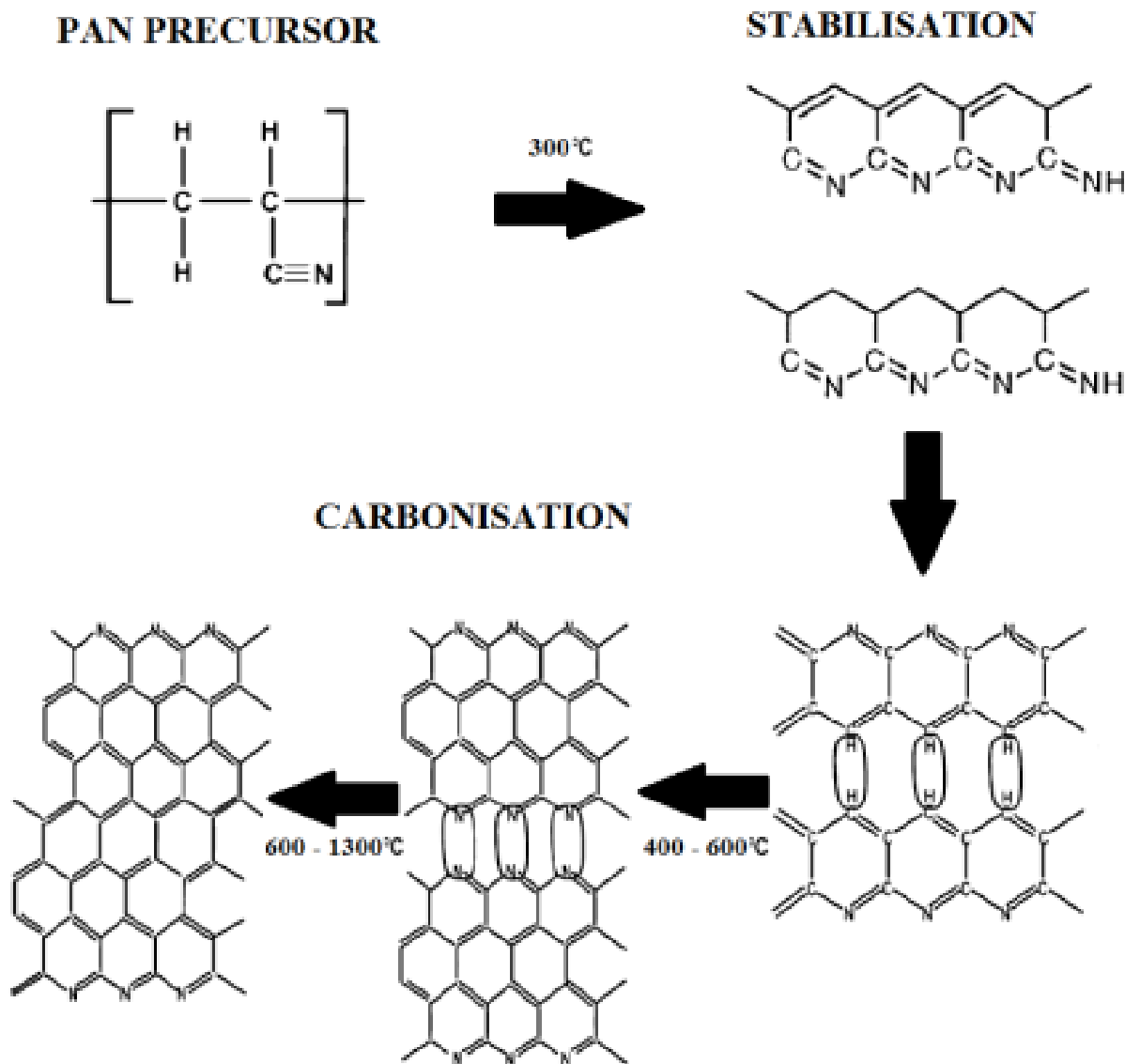


Figure 2.5: Graphical representation of the stabilisation and carbonisation procedure in order to achieve carbon fibers from PAN fibers (Figure has been reproduced from reference [74])

The stabilized PAN nanofibers are then converted into CNFs by a heating process called carbonisation, at temperatures greater than 800°C in an inert gas environment [47]. During this step, the carbon content increases significantly whilst maintaining an amorphous structure with partial crystallinity. The majority of non-carbon elements are then removed during the carbonisation process. This results in the production of high strength CNFs according to the mechanical behaviour of microscale carbon fibers. Further high temperature ($2000\text{-}3000^\circ\text{C}$) graphitization increases the crystallite size and improves the crystallite orientation along the fiber axis which results in an increased modulus monotonically. However, high temperature graphitization does reduce the strength

of the fibers above 1500°C due to the crystallite size becoming too large which initiates cracks that reduce the overall fiber strength [37].

Sancaktar *et al.* [73] produced both electrospun ECNF mats and short ECNFs; and impregnated them with epoxy resin. The mechanical properties of as-prepared nanofibers in the mat and short fiber filled epoxy nanocomposite forms were determined to demonstrate the effect of fiber aspect ratio on those properties. Their experimental results revealed that epoxy nanocomposites containing ECNFs with high fiber aspect ratio in the nonwoven mat form yielded better mechanical properties, both Storage modulus and Young's modulus, than those filled with short ECNFs.

2.2.2 *Hybrid PCs*

Research into the use of multiple different fillers to reinforce polymer matrices has also shown more controllable designs of the mechanical properties of the polymer composites. These composites are known as hybrid composites and have revolutionized the material science field. By hybridizing two or more types of fillers in a matrix allows a closer tailoring of composite properties to satisfy specific requirements. Conventional hybridization generally makes use of reinforcement fillers on the same scale of size; however, recent attention has been given to the performance of multiscale reinforced PCs, whereby the various reinforcement fillers are sized on different scales. The benefit of such a material is the improvement of physical and mechanical properties without reducing the volume fraction of the overall PC.

With nanofibers, the change in reinforcement scale relative to macro fibers offers the opportunity to combine the potential benefits of the nanoscale reinforcement with well-established fibrous composites to create multiscale hybrid micro/nano PCs. The addition of nanofibers to conventional macro fiber PCs are believed to create a synergy between the reinforcements at the two different scales, in which the final mechanical properties of the multiscale PC is improved. This synergy is formulated in the interfacial regions between fillers, and result in the improvements of the interfacial strength of the composite, likely caused by the increased shear modulus, yield strength and stiffening of the nano-reinforcement with the polymer matrix surrounding the microfiber/matrix interface and improving the local load transfer between fillers and matrix [84]. The synergetic role of the multi-scale reinforcements can be explained by the critical changes in the stress distribution near the fiber surface and the plastic zone ahead of the crack tip [85]. By varying the reinforcement scale, it may be possible to tailor the mechanical and physical properties of the composites even further, which is why the synergy of multi-scale fillers is expected to open up new opportunities to formulate high performance composites [86].

In a study by Chen *et al.* [4], CF/ECNF-epoxy composites and conventional macro CF-epoxy composites were fabricated by the method of vacuum assisted resin transfer moulding (VARTM); and their interlaminar shear strength, flexural properties, and electrical conductivities were evaluated.

Their research revealed that the incorporation of ECNF mats significantly improved the interlaminar shear strength and flexural properties of the resulting composite. The improvement of interlaminar shear strength was an increase of roughly 86%; as compared to the conventional macro CF-epoxy composite.

In a more recent study by Chen *et al.* [6], PAN nanofibers were first electrospun directly onto conventional T300 CF fabrics; subsequently, the precursor nanofibers were converted into ECNFs through heat treatments of stabilisation in air followed by carbonisation in argon. They then prepared ECNF-CF fabrics/mats and used them as novel reinforcement fillers for the fabrication of hybrid multiscale composites with SC-15 epoxy resin through the VARTM technique. The study revealed that the interlaminar mechanical properties of the ECNF-CF/epoxy composites were improved significantly when compared to those of the conventional macro CF/epoxy composites. The improvement of mechanical properties was due to the high mechanical strength of ECNFs, as well as the strong interfacial bonding strength between the ECNF-CF fabrics/ mats and the epoxy resin.

The concept of embedding aligned nanofillers into a nanofiber matrix, or doping, using electrospinning to form composite materials appears to be very promising. The combination of high aspect ratio, high strength and stiffness, low density and high flexibility of the nanofillers combined with the continuous nature of electrospun polymeric nanofibers, could improve the dispersion of nanofillers as well as the interfacial adhesion between fiber and matrix [87].

Salalha *et al.* [88] used the electrospinning process to successfully embed single-walled carbon nanotubes (SWCNTs) into a poly(ethylene oxide) (PEO) matrix, forming composite nanofibers. It was found that CNT alignment within the PEO nanofibers was strongly dependant on the quality of the initial mixing conditions, where good dispersion was characterised with separated CNTs embedded in an aligned form, whilst poor dispersion was shown as entangled non-separated CNTs incorporated as dense agglomerations.

Reneker *et al.* [89] electrospun CNTs embedded in PAN and observed that the orientation of the CNTs within the PAN nanofibers was much higher than that of the PAN's molecular crystal lattice. A strong interfacial bonding between the CNTs and the negatively charged (C:N) functional groups of the PAN polymeric chains was shown, caused by the formation of charged transfer complexes. As a result of the highly anisotropic orientation and the formation of these complexes, the composite nanofibers showed enhanced mechanical out of plane properties.

Haddon *et al.* [90] studied single walled carbon nanotubes (SWCNT) reinforced polystyrene composite nanofibers using the electrospinning process. They produced nanofibers with diameters in the range of 50–100nm which were shown to be well oriented parallel to the nanofiber axis.

Ko *et al.* [91,92] used the electrospinning process to embed both SWCNTs and multiwalled carbon nanofibers (MWCNTs) to reinforce PAN composite nanofibers. Both reinforcement and the rupture

behaviour of CNT/PAN nanofibers were studied whereby a two-stage rupture behaviour of the composite fibers under tension was shown. Distribution of CNTs within the PAN and interfacial adhesion between CNTs and PAN are the two major factors that determined the reinforcement effect. The main mechanisms of failure of the reinforced composite fibers were via CNT pull-out and the bridging mechanism [92].

The main objective in the manufacturing of continuous ECNF mat nanocomposites is to achieve excellent adhesion between the ECNF mats and the polymer matrix. Each polymer/nanofiller blend is unique and as such so is the manufacturing technique used to form a specific composite. Recently, the VARTM technique has become a useful tool for the fabrication of hybrid multiscale fiber reinforced composites. Wichmann *et al.* [79] prepared three types of multiscale fiber reinforced composites containing fumed silica, carbon black, and CNTs, respectively, using the VARTM technique. They found that the nanofiber reinforcement resulting in hybrid multiscale fiber reinforced composites significantly improved the mechanical properties whilst utilising this technique. However, only limited research has been dedicated to the development of three-phase hybrid multiscale fiber reinforced composite utilizing ECNFs [2,4,5,6,71].

In conclusion, the purpose of this study was to design a multiscale hybrid PC for application in the aerospace industry, by introducing additional reinforcement of continuous ECNF-doped polymeric fibrous mats with a conventional macro fiber PC, via VARTM, to improve its physical and in-plane mechanical properties.

3 METHODOLOGY

3.1 Materials

3.1.1 Matrix

The chosen matrix was a Bisphenol-A epoxy resin, with both the resin and hardener used in the experiments being purchased from AMT Composites Pty Ltd (South Africa) with the product name AMPREG 21 Resin and AMPREG21 standard Hardener respectively. Ampreg 21 has been designed specifically to provide excellent mechanical and thermal properties from both ambient temperature cures, and moderate temperature post cures (50°C). It is optimised for use between 18-25°C, with curing at lower temperatures resulting in the thickening of the product, which becomes unworkable, and curing at higher temperatures resulting in rapid and therefore inadequate working times. The recommended mix ratio of the resin to hardener is shown below in Table 3.1.

Table 3.1: Mix ratio of hardener to resin for Ampreg 21[104]

Hardener	Mix Ratio (Resin:Hardener)	
	by weight	by volume
Standard	100:33	100:38

An initial cure of at least 16 hours with fast hardener at 18°C is recommended by the manufacturer before demoulding. However, the system achieves similar properties with a cure time of 16 hours at 50°C or 24 hours at 21°C [104]. It was also recommended by the manufacturer to use a temperature ramp rate of 10°C/hour, when heating from ambient temperature to the post curing temperature. This was performed so as to ensure that the thermal performance of the laminate stayed above the oven temperature and no thermal shock effects would occur during the curing process. Table 3.2 shows both the physical and mechanical properties of the AMPREG 21 resin and hardener which was used to manufacture all the sample materials in the experiments performed.

Table 3.2: Physical & mechanical properties of AMPREG 21 and hardener at 25°C [104]

Resin/ Hardener (Standard)					
Initial Mixed Viscosity (cP)	Gel Time (mins)	Demould Time (mins)	Tensile strength (MPa)	Tensile Modulus (GPa)	Cured Density (g/cc)
1194	21	143	72.7	3.3	1.148

3.1.2 *Fillers/Fibers*

The primary reinforcing fillers used in the fabrication of the hybrid multiscale composite material were woven E-glass fibers donated by the Composites Facility Laboratory of the University of the Witwatersrand, Johannesburg. Table 3.3 shows the physical and mechanical properties of the E-glass fibers.

Table 3.3: Physical & Mechanical properties of E-glass woven fibers [25]

Property	Value	Unit
Specific Gravity	2.6	g/cm^3
Tensile Elongation	2.4	%
Young's Modulus	72	GPa
Tensile Strength	1.72	MPa

E-glass fiber was chosen as the primary reinforcing fiber because of its commonality, availability and reduced cost as compared with stronger S-glass fiber, which plays an important role in the African context where low cost and high availability is important [27]. In reality, the use of S-glass fibers in composite material only results in a 10% improvement of tensile strength as compared with E-glass, at twice the price [25].

The secondary reinforcing fillers used in the fabrication of the hybrid multiscale composite material were continuous electrospun PAN nanofibrous mats produced via the process of electrospinning, layered between the glass fiber mats. The PAN polymer and the DMF solvent were both obtained from Sigma Aldrich Pty Ltd (South Africa). The average diameter of the PAN fibers was below 500nm.

The tertiary or final reinforcing fillers used in the fabrication of the hybrid multiscale composite material were electrospun PAN nanofibers doped with short carbon nanofibers, also produced via the process of electrospinning, in the form of ECNF nanomats. The short carbon nanofibers were produced from stabilising and carbonising crushed electrospun PAN nanofibers and were on average below 200nm in diameter.

3.2 Experimental Process Design

The major purpose of this research was to characterise the mechanical properties of a glass fiber hybrid multiscale composite with respect to doped variations in ECNF volume fractions. In order to

fully characterise such a material, required the optimisation of three distinct composites, namely a neat glass fiber epoxy composite, followed by the addition of PAN nanomats as a secondary reinforcement of the optimum glass fiber epoxy composite and finally the addition of tertiary reinforcement in the form of ECNF doped PAN nanomats to the optimum PAN reinforced glass fiber hybrid composite. Therefore, three distinct experiments were performed in order to characterise the mechanical properties of the final composite material. The experimental designs of these experiments are explained in detail in this section of the report.

3.2.1 GRPC

The first experiment was performed in order to obtain the optimum volume fraction of glass fiber so as to produce the composite with the best in-plane mechanical strength and toughness. Three variations of glass fiber volume fractions, 16%, 24% and 32%, were chosen to be incorporated as reinforcement, ultimately for the further inclusion of PAN nanomats (experiment 2) and ECNF doped PAN nanomats (experiment 3).

In order to manufacture the GRPCs, it was necessary to first calculate the number of glass layers required to attain 16%, 24% and 32% glass fiber volume fractions. To achieve this, the average mass of a single woven glass fiber layer with the mould dimensional area of 19cm x 19cm was weighed and found to be 14.5g. Therefore, the mass per area of a single layer was calculated to be;

$$\frac{14.5\text{g}}{19\text{cm}\times 19\text{cm}} = 0.040166\text{g}/\text{cm}^2$$

The number of glass layers required for the glass volume fraction was calculated using Equation 3.1.

$$n_{\text{layers}} = \frac{\rho_{\text{glass}} \times t_{\text{mould}} \times V_{\text{glass}}}{m_{\text{Area}}} \quad (3.1)$$

where, $\rho_{\text{glass}} = 2.58\text{g}/\text{cm}^3$

$t_{\text{mould}} = 0.4\text{cm}$

$V_{\text{glass}} = 0.16, 0.24$ or 0.32

$m_{\text{areal}} = 0.040166\text{g}/\text{cm}^2$

Therefore, by substituting the variables into the above equation the number of layers for each of 16%, 24% and 32% were calculated as 4, 6 and 8 glass layers, respectively. The different number of layers per volume fraction of 16%, 24% and 32%, were then layered in the VARTM mould, processed and cured, after which samples were prepared and the material properties were determined. The simplified manufacturing process of the neat glass fiber composites is shown below in Figure 3.1.

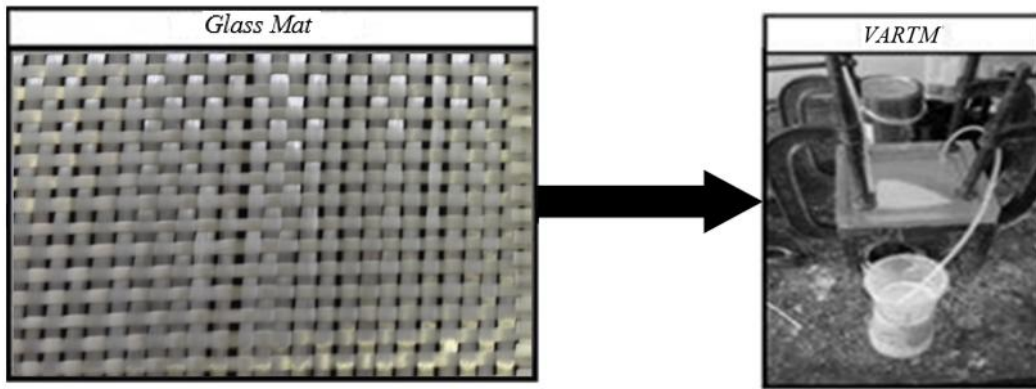


Figure 3.1: Simplified manufacturing process of the neat glass fiber composites

The VARTM setup used in the research consisted of a 3 stage mould, piping, valves and a vacuum pump as shown in Figure 3.2. The vacuum pump was able to provide a maximum pressure of $100kPa$. The mould itself was modelled according to moulds used previously for VARTM composites and manufactured in the laboratory workshop. The mould consisted of a steel stand, rubber seals, a bottom steel plate, centre steel frame and Perspex top mould. The casting process was identical for each sample prepared using the VARTM process with the conditions of the mould, resin flow rate, cleaning process, epoxy mix ratio, fiber mat layup and environment being unaltered throughout the complete casting process for all samples.

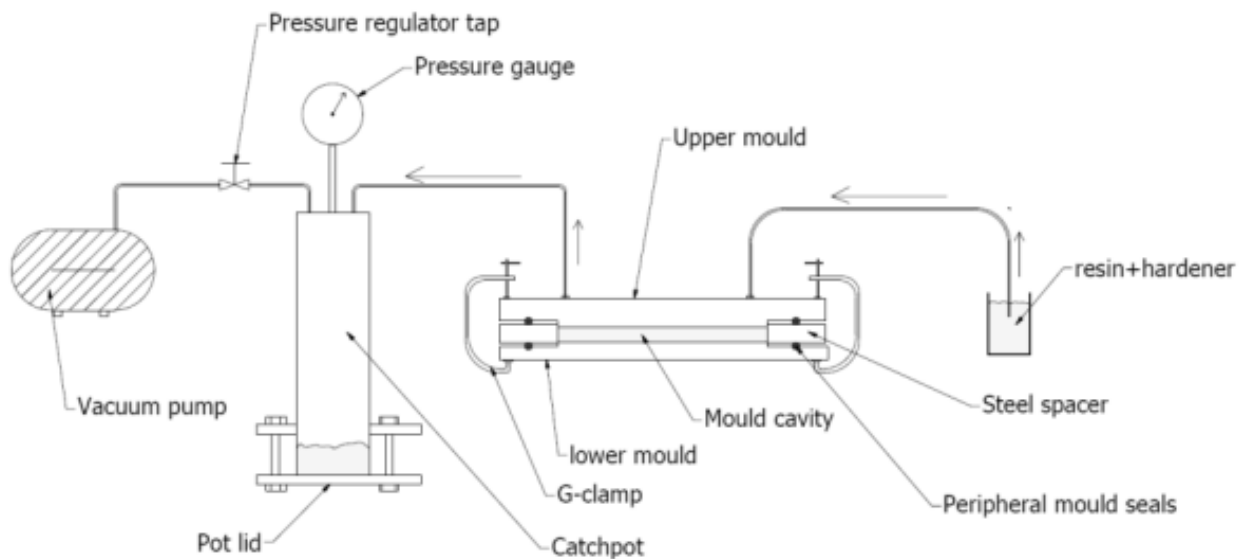


Figure 3.2: Schematic drawing of the VARTM setup used to cast all composite plates

The fabrication of composite plates began with the waxing of all surfaces that would be in contact with the resin using Ram wax and was allowed five minutes to dry before placing any mats. The O-ring seals were then inserted into the seal glands/grooves of the male and female mould components, after which the female mould was placed onto the stand and the middle mould component then was placed on top of the female mould component.

The male mould component was then placed on top of the stacked mats, and then all three components were tightly compressed together with the application of G-clamps on each corner of the mould such that both seals were fully compressed. The tube fitting plugs were then connected to both the mould adaptor inlet and outlet adaptors of the male mould, after which the other end of the tube fitting plug was connected from the male mould outlet to the vacuum resin trap inlet adaptor. The resin was then prepared by measuring out 124ml of epoxy resin into a measuring cup and then adding 76ml of standard hardener. This gel solution was then stirred gently with a spoon until the hardener had completely mixed with the resin.

The inlet resin tube was then placed into the measuring cup and the vacuum pump was turned on with the in-line check valve closed. The in-line check valve was slowly opened until the pressure on the gauge rose to 40kPa, after which the valve was then closed to maintain the system pressure at 40kPa. At this pressure, the resin mixture started to flow into the mould cavity as shown in Figure 3.3.

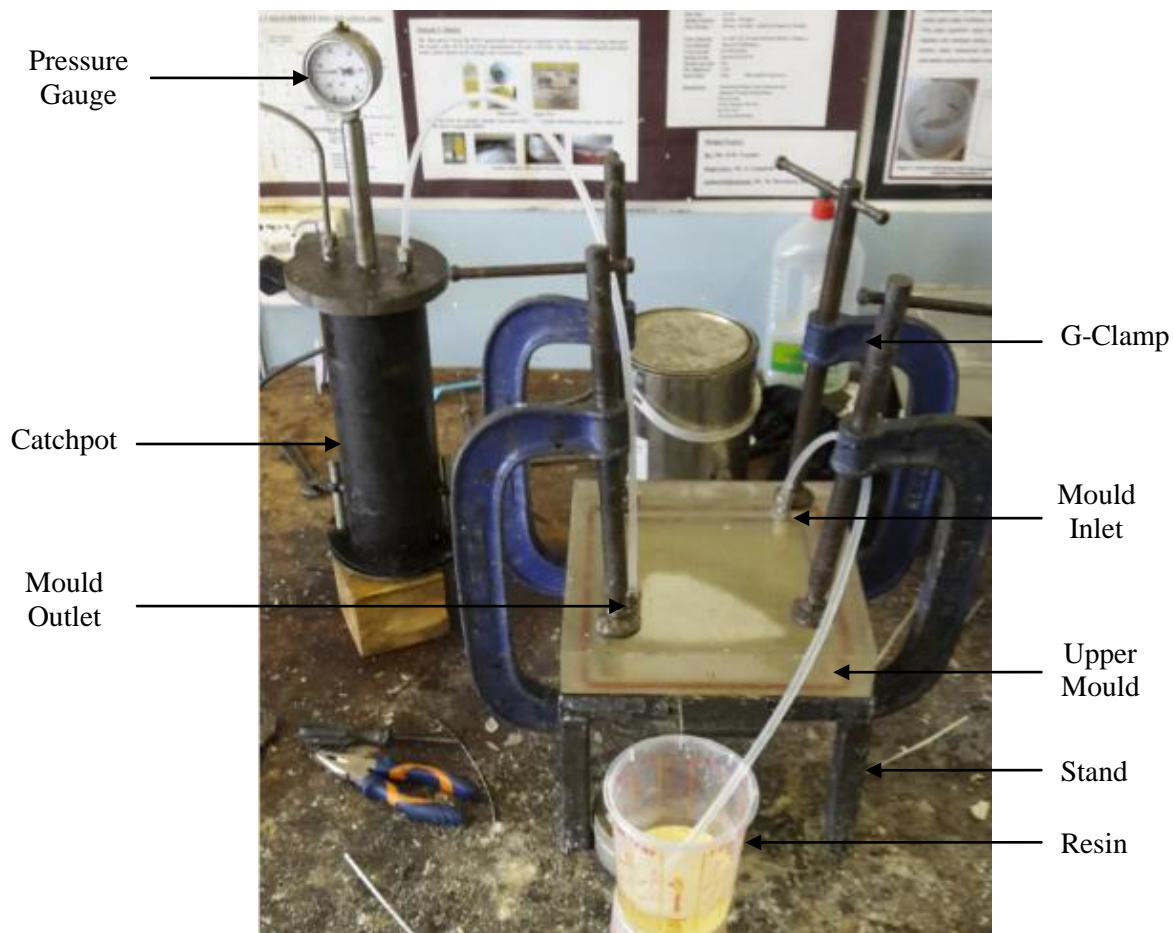


Figure 3.3: VARTM setup during operation

When the mould cavity had filled and the vacuum tube was full of resin, the pump was turned off and all tubing was then removed from the mould and cleaned in acetone. The mould was then left for 24hrs in order for the resin mixture to cure, and the solidified plates were removed from the mould cavities.

In order to determine the mechanical properties of the composite materials, a series of mechanical tests were carried out which included tensile testing, flexural testing and impact testing according to the standards developed by the American Society for Testing and Materials (ASTM). However, before testing could be performed the testing samples had to be prepared from the VARTM plates in accordance with the various testing ASTM standards. The testing samples required for tensile testing were obtained from a single VARTM produced plate whereas both impact and flexural testing specimens were obtained from sharing a single plate.

Five specimens per test (tensile, flexural and impact) were used according to ASTM D638:2010, ASTM D790:2010 and ASTM D256:2010 respectively. A marking pen and steel ruler were used to divide the tensile plate into 5 rectangular strips – 165mm long and of width 20mm, for use in tensile testing. 5 rectangular strips were then also divided - 124mm long and 13mm wide on the second plate, for use in flexural testing. On the same plate, 5 rectangular strips were marked - 64mm long and 10mm wide, and a 2.5mm depth notch for use in impact testing. The DoAll contour band saw, shown in Figure 3.4, was then used to cut out all the marked rectangular shapes on each plate.



Figure 3.4: Image of the DoALL band saw which was used to cut composite plates

Rectangular tensile samples were then machined into dog-bone specimens for tensile testing using the high pressure compressed air TensilKut machine as shown in Figure 3.6, in conjunction with the shaping tool template, Figure 3.5. The rectangular specimens were placed into the shaping jig with a gauge section which is 60mm long and 10mm wide, with upper and lower guide bars which were tightened at either end to hold the test specimen firmly in place.



Figure 3.5: Stainless steel template used to hold the rectangular tensile specimen during shaping

The TensilKut machine was then run at full speed during which the jig was slid into the guide rails and slowly pushed through the slot so that the cutting tool passed along the entire edge of the test specimen. The jig was then slid out of the slot and turned around so that the other side of the test specimen could be shaped.



Figure 3.6: TensilKut diamond shaping tool used to shape the tensile dog-bone specimens

The cutting equipment described above generated a substantial amount of dust and flying debris during the cutting operation which was a respiratory safety hazard, and could cause injury. To reduce this potential safety hazard, a dust extractor was used. Figure 3.7 shows the visual comparison between the finalised neat epoxy samples (A) and the glass reinforced samples (B).

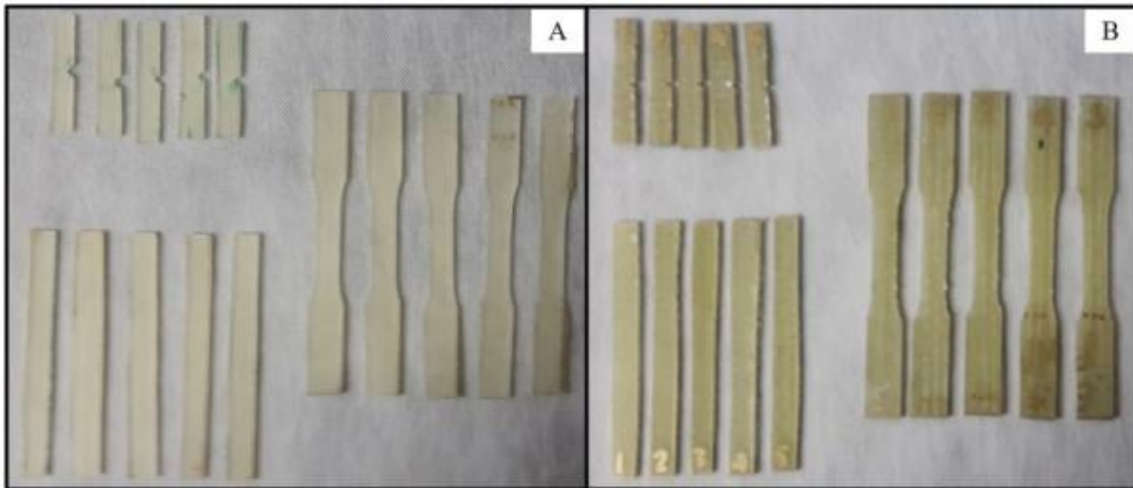


Figure 3.7: Visual comparison between the neat epoxy samples (A) and the glass reinforced samples (B)

As discussed, all testing performed in this experimental research was performed in accordance with the ASTM standards for each particular test with all samples failing within the corresponding gauge lengths. The full set of raw data obtained from all the mechanical tests can be found in Appendix A. Sample calculations can also be found in Appendix B, to help the reader better understand the data processing procedure.

3.2.2 *PAN Nanomat Reinforced GRPC*

The second experiment was performed using the optimum volume fraction GRPC (32%) obtained from the results of Experiment 1, and adding secondary reinforcement in the form of layered interlaminar PAN nanomats electrospun directly onto the glass fiber mats. The main role of the nanofibers was to reduce the stress concentration due to the mismatch of ply properties, typical of multidirectional laminates, as well as to bond the adjacent plies without increasing either the composite weight or the laminate thickness. As with the GRPCs, three volume fractions were experimented with in order to obtain the optimum volume fraction of PAN fibers to produce the composite with the best in-plane mechanical properties. The three volume fractions of PAN used were 0.1%, 0.2%, 0.5%. Figure 3.8 shows the simplified manufacturing process of the PAN mat reinforced glass fiber composites.

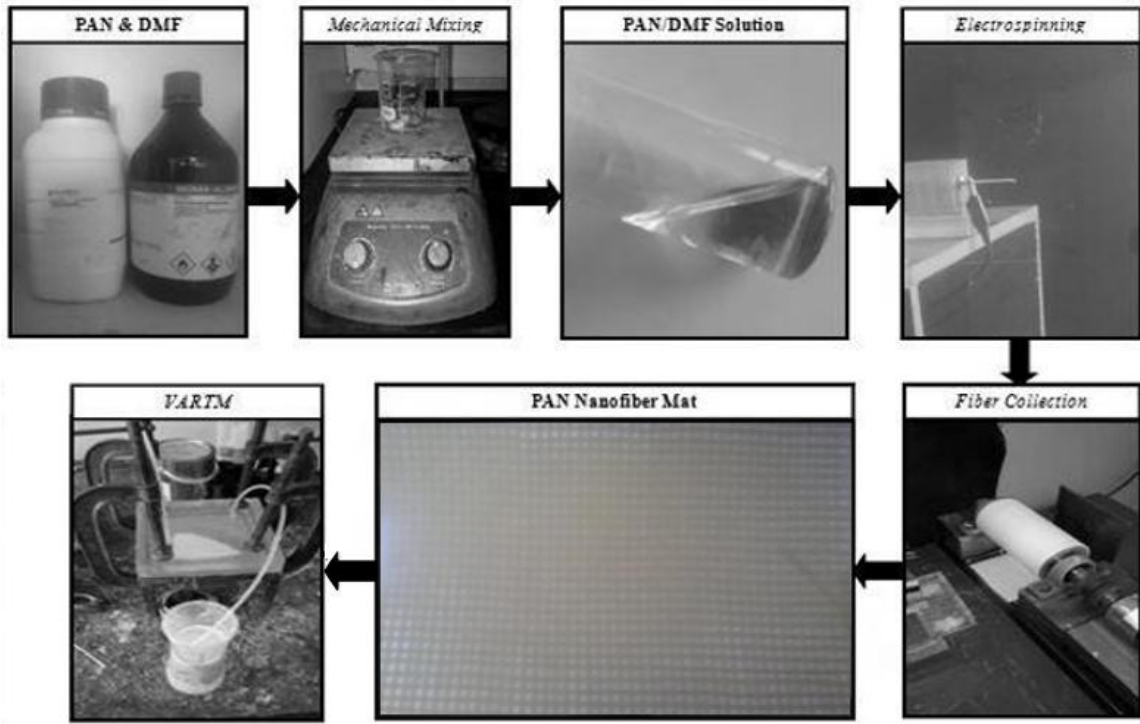


Figure 3.8: Manufacturing process of the PAN mat reinforced glass fiber composites

Before experimentation could begin, the design of the composites needed to be performed. The first step was to calculate the density of the entire composite using the rule of mixtures for laminate composites shown below in Equation 3.2.

$$\rho_{comp} = V_{fglass} \rho_{glass} + V_{fepoxy} \rho_{epoxy} + V_{fpan} \rho_{pan} \quad (3.2)$$

where, $\rho_{glass} = 2.58g/cm^3$

$\rho_{epoxy} = 1.14858g/cm^3$

$V_{fglass} = 0.32$ (Optimum GRPC)

$V_{fepoxy} = 1 - V_{fglass} - V_{fpan}$

$\rho_{pan} = 1.184 g/cm^3$

$V_{fpan} = 0.01, 0.02$ or 0.05

By substituting the V_{fepoxy} variables into the above equation, the density of the composite for each of 0.1%, 0.2% and 0.5% were calculated as $1.6061 g/cm^3$, $1.6073 g/cm^3$ and $1.6084 g/cm^3$, respectively. Clearly, the volume fractions of the PAN have a negligible effect on the density of the overall composite. With the density of the entire composite and the volume of the mould known, the mass of the composite was found using Equation 3.3.

$$\begin{aligned}
m_{comp} &= \rho_{comp} \times V_{mould} & (3.3) \\
&= 1.61g/cm^3 \times 144.4 cm^3 \\
&= 232.5g
\end{aligned}$$

where, V_{mould} = width (19cm) x length (19cm) x thickness (0.4cm)

$$= 144.4cm^3$$

The next step was to convert the PAN volume fractions into mass fractions in order to determine the PAN mass required, which makes use of Equation 3.4.

$$\begin{aligned}
W_{fpan} &= \frac{\rho_{pan} \times V_{fpan}}{\rho_{comp}} & (3.4) \\
&= \frac{1.184g/cm^3 \times V_{fpan}}{1.61g/cm^3}
\end{aligned}$$

By substituting the V_{fpan} variables into the above equation, the W_{fpan} for each of 0.1%, 0.2% and 0.5% were calculated as 0.07%, 0.15% and 0.37%, respectively. Substituting the results from Equation 3.3 and Equation 3.4 into Equation 3.5 below resulted in the determination of the required mass of PAN needed to be collected on the plate to provide for the correct volume fractions of PAN.

$$m_{pan} = W_{fpan} \times m_{comp} \quad (3.5)$$

By substituting the W_{fpan} variables into the above equation, the m_{pan} for each of 0.1%, 0.2% and 0.5% were calculated as 0.17g, 0.34g and 0.86g respectively. The mass of PAN was then converted into the volume of PAN required, using Equation 3.6.

$$V_{pan} = \frac{m_{pan}}{\rho_{pan}} \quad (3.6)$$

where, $\rho_{pan} = 1.184 g/cm^3$

By substituting the m_{pan} variables into the above equation, the V_{pan} for each of 0.1%, 0.2% and 0.5% were calculated as 0.14ml, 0.28ml and 0.72ml, respectively. With the volume of PAN required to electrospin known, the volume of PAN/DMF was equated using Equation 3.7.

$$V_{pan/dmf} = \frac{V_{pan}}{pan_{conc.}} \quad (3.7)$$

where, $pan_{conc.} = 0.08$ (8% solution – see Section 4.2 for more detail)

Therefore, by substituting the V_{pan} variables into the above equation, the $V_{pan/dmf}$ for each of 0.1%, 0.2% and 0.5% were calculated as 1.8ml, 3.6ml and 9.0ml, respectively. Thus, at a dispensing speed of 1ml/hr per needle and with 6 needles (see Section 4.1 for more detail), these volumes were fully dispensed after 18mins, 36mins and 90mins, respectively. However, because there are 8 glass layers, this becomes electrospinning for 2.3 mins/sheet, 4.6 mins/sheet and 11.3 mins/sheet. Therefore, to conclude, the amount of PAN/DMF solution required to be electrospun for each layer was calculated by dividing the $V_{pan/dmf}$ result calculated from Equation 3.7 by the number of layers calculated using Equation 3.1 and the number of needles utilised - six.

With the design phase of the experiment complete, the experimental process then began with firstly preparing the PAN/DMF solution required to electrospin, by mechanical mixing the constituents with a magnetic stirrer for 24hrs. The electrospinning of PAN fibers onto the glass mats was then performed using the electrospinning facility, to be described in more detail in section 4.1, located at the University of the Witwatersrand's nanocomposite lab. The first step of the electrospinning procedure was to fill the syringes with the required amount of 8% PAN/DMF solution as calculated using Equation 3.7. The filled syringes were then loaded into the syringe holder blocks and tightened in place in order to prevent the syringes from moving during operation as shown in Figure 3.9. The PTFE Teflon tubing was then attached to the nozzles of the syringes with the other end of the PTFE Teflon tubing attached to the luer lock connectors with the 17G needles connected to the other end of the luer lock connectors.



Figure 3.9: Loaded Syringes in NE-1600 syringe pump

The slider piece was then adjusted to set the required distance of the needle tips from the collectors' surface. A small Petri dish filled with acetone was placed beneath the needle tip, between the syringe pump and collector, so as to evaporate the solvent during the electrospinning process. Woven fiber glass sheets were then weighed, cut into the mould dimensions and then secured onto the drum collector with rubber bands. The syringe pump was then pre-set to the required; syringe diameters, flow rates as well as the volume to be dispensed, before which the drum motors rotational speed was slowly increased, using the motor controller, to the required electrospinning collection speed. The high voltage power supply, shown in Figure 3.10, was then adjusted to the predetermined voltage or until a Taylor cone was reached and fibers were being spun onto the collector.



Figure 3.10: High voltage power supply used to supply the electric field for the electrospinning process

When the correct voltage was reached, the perspex casing surrounding the facility was closed and the syringe volume was monitored until the syringe pump reached the preset dispensation. Finally, the high voltage power supply was then turned off and the equipment was de-energised before the mat was removed from the drum. The glass fiber/PAN mats were then layered in the VARTM mould as shown in Figure 3.11, processed and cured, after which samples were prepared and the material properties were determined.

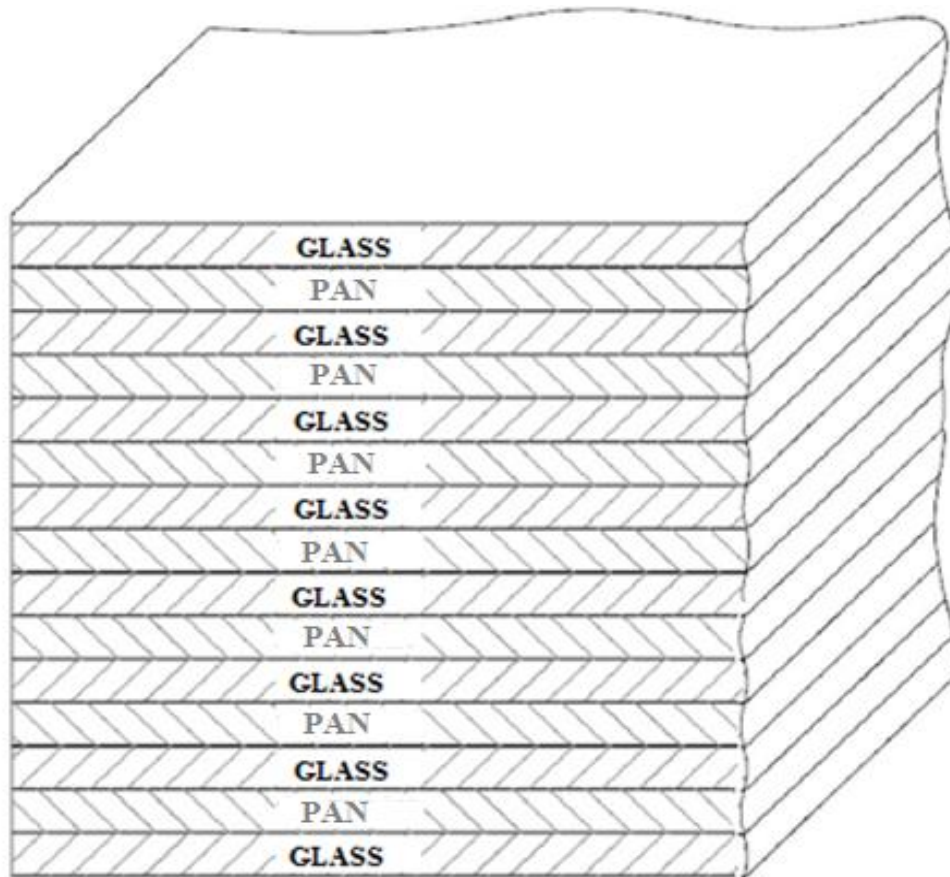


Figure 3.11: Fiber mat layup placed into the VARTM

The VARTM procedure followed for the PAN/GRPC was identical to that of the neat GRPC, however during the VARTM processing of the PAN/GRPC it was observed that there was an increase in required pressure for the correct flow rate, as the PAN volume fraction increased. This was caused by the PAN coatings covering the spaces between the glass fiber bundles in the mats. Therefore, the denser the PAN coatings were, the higher the required pressure required was, and was therefore controlled accordingly. It was also observed during the moulding process that the resin tended to take the path of least resistance around the fiber mats which caused a dry area near the exit of the mould, as shown in Figure 3.12. This dry area was eventually wetted however small bubbles were observed near and around this area for the majority of the PAN coated samples. Therefore, areas of partial wetting were discarded from the plates used for preparing testing samples.

The cleaning of the mould as well as the cleaning of the tubes and auxiliary equipment was vital in producing low void plates. Any blockages of the pipes, lack of a good seal/vacuum of the mould or foreign particles in sample plates showed a rise in voids and ultimately provided lower strength sample plates. The mixture ratio of the epoxy to hardener was also crucial as the incorrect mixing ratio could lead to the matrix not curing properly or curing too quickly (decreasing the gel time) which could result in the blockages of the tubes.

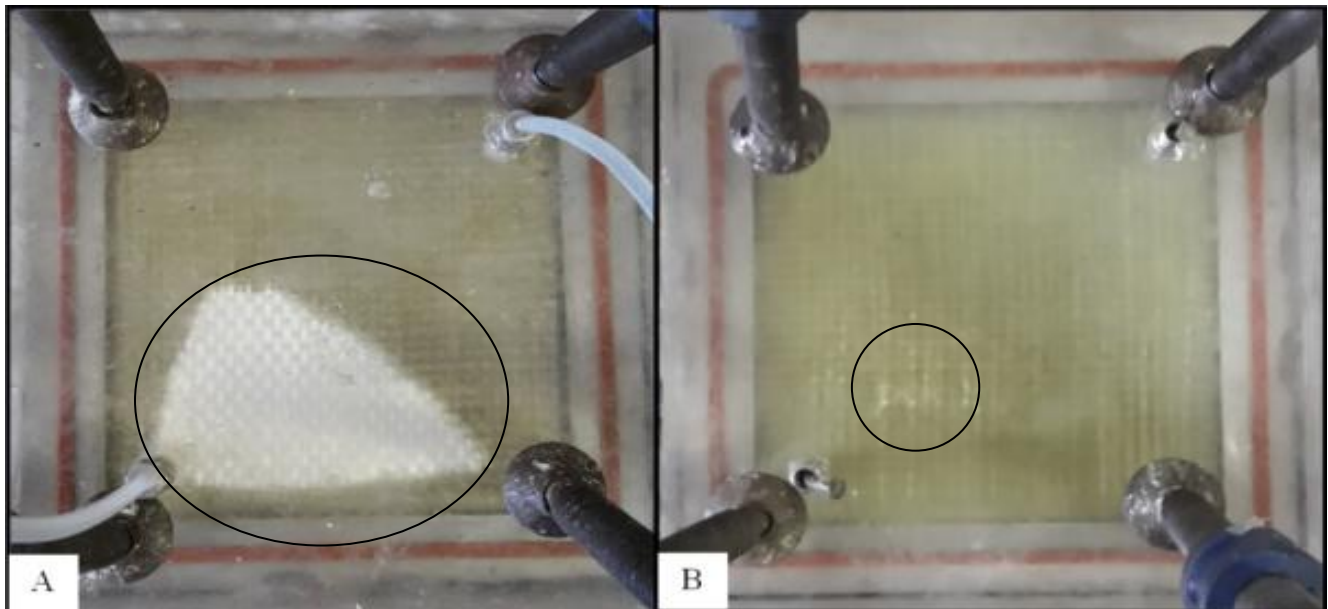


Figure 3.12: Time lapsed images of a VARTM casting process showing the remnants of an un-wetted fiber zone of a sample with high PAN fiber volume fraction reinforcement

As with the neat GRPC, the casting process was identical for each sample prepared using the VARTM process with the conditions of the mould, resin flow rate, cleaning process, epoxy mix ratio, fiber mat layup and environment being unaltered throughout the complete casting process for all samples. Also, as with the GRPC, in order to determine the mechanical properties of the composite materials, a series of mechanical tests were carried out which included tensile testing, flexural testing and impact testing according to the standards developed by the American Society for Testing and Materials (ASTM). Five specimens per test (tensile, flexural and impact) were used according to ASTM D638:2010, ASTM D790:2010 and ASTM D256:2010 respectively.

3.2.3 *ECNF Doped PAN Nanomat Reinforced Hybrid Composite*

The final set of samples prepared were that of the ECNF reinforced PAN fiber reinforced glass fiber epoxy composite whereby 2 variations of ECNF volume fractions, 0.5% and 1%, were incorporated into each of the PAN volume fraction 0.1%, 0.2% and 0.5% composites, to obtain the optimal hybrid composite material properties. The process began with preparing the PAN/DMF solution required to electrospin, also using the process of mechanical mixing. PAN fibers were then collected and carbonised to form ECNFs in a vacuum tube furnace. The resultant ECNFs were then refined and sonicated with DMF before being electrospun directly onto the glass fiber mats, with different volume fractions of ECNFs 0.5% and 1.0%, respectively. The overall methodological process flow for the fabrication of the goal, ECNF/PAN hybrid composite material is shown in Figure 3.13, which is discussed in detail in the remainder of this chapter.

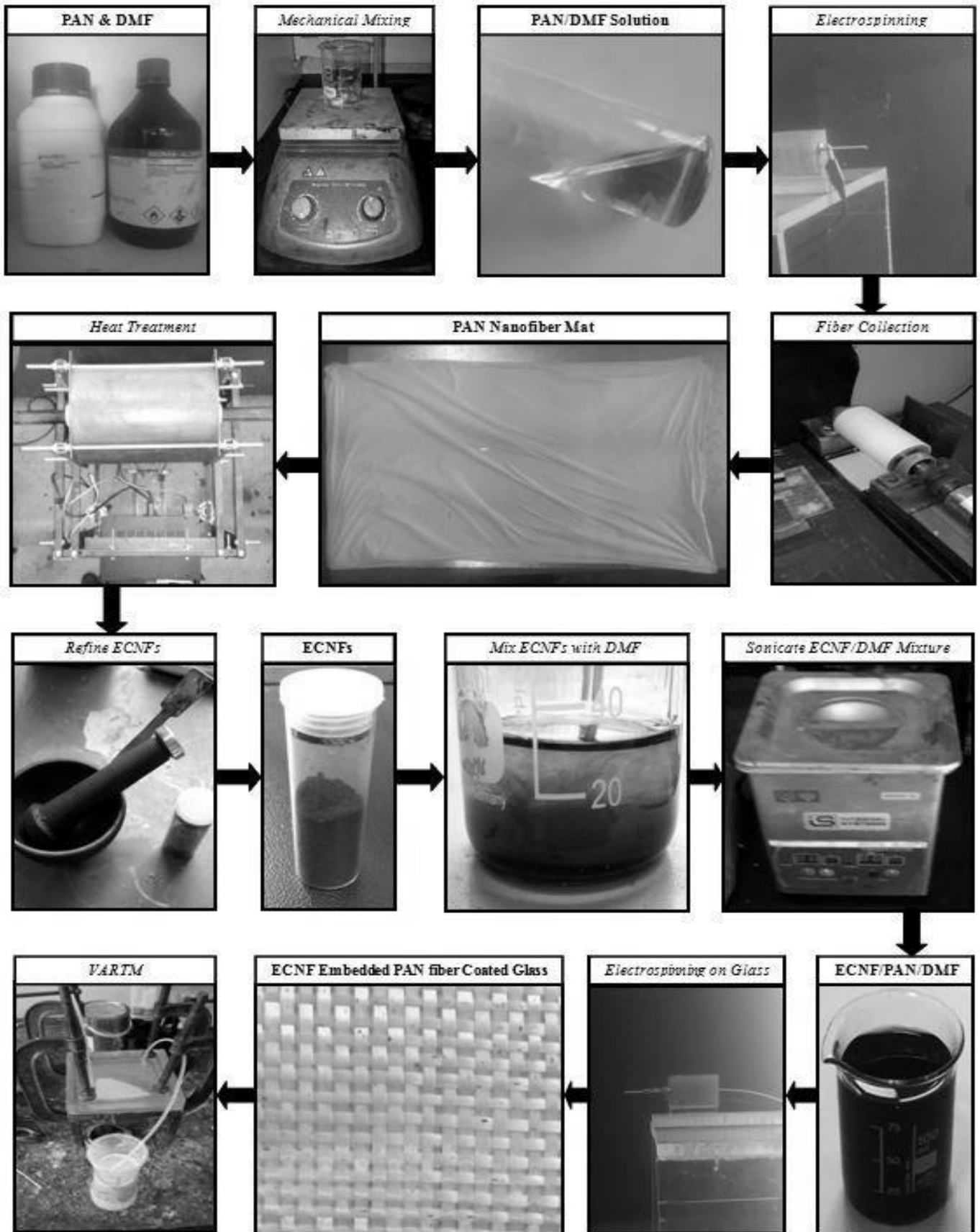


Figure 3.13: Full process schematic showing the experimental procedures performed

The first step in the research design process was to calculate the volume of PAN/DMF to prepare in order to achieve the volume fractions of ECNFs (0.5% and 1.0%). In order to achieve this, the density of the entire composite needed to be calculated. The rule of mixtures for laminate composites was used to calculate the overall composite density as shown below in Equation 3.8. The density of the final ECNFs was assumed to be 2.00g/cm³, according to Zussman *et al* [44].

$$\rho_{comp} = V_{fglass} \rho_{glass} + V_{fepoxy} \rho_{epoxy} + V_{fcnf} \rho_{cnf} \quad (3.8)$$

where, $\rho_{glass} = 2.58g/cm^3$

$\rho_{epoxy} = 1.14858g/cm^3$

$V_{fglass} = 0.32$

$V_{fepoxy} = 1 - V_{fglass} - V_{fcnf}$

$\rho_{cnf} = 2.00g/cm^3$

$V_{fcnf} = 0.005$ or 0.01

With the density of the entire composite and the volume of the mould known, the mass of the composite was found using Equation 3.9.

$$m_{comp} = \rho_{comp} \times V_{mould} \quad (3.9)$$

where, $V_{mould} = \text{width } (19cm) \times \text{length } (19cm) \times \text{thickness } (0.4cm)$

$= 144.4cm^3$

The next step was to convert the ECNF volume fractions into mass fractions in order to determine the ECNF mass required, which makes use of Equation 3.10.

$$W_{fcnf} = \frac{\rho_{cnf} \times V_{fcnf}}{\rho_{comp}} \quad (3.10)$$

Substituting the results from Equation 3.9 and Equation 3.10 into Equation 3.11 below, resulted in the determination of the required mass of ECNFs needed to be collected on the plate to provide for the correct weight fractions of CNFs.

$$m_{cnf} = W_{fcnf} \times m_{comp} \quad (3.11)$$

During stabilisation and carbonisation, the PAN nanofibers' weight is reduced by between 45-55% depending on the heat treatment conditions used [112]. Therefore, a PAN mass degradation ratio of 0.5 was chosen to apply to the PAN mass so as to account for mass losses during carbonisation, as shown in Equation 3.12.

$$m_{pan} = (1 + m_{deg}) \times m_{cnf} \quad (3.12)$$

$$V_{pan} = \frac{m_{pan}}{\rho_{pan}}$$

where, $m_{deg} = 0.5$

$$\rho_{pan} = 1.184 \text{ g/cm}^3$$

With the mass of PAN required to electrospin to obtain the required CNF volume fractions known, the volume of PAN/DMF was equated using Equation 3.13, where the $pan_{conc.} = 0.08$ (8% solution).

$$V_{pan/dmf} = \frac{V_{pan}}{pan_{conc.}} \quad (3.13)$$

Therefore, the amount of PAN/DMF solution needed to be spun for each layer was calculated by dividing the $V_{pan/dmf}$ result calculated from Equation 3.13 by the number of layers calculated using Equation 3.1. The ECNF volume fractions were calculated based on these $V_{pan/dmf}$ values and were added by mass to the solution. As a result, the volume fractions of 0.5% ECNFs and 1.0% ECNFs correlated to an addition of 0.15g and 0.30g to the $V_{pan/dmf}$ solution, respectively. When calculated as an addition of ECNFs to the overall volume fraction of the composite, the results were an addition of 0.03% and 0.06% ECNFs, respectively.

The chosen 8% volume fraction PAN/DMF solution mixture was unchanged for the electrospinning of the ECNFs embedded in the PAN nanofibers. Sonication was performed for 30mins on the ECNF/DMF mixtures to ensure even distribution of the fibers in the DMF. After sonication, the mixtures were visually opaque, as shown in Figure 3.14, which was an indication of good dispersion.



Figure 3.14: Sonicated ECNF/DMF solution

The PAN masses as calculated in Equation 3.12 for each of the volume fractions 0.1%, 0.2% and 0.5% PAN was then added to separate ECNF/DMF mixtures and magnetically stirred for a further 24hrs to completely dissolve the PAN and evenly disperse the ECNFs in the solution. The 0.5% and 1.0% volume fraction ECNF/PAN mixtures were then electrospun with the electrospinning parameters as to be described in Section 4.2. Figure 3.15 shows the final collection of ECNF/PAN fibers in mat form, directly electrospun onto a glass fiber mat.

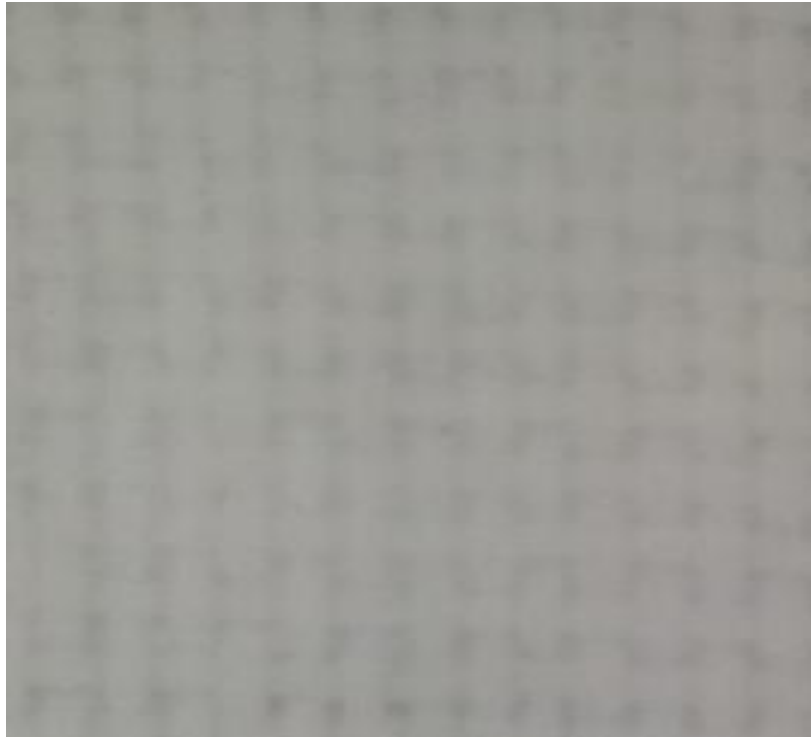


Figure 3.15: Good dispersion of PAN nanofibers on a woven glass mat

However, volume fractions of above 1.0% ECNF/PAN/DMF mixtures could not be electrospun in the same manner because of the increased viscosity, and as such the applied voltage was decreased to 12kV and the distance between the electrodes was increased to 25cm, or until smooth fiber production was reached. Constant clogging of the needles was observed at the higher ECNF concentration which could have been caused by agglomeration of ECNFs into micro sized bundles as well as the increased viscosity.

The final collection of >1% volume fraction ECNF embedded in 0.5% volume fraction PAN nanofibers on a glass mat shown in Figure 3.16. From this image it can be seen that there are in fact large agglomerations of ECNFs which were encapsulated in the PAN fibers during electrospinning. The uniformity and distribution of ECNFs hence not evident in volume fractions above 1%, however further analysis using SEM and TEM was required in order to characterise the distribution of ECNFs within the PAN nanofiber, which will be discussed later.

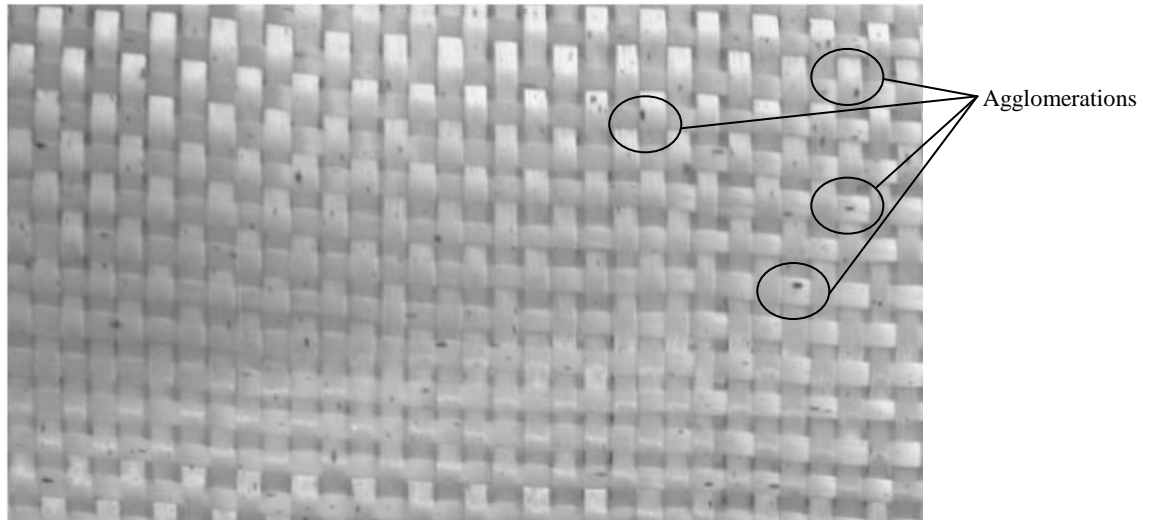


Figure 3.16: Macro-agglomerations of ECNFs imbedded in the PAN fibers electrospun onto the woven glass mats

The glass fiber/PAN/ECNF mats were then layered in the VARTM mould as per the neat GRPC, processed and cured, after which samples were prepared and the material properties were determined. As with the GRPC, the casting process was identical for each sample prepared using the VARTM process with the conditions of the mould, resin flow rate, cleaning process, epoxy mix ratio, fiber mat layout and environment being unaltered throughout the complete casting process for all samples.

Also, as with the GRPC, in order to determine the mechanical properties of the composite materials, a series of mechanical tests were carried out which included tensile testing, flexural testing and impact testing according to the standards developed by the American Society for Testing and Materials (ASTM). Five specimens per test (tensile, flexural and impact) were used according to ASTM D638:2010, ASTM D790:2010 and ASTM D256:2010 respectively. During specimen preparation, it was observed that burring did occur on the gauge sections of all the ECNF/PAN reinforced composite tensile dog bone samples caused by the TensilKut machine not being able to apply the necessary rotational speed/force to shape the stronger reinforced samples. This was particularly evident with the 0.5% ECNF/PAN samples whereby the heat generated from the shaping burnt the gauge length edges, but this had no effect on the gauge width. The burrs were easily removed with a flat hand file and Stanley knife.

3.3 Mechanical Testing

3.3.1 *Tensile Testing*

The standard guidelines that pertain to the tensile testing of plastic composite materials are given in the ASTM D638:2010, which specifies that a tensile composite specimen be cut into the ‘dog-bone’ dimensions shown in Figure 3.17. This particular shape of the dog-bone specimen guarantees that failure would occur at the region of minimum cross section, called the gauge length, which allows for repeatability and accuracy in the tensile testing of all composite materials.

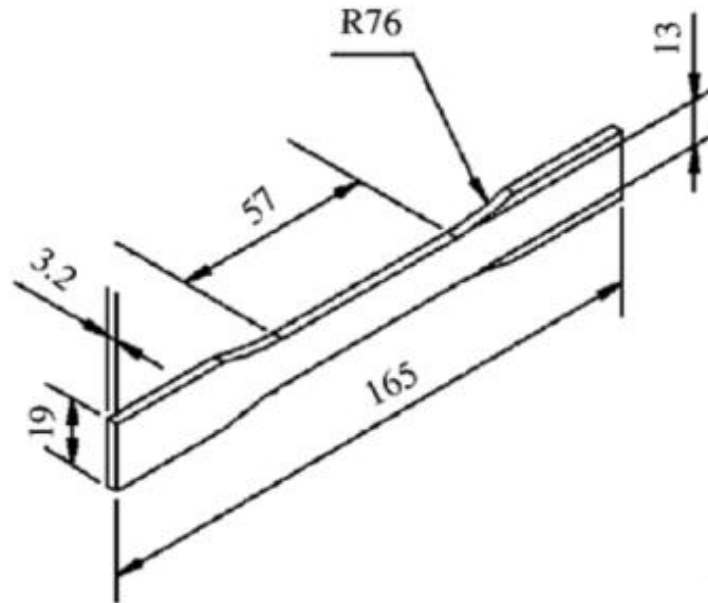


Figure 3.17: Tensile testing sample dimensions as per ASTM D638:2010

The general apparatus required to perform a tensile test according to ASTM standards include a universal testing machine with self-aligning grips, a load indicator, a set of Vernier callipers and an extension indicator such as an extensometer. The parameters and conditions under which the tensile test should be performed are given in Table 3.4 below.

Table 3.4: Parameters and conditions for Tensile Test

Parameter	Value
Temperature	$23 \pm 2^{\circ}\text{C}$
Relative humidity	$50 \pm 5 \%$
Test speed	$2 \pm 25\% \text{ mm/min}$

The tensile testing was performed using the Shimadzu AG-IS Autograph machine as shown in Figure 3.18 with a 20kN load cell used for testing. The laser extensometer was used to measure the change in length of the gauge section of the tensile testing specimen. The laser extensometer recorded change in length which was combined with the corresponding force recorded by the load cell and combined using an 8-channel data acquisition tool.

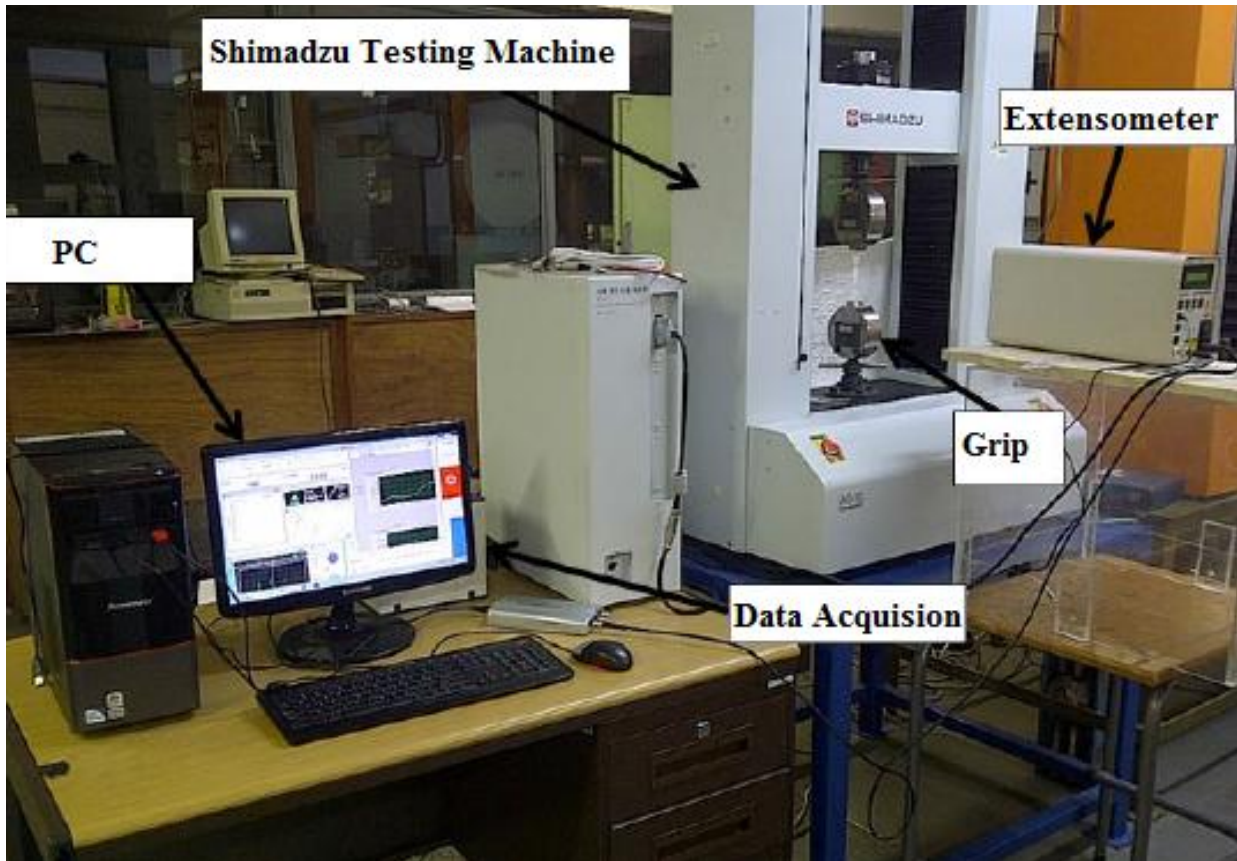


Figure 3.18: The Shimadzu testing equipment in operation

ASTM D638:2010 required a minimum of five specimens to be tested, of which all have to break along the gauge length of the specimen for the test result to be rendered valid. The general testing procedure, as specified by ASTM D638:2010 for the determination of tensile properties of plastic composites was followed [93]. Firstly a set of Vernier callipers was utilised to measure the width and thickness of each test specimen at three points along the gauge length. Secondly, the machine was configured for tensile testing by using the tensile testing attachment jaws also shown in Figure 3.19. The bottom jaw remained fixed while a velocity was pre-set to the top jaw using the user software. The test specimen was then placed into the jaws of the machine grips and tightened so that the specimen was held firmly enough in the jaws not to slip during testing. The Shimadzu testing machine possesses an internal encoder which measures the displacement of the jaws, however for the tensile testing dog-bone specimens, which do not have a constant cross sectional area, the use of the laser extensometer was required. Extension indicator strips were then fitted horizontally onto the gauge length of the test specimen. The machine was then set to the desired testing speed of $2\text{mm}/\text{min}$ and the test was then run.

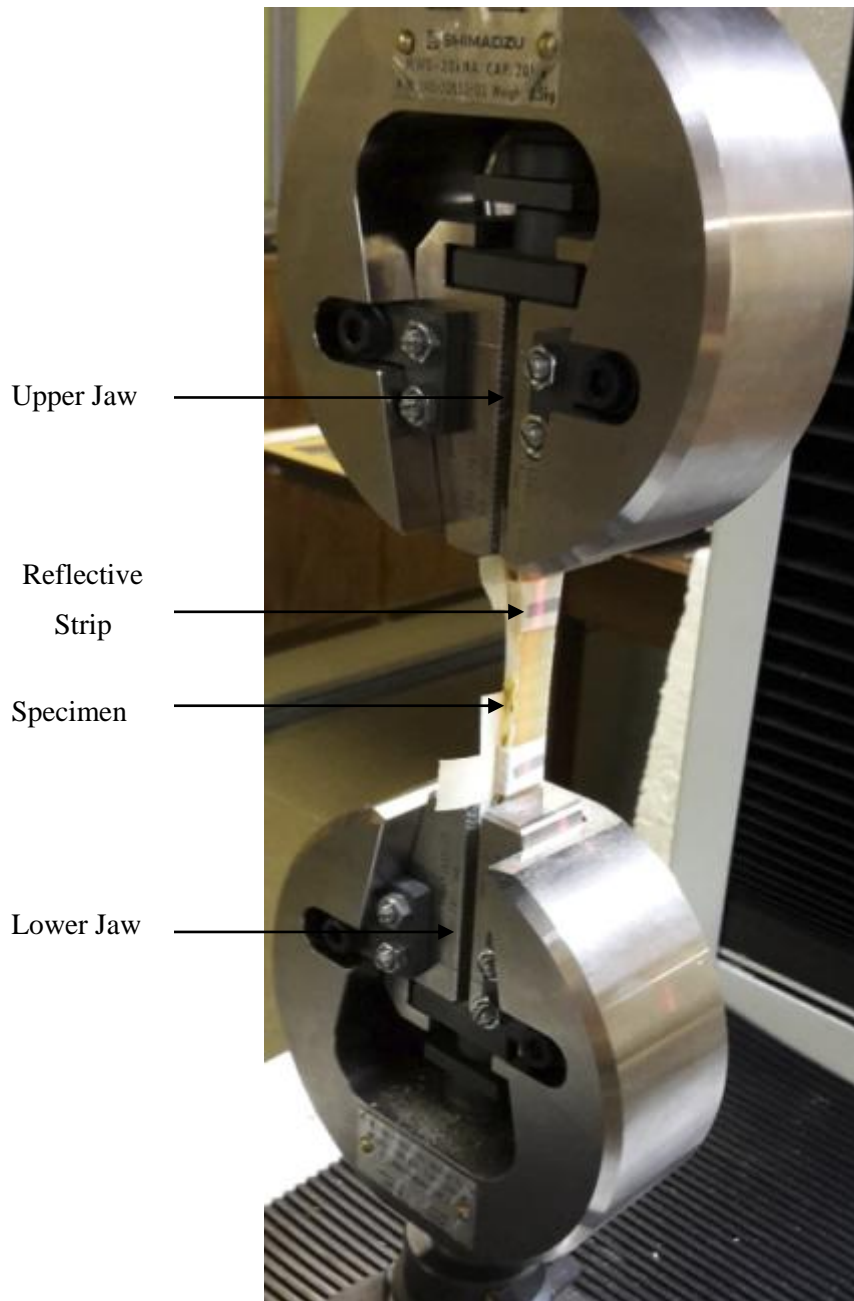


Figure 3.19: Tensile grip attachments for the Shimadzu testing machine

Figure 3.20 shows the laser extensometer model LE-05 obtained from Epsilon Technology Corp which uses a laser that is aligned, at a distance, with reflective tape on the gauge length of the specimen and when the specimen begins to elongate, the jaws at the contact points move and the sensor sends the elongation value to the data acquisition software. The distance between the points at which the instrument grips the specimen was set to 50mm.



Figure 3.20: Laser extensometer used to measure the jaw displacement under tensile loading

The data recorded during the testing procedure for each specimen was then used to calculate the tensile properties of the material. This was achieved by averaging the sum of all the individual specimens per test batch of 5 samples and by using the following calculations.

Using the averaged values of the three widths and thicknesses measured from the specimen, the average cross-sectional area of the gauge test section is given by Equation 3.14 below as:

$$A = w \times t \quad (3.14)$$

where:

A = Cross sectional area of the gauge test section [mm]

w = Width of the gauge test section [mm]

t = Thickness of the gauge test section [mm]

The maximum tensile force at the point of failure, as well as the measured average cross-sectional area of the specimen may then be used to calculate the ultimate tensile strength of the specimen which is given by Equation 3.15 as:

$$\sigma_{uts} = \frac{F_{max}}{A} \quad (3.15)$$

where:

σ_{uts} = Ultimate tensile strength of specimen [MPa]

F_{max} = Maximum load during test [N]

Using the data recorded by the extensometer, the tensile strain of the specimen can be calculated which is given by Equation 3.16 as:

$$\varepsilon = \frac{\Delta l}{l} \quad (3.16)$$

where:

ε = Tensile strain [mm/mm]

Δl = Extensometer displacement [mm]

l = Extensometer gauge length [mm]

If a graph is plotted of the tensile stress versus tensile strain, the slope of the graph is the modulus of elasticity also known as Young's Modulus. Using the tensile stresses and strains calculated by Equations 3.15 and 3.16; the Young's Modulus can be calculated which is given in Equation 3.17 as:

$$E = \frac{\Delta \sigma}{\Delta \varepsilon} \quad (3.17)$$

where:

E = Tensile modulus of elasticity of the specimen [GPa]

$\Delta \sigma$ = Difference in stress between two data points lying on the linear portion of the data set [MPa]

$\Delta \varepsilon$ = Difference in strain between two data points lying on the linear portion of the data set [mm/mm]

3.3.2 *Flexural Testing*

The standard guidelines that pertain to the flexural testing of plastic composite materials are given in ASTM D790:2010 which makes use of the 'three-point bending' method to induce bending loads in the test specimen until the specimen fractures. The preferred dimensions for the test specimen according to the standards are given below in Figure 3.21.

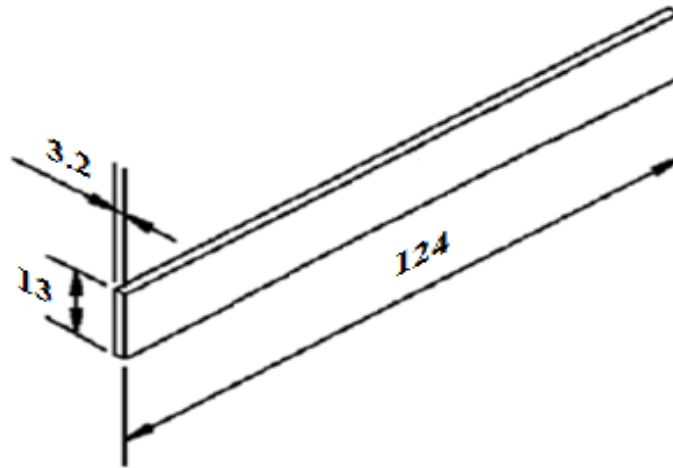


Figure 3.21: 3 point bending sample dimensions as per ASTM D790:2010

The Shimadzu testing machine was also used to test the rectangular composite test specimens under flexural loading. Flexural testing makes use of a similar procedure to that described in tensile testing, with the exception that an internal encoder was used to measure the extension and the tensile test jaws were replaced by the three point bending mechanism. In order to calculate the flexural stresses, and as per ASTM recommendations, the width and thickness of each test specimen was measured, using a Vernier calliper, at the point where the load was going to be applied. The mean width and thickness for the 5 specimens from each batch was then calculated and recorded.

The following steps detail the procedure that was followed when performing the flexural tests on the test specimens; firstly the tensile testing rig was removed and replaced with the three-point bending test rig which operates by converting the upward movement of the Shimadzu testing machine into a downward movement of the force applying edge. The same load cell was used for tensile testing as was used for the flexural testing setup and the same data acquisition software was also used. The specimen was placed on the simple support with the force member perpendicular to the specimen. The flexural testing parameters were entered with a test speed of $2\text{mm}/\text{min}$ and the tests were run. The software produced a load vs. extension graph during the test. Indication of a specimen failure occurred when the displayed load began to decrease or when the specimen broke. Figure 3.22 shows an image of a flexural test being performed as described above.



Figure 3.22: Close up image of the 3-point flexural test attachment during a test

The same number of specimens used in the tensile testing, five, was also used for flexural testing. The flexural properties were obtained by averaging specimen properties using the same method as that used for the tensile properties.

Using the averaged values of the three widths and thicknesses measured from the specimen as well as the load applied and the distance between the supports, the flexural stress in the specimen was calculated using Equation 3.17 below.

$$\sigma_f = \frac{3F_{max} L}{2bh^2} \quad (3.17)$$

where:

σ_f = Specimen flexural stress [MPa]

F_{max} = Load applied [N]

L = Length between supports [mm]

b = Width of specimen measured at its centre [mm]

h = Thickness of specimen measured at its centre [mm]

Using the data recorded by the extensometer, the flexural strain of the specimen was calculated, which is given by Equation 3.18 as:

$$\varepsilon_f = \frac{6hD}{L^2} \quad (3.18)$$

where:

ε_f = Flexural strain of specimen [mm/mm]

D = Vertical deflection of the specimen at the point of load application [mm]

The flexural elastic modulus was calculated in the same manner as that used for the calculation of the tensile elastic modulus. Using the flexural stresses and strains calculated by Equations 3.17 and 3.18; the flexural elastic modulus was calculated as given in Equation 3.19 as:

$$E_f = \frac{\Delta\sigma_f}{\Delta\varepsilon_f} \quad (3.19)$$

where:

E_f = Flexural modulus of elasticity [MPa]

$\Delta\sigma_f$ = Change in Flexural stress of specimen [MPa]

$\Delta\varepsilon_f$ = Change in Flexural strain of specimen [mm/mm]

3.3.3 Impact Testing

The standard guidelines that pertain to the impact testing of plastic composite materials are given in ASTM D256:2010 which makes use of a destructive testing method used to measure the shock resistance, or toughness of a material. This is determined by the amount of energy that is absorbed by a test specimen upon impact, or the work done in fracturing the test specimen. The ASTM D256 standards require that a batch of at least five notched specimens with dimension shown in Figure 3.23 be tested in order to obtain an average result per batch of the specimens tested [94].

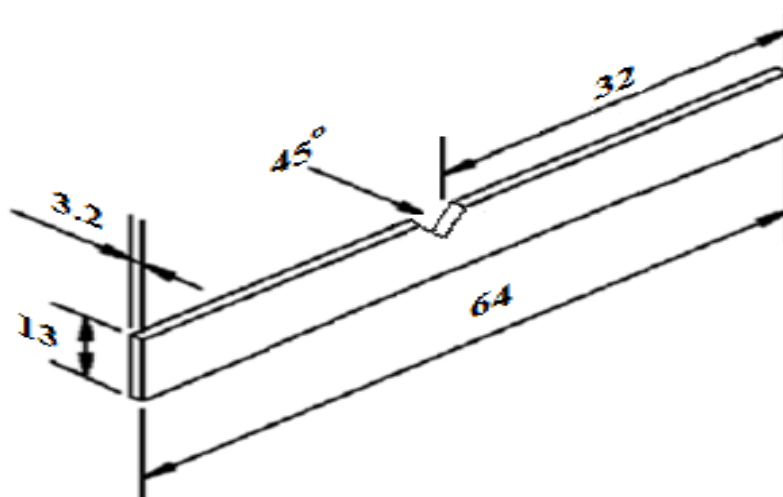


Figure 3.23: Impact testing sample dimensions as per ASTM D256:2010

An Avery pendulum impact testing machine shown in Figure 3.24 was used to perform the impact testing. The machine has a static dial arm which can be manually moved and positioned prior to

testing to the 4.2J mark. When the pendulum is released with no specimen being tested, the dynamic dial arm moves up to the zero mark on the absorbed energy dial gauge which indicates that no energy was absorbed. When a specimen is placed in the machine's grip it absorbs the energy from the pendulum and hence the dynamic dial arm does not swing to the zero mark. This value which is read off the dial gauge gives the energy required to break the specimen. The testing machine ranges from 0 to 4.2 Joules with a resolution of 0.025 Joules.

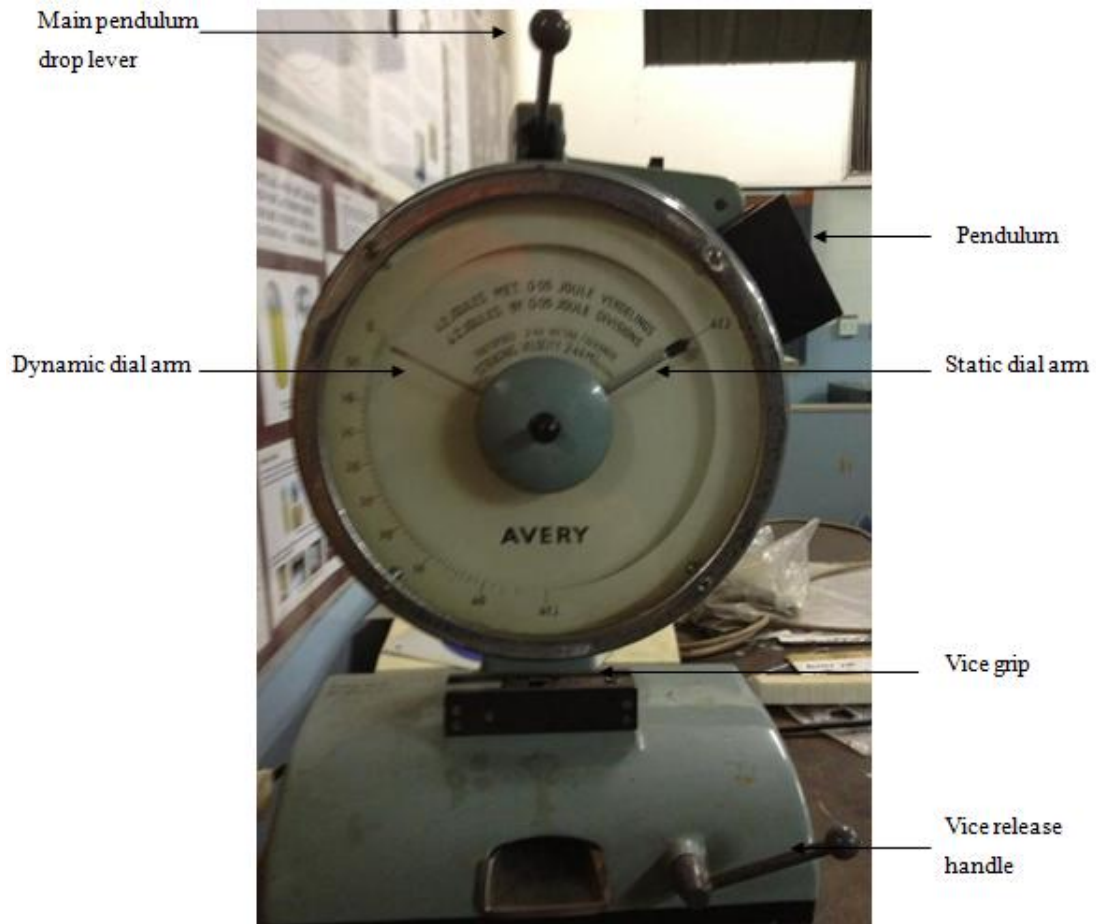


Figure 3.24: Avery pendulum impact testing machine used to test the impact specimen

The following steps detail the procedure that was followed when performing impact testing on the test specimens. Firstly, the pendulum was swung back into its maximum energy position and locked into place. The base lever of the machine was then opened for the placement of the specimen between the grips with the notch of the specimen positioned towards the left side of the grip away from the point of impact with the pendulum. The centre dial was then turned so as to move the static dial arm to the 4.2 Joules marking. The release lever on the top of the machine was then pulled downwards to release the pendulum and the resultant value that the dynamic dial arm corresponds to was recorded.

In order to break the specimen, the pendulum arm has to lose a certain amount of energy in fracturing the test specimen. By recording the initial height of the pendulum and the height which the pendulum

reaches after impact, the energy absorbed by the specimen was found. The impact toughness is expressed as the energy lost per unit cross-sectional area. This was calculated using equation 3.20.

$$K_I = \frac{\Delta e_I}{A_I} \quad (3.20)$$

where:

K_I = Impact toughness [J/m^2]

Δe_I = Energy lost by pendulum due to impact [J]

A_I = Cross-sectional area of impact specimen [m^2]

3.4 Morphological Characterisation

Morphological characterisation in materials is focused on two major aspects namely; chemical composition and compositional homogeneity. Various morphological characterisation techniques exist and are used to gain a better insight in to the physical structures of materials surfaces and analyse surface defects and impurities influencing the properties of the materials. The specific characterisation techniques used in this research include Scanning Electron Microscopy (SEM), Transmission Electron Microscopy (TEM), Raman Spectroscopy (RS), Thermo Gravitational Analysis (TGA) and Energy-Dispersive X-ray Spectroscopy (EDX).

3.4.1 *Microscopy*

The Scanning Electron Microscope provided the capability to visually inspect the effects of filler dispersion on the composites chemical structure as well as verify failure modes associated with a specific destructive test. This then allowed for various filler geometries and processing methods to be directly compared and related to the macroscopic properties of the final composite material. SEM works by accelerating a beam of electrons that scans over the surface of the material and is then reflected or scattered off the specimens' surface. A cathode ray tube collects and displays these reflected electrons at the same rate at which they had been emitted. This produces an image which represents the surface of the material being scanned [100]. Use of the scanning electron microscope for this research was offered by the Microscopy and Microanalysis Unit (MMU) at the University of the Witwatersrand. The scanning electron microscope used for the morphological characterisation of failed tensile, bending and impact samples was a FEI Quanta 400 FEG. The SEM has the capabilities of capturing images of non-conductive samples at resolutions as low as 0.8nm due to the high voltages (30kV) and high vacuum used. Samples were firstly cut and prepared utilising a Reichert Ultramicrotome and were then sputter coated with a 15 – 30nm thick layer of gold-palladium (Au, Pt) for 3 minutes using an Emitech coater so as to minimise the charging effects of the non-conducting sample under the microscope. Sputter coating is the standard method for preparing non-conducting or poorly conducting specimens for observation in a scanning electron microscope.

TEM works in a similar principle to the scanning electron microscope, however instead of reflecting electrons with a focused point on the samples surface, it absorbs electrons from the entire sample to better visualize internal structures. This is achieved by shining a high energy beam of electrons through a very thin sample. The interactions between the electrons and the atoms can be used to observe features such as the crystal structure and features in the structure like dislocations and grain boundaries.

Use of the transmission electron microscope for this research was also offered by the Microscopy and Microanalysis Unit (MMU) at the University of the Witwatersrand. The transmission electron microscope used for the morphological characterisation of the diameters and quality of ECNFs obtained from electrospinning was a FEI TecnaiT12. The TEM has the capabilities of capturing images of samples at much higher resolutions than the SEM and can resolve images at 700000 times magnification at voltages of up to 120kV.

3.4.2 Raman Spectroscopy

Raman Spectroscopy is a spectroscopic technique based on the inelastic scattering of monochromatic light. The inelastic behaviour is caused by the frequency of the incident light being altered upon interaction with the specimen, which is due to the absorption of photons by the specimen. The upward or downward shift of the frequency is called the Raman Effect. Figure 3.25 shows a very simplified diagram of the components and working method of the Raman spectroscopy.

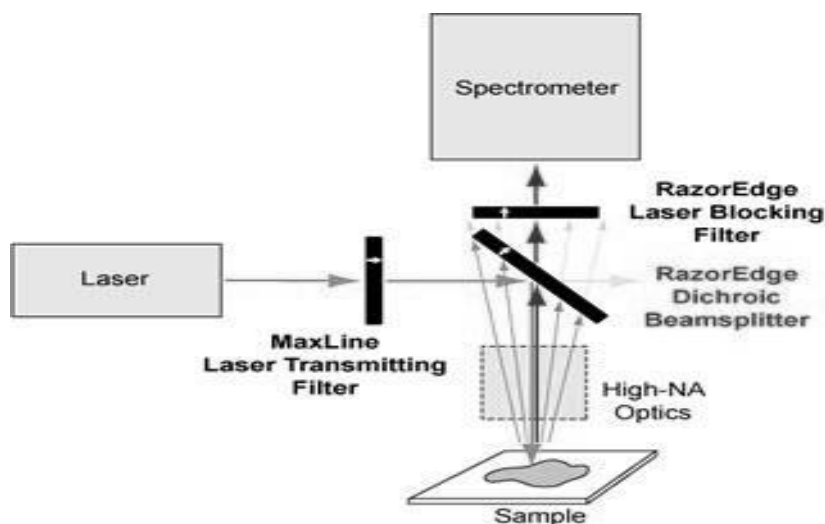


Figure 3.25: Simplified diagram showing the working method of the Raman Effect

Figure 3.26 shows a simple illustration of the dispersion of light due to the presence and respective vibrational states of molecules. Only some of the light is absorbed by the molecules and emitted with the exact same frequency which is known as elastic Rayleigh scattering. 99.9% of all incident photons undergo Rayleigh scattering and as such special measures must be taken to isolate the relevant Raman scattering.

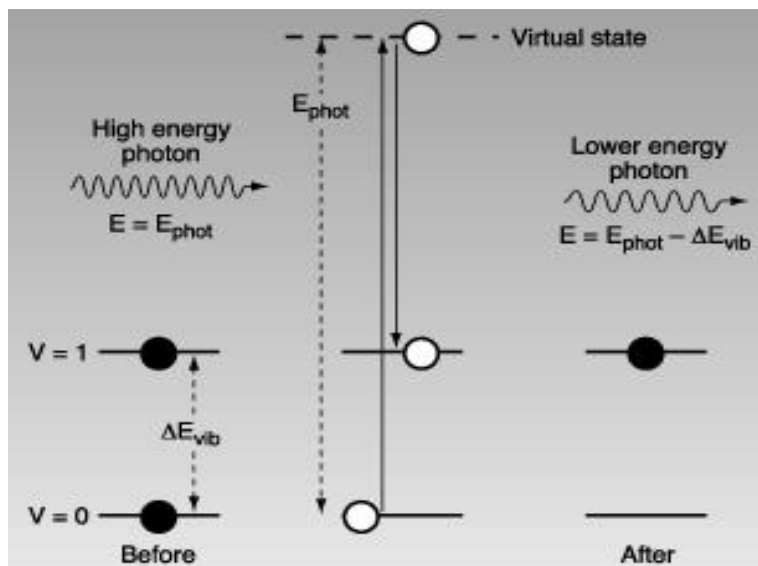


Figure 3.26: Fundamental concept behind the Raman Effect

The Raman spectroscopy was performed in the Physics Department of the University of the Witwatersrand with the assistance of Dr. Rudolph Erasmus. Raman spectra were acquired using a Jobin-Yvon T64000 Raman spectrograph operated in single spectrograph mode. The excitation source was a 514.5nm line of an argon ion laser. The incident beam was focused onto the sample via a 20x magnified ultra-long working distance objective lens of tan Olympus BX40 microscope attachment. The power at the sample was kept low (1.2mW) to prevent localised heating by the argon ion laser beam. The backscattered light was dispersed via a 600 lines/mm grating onto a liquid-nitrogen cooled CCD detector. The data acquisition was done on a Windows Xp compatible PC with LabSpec v4.18 software.

3.4.3 Thermogravimetric Analysis

Thermogravimetric analysis (TGA) is a process of thermal analysis whereby changes in physical and chemical properties of materials are measured as a function of increasing temperature or as a function of time [102]. TGA is mainly used to characterise the thermal stability of a material but is also a useful tool to determine the starting temperature of oxidative stabilisation and carbonisation of PAN nanofibers which is vital in producing well carbonized graphitic CNFs. TG analyses in air were performed on ECNF samples and neat PAN samples, with the aid from the Chemistry Department at the University of the Witwatersrand, in order to find the optimum oxidising treatment temperature as well as to better understand the thermal transitional/cyclization temperatures (T_C). This is discussed in more detail in Section 4.3.

4 PAN NANOMAT & ECNF: PRODUCTION, OPTIMISATION & MORPHOLOGICAL CHARACTERISATION

The purpose of this Chapter is to outline the processes and discuss the production of PAN nanomats and ECNFs. This begins with the design of the facility utilised to produce the ECNFs and finishes with the morphological characterisation of the fibers produced, that would ultimately be used as the additional reinforcement for the glass fiber epoxy composites.

4.1 Design & Development of Electrospinning Setup

For the purposes of this research, it was required to design and fabricate an electrospinning facility that was capable of producing continuous polymeric nanofibers below $500nm$ in diameter, at very low costs. The electrospinning setup required three major components, namely; a variable high voltage power supply with a range of up to $30kVDC$, a grounded collector capable of collecting large amounts of continuous fibers to form a square fibrous mat, and a capillary tube setup capable of controlling the flow rate of the polymeric solution.

4.1.1 Capillary Network Design

The first step in the design of the electrospinning setup was to design a capillary network based on the specifications provided. One of the objectives of the research was to design a cheap electrospinning device, and as such to reduce costs. Initially, a syringe pump utilising an Arduino Uno chip, stepper motor, motor controller and various other components obtained from MicroRobotics Pty Ltd (South Africa), as shown in Figure 4.1, was used.

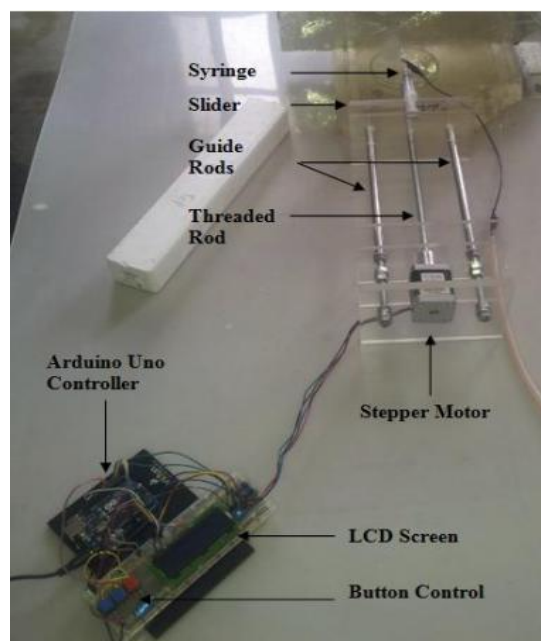


Figure 4.1: Syringe pump designed and built by author using an Arduino uno

The syringe pump stepper motor controller was programmed with a written code that incrementally stepped the motor which in turn rotated the threaded rod and thus linearly pushed the perspex slider along the length of the rod, resulting in the dispensation of the polymer solution from the syringe. The Arduino based syringe pump performed well and cost much less than a standard commercial syringe pump, however it was found that a commercial syringe pump would perform better for the purposes of this study. Then, a high precision NE-1000 syringe pump was purchased from New Era Pump Systems Inc. (USA) which has been used previously in electrospinning research [109,110,111]. This pump was used to test all the variable conditions prior to the purchase of a NE-1600 syringe pump, with 6 syringe capacity and used for the production of the required nanofiber mats, which was also purchased from New Era Pump Systems Inc. (USA).

The finalised electrospinning capillary network consists of 6 syringes to hold the polymer solution, a means of pumping the solution in the form of a syringe pump and needles in the range of 0.5mm nozzle diameters through which the solution is dispensed. The syringes and needles were not attached directly to one other but instead were separated by small diameter lengths of PTFE Teflon tubing, with luer lock connections, so as to remove the syringe pump from the vicinity of the electric field which would affect the operation of the pump. The complete electrospinning capillary network is shown in Figure 4.2.

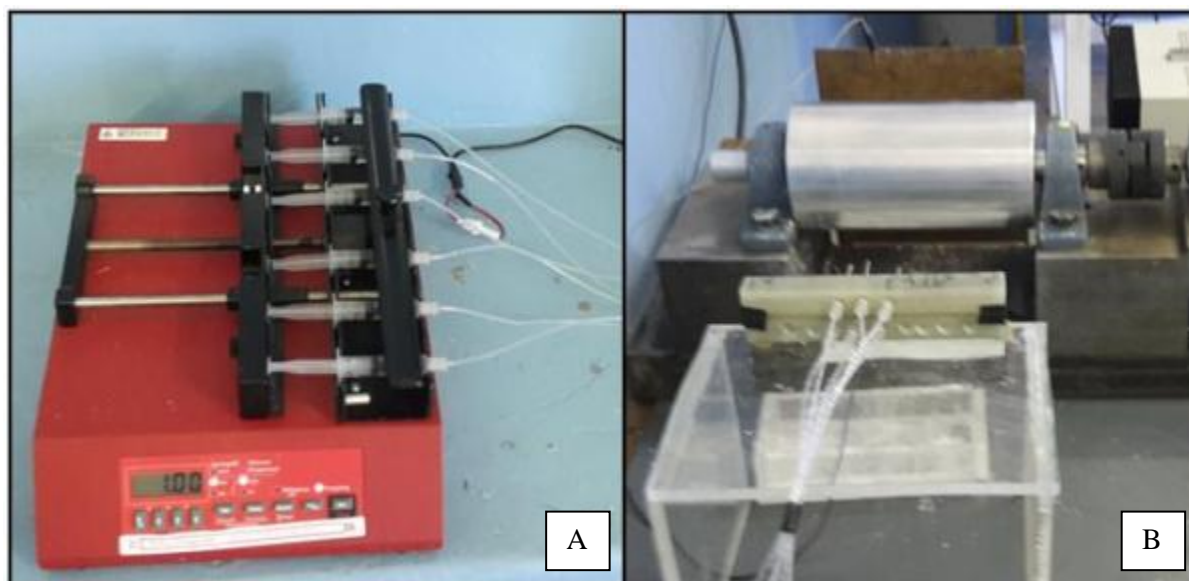


Figure 4.2: Electrospinning capillary network from the syringes (A) to the needles (B) using PTFE tubing with luer lock connectors

Syringes with various volumes and hub connectors as well as needles with various diameters and tip designs required for electrospinning were manufactured by the Hamilton Company (USA) and obtained through Separations Pty Ltd (South Africa). Very little data has been provided by researchers on the effects of needle size or tip design but it was found that most researchers used needles with a 90° tip angle and diameters of between 0.5mm and 1.5mm, depending on the polymer

solution[10,76,50,54,64,105,107]. It was also found that the disposable luer lock hub connector syringes with volumes of smaller than 10ml were ideal for the electrospinning setup. Research has also shown that the ideal flow rate of dispensing polymer solutions to obtain continuous nanofibers is around 1ml/min which is only achievable with highly accurate syringe pumps.

4.1.2 High Voltage Power Supply

The final step in the design of the capillary network was to specify a high voltage power supply that was capable of producing DC voltages as high as 30kV. The high voltage power supply obtained for this research was purchased from Gamma High Voltage Research (USA) with the product code ES50P-5W and specifications shown in Table 4.1.

Table 4.1: Gamma HVPS specifications

Specifications	
Output Voltage	0-50kV
Output Current	0-100 μ A
Input Voltage	240VAC, 60Hz
Ripple	0.1%
Power	5W

4.1.3 Collector Design

The next step in the design of the electrospinning setup was to choose the collector based on the specifications provided. Recent research has shown that the nature of the collector influences the morphological and the physical characteristics of the electrospun fibers significantly [105,106]. The density of the fibers as collected on a collector and fiber orientation are influenced by the amount of charge dissipated during fiber deposition. Liu *et al.* [106] showed this when electrospinning cellulose acetate fibers on various collectors including copper, aluminium foil, paper and water collectors. They discovered that the use of metal and conductive collectors helped dissipate the charges and also reduced the repulsion between the fibers, thus improving both the surface finish and density of fibers.

The most commonly used collector target is the conductive metal plate that results in collection of randomly oriented fibers in non-woven form as shown in Figure 4.3A. However, in this study it was required to collect continuous and homogenous fibers for better reinforcement, which is difficult to achieve with the collector plate design. The fibers can also be collected on specially designed

collector targets so as to obtain highly aligned fibers. A common collector design used to collect highly aligned fibers is the parallel plate collector, as shown in Figure 4.3A. The advantages of this collector design is the simplicity of the setup and the ease of collecting highly aligned fibers which are due to the air gap between the electrodes which creates residual electrostatic repulsion between the spun fibers [10]. However, there is a limit in the length of the aligned fibers and as such they are not continuous enough for the use as reinforcement in composite materials, to date.

Recently, researchers have focused on achieving highly aligned and continuous fibers by using mechanical and electrostatic control methods to control the behaviour of the electrospinning polymer jet and its trajectory. One such collector design that is commonly used to collect aligned and continuous fibers is the collecting drum or disc collector. The rotating cylindrical drum collector is preferred over the disc because a larger mat can be collected which is better suited for reinforcement purposes. The rotating drum collector is capable of rotating at high speeds and aligns the fibers circumferentially. In addition, the diameter of the fibers can be controlled and tailored based on the rotational speed of the drum [107,108]. The linear rate of the rotating drum must match the evaporation rate of the solvent, such that the fibers are deposited and taken up on the surface of the drum. If the rotational speeds of the drum are slower than the fiber take-up speed, randomly oriented fibers are obtained on the drum. Conversely at higher speeds, the take-up velocity breaks the depositing fiber jet and continuous fibers are not collected. Sundaray *et al.* [107] have shown that the fiber take up speed for varying PAN/DMF concentrated solutions varies from between 2m/s and 5m/s and as such the drum collector needs to match this speed. The three types of collector designs that were experimented with, namely; a parallel plate (A), a fixed plate (B) and a rotating drum design (C) as shown below in Figure 4.3.

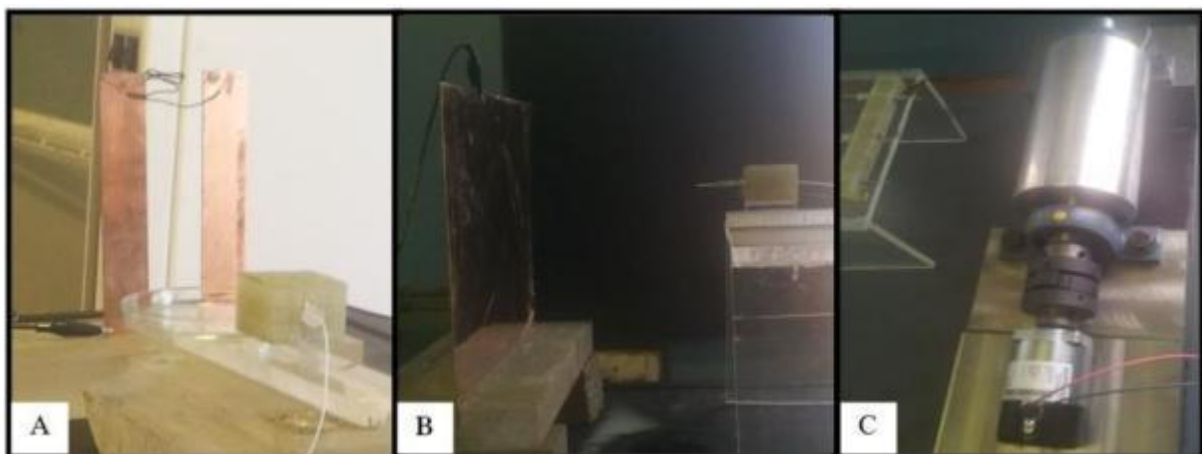


Figure 4.3: Images showing the three collectors experimented with in order to collect quality nanofibers; (A) parallel plate, (B) fixed plate and (C) rotating drum

It was thus concluded that collection on a rotating drum would be easy to setup and would require little additional cost whilst providing for the collection of the greatest amount of aligned and

continuous fibers. The drum collector needed to be constructed out of a lightweight and conductive material, such as aluminium, and needed to be isolated from the rest of the system in such a way that it could be grounded without also grounding any adjacent objects. The drum collector was required to rotate within the range of fiber take-up speeds for the PAN/DMF solutions. This required a choice of motor to achieve these rotating speeds as well as support bearings to allow for the rotation of the drum at these speeds. Equation 4.1 below was used to calculate the required Revolutions per Minute (RPM) and diameter of the drum collector:

$$RPM = \frac{60 \times v}{2\pi \times r} \quad (4.1)$$

where;

v = linear velocity (m/s)

r = radius (m)

RPM = revolutions per minute (rev/min)

The diameter and length of the drum were determined by the size of the resin transfer mould as this determined the dimensions of the spun mat. The mould dimensions used, as described later, were $190mm \times 190mm$ and as such the minimum required dimensions of the drum were calculated as using Equation 4.2 shown below so that the required RPM for the PAN/DMF solutions could also be calculated.

$$\begin{aligned} r &= \frac{D_c}{2\pi} \\ &= \frac{190}{2\pi} \\ &= 30.23mm \end{aligned} \quad (4.2)$$

Where;

D_c = Minimum drum circumference (mm)

r = radius (mm)

Therefore from Equation 4.2 it can be seen that the minimum required diameter for the drum collector is $60.46mm$. Also from the given mould dimensions it can be seen that the minimum required length of the drum is $190mm$. Therefore, using this information and Equation 4.1, the required RPM of the drum could be calculated as shown below.

$$\begin{aligned} RPM_{REQ} &= \frac{60 \times 5m/s}{2\pi \times 0.0302m} \\ &= 1581rpm \end{aligned}$$

Therefore, the required RPM for a drum shaft with a diameter of $60.46mm$ is $1581rpm$. However, because this is based on a minimum required radius from the resin transfer mould dimensions, the radius of the drum could be increased so as to reduce the required rpm so that the drum collector could be operated under safer, lower rpm, conditions. It was thus decided to double the diameter of the drum to $120mm$ so as to reduce the rpm requirements as can be shown below.

$$RPM = \frac{60 \times 5m/s}{2\pi \times 0.06m} = 796rpm$$

Therefore, the overall required RPM for the drum shaft was reduced to $796rpm$ for a drum diameter of $120mm$. This resulted in a larger diameter and heavier drum but reduced the required rpm which lead to safer operating conditions. The length of the drum was also specified to be slightly longer than the minimum requirement of $190mm$ and it was decided to be $220mm$.

The next step of the collector design was to specify a motor that was capable of turning the drum at the required $796rpm$. A brushed DC motor was selected from RS Components' (Pty) Ltd. motor catalogue with the product code MPM10-0005/CONT and specifications as shown in Table 4.2.

Table 4.2: Table showing the drum collector's motor specifications

Motor Specifications	
Current Rating	$2.7A$
Maximum Output Torque	$0.14Nm$
Output Speed	$4000rpm$
Power Rating	$60W$
Supply Voltage	$24Vdc$
Length	$106.7mm$
Shaft Diameter	$7.927mm$

The drum shafts diameters were specified at $30mm$ so as to stabilise the setup and the motor shaft diameter provided was $8mm$. The motor shaft and drum shaft were then coupled and bolted to the frame. Pillow block bearings for the drum shafts were also specified to handle the $796rpm$ required and bought through BMG Hydraulics (Pty) Ltd. with the product code UCP206D1.

4.2 PAN Nanomats

The electrospinning of PAN nanomats was performed using the electrospinning facility described above and shown in Figure 4.4, located at the University of the Witwatersrand's nanocomposite lab. The electrospinning experimental observations as well as the morphological characterisation data of the fiber morphologies, both qualitative and quantitative, are presented in this section.

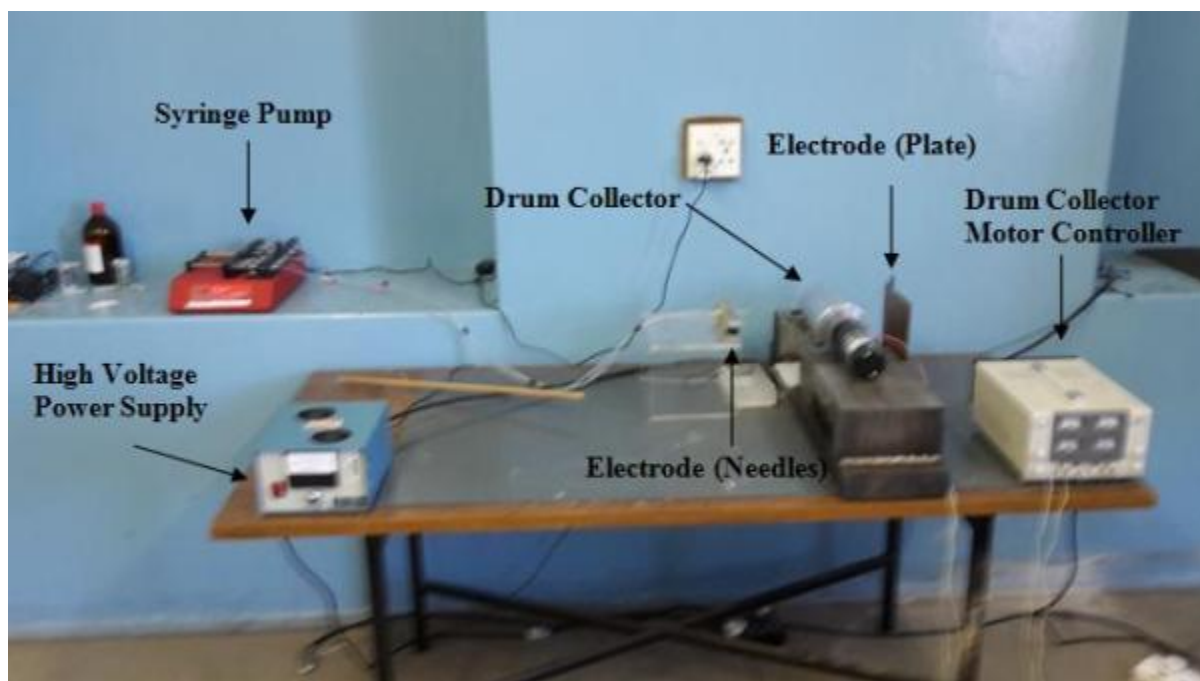


Figure 4.4: Electrospinning Setup designed and built at the University of the Witwatersrand

4.2.1 *Solution Parameters*

The relevant solution parameters, such as polymer concentration, viscosity, surface tension, molecular weight and conductivity were considered. Viscosity, polymer concentration and molecular weight are directly related. These related aspects were found to be critical in determining the fiber morphology. Surface tension was controlled mainly by the solvent composition whereas conductivity was controlled mainly by the polymer composition.

In order to obtain the ideal electrospinning viscosity of the solution to yield smooth uniform nanofibers, the solution concentration was varied. A variety of polymer concentrations were experimented with ranging from 1% PAN up to a maximum of 16% PAN. Four critical stages of fiber formation were observed to be linked to the concentration of PAN as shown in Figure 4.5.

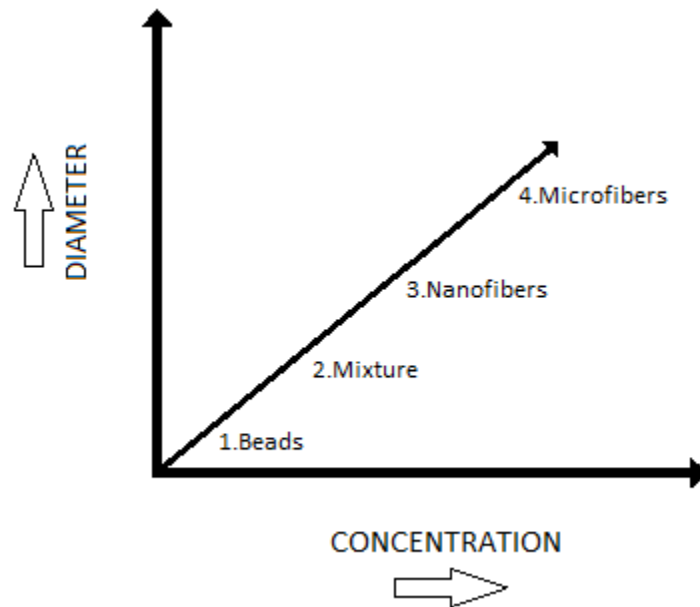


Figure 4.5: Graph showing nanofiber diameter vs. PAN concentration

At very low PAN concentrations, 1% - 4%, no nanofibers were formed, only small amounts of discontinuous particles were collected with a lot of wasted solution caused by excessive dripping from the needle tips. The low viscosity and high surface tension led to electro spraying instead of electro spinning. At low PAN concentrations, 4% - 8%, a mixture of fibers and beads were collected. The fiber diameters ranged from nano to micro with much inconsistency as shown in Figure 4.6.

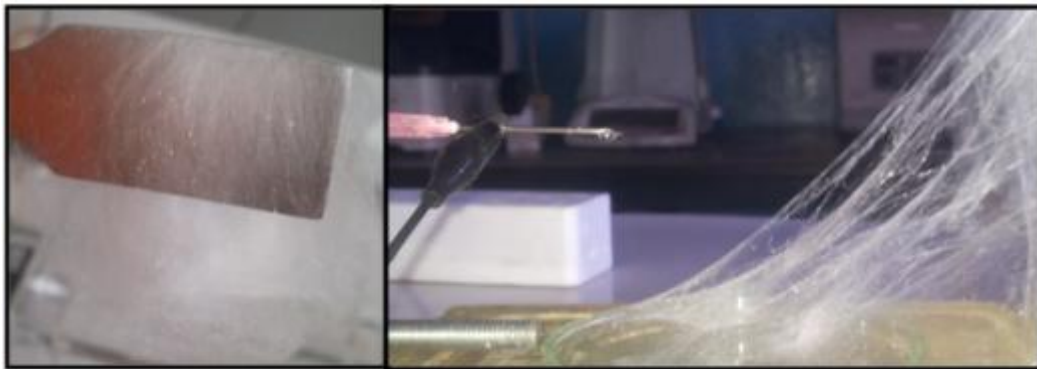


Figure 4.6: Images showing the phenomenon of beading of PAN fibers caused by poor electro spinning processing

At suitable PAN concentrations, 8% - 12%, smooth nanofibers with consistent fiber diameters were collected as shown in Figure 4.7.

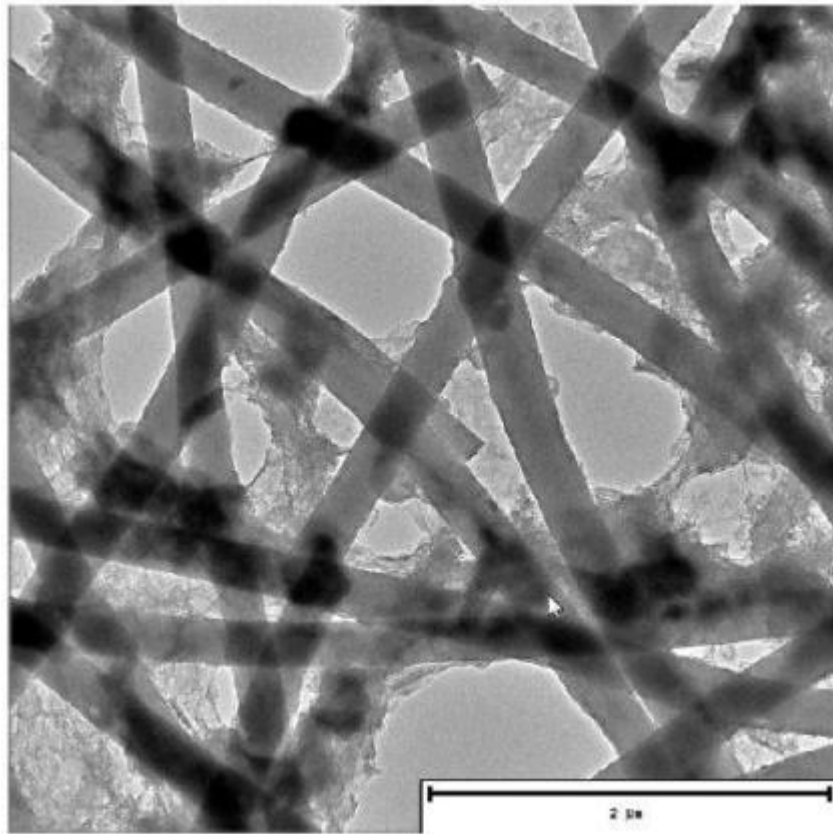


Figure 4.7: TEM image showing diameter and structural homogeneity of PAN nanofibers

At high PAN concentrations, 12% - 16%, rough, distorted and pitted microfibers were formed with very few nanofibers. Fibers looked almost ribbon-like in morphology, as shown in Figure 4.8.

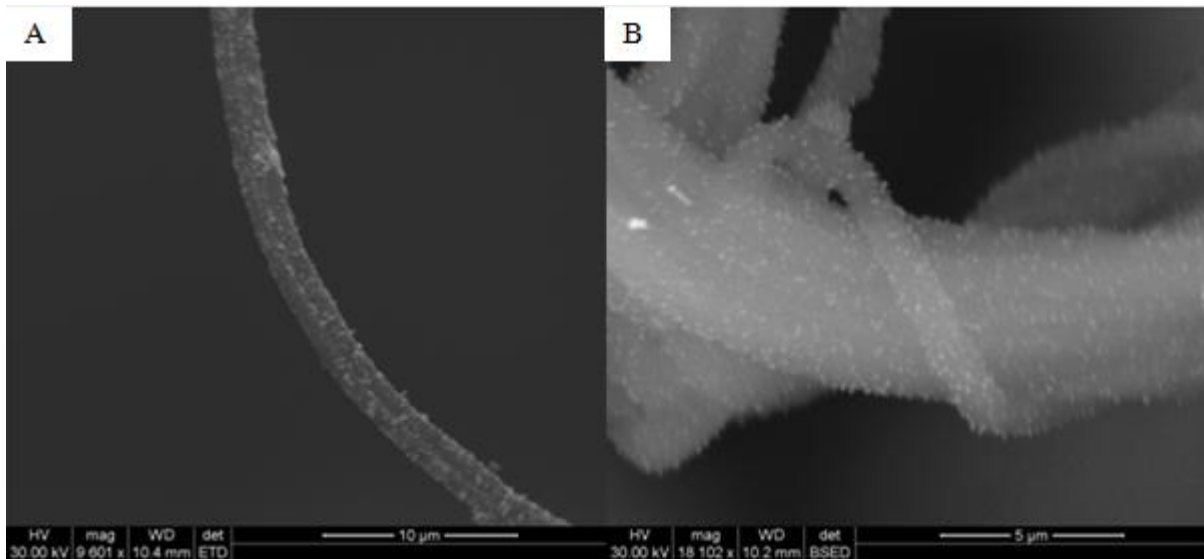


Figure 4.8: SEM images showing ribbon like structure (A) and poor surface morphology (B) of PAN nanofibers electrospun with high PAN concentrations

4.2.2 *Operating Parameters*

The relevant operating parameters such as flow rate, electric field strength, collector type and needle diameter were investigated. The volumetric flow rate was closely controlled with the use of a syringe pump and the field strength was varied by changing either the applied voltage or the distance between the electrodes. The needle diameters were also varied from diameters ranging between 32G and 18G.

A variety of flow rates ranging from 0.5ml/hr up to 5ml/hr were experimented with in order to find the ideal flow rate for smooth uniform nanofiber formation. At the lowest flow rates, it was observed that the solution droplets formed at the needle tips would harden and prevent further electrospinning after a few minutes of spinning. Also the electrospinning time required to collect enough fibers made the low flow rates experiments difficult and time intensive.

Between 1ml/hr and 2ml/hr was found to be the optimum flow rate range as this provided for the optimum formation of the Taylor cone with very little loss of solution from the needle tip droplets.

Above 2ml/hr , it was observed that the fiber diameters were thicker, beads were formed and the fibers collected were still wet with DMF. This is as a result of short drying time and low stretching forces. At very high flow rates, pulsed electrospinning was observed and a lot of solution wastage was also observed.

It was observed that both increasing the distance from electrodes and increasing the applied voltage decreased the formation of beads. However, an increase in applied voltage did result in small increases in fiber diameter. When the distance between the electrodes was too small, $<10\text{cm}$, the fibers did not have sufficient time to solidify before collection and as a result the fibers were collected wet which led to disfiguration of the fibrous structure. On the contrary, when the distance between the electrodes was too far, $>25\text{cm}$, the fibers thinned and broke-up prior to collection which resulted in discontinuous fiber formation and beading.

There were major challenges with achieving uniformity of fiber dispersion with the parallel plate and fixed plate collectors due to the limited size of the whipping diameter. The distance between the parallel plates was also limited by the diameter of the whipping cone which was found to be insufficient to collect on the required glass mat sizes. Figure 4.9 shows the lack of uniformity of PAN fibers collected on the glass fiber woven mats as shown by the circled areas lacking fiber deposition.



Figure 4.9: Image showing poor dispersion of PAN nanofibers collected on the woven glass fiber mats

On the contrary, the rotating drum collector provided much better uniformity as can be seen from the PAN sheet peeled off a woven glass fiber sheet, Figure 4.10. Overall, the collector designs had very little effect on the morphology of the fibers formation, with average diameters being very similar. However, clearly the uniformity of the fibers produced from collection on the drum collector is superior to that of the other collectors.

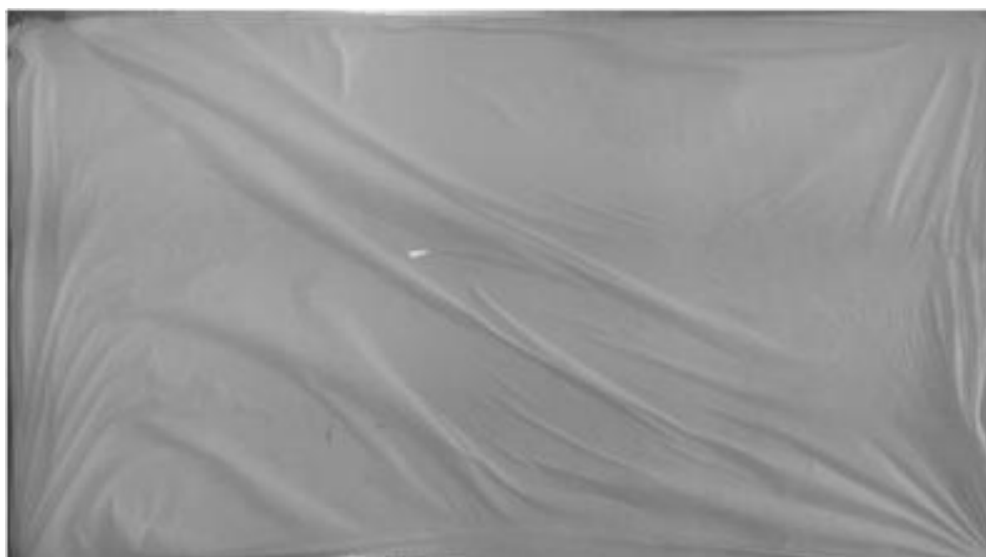


Figure 4.10: Electrospun PAN nanofibrous mat collected using the rotating drum collector

A variety of needles and syringes were used to find the optimum setup to produce the best quality nanofibers. Needles ranging from 32G to 18G (both 90° and 30° angled tips) were experimented with both glass and plastic syringes were also tested ranging from 5ml volumes up to 50ml. The smaller

diameter needles, 32G and 25G, increased the fiber diameter and produced far less continuous fibers most likely caused by the constant blocking and hardening of PAN within the needles. The larger diameter needles, 20G and 18G, showed improved fiber diameters and more continuity as well as very little to no hardening of PAN and no clogging of the needles. Both 90° and 30° angled tips, Figure 4.11, were experimented with and it was discovered that the 90° end tips provided for the better spinning conditions as the droplets exited the needle more uniformly which resulted in a more accurate whipping cone diameter as well as fewer fiber breakages.

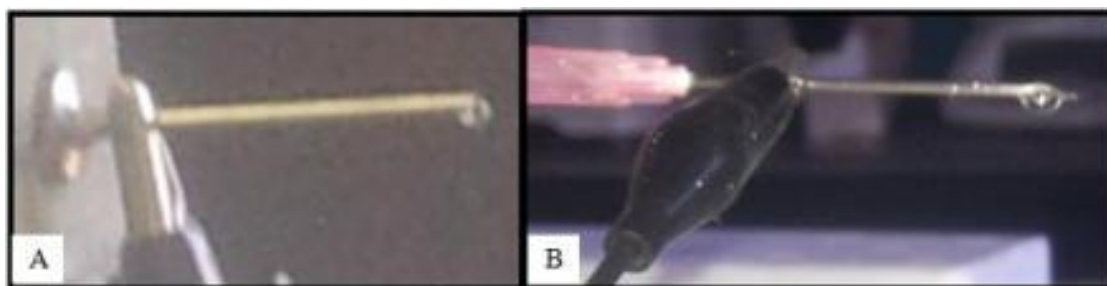


Figure 4.11: Comparison between droplet formation of a 90° end tip (A) and a 30° angled tip (B)

The glass syringes required a metal hub for the needle connection which during electrospinning resulted in back current to the syringe pump caused by excessive corona charge build-up as a result of the high electric field. This back current was high enough to destroy the electronics within the syringe pump power supply on numerous occasions. It was discovered that the plastic disposable luer lock syringes, as shown in Figure 4.12 (B), performed better during experimentation than the glass syringes (A), as no corona charge was experienced with these disposable plastic syringes.

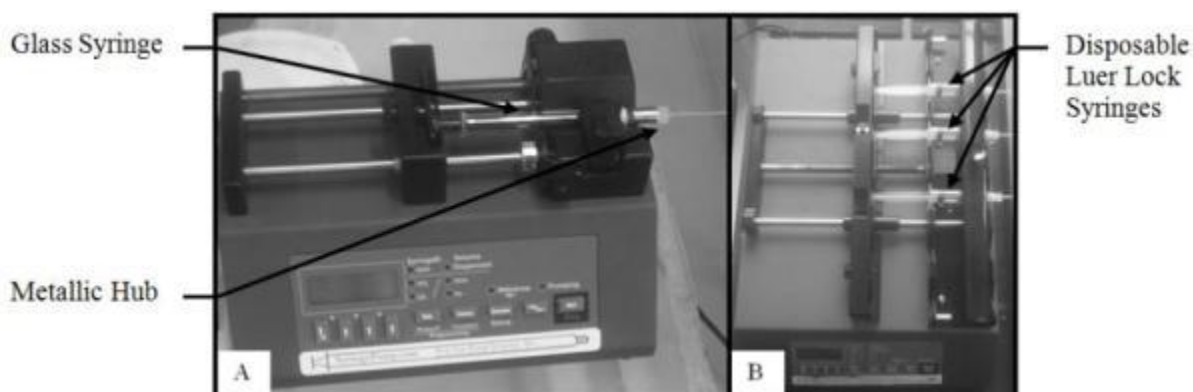


Figure 4.12: Images showing glass syringe (A) and disposable plastic syringes (B)

4.2.3 *Experimental Matrix*

The two major factors that affect the ability to electrospin polymer solutions and that affect the final quality of the fibers themselves are the solution parameters and the operating parameters as discussed in Section 4.2.1 and 4.2.2. Both sets of parametric factors are interlinked and as such an experimental matrix was required in order to test each factor to better understand their relationships between each

other. The three main parameters that were investigated were applied voltage, distance from electrodes and PAN concentration. During this experimental phase, the following parameters were kept constant; needle size, syringes, collector design and flow rate. The experimental matrix is shown in three dimensions in Figure 4.13 with the nodal parameter details shown in Table 4.3.

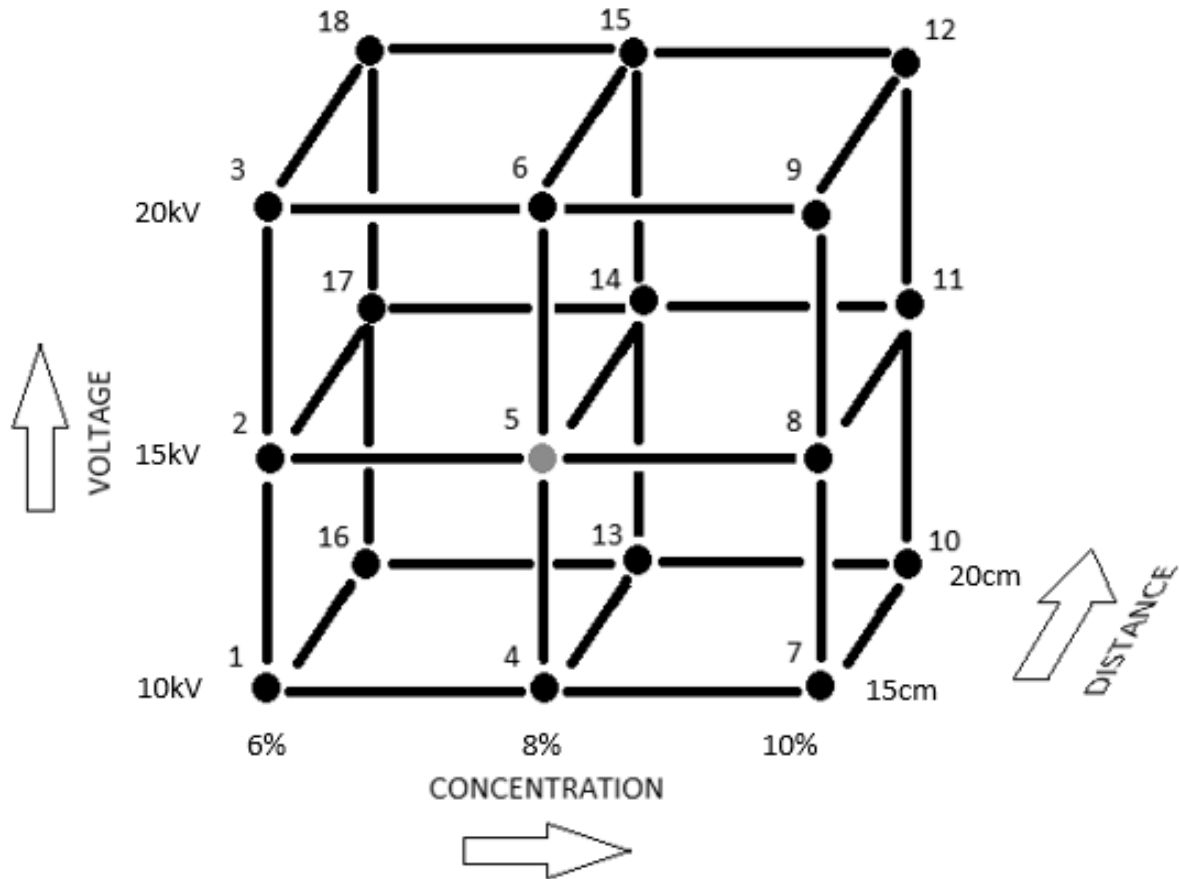


Figure 4.13: Graphical representation of the 3-dimensional experimental matrix

In order to perform the testing of this experimental cube; the three parameters were varied mutually exclusively as shown in the experimental matrix cube. Firstly, the applied voltage was varied, between 10kV, 15kV and 20 kV, whilst the distance from the collector was kept constant. Secondly, the distance from the collector was varied, 15cm or 20cm, whilst the applied voltage was kept constant. This was performed for each of three PAN concentrations namely; 6, 8 and 10% volume fraction. The observations from the experimental cube are shown below in Table 4.3.

Table 4.3: Experimental observations made regarding the electrospinning process

Node	PAN Conc. (%)	Applied Voltage (kV)	Distance (cm)	Comment
1	6	10	15	Beaded and broken fibers formed, distance was too far and surface charge was too large to maintain any consistency.
2	6	15	15	Beaded fibers formed, surface charge was high and caused irregular fiber morphology on collection of fibers.
3	6	20	15	No fibers formed, surface charge was too high which caused excessive dripping of solution at needle tips.
4	8	10	15	Broken fibers formed, surface charge was not high enough to form continuous collection.
5	8	15	15	Good fibers formed, Taylor cone was formed and showed consistent shape.
6	8	20	15	Good fibers formed, Taylor cone was formed and showed fairly consistent shape. Intermittent dripping occurrences.
7	10	10	15	Fairly good fibers formed, Taylor cone shape was consistent but was distorted and angled upwards from the droplets.
8	10	15	15	Fairly good fibers formed, some beading was observed but for the most part continuous fibers were formed.
9	10	20	15	Inconsistent fibers formed, the Taylor cone shape changed throughout spinning.
10	10	10	20	No fibers formed, surface charge was not sufficient to overcome surface tension.
11	10	15	20	Beaded and broken fibers formed, surface charge was barely able to overcome surface tension.
12	10	20	20	Fairly good fibers formed, some beading was observed but for the most part continuous fibers were formed.
13	8	10	20	Good fibers formed, Taylor cone was formed and showed fairly consistent shape. Intermittent dripping occurrences.
14	8	15	20	Good fibers formed, Taylor cone was formed and showed consistent shape. However, collection area was too large and difficult to control at this distance.
15	8	20	20	Beaded fibers formed, collection area was haphazard and difficult to control
16	6	10	20	No fibers formed, distance was too far away which meant that the fibers that did form never reached the collector.
17	6	15	20	No fibers formed, surface charge was too high and distance was too far away which caused spraying of solution.
18	6	20	20	No fibers formed, surface charge was too high and distance was too far away which caused spraying of solution.

The effect of electrospinning conditions on the morphology of PAN nanofibers was investigated through experimentation with the objective to obtain smooth, strong and stiff PAN nanofibers with

improved molecular orientation. Based on these experiments, the optimum electrospinning conditions for high strength and stiffness PAN nanofibers were identified.

In order to characterize the PAN nanofibers properties, experiments were first carried out at the University of Witwatersrand to optimize the electrospinning process, as discussed above. Prior to these experiments, it was found that the two main operating parameters of electrospinning were the applied voltage and the distance from the electrodes to the collector. These parameters were found have a profound effect on the molecular orientation and thus the mechanical properties of the PAN nanofibers. The experimental cube was thus designed around these parameters to obtain the ideal parameters.

During experimentation, it was observed that an increase in the distance from electrodes decreased the formation of beads and decreased the diameter of fibers. This was as a result of the greater stretching of the solution jet and the polymeric solution having more time to dry before being collected. Also, shorter distances incurred dripping tendency and wet fiber collection which thus increased the occurrence of beads as shown in Figure 4.14.

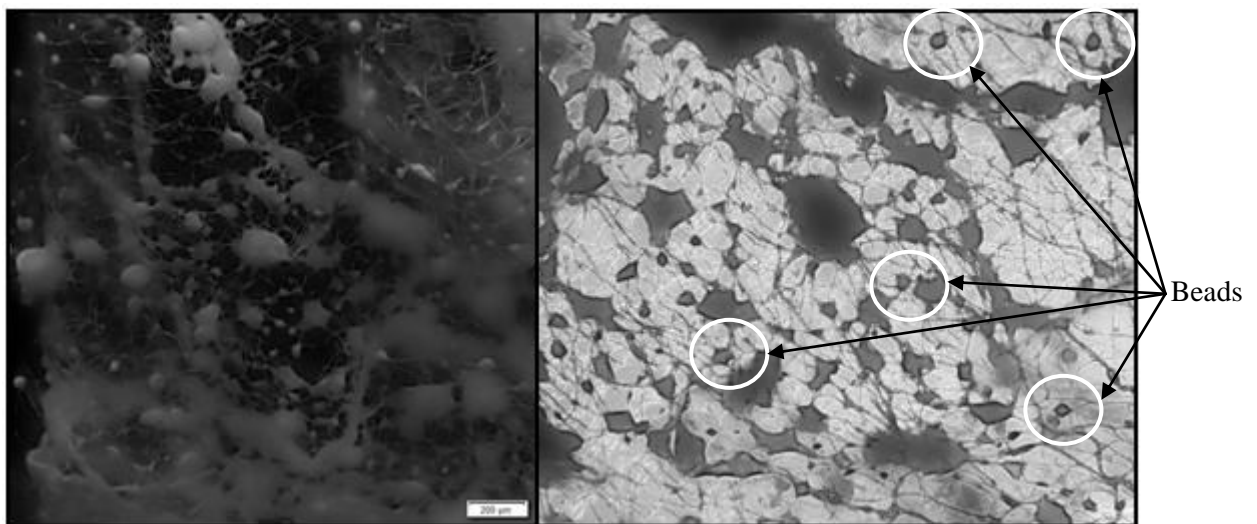


Figure 4.14: Microscopic images showing the beading phenomenon caused by poor electrospinning parameter control

It was also observed that increasing the applied voltage decreased the formation of beads but increased the fiber diameter which was as a result of the increased whipping instability and increased flow rate. This result agrees well with the findings of Yarin *et al.* [62] who also showed an increase in fiber diameter with increasing applied voltage.

The viscosity of the solution, or more directly the concentration of the PAN in the PAN/DMF solution, was found to be the main solution parameter of electrospinning. According to present research, the potential domain for the PAN/DMF solution was predicted as between 8% and 10% PAN. Through experimentation it was found that the 8% PAN solution with a 15kV applied voltage to an electrode distance of 15cm produced the most uniform and low diameter nanofibers. This

corresponds to node 5 in the experimental cube. Researchers have shown that the ratio of $0.9kV/cm$ to $1kV/cm$ do provide optimum PAN nanofibers [44].

4.2.4 Morphological Characterisation of PAN Fibers

The nanofibers produced from the optimum experimental node, node 5, were further investigated with the use of SEM and TEM imaging. Figure 4.15 shows the diameter of the as spun PAN nanofibers obtained from the spinning of an 8% volume fraction PAN solution with an applied voltage of $15kV$ and an electrode distance of $15cm$. It can be seen that the fiber diameters of the optimum spun PAN nanofibers is roughly $400nm$. Fiber diameters of this range are said to be of high mechanical strength because of the high aspect ratio of the fibers. The uniformity of the PAN structure is also of a high quality due to the confined molecular orientation of the amorphous regions, and there was no waviness along the fiber lengths. Further morphological characterisation of the PAN nanofibers is discussed in Section 4.3.2 when comparing PAN nanofibers to ECNFs.

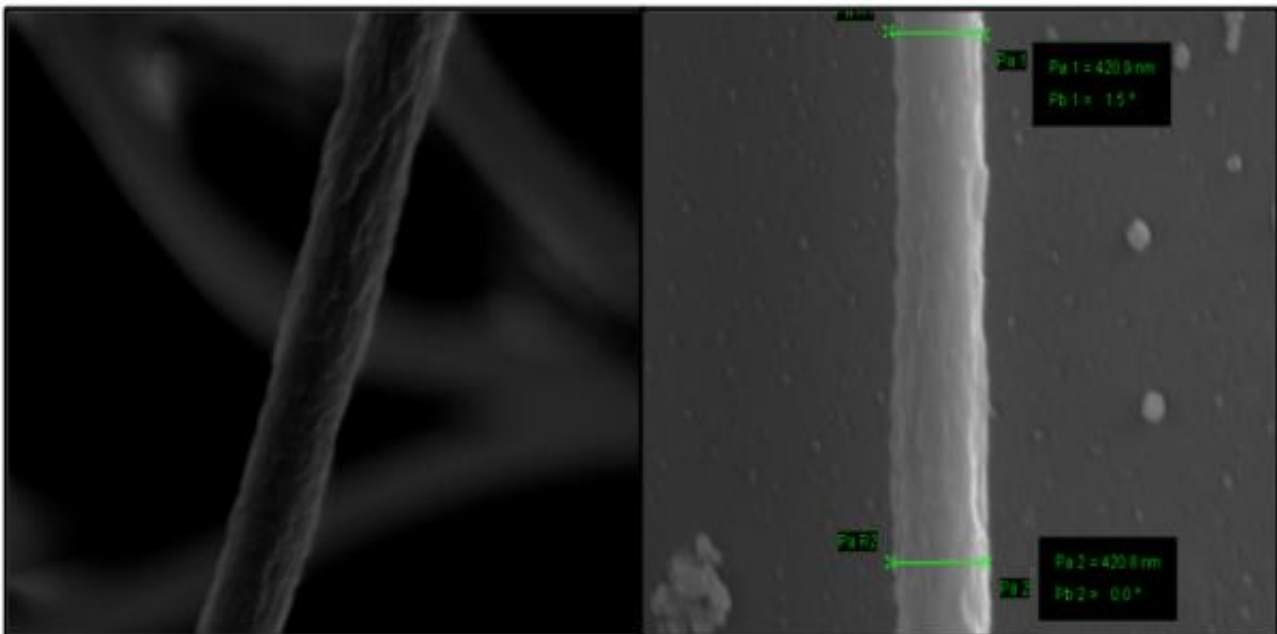


Figure 4.15: SEM images showing the optimized PAN nanofiber diameters and the quality of the morphological structures

4.3 ECNFs

4.3.1 PAN to ECNF Conversion

The capabilities of a variety of furnaces for the heat treatments of the PAN nanofibers were tested and carried out in three different types of furnaces, namely; a muffle furnace, a box furnace and a tube furnace. The muffle furnace, image B in Figure 4.16, proved ineffective in converting the stabilized PAN polymer into ECNFs during the carbonisation stage as the nitrogen gas was not completely sealed in the chamber causing the PAN to burn up in the presence of air at temperatures above 300°C. The flow rate of nitrogen could be accurately controlled and the temperature was also accurately controlled, however the butterfly valve and furnace door could not be completely sealed which resulted in the leakage of nitrogen during carbonisation. The box furnace, image A in Figure 4.16, with a steel insert for environmental control proved better at carbonisation, however due to lack of accurate temperature control and accurate low nitrogen flow rate control, the PAN sheets showed major cracking and wrinkling caused by the shrinkage of fibers as a result of inaccurate process control.

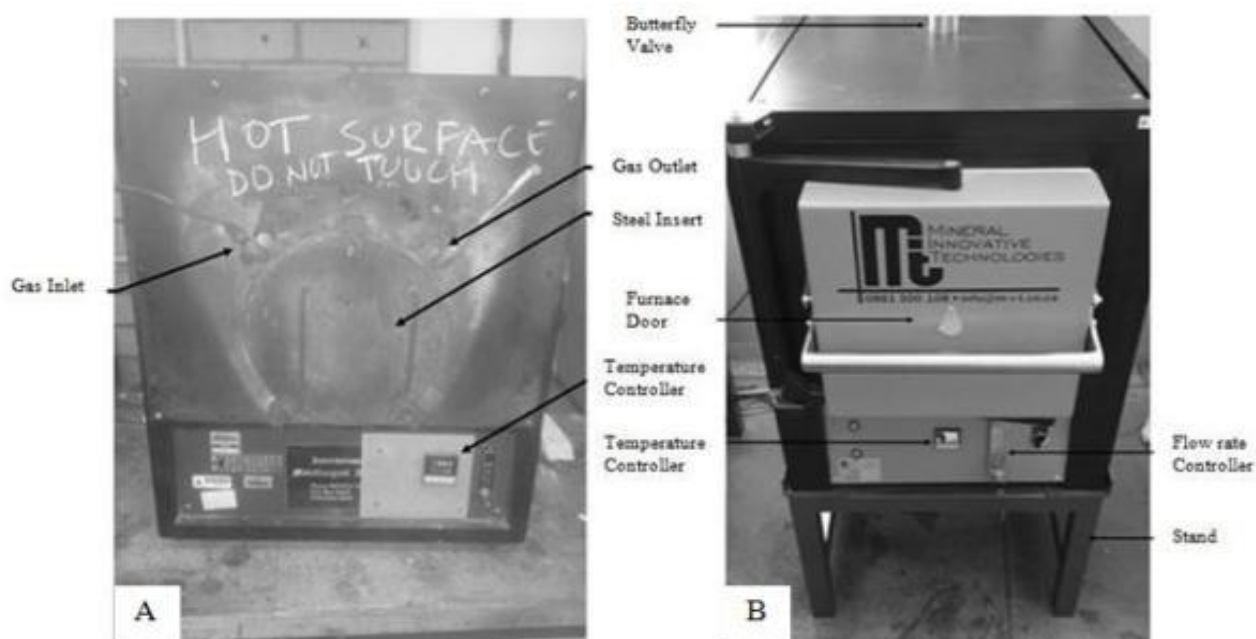


Figure 4.16: Images of the box furnace (A) and the muffle furnace (B) experimented with in order to achieve well graphitized carbon nanofibers

The tube furnace was found to be the best for heat treatments of the PAN polymer, as the nitrogen environment, temperature and flow rate could be accurately controlled. Also the heating zone was more uniform and as such provided for more consistent diameter fibers. A major disadvantage of using the tube furnace, however, was the limited sample size of the ceramic boat which meant that in order to make a substantial amount of ECNFs, many runs were performed. The tube furnace used to stabilize and carbonize the electrospun PAN nanofibers is shown in Figure 4.17 and was utilized at the School of Chemistry at the University of the Witwatersrand. The tube furnace used was designed

and built by the School of Chemistry at the University of the Witwatersrand and was capable of reaching temperatures of up to 1400°C.

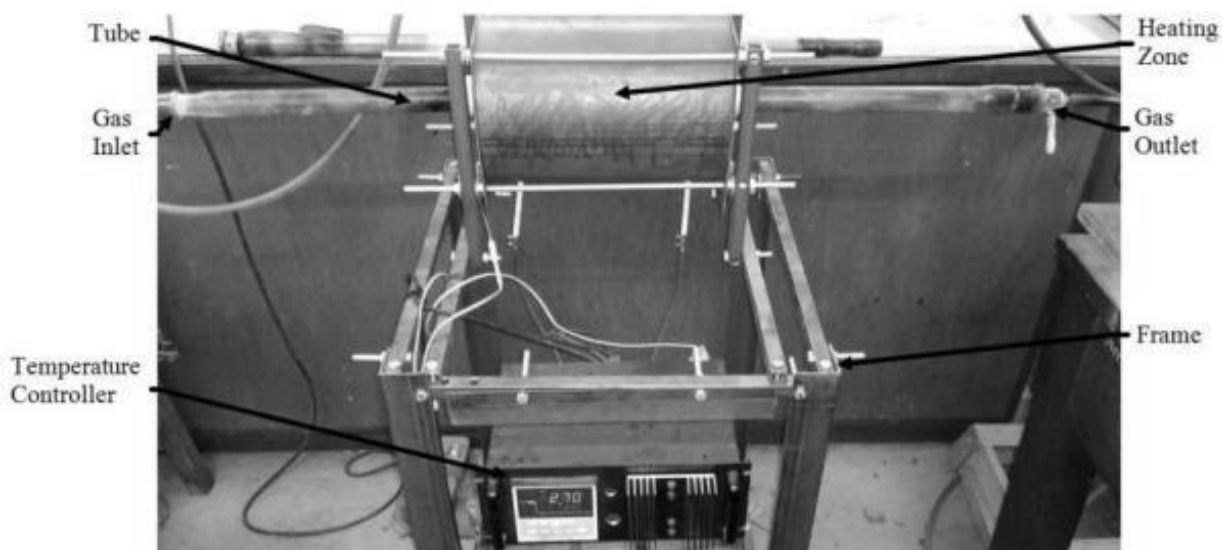


Figure 4.17: Carbonisation furnace used to convert PAN fibers into carbon nanofibers

The experimental process in the manufacture of the ECNFs was performed in a well ventilated room with a nitrogen gas outlet which was vented outside the building via a louver. The use of nitrogen gas was explicitly controlled with care as the gas properties of nitrogen are asphyxiating in nature. All tubing and connections were checked for leaks prior to opening any gas inlets, and high insulation gloves were worn when handling the furnace, hot glass tube and sample boat.

The procedure followed in order to carbonise the fibers is discussed as follows; firstly the weight of the electrospun PAN sample was measured before placing said sample into a clean ceramic boat within a clean glass tube. The boat was placed centrally within the tube so as to be aligned with the heating zone of the furnace, after which the glass tube connectors were tightly connected to either end of the tube. A line of tubing from the nitrogen inlet regulator was then connected to the inlet tube connector and sealed with paraffin tape, after which another line of tubing from the tube outlet connector was connected to a one way valve beaker filled with water. The temperature and time intervals, as shown below, were then set using the P4 temperature controller connected to the furnace element.

- Temp 1: 270°C
- Time 1: 27 mins (10°C/min)
- Temp 2: 270°C
- Time 2: 60 mins (hold)
- Temp 3: 800°C
- Time 3: 53 mins (10°C/min)
- Temp 4: 800°C

- Time 4: 60 mins (hold)
- Temp 5: 30°C
- Time 5: 120 mins (natural cooling)

After 87 minutes had elapsed, the main nitrogen in-valve was opened until a steady stream of bubbles, one second apart, formed in the one way valve beaker, so as to allow the nitrogen to purge and flow continuously through the tube. After the preset intervals were performed and the temperature of the furnace had reached 100°C or lower, the main nitrogen valve was shut off and the glass tube connectors were disconnected from either end of the tube, before removing the tube from the furnace. The ECNF sample was finally removed from the boat using a spoon and weighed on the electronic scale, before being crushed into a fine powder using a pestle and mortar.

4.3.2 *Morphological Characterisation*

Figure 4.18 shows 1g of the final ECNF produced in the tube furnace, after crushing with a pestle and mortar, which resulted in velutinous textured ECNFs. The diameter and quality of the ECNF are shown in Figure 4.18, and will be discussed in more depth in the remainder of the chapter. The nanofiber nanostructural features, such as crystallite size and density were studied by Transmission Electron Microscopy (TEM) and were also found to increase with heat treatment temperature, which is discussed in more detail in the next section.

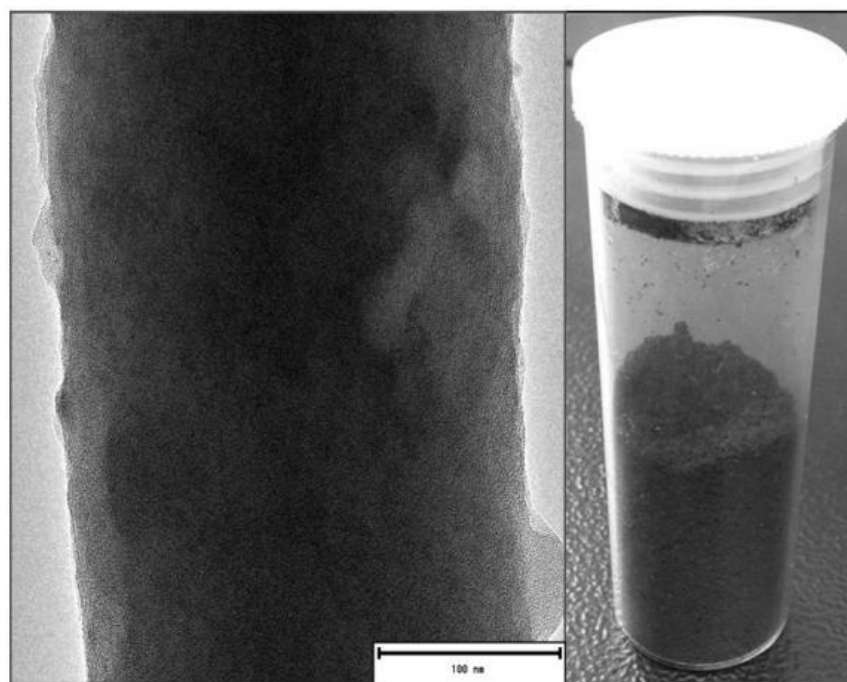


Figure 4.18: TEM image of the final ECNFs as produced by electrospinning and carbonisation of the PAN nanofibers

TEM was then also performed on the ECNF samples in order to better understand the surface morphology by characterizing the NC-Graphitic carbon structure as well as to characterize the fiber diameters accurately. The disordered graphitic structure is shown in Figure 4.19 where the surface of

the nanofiber is irregular and neither crystalline nor amorphous which corresponds well with the Raman spectra interpretation.

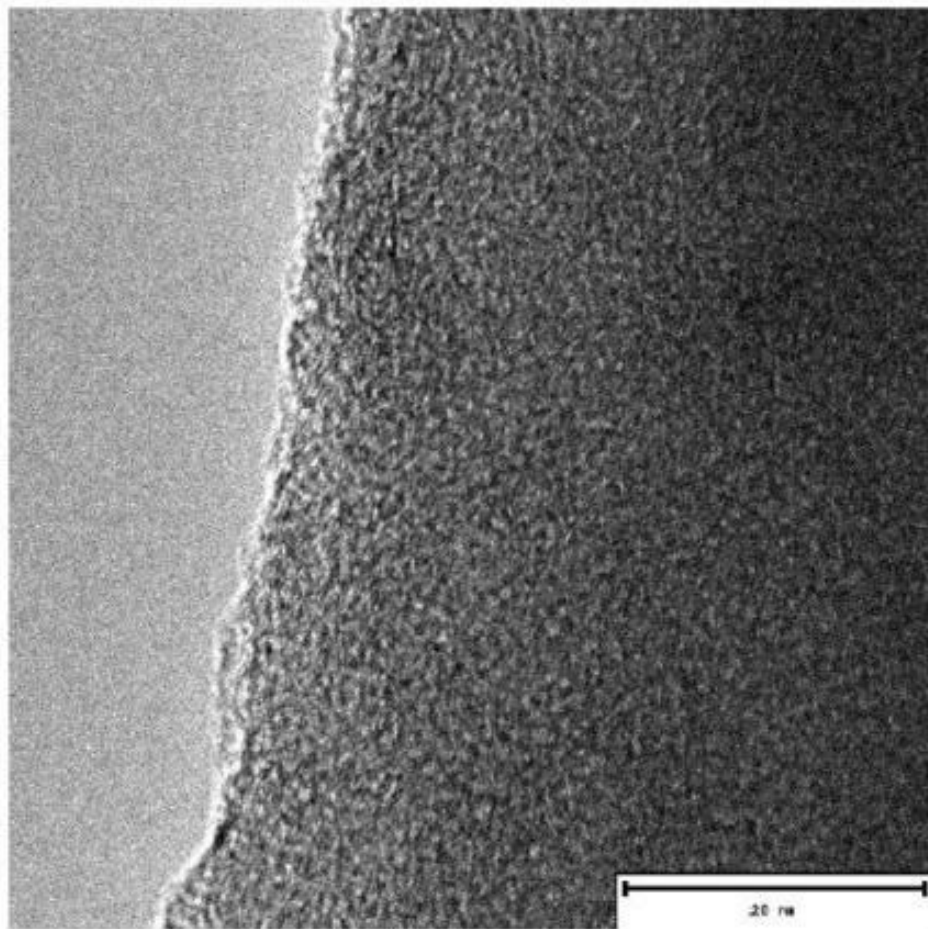


Figure 4.19: TEM image of the disordered graphitic structure of the nanofiber surface

Previous studies [43,44] identified the heterogeneous skin-core structure as the major cause for limited mechanical properties in ECNFs. The TEM image in Figure 4.19 shows this thin skin-core structure for the fiber cross-section. The skin region is made up of layered planes oriented primarily parallel to the surface as shown in Figure 4.19. There are however some crystallite's in the skin region which were mis-oriented with respect to the fiber spinning axis which makes these layered planes heterogeneous. Such turbostratic structures have been reported previously by both Zussman and Zhou [43,44], and shown in Figure 4.20.

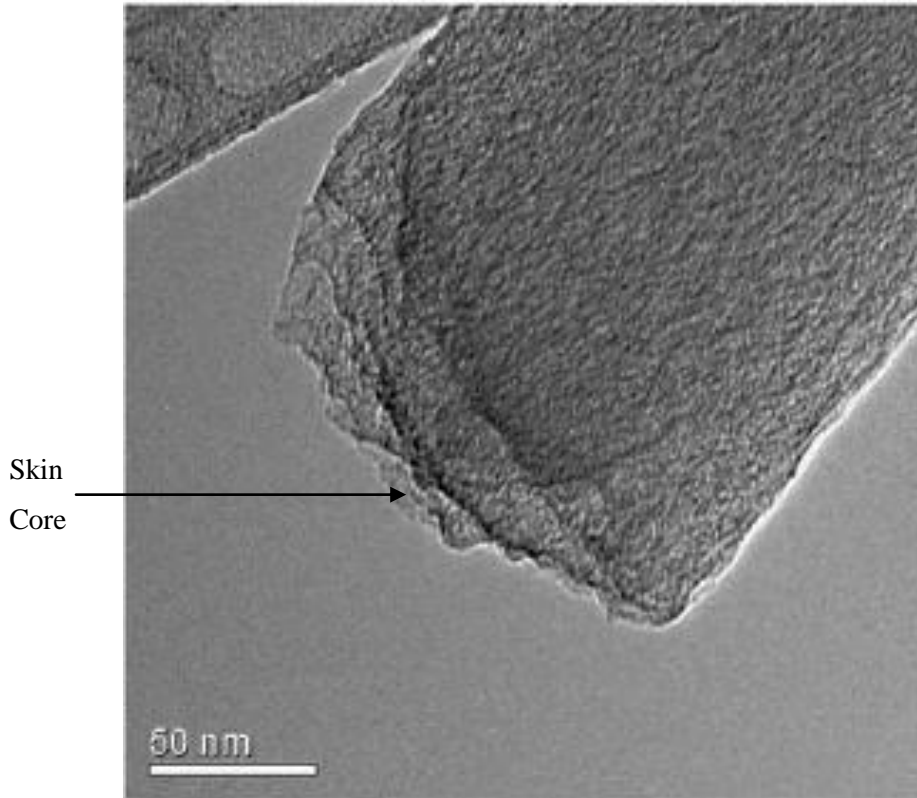


Figure 4.20: TEM image of CNT showing thin skin-core structure [44]

The turbostratic carbon crystallite thickness shown in Figure 4.19 is also relatively small in comparison to the PAN carbonized at 1300°C as shown in Figure 4.21, which is well below the critical flaw size. The larger randomly oriented turbostratic carbon crystallites have been shown to be as a result of increased carbonisation temperatures and can cause premature breakage due to the stress difference between the graphitic crystallites and the surrounding amorphous carbon, as well as can cause crack initiation and brittle fracture.

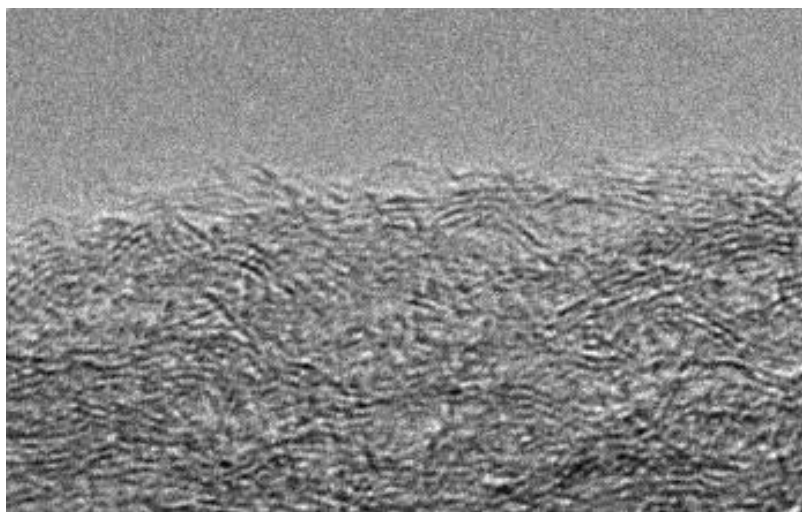


Figure 4.21: Turbostratic carbon crystallite thickness of skin-core structure of PAN carbonized at 1300°C

The diameters of the fibers were also measured using TEM images as shown in Figure 4.22, where the average fiber diameter was found to be roughly 200nm , which had roughly reduced by 50% from the neat PAN prior to heat treatments. The surfaces of the nanofibers are mostly smooth and uniform with some small deposits of particles, but no pitting or major irregularities are visible. The surface roughness could be as a result of the humidity variations during experimentations where it has been shown that smoother fibers are produced at lower humidities.

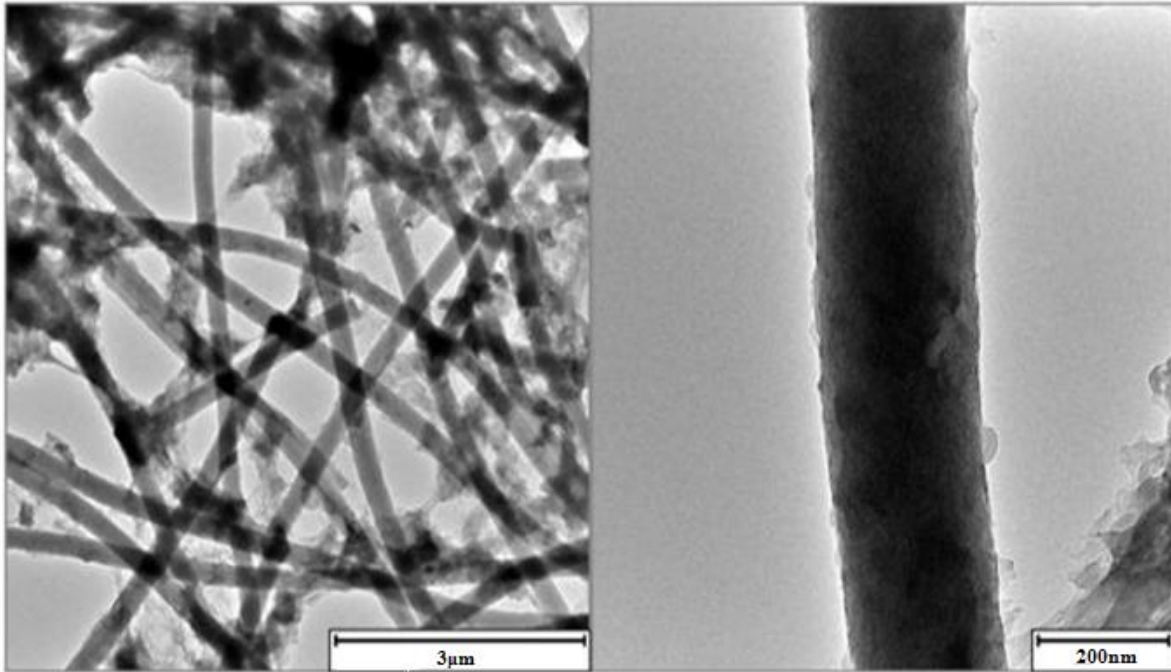


Figure 4.22: TEM images of ECNFs used to characterise fiber diameter and quality of fiber structures

PAN samples, prepared using the electrospinning facility at the University of the Witwatersrand, were carbonized at 800°C for one hour and were then analysed in order to interpret the quality of the nanofibers. Figure 4.23 shows the Raman spectrograph for the ECNF sample with a G/D Band ratio ($I_{\text{D}}/I_{\text{G}}$) of roughly 1:1 which shows a slightly disordered graphitic or crystalline structure, characterised by the high amplitude of the D band that could be attributed to localised defects or lattice distortions [122]. μ

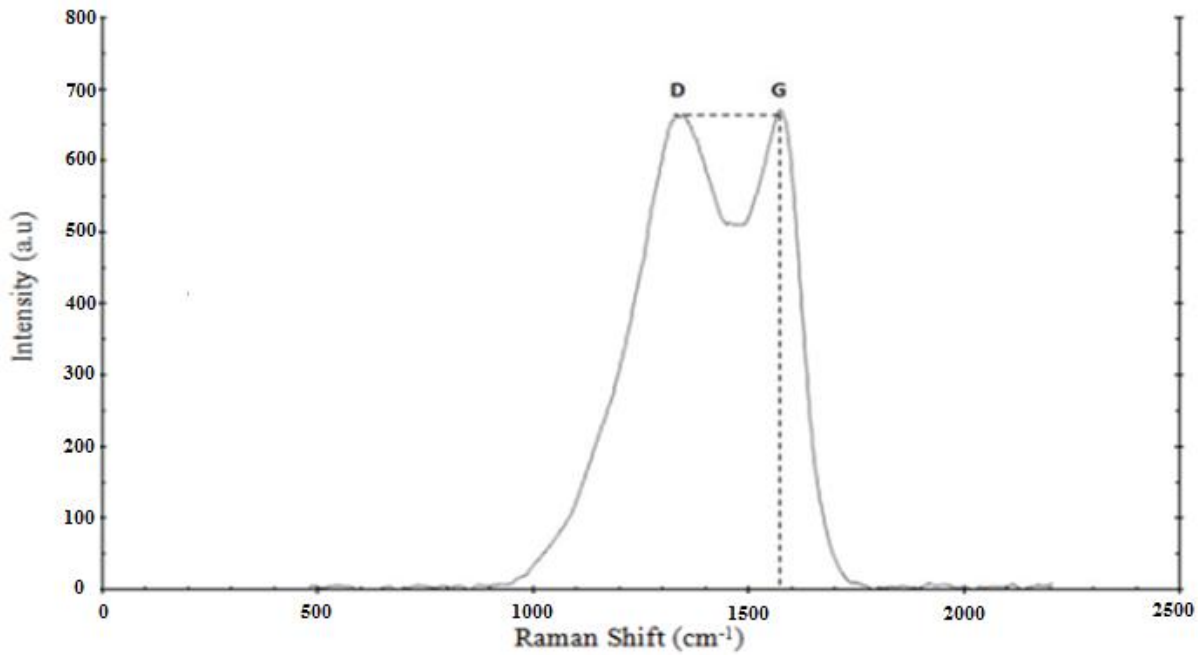


Figure 4.23: Raman spectrograph for the ECNF sample prepared at carbonisation temperature of 800°C for one hour

The ratio between the G band and D bands peaks are commonly used to show the quality of the carbon nanostructures. The G band peak, which is higher, characterises strong Carbon-Carbon graphitic layers, which represent a well graphitized carbon structure. A flawed graphite structure is represented by the D peak which is caused by amorphous carbon fragments rather than well structured graphitic layers. In general, it is safe to assume that for most CNFs and polymer blends with an intensity ratio of the G to D band of greater than one will indicate well graphitized carbon nanostructures [97].

Wang *et al.* [98] prepared PAN-based carbon nanofibers using electrospinning and subsequent heat treatment methods. Raman characterisation revealed D and G peaks which were used to characterise the graphitic crystallite size and mole fraction of the CNFs. They showed that both graphitic crystallite size and mole fraction increased with the increase of carbonisation temperatures.

Pashaloo *et al.* [99] also performed Raman Spectroscopy on PAN-based carbon nanofibers using electrospinning and carbonisation temperature of 800°C. The Raman spectra of their carbonized nanofibers at 800°C showed that the G-band was attributed to the C=C stretching vibrations in the graphite crystallites and the D-band was attributed to the turbostratic and disordered carbonaceous structure. They found that the D to G band ratio of the carbon nanofibers was less than one which indicated a disordered graphitic structure possibly caused by the low carbonisation temperature which didn't allow for efficient carbonisation.

Further interpretation of these Raman spectra show disordered NC-Graphitic (Nano Crystalline Graphite) bonds with no sp^3 (diamond-like) bonds rather than completely a-C (amorphous Carbon)

bonds which contain sp^3 bonds. This is shown in Figure 4.24 where the I_D/I_G ratio of roughly 1:1 and the G band positioning of 1590cm^{-1} correspond to Stage 1, more specifically in between graphite and NC-Graphite. This graphitic ordering of the carbon atoms from the entirely sp^2 chemical bonds, which provide more orbital overlapping that leads to stronger bonding and lower free energy, shows an improved hybridised system over that containing sp^3 bonds [122].

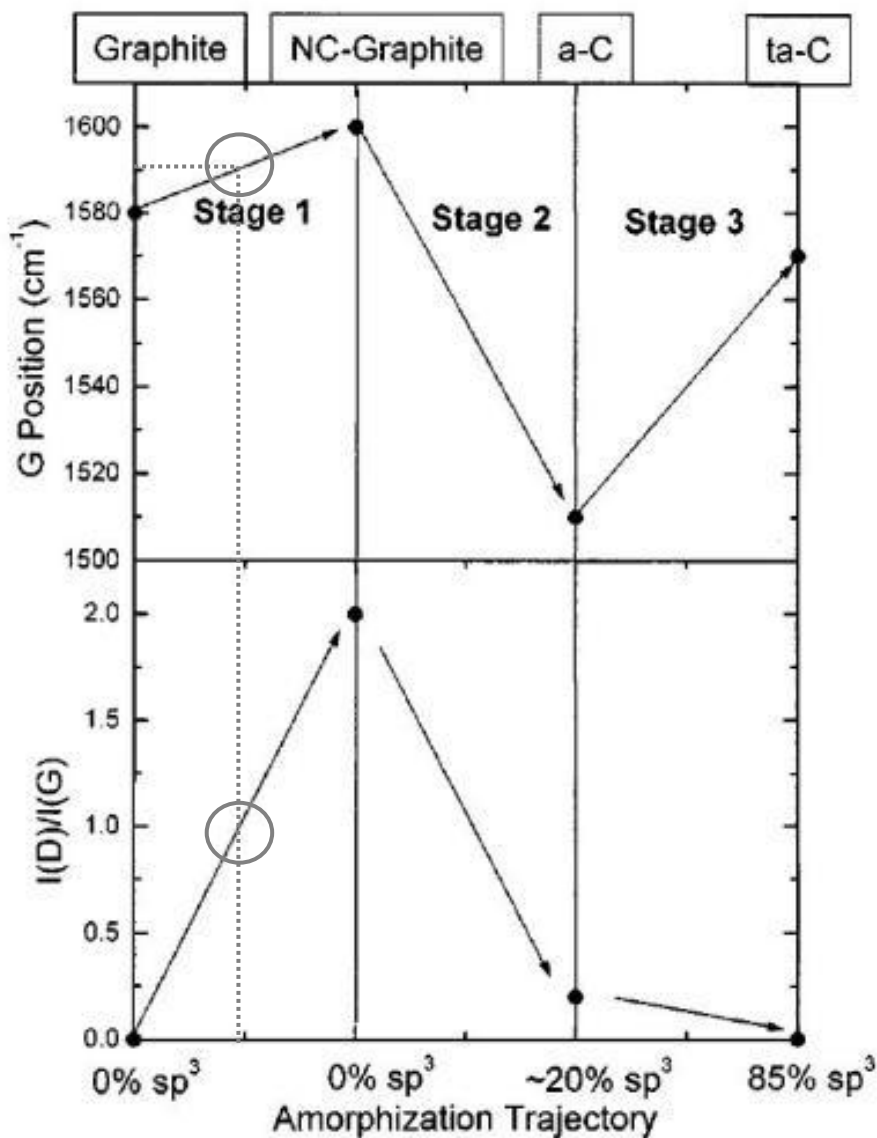


Figure 4.24: Amorphization trajectory, showing a schematic variation of the G position and $I(D)/I(G)$ ratio [122]

TG and DSC analyses in air were also performed on ECNF samples and neat PAN samples in order to find the optimum oxidising treatment temperature as well as to better understand the thermal transitional/cyclization temperatures (T_c). Figure 4.25 shows the TG graph comparing the thermal degradation of both the neat PAN and the ECNFs in terms of weight loss as a percentage. It can be seen that thermal degradation of the PAN sample began to rapidly increase at roughly 300°C . From this it can be seen that the stabilisation temperature in air should not exceed 300°C as the mass of the sample decreases by roughly 30% between 300°C and 320°C . The ECNF sample showed more

gradual thermal degradation until around 500°C where the sample began to rapidly degrade. This then confirms that the stabilisation temperature of 270°C was satisfactory in order to cyclize the PAN polymer prior to carbonisation.

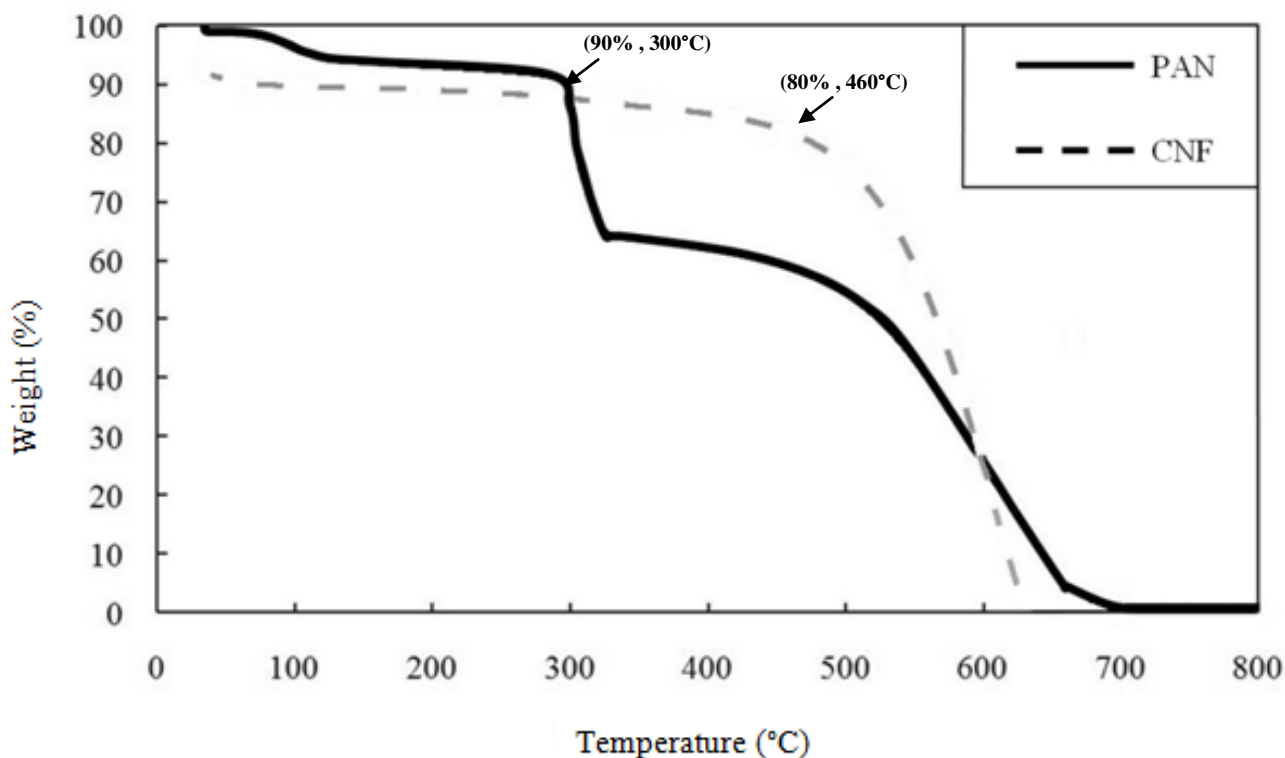


Figure 4.25: TG graph comparing the thermal degradation of both the neat PAN and the ECNFs in terms of weight loss as a percentage

Figure 4.26 shows the DSC thermogram which was used to further characterize the cyclization temperature of the PAN polymer during the oxidative exothermic stabilisation process. This exothermic reaction can be seen by the peak 300°C which corresponds well with the results from the TGA which showed mass degradation also at 300°C. The change in enthalpy of the reaction can be found by calculating the area under this curve, from the baseline (heat capacity of sample) to the tip of the peak. The effect of carbonisation on the PAN structure can also be visualized in Figure 4.26 whereby the exothermic reaction shifts right as the required temperature for further crystallization increased. The amplitude of the peak was also reduced as a smaller amount of heat was required for further cyclization, and finally the band broadened as the reaction time increased.

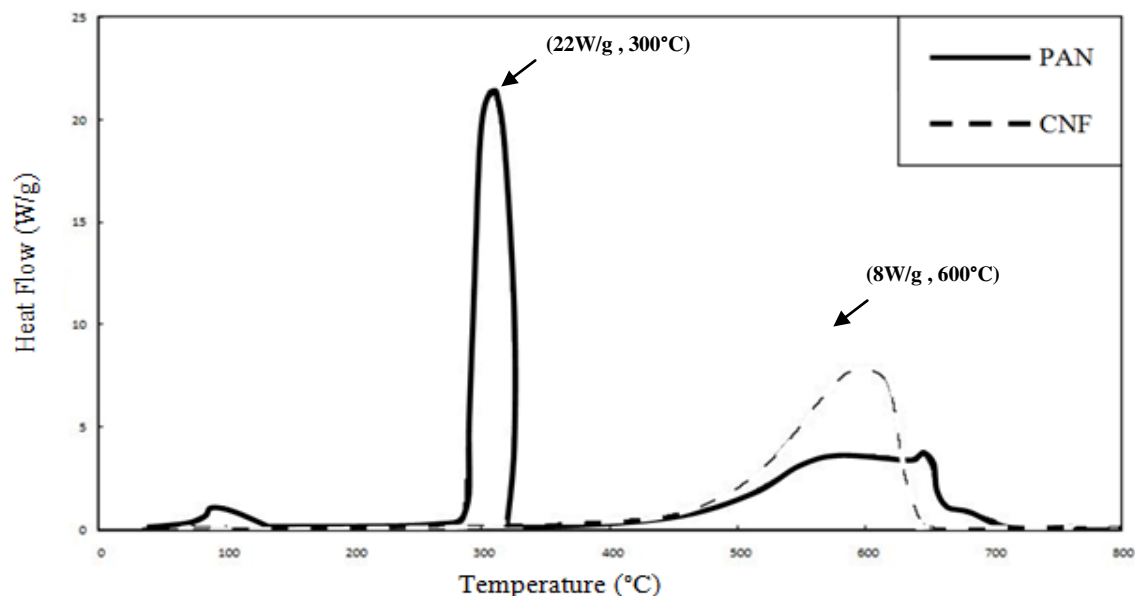


Figure 4.26: DSC thermogram which was used to further characterize the cyclization temperature of the PAN polymer during the oxidative exothermic stabilisation process

Energy-dispersive X-ray spectroscopy (EDX) was used as an Elemental analysis tool to analyse the samples prepared at the holding carbonisation temperature of 800°C. This was performed in order to quantifiably analyse the carbon content at this carbonisation temperature. The sample showed a carbon weight percentage of roughly 83% and an atomic weight percentage of 89.9% as shown in Figure 4.27, which is a good indication that carbonisation was successful whilst maintaining a semi-amorphous structure with partial crystallinity. It has been shown in previous studies [6,117,121] that higher carbon weight percentages of CNFs result in more dense fibers with much improved mechanical properties.

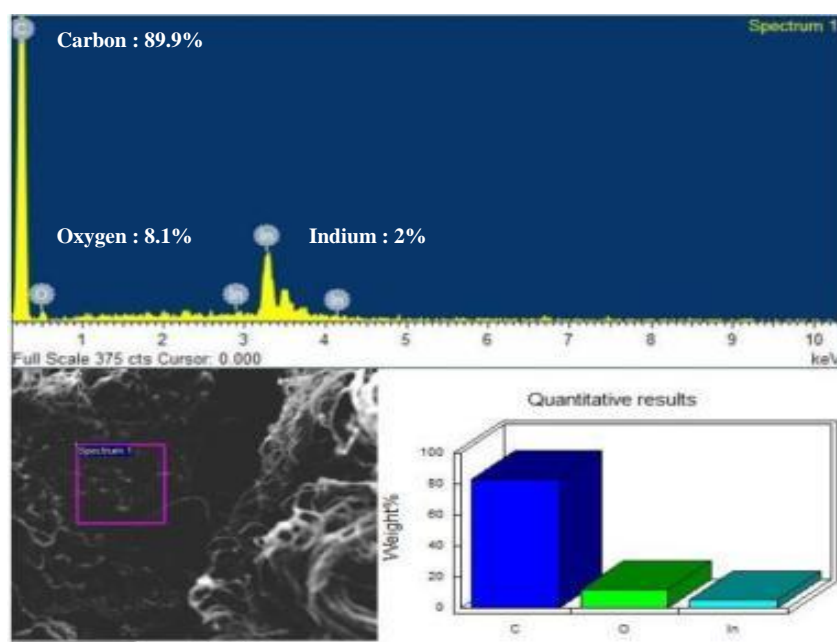


Figure 4.27: Elemental analysis of the sample prepared at the holding carbonisation temperature of 800°C

5 RESULTS AND DISCUSSION

The following section presents the final processed mechanical characterisation data according to the methods discussed in Chapter 3 as well as the morphological characterisation results from Chapter 4, and sheds some light on these results. The following Chapter is divided into three sections, namely; the effect that the fiber volume fraction has on the mechanical properties of the glass (Section 5.1), PAN/glass (Section 5.2) and ECNF/PAN/glass reinforced composites (Section 5.3). Only graphical and relevant results are shown here whilst the complete set of results can be found in Appendix A.

5.1 Glass Reinforced Epoxy Composite

Commercially, GRPCs are widely used in a variety of engineering industries such as aviation, aerospace, automobile and ship construction, mainly because the composites are extremely strong, stiff, lightweight, cheap and less brittle than CRPCs. Therefore, there is much interest in optimizing the mechanical properties of said composites and hence the purpose for performing this experiment.

Firstly though, it is pertinent to discuss the reasons for selecting the three glass fiber volume fractions used in the experiment. The three volume fractions of glass fibers were chosen according to the application of the composites rule of mixtures for fiber reinforced matrices as shown in the following analysis and based on the results from previous studies also discussed in this section [8,34,127,128].

The theoretical analysis begins with assuming that all fibers have the same diameter and can all be arranged perfectly parallel to one another, then the theoretical maximum fiber volume fraction could be attained with a hexagonal close packing arrangement as shown in Figure 5.1. The volume fraction thus equates to the area fraction when the alignment of the fibers is fixed [127]. In the triangular unit cell, also shown in Figure 5.1, the total area occupied by fibers is equal to three 60° segments and thus the unit cell has an area equal to $\sqrt{3} R^2$, so that;

$$V_f^{\max} = \frac{3 \times \pi R^2 / 6}{\sqrt{3} R^2} = \frac{\pi}{2\sqrt{3}} = 0.907 \approx 91\% \quad (5.1)$$

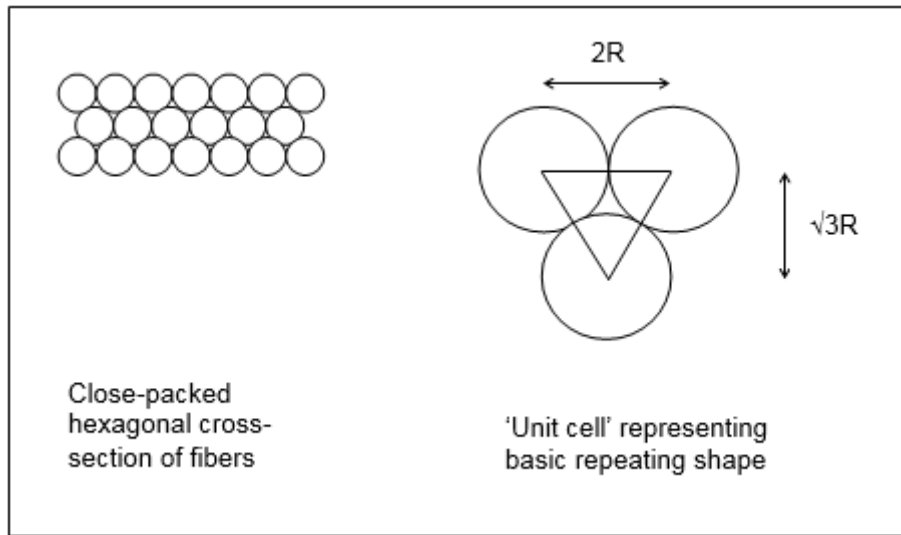


Figure 5.1: Triangular unit cell in hexagonal close packing arrangement [127]

Such a high volume fraction is however not achievable in reality due to the fact that adjacent fibers, in direct contact with each other, would result in an ineffective composite with poor matrix wetting. When the fibers are arranged in a non-unidirectional form, such as woven fabrics, a proportion of the reinforcement is then oriented out of plane. Therefore, close packing is no longer possible, and the maximum fiber volume fraction becomes reduced. Table 5.1 gives typical values for fiber volume fractions in polymer composites, however exact values will be both material and process-dependent. The experimental volume fractions of glass fibers used in this research were thus based on these results shown below for woven fibers.

Table 5.1: Typical values for fiber volume fractions in polymer composites [127]

Reinforcement	Range of fiber volume fractions (%)	Optimum fiber volume fraction (%)
Unidirectional	40 – 60	50
Woven	20 – 40	30
Random Mat	10 – 20	15

Previous studies [8,34,114,128] show that fiber volume fractions within the ranges shown in Table 3.2 are ideal for improving matrix toughening as well as improving material strength. Singh *et al.* [34] presented their investigations of mechanical behaviour of random mat glass fiber reinforced epoxy composites and revealed that the tensile strength and flexural strength was greatly influenced by the fiber content of reinforcement in the matrix with 20% volume fraction of glass fibers resulting in the

optimum mechanical properties. Rathnakar *et al.* [128] experimented with the effect of fiber orientation on the flexural strength of woven glass fiber reinforced epoxy laminated composite materials and showed that 35% fiber volume fraction was the optimum volume fraction. Thwe *et al.* [8] showed an increase in ultimate tensile strength of bamboo reinforced PP with fiber content ranging from 10 to 30% above which the strength decreased, being attributed to poor adhesion between the fiber and matrix, thus promoting void formation.

Therefore, the mechanical tests (tensile, flexural and impact) performed on the 16%, 24% and 32% volume fraction glass fiber reinforced epoxy composites were performed in order to characterize the optimization of the glass loading for the further production of the hybrid multiscale composites. Subsequently, the results and discussion of the mechanical and morphological characterisation are presented in this section.

5.1.1 *Tensile Properties*

The tensile strength and tensile modulus for the 16%, 24% and 32% glass fiber volume fractions were plotted and shown in Figure 5.2 and Figure 5.6, respectively. The error bars in these figures represent the standard deviation in results which is a direct correlation to the consistency of the obtained results. In tensile testing, the major mechanism of failure is generally by tension, which can be characterized as brittle failure, or by the fiber pull out phenomenon. This is as a result of the mismatch in strengths between the tensile strength of the glass fibers and the weaker epoxy matrix.

The effect of woven glass fiber [0°/90°] additions on the tensile strength of the neat epoxy resin is shown in Figure 5.2. For all fiber volume fractions, the composites achieved a higher tensile strength when compared to the unreinforced epoxy. From this it was evident that the glass fibers had thus improved the tensile strength of the epoxy matrix, where the fibers were able to carry the majority of the tensile loading forces. This trend was also shown by Al-Jeebory *et al.* [114], whereby the tensile strength of epoxy increased as the glass fiber percentage increased. The initial increase in tensile strength from the neat epoxy to the 16% fiber volume glass composite was significant with a 540% increase in tensile strength. The relative increase in strength then showed linear improvements of 13% and 28% as the fiber volume fraction increased from 16% to 24% and from 24% to 32%, respectively. This linear increase in tensile strength is as a direct result of the increased number of higher strength glass fibers acting as reinforcement, which, with good matrix wetting allowed for better stress distribution during tensile failure throughout the composite material.

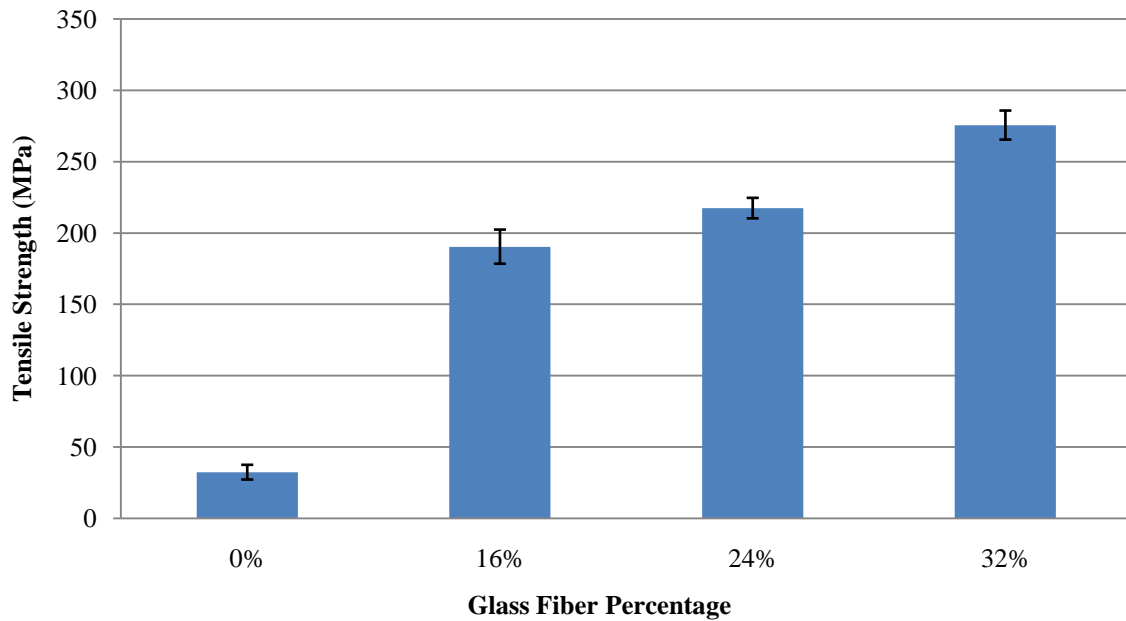


Figure 5.2: Tensile strengths of varying glass fiber volume fractions

Figure 5.3 shows the SEM image of the fracture surface of a 16% fiber volume fraction composite sample whereby the weak bonding adhesion between the fibers and the matrix is characterised by the fiber pull out phenomenon. All of the 16% GRPCs failed samples showed fiber pull out as the major contributor to failure, confirming poor interfacial bonding and therefore poor load distribution, which resulted in the fibers being easily pulled out rather than taking the full loads applied to the composite samples, making the glass fibers less effective in providing for the tensile strengths assumed to be achieved with incorporating the fillers as reinforcement.

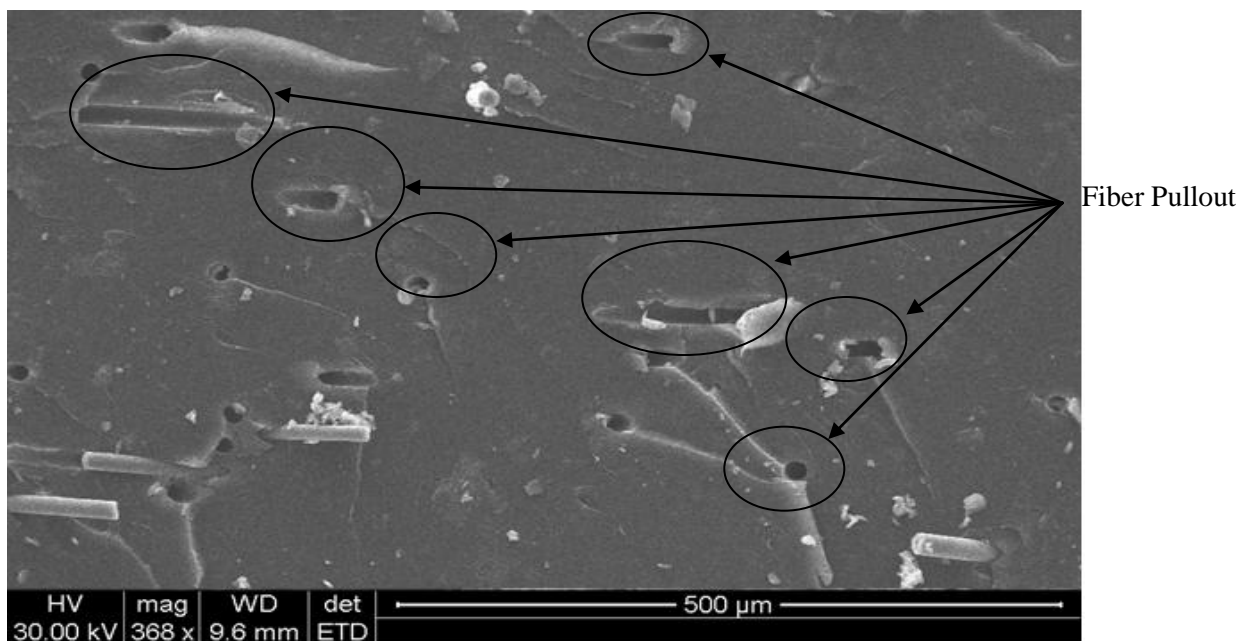


Figure 5.3: SEM image of a 16% volume fraction GRPC sample showing poor interfacial bonding as shown by the fiber pullout of the glass fiber after tensile failure

The SEM image of a failed 24% volume fraction GRPC sample, as shown in Figure 5.4, exhibits both the fiber pull out phenomenon, whereby the surfaces of the glass fibers are smooth, which was representative of poor interfacial bonding, as well as failure of the glass fibers in breakage and the brittle matrix failure. The more fibers present in the 24% glass fiber volume fraction samples therefore resulted in more significant increases in interfacial bonding caused by the increase in the surface area of fiber/matrix bonding and the reduction in matrix rich zones which explains the improvement of tensile properties with increased fiber volume fraction additions.

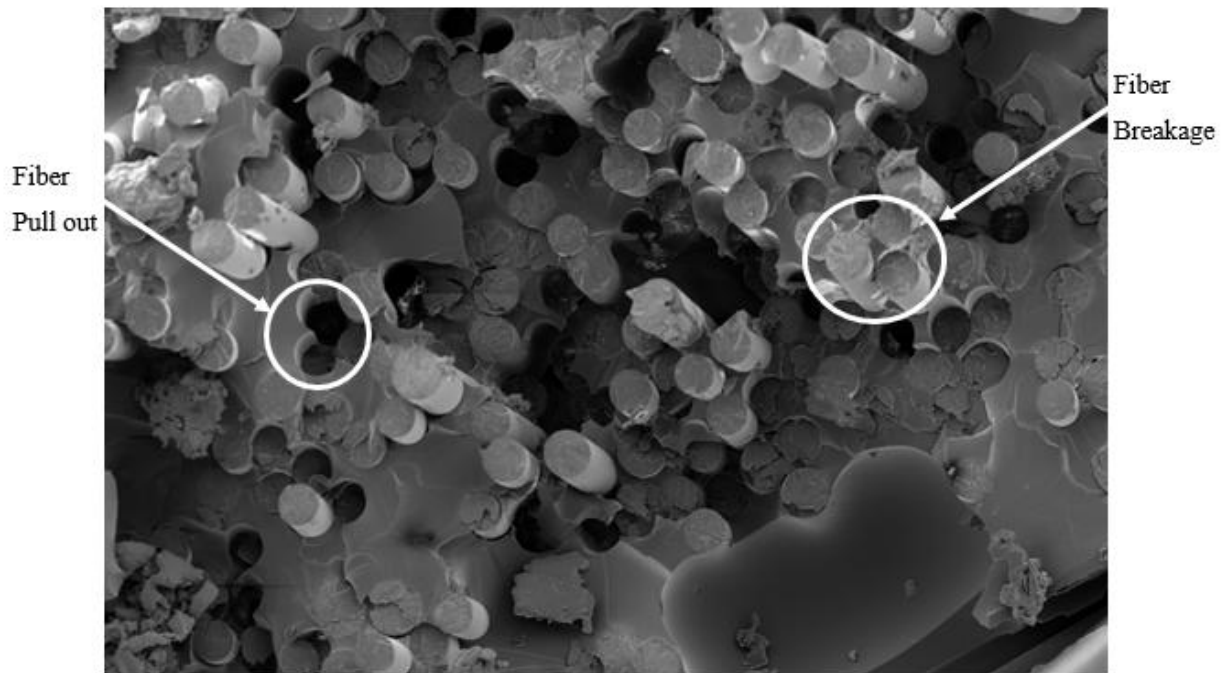


Figure 5.4: SEM image of a 24% volume fraction GRPC sample showing a mixture of both fiber pullout and breakage which is indicative of improved interfacial bonding between fibers and matrix over that of the 16% fiber volume fraction samples

The SEM image of a failed 32% glass fiber volume fraction tensile sample is shown in Figure 5.5 which shows little to no evidence of fiber pullout with the failure mechanism of the sample being attributed entirely to fiber breakage, which is indicative that the interfacial bonding between matrix and fibers was much improved to that of the lower fiber volume fraction samples and therefore the improved tensile strengths.

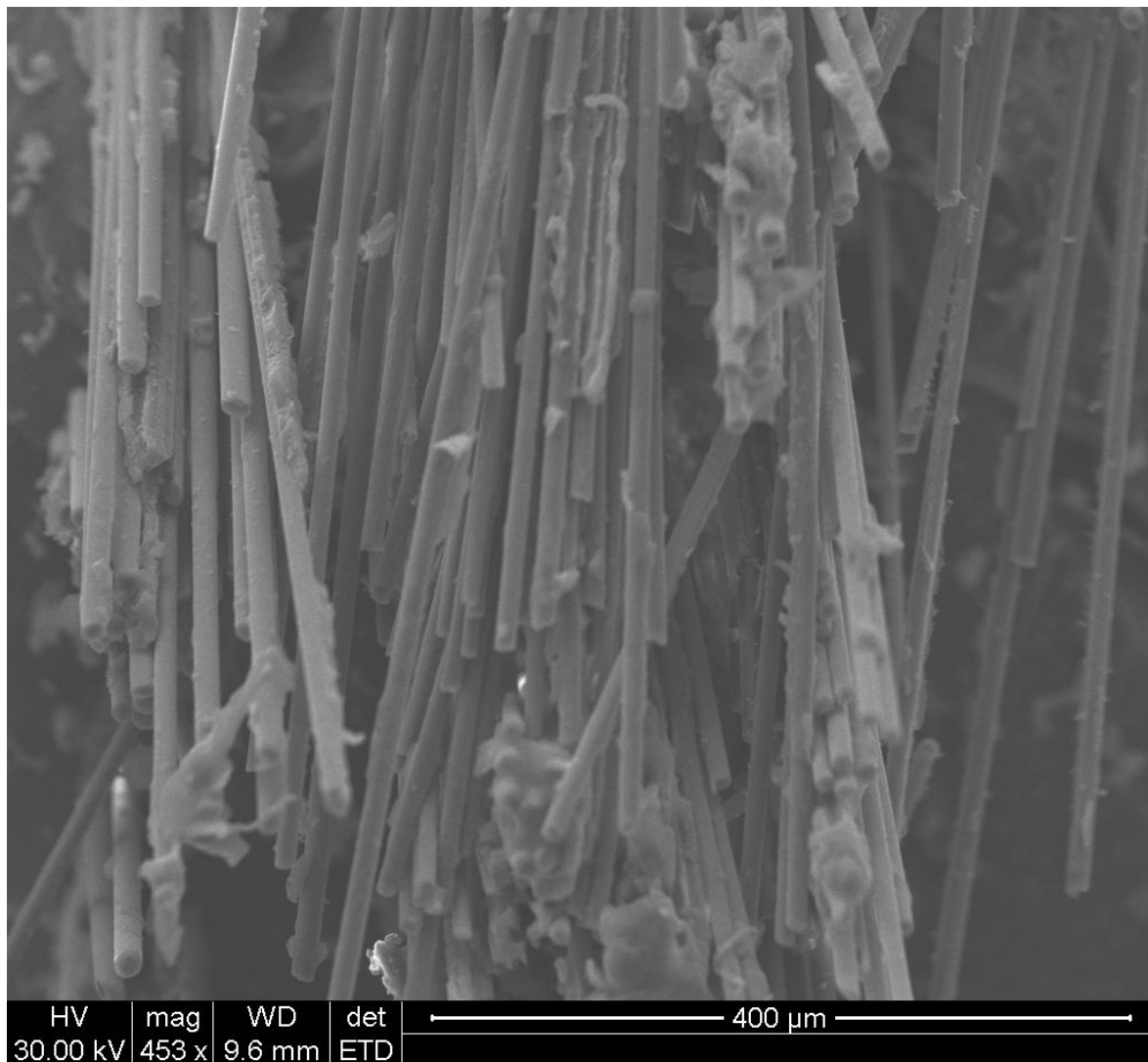


Figure 5.5: SEM image of a 32% volume fraction GRPC sample showing the lack of fiber pullout which is indicative of good interfacial bonding between fibers and matrix

The effect of woven glass fiber [0°/90°] additions on the tensile modulus of the neat epoxy resin is shown in Figure 5.6. As with the tensile strength, all fiber volume fractions achieved a higher tensile modulus when compared to unreinforced epoxy. The initial increase in tensile modulus from the neat epoxy to the 16% fiber volume glass composite was significant with a 430% increase in tensile modulus. The relative increase in modulus was then linear as the fiber volume fraction increased, 44% and 27% fiber volume fractions, respectively. The glass fibers themselves showed an average tensile modulus of 72GPa and the epoxy matrix showed a tensile modulus of 3.3GPa . According to composite theory, it is accepted that the modulus increases with the percentage of reinforcement, as the addition of fibers to the matrix results in the composite consequently becoming stiffer.

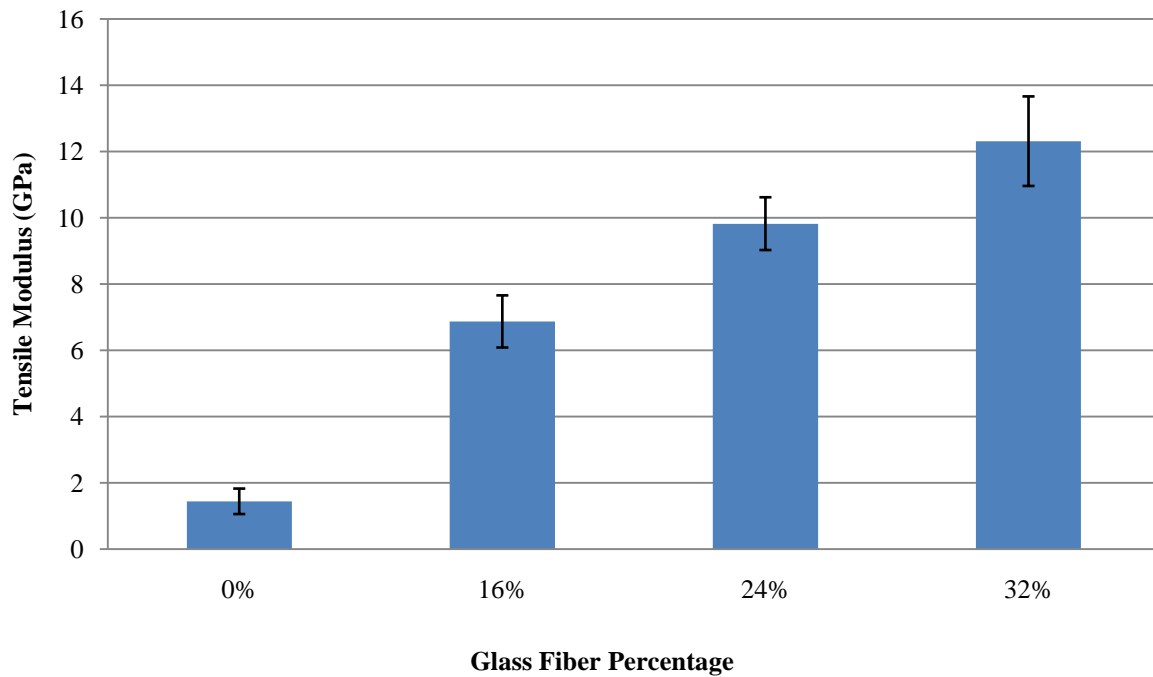


Figure 5.6: Tensile moduli of varying glass fiber volume fractions

5.1.2 Flexural Results

The flexural strength and flexural modulus, for the 16%, 24% and 32% glass fiber volume fraction composites are shown in Figure 5.7 and Figure 5.9. The error bars in these figures show the standard deviation in results which is a direct correlation to the consistency of the obtained results. In flexural testing, various mechanisms of failure exist such as tensile, compressive, shear and delamination which were all likely to occur simultaneously throughout the failure of the GRPC samples under three point testing loads. More specifically though, in the three-point flexural tests performed, the most common failure occurred due to compressive and shear failure which generally occurred in the transverse fiber direction in between fiber layers, in the matrix rich zones, where reinforcement was non-existent.

As mentioned before, the epoxy resin is brittle and as such its flexural strength is also very low. The effect of woven glass fiber [0°/90°] additions on the flexural strength of the neat epoxy resin is shown in Figure 5.7. For all fiber volume fractions, the composites achieved higher flexural strengths when compared to the unreinforced epoxy. From this it was evident that the glass fibers had improved the flexural strength of the epoxy matrix, where the high strength and modulus of these fibers aided in carrying a large amount of the loads. The initial increase in flexural strength from the neat epoxy to the 16% fiber volume glass composite is significant with an increase in flexural strength of 124%. The relative increase in strength was then linear as the fiber volume fraction increased, 24% and 22% flexural strength improvements, respectively. According to Singh *et al.* [34], a 20% volume fraction of glass fibers resulted in the tensile strength and flexural strength increase of 14.5% and 123.65% respectively. The overwhelming contribution to improved flexural strengths, as with the tensile

strength, can be attributed to the presence of the rigid glass fibers which increased the overall stiffness of the composites caused by their reinforcing effects.

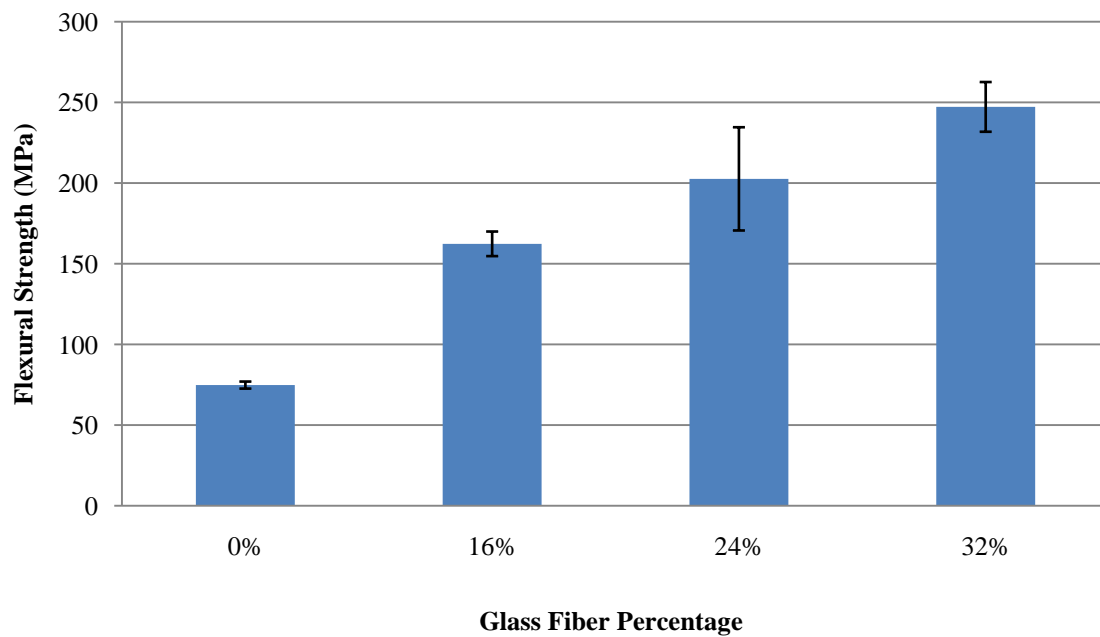


Figure 5.7: Flexural strengths of varying glass fiber volume fractions

Once again, this increase in flexural strength can be explained by looking at the interfacial zone where bonding between the glass fibers and the epoxy matrix exists. More specifically though, the increased flexural strengths can be explained by the mechanical interlocking of the glass fibers in the plain weave of the glass fiber mats, which was maintained throughout the composite curing process. Also, the plain woven glass fabric was symmetrical, with good stability and reasonable porosity, which led to good wetting of the fibers in the epoxy matrix, hence improving the contact surface area of the fibers with the matrix. This ultimately led to improved interfacial bonding between the fibers and the matrix evidenced by the epoxy particulates' adherence to the once smooth glass fibers as shown in Figure 5.8, which in turn improved the overall strength of the composite

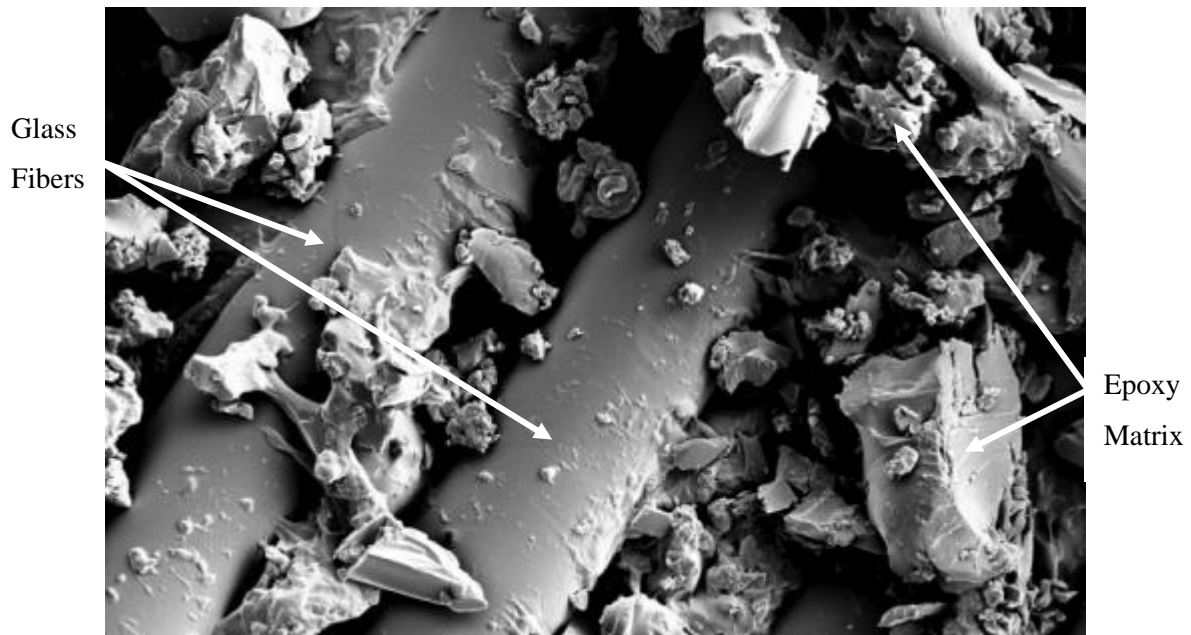


Figure 5.8: SEM image showing good interfacial bonding between fibers and matrix characterised by the uneven surfaces of the glass fibers, as well as reduced matrix rich zones

Thus, as a result of the increased glass fiber content, the flexural strength increased due to the increased resistance to shearing and compression; as well as the reduction in matrix rich zones between fibers, as shown in Figure 5.8. The 32% fiber volume fraction achieved the highest flexural strength which correlates well with Al-Jeebori *et al.* [114]. Ratna *et al.* [115] experimented with 30% glass fiber volume fraction reinforced epoxy and showed a flexural strength of 460MPa and flexural modulus of 19GPa. These researchers used different manufacturing techniques and resin systems, however the trend is consistent, which indicates that large improvements will most likely not be seen above a fiber volume fraction of 30% as discussed before.

The effect of woven glass fiber [0°/90°] additions on the flexural modulus of the neat epoxy resin is shown in Figure 5.9. For all fiber volume fractions, the composites achieved higher flexural modulus when compared to the unreinforced epoxy. From this it was evident that the glass fibers improved the flexural modulus of the epoxy matrix, where the high modulus of these fibers added to the overall stiffness of the composite, causing increased modulus. The initial increase in flexural modulus from the neat epoxy to the 16% fiber volume glass composite was significant with an increase in flexural modulus of 60%. The relative increase in strength was then linear as the fiber volume fraction increased, 16% and 36% flexural modulus improvements, respectively.

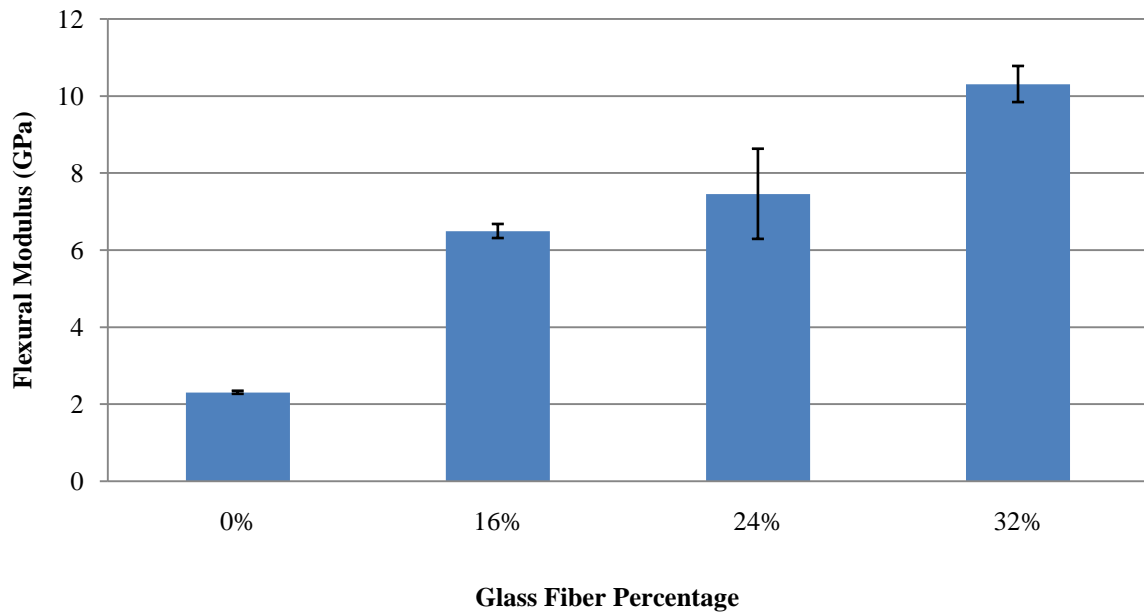


Figure 5.9: Flexural moduli of varying glass fiber volume fractions

5.1.3 *Impact Results*

The raw data was processed from each impact specimen tested for the, 16%, 24% and 32%, glass fiber volume fractions, and the impact resistance was determined and are shown in Figure 5.10. The error bars in the figure show the standard deviation in results. Impact strength, directly related to overall toughness, is defined as the ability of a material to resist the fracture under stress applied at high speed. Generally, the impact strength of epoxy resin is considered to be very low due to brittle nature of the resin.

The effect of woven glass fiber [0°/90°] additions on the impact resistance of the neat epoxy resin is shown in Figure 5.10. For all fiber volume fractions, the composites achieved a higher impact resistance when compared to unreinforced epoxy. From this it was evident that the glass fibers had improved the impact resistance of the epoxy matrix, where the glass fibers were able to absorb the maximum impact energy during loading and disperse these loads amongst adjacent fibers, thus sharing the loads. The initial increase in impact resistance, from the neat epoxy to the 16% fiber volume glass composite, increased by a factor of roughly 30 times. The impact resistance continued to improve with increased fiber reinforcement. The relative increase in resistance then plateaued as the fiber volume fraction increased, 45% and 3% impact resistance improvements, respectively.

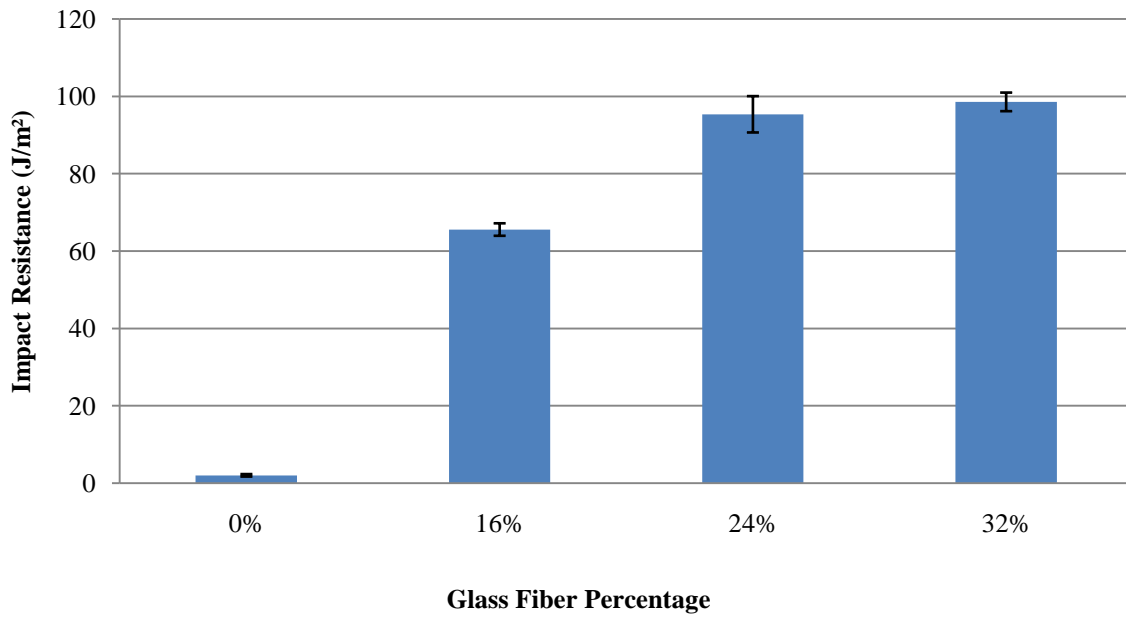


Figure 5.10: Impact resistance of varying glass fiber volume fractions

Composite fracture toughness was affected by interlaminar and interfacial strength parameters whereby the fibers played an important role as they interacted with the crack formation in the matrix and acted as stress transferring mediums during failure. Figure 5.11 shows a failed 32% impact sample whereby it can be seen that the glass fibers were able to accommodate for the shearing load and showed fiber breakage as well as resin cracking as opposed to fiber pull out.

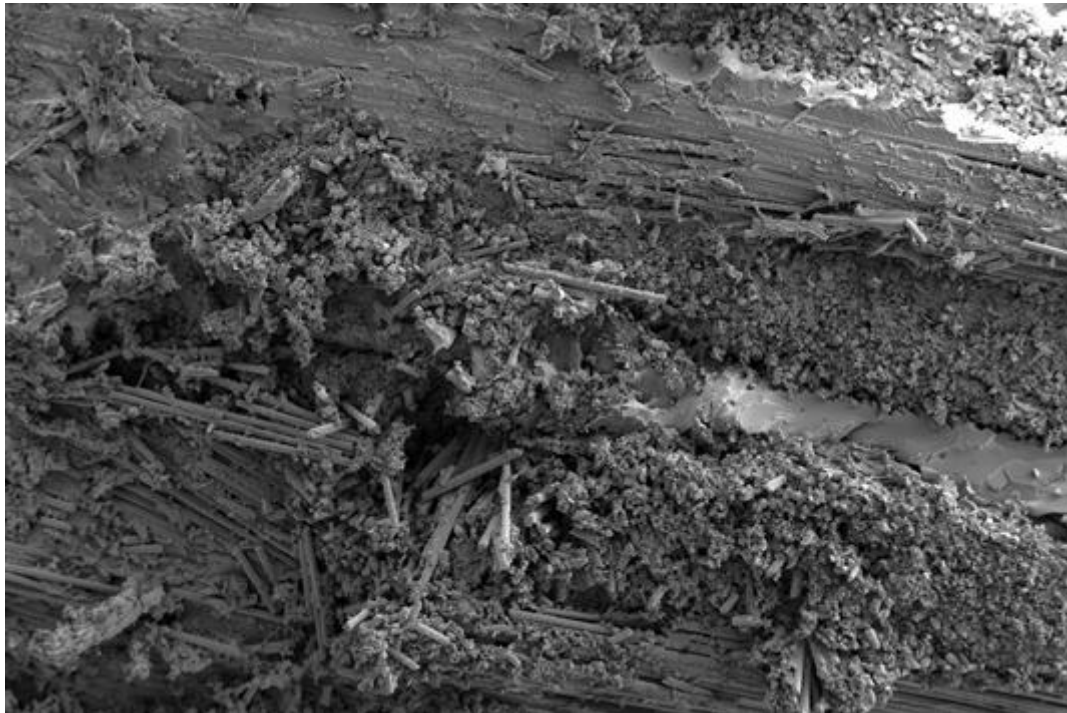


Figure 5.11: SEM image of a 32% volume fraction GRPC sample showing the debris of glass fibers left after failure whereby the glass fibers accommodated for the shearing load and showed fiber breakage

5.2 PAN Nanomat Reinforced GRPC

Recent research has shown that there is great potential in significantly improving the mechanical properties of microfiber reinforced laminated composites, such as GRPCs, by adding a secondary reinforcement made of polymer nanofibers located at one or more ply interfaces. This secondary reinforcement of nanofibers was included so as to reduce the mismatch of ply properties between fibers and matrix, as was found with the multidirectional GRPC samples. Also, the nanofibrous mats act as bonding plies that join the adjacent woven glass fiber plies without increasing the composites weight or the laminates thickness. This has been shown to improve both the fracture toughness and strength of the GRPCs with respect to both static and impact loadings as a result of the continuous, large surface area and porous nature of the non-woven nanofibers allowing for improved resin infusion. This porous characteristic of the polymeric nanofiber mats therefore allowed for the flow of resin during VARTM to permeate through the laminates, thus ensuring complete impregnation of reinforcements. However, research has shown through careful SEM observations of composite cross-sections that mechanical properties are improved only when the electrospun nanofibrous sheets are completely impregnated in the matrix, a condition that is more difficult to achieve at higher membrane thicknesses, and thus higher fiber volume fractions. This is probably because of the formation of voids/defect in the resin when high amounts of nanofiber were used.

It should also be noted that from the experimental findings as discussed in Section 3.2.2, there do exist negative effects when using higher nanofiber volume fractions on the process ability of the VARTM because of the reduction in nanomat permeability. Therefore, with this in mind, the three variations of PAN fiber volume fractions, 0.1%, 0.2% and 0.5%, were considered, also with the aid of experimental results from a number of researchers, as shown in Table 5.2. However, it should also be noted that differing values of critical fiber volume fraction exist because they are dependent on the different ability of the matrix to impregnate the different materials. Also, many parameters such as the quantity or the thicknesses of the nanofibrous mats obtained from various kinds of polymer nanofibers which affect the fracture toughness and strength, as well as the interfacial characteristics between the nanofibers and the polymer, are still left unknown.

Table 5.2: Optimum nanofiber volume fractions from a variety of researchers in the field of polymeric nanofiber reinforcement for composites

Research	Polymer Nanofiber Reinforcing Material	Primary Composite	Optimum fiber volume fraction (%)
Zhang <i>et al.</i> [53]	Polyetherketone cardo (PEK-C)	Carbon Fiber Reinforced Epoxy	0.4
Chen <i>et al.</i> [117]	Nylon 6	Poly(methyl methacrylate) (PMMA)	1.7
Neppalli <i>et al.</i> [129]	Nylon 6	Poly(e-caprolactone) (PCL)	2
Ozden <i>et al.</i> [70]	Poly(styrene-co-glycidyl methacrylate) P(S-co-GMA)	Araldite epoxy	0.2
Molnár <i>et al.</i> [130]	PAN	Carbon Fiber Reinforced Epoxy	0.2
Tian <i>et al.</i> [131]	Nylon 6	BIS-GMA/TEGDMA	1.5

Finally, the mechanical tests (tensile, flexural and impact) of the glass/PAN fiber multiscale hybrid reinforced epoxy composites were performed in order to optimize the PAN loading for the improvement of mechanical properties of the optimum, 32% volume fraction, GRPC. Subsequently, the results of the mechanical characterisation are presented in this section.

5.2.1 *Tensile Properties*

The tensile strength and tensile modulus, for the various glass/PAN fiber multiscale reinforced hybrid composite volume fractions are shown in Figure 5.12 and Figure 5.16. The error bars in these Figures show the standard deviation in results which is a direct correlation to the consistency of the obtained results. In hybrid composites, the mechanical properties of the composites are largely reliant on both the modulus and percentage of elongation at break of the individual fibers. In particular, the moduli of glass fibers, 72GPa , are much higher than that of the epoxy matrix and as such stress concentration sites arise within the interfacial zones between fibers and matrix formed by this stress mismatch, causing premature failure. However, the modulus of the PAN fibers, 7GPa [116] – 48GPa [66], are relatively higher than that of the epoxy, but not as high as the glass fibers; and the extensibility of PAN is much higher in comparison to the glass fibers, thus allowing for more elastic behaviour, or elongation at break, of the fibers within the composite during failure. Therefore, during tensile

composite failure, there is a transfer of high stresses from the rigid glass fibers to the less rigid PAN nanofibers and then to the weaker, more brittle, epoxy matrix, which leads to the premature failure of the PAN fibers instead of the pure matrix failure as seen in the GRPC samples. Therefore the improvement in tensile strengths of the hybrid composite at 32% volume fraction of glass fiber loadings with the addition of PAN nanofiber mats depended on whether the PAN fibers could effectively transfer the loads from the glass fibers to the matrix, without considerably increasing the ply thickness, which is critical for the improvement of impact resistance discussed in section 5.2.3.

The effect of PAN additions on the tensile strength of the 32% volume fraction GRPC samples is shown in Figure 5.12. For all fiber volume fractions, the composites achieved a lower tensile strength when compared with the neat 32% volume fraction GRPC. From this it was evident that the PAN fibers did not improve the tensile strength of the neat 32% volume fraction GRPC at these loading volume percentages. However, there was still an increasing trend with increased PAN loading. The 0.5% PAN reinforced GRPC was found to have roughly the same tensile strength as the unreinforced GRPC, and the 0.1% and 0.2% PAN loadings showed a reduction of 25% and 15%, respectively. This trend was also shown by Chen *et al.* [117], whereby the tensile strength and modulus of Nylon 6 nanofiber reinforced PMMA was significantly improved as the fiber percentage increased above a fiber content of 2.5%, caused by the increasing reinforcing effect of the fibers, after which the strengths then decreased due to the non-porous nature of the thicker mats causing improper fiber impregnation.

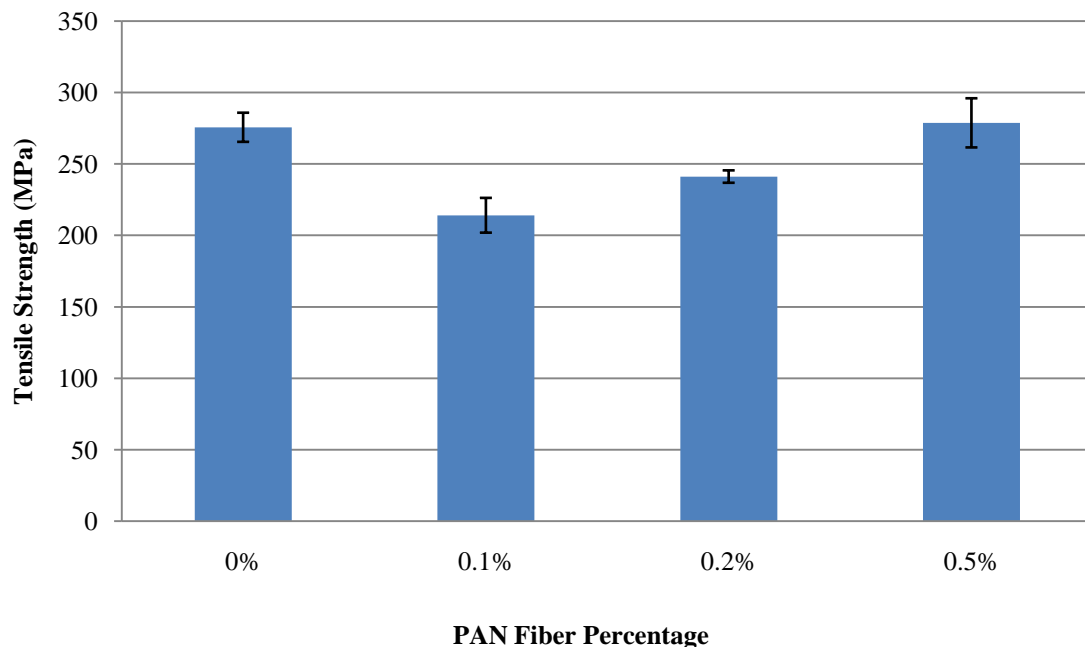


Figure 5.12: Tensile strengths of varying PAN nanofiber volume fraction GRPC

The drop off in tensile strength was contradictory to what was expected from the incorporation of these PAN nanofibers; which was to improve the tensile strength of the composite material without a

sacrifice in strain at break. However, as mentioned before, for hybrid composites, the mechanical properties are largely reliant on both the orientation of the individual fibers, therefore SEM imaging was performed on the PAN nanofibers that had been electrospun onto the glass fiber mats in order to characterise the fiber orientations.

Figure 5.13 shows a PAN nanofiber that was electrospun onto the glass fiber mat that is aligned along the fiber axis as a result of the high stretching rate and the high elongation of the solidifying PAN jet. Arinstein *et al.* [118], found that the increase in mechanical properties of individual PAN nanofibers could be related to the orientation of the nanofibers, which became rather difficult to obtain as the diameter decreased. The observation from the SEM imaging then strengthens the argument that the tensile strength of the samples should improve with the addition of such well orientated secondary fiber reinforcements.

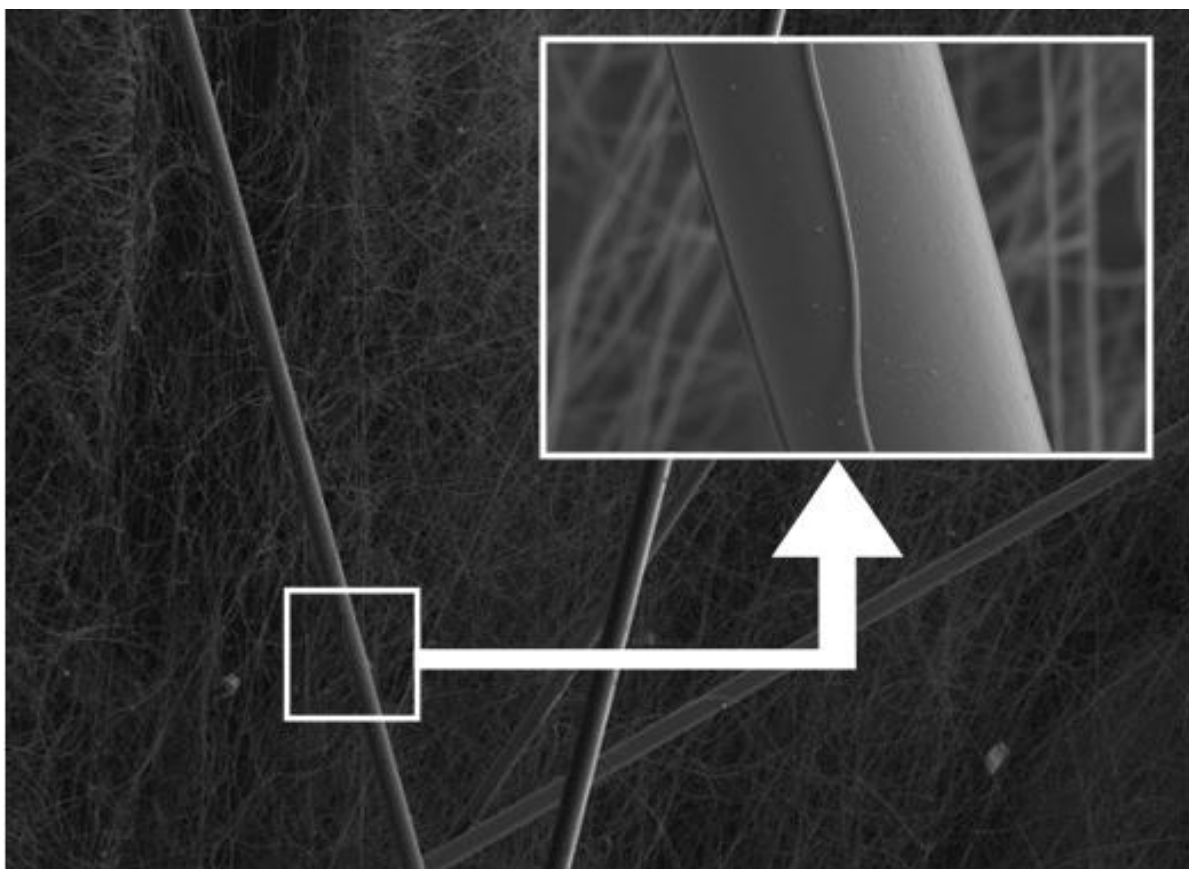


Figure 5.13: SEM image showing a PAN nanofiber aligned along the glass fiber axis

This initial reduction in tensile strength for the 0.1% and 0.2% PAN reinforce samples, is now believed to exist because of the stress concentration sites that have arisen; caused by the non-uniformities formed from having only a small amounts of secondary strengthened glass fibers and large areas of non-strengthened glass fibers within the composite material. This mismatch in localised strengths caused the stress concentration sites that ultimately reduced the tensile properties of the composites. This can be confirmed by the improved tensile strength of the 0.5% volume fraction PAN

reinforced GRPC samples whereby the higher volume fraction allowed for a more uniform distribution of nanofibers with less localised stress intensive zones.

The increase in tensile strength from the 0.1% to the 0.2% and from the 0.2% to the 0.5% volume fractions can also be explained by looking at the interfacial bonding between the glass fibers, PAN fibers and the epoxy matrix. As with the addition of glass fibers, the more fibers present, the more significant the increase in interfacial bonding caused by the increase in the surface area of fiber/matrix bonding and as was discussed previously; the uniformity of the material to equally distribute the loads. Figure 5.14 shows a SEM image of the fracture surface for the 0.5% PAN/ GRPC whereby the good mechanical interfacial bonds between the PAN and epoxy is shown.

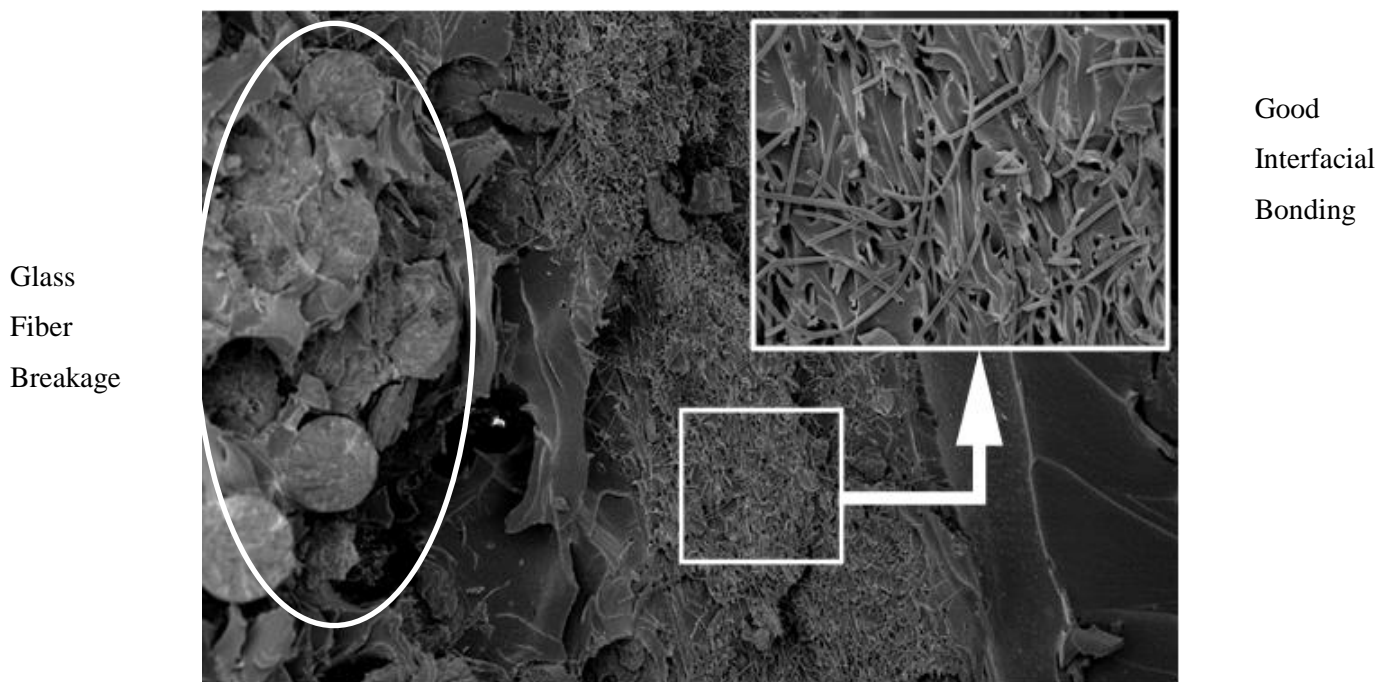


Figure 5.14: SEM image of the fracture surface for a 0.5% PAN/ GRPC whereby the good interfacial bonds between the PAN and epoxy are shown

Unlike the neat glass failure mechanism of fiber pull-out, the major mechanism of failure with the addition of PAN was by nanofiber stretching and then matrix failure which can be characterised as brittle. This showed an improved result, as the mismatch in strengths between the tensile strength of the glass fibers and the weaker epoxy matrix are no longer evident as the PAN nanofibers were able to stretch and allowed the forces to be transferred to the stronger glass fibers. The SEM images of the failed 0.2% volume fraction glass fracture surface, as shown in Figure 5.15, exhibits this phenomenon.

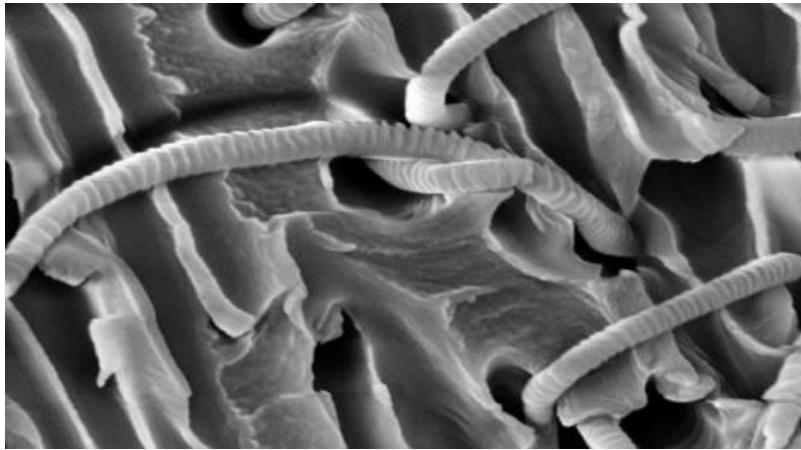


Figure 5.15: SEM image showing stretched PAN nanofibers which allowed the tensile loads to be transferred to the stronger glass fibers

The effect of PAN additions on the tensile modulus of the 32% volume fraction GRPCs is shown in Figure 5.16. For all fiber volume fractions, the composites achieved a lower tensile modulus when compared with the neat 32% volume fraction GRPC. From this it was evident that the PAN fibers had decreased the elastic modulus of the neat 32% volume fraction GRPC caused by the global non-uniform distribution of nano-strengthened glass fibers at these loading volume percentages. The 0.1% PAN showed the least reduction in tensile modulus, roughly 10%, but also showed the largest standard deviation. The 0.2% and 0.5% PAN loadings showed a reduction of 18% and 14%, respectively. The tensile modulus results showed the addition of such low fiber volume fractions has little effect on the tensile modulus which is as would be expected as the layers are only microns thick with the loading taking place in a transverse direction to the reinforcing fibers. However, this does show that with the addition of PAN interleaves, there was a reduction in stiffness caused by the flexible bonding interface between PAN interleaves and matrix, characterised by the stretching phenomenon shown in Figure 5.15, allowing the material to deform more under less strain.

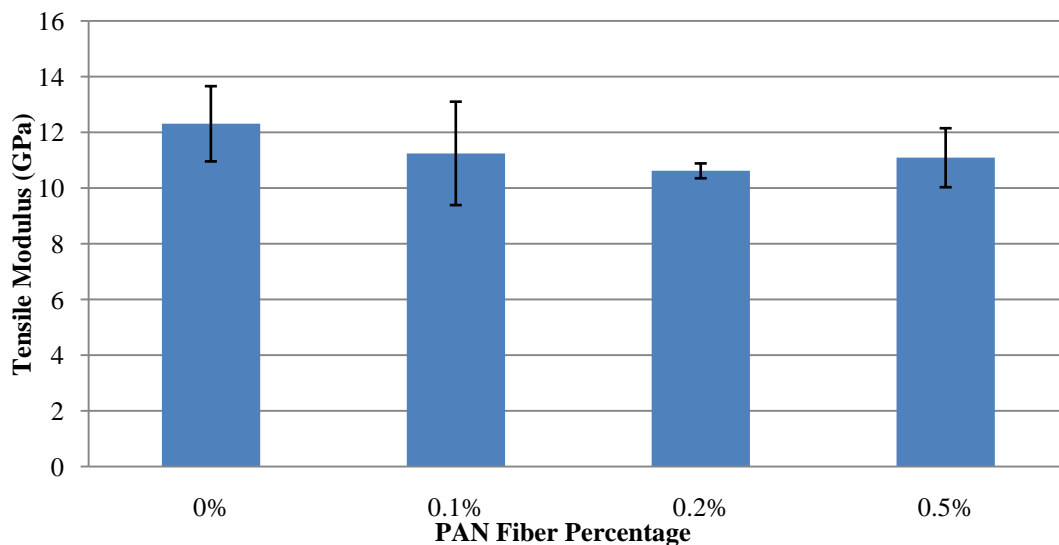


Figure 5.16: Tensile moduli of varying PAN nanofiber volume fraction GRPC

5.2.2 Flexural Results

As mentioned before, nanofibers with diameters in the range of a few hundred nanometers can be on a small enough scale to reinforce and strengthen the weaker matrix rich zones in the epoxy matrix located at the interfaces between neighbouring glass plies in the laminate. As discussed earlier with the GRPC, the flexural failure mechanism caused under bending loads generally occurred in the epoxy rich micro volumes, where the matrix was not reinforced and hence experienced high stress concentrations that caused composite failure. Therefore, it was necessary to reduce these matrix rich zones and improve the load transfer from the matrix to the glass fibers through the PAN nanofiber mat interply networks. The results, ultimate flexural strength and flexural modulus, for the various glass/PAN fiber multiscale reinforced hybrid composite volume fractions shown in Figure 5.17 and Figure 5.18. The error bars in these Figures represent the standard deviation in results which is a direct correlation to the consistency of the obtained results.

The effect of PAN additions on the flexural strength of the 32% volume fraction GRPCs is shown in Figure 5.17. All fiber volume fractions of the composites achieved a higher flexural strength when compared with the 32% volume fraction GRPC. From this it was evident that the PAN fibers had improved the flexural strength of the neat 32% volume fraction GRPC, where the high strength and modulus of both fillers were able to support the majority of the load. The initial increase in flexural strength from the 32% volume fraction GRPC to the 0.1% volume fraction PAN reinforced hybrid GRPC was relatively low with an increase in flexural strength of only 4%. The relative increase in strength then increases significantly as the fiber volume fraction increased, 60% and 80% flexural strength improvements, respectively.

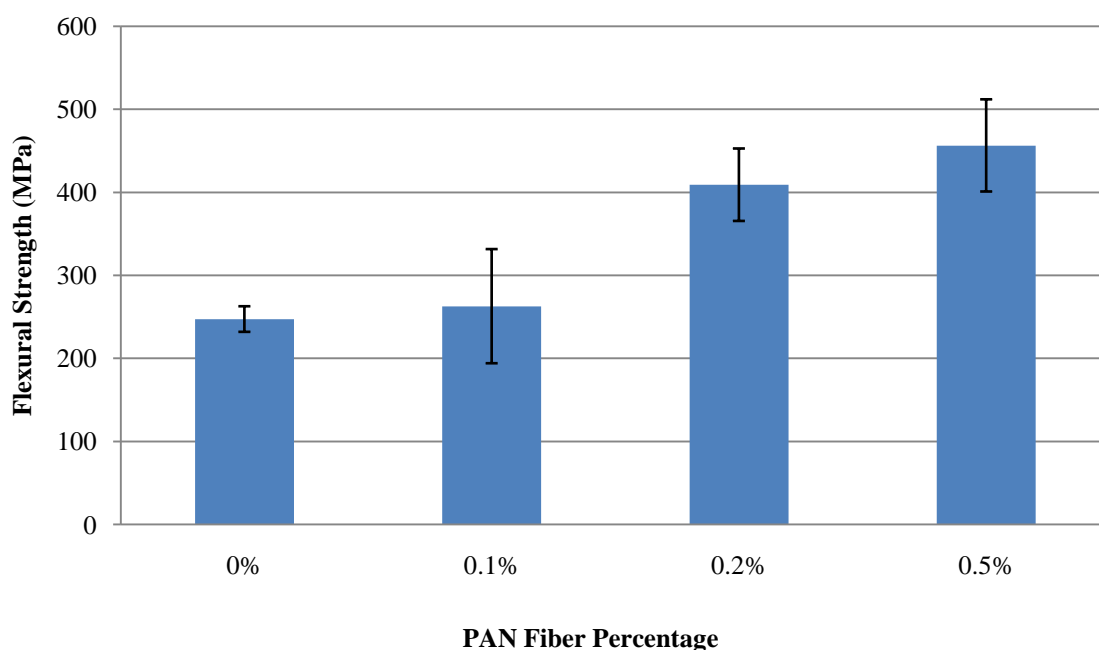


Figure 5.17: Flexural strengths of varying PAN nanofiber volume fraction GRPC

The effect of PAN additions on the flexural modulus of the 32% volume fraction GRPCs is shown in Figure 5.18. All fiber volume fractions of the composites achieved higher flexural moduli when compared with the 32% volume fraction GRPC. From this it was evident that the PAN fibers had increased the flexural modulus of the neat 32% volume fraction GRPC. The initial increase in flexural modulus followed a similar trend to that of the flexural strength, with an increase in flexural modulus of 25%. The relative increase in strength from the 0.1% volume fraction to the 0.2% volume fraction was negligible, however the standard deviation of error was rather high in the 0.1% volume fraction composite sample set. The relative increase in modulus from the 0.2% volume fraction hybrid composite to the 0.5% volume fraction hybrid composite increased significantly, by roughly 100%. This result agrees well with Ozden *et al.* [119], who prepared a single layered 0.2% volume fraction poly(styrene-co-glycidyl methacrylate), electrospun fibrous mat reinforced epoxy composite, where an increase of 30% in the composites flexural modulus with respect to that of the neat epoxy was observed.

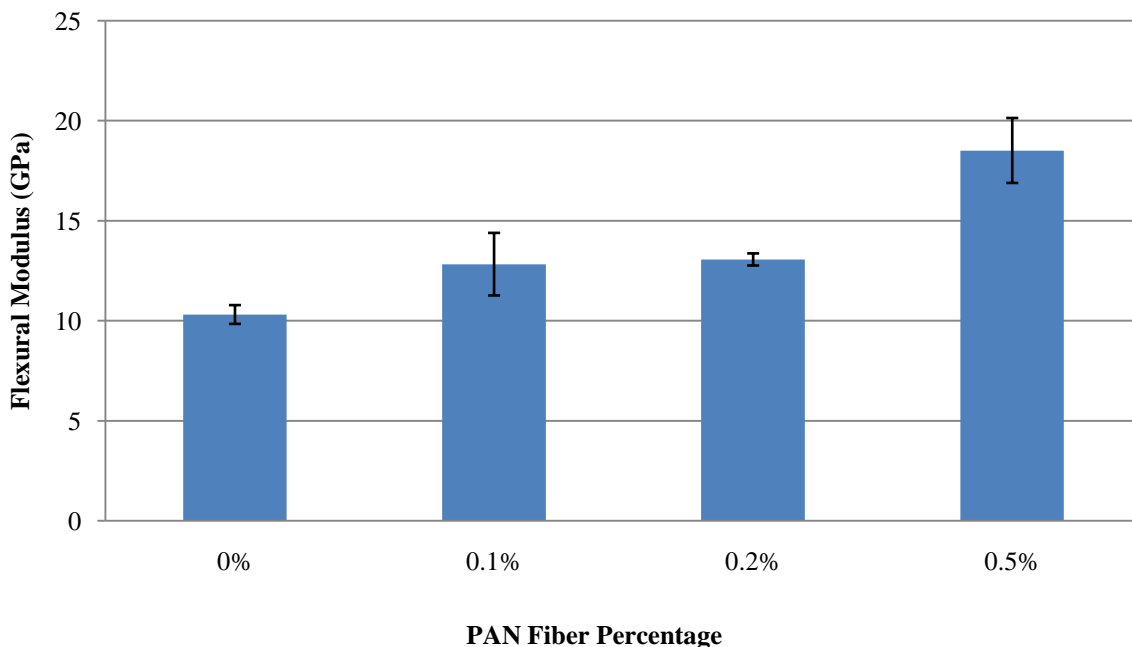


Figure 5.18: Flexural moduli of varying PAN nanofiber volume fraction GRPC

The increased flexural strength and modulus from the addition of the PAN nanofiber reinforcement mats can be explained by the prevention of the epoxy chains from moving in segmental motions within the matrix when the nanofibers are well dispersed and adhered well to the epoxy. This is explained with the 0.5% PAN reinforced GRPCs failed three point bending test sample shown in Figure 5.19, which resulted in improved strength and modulus. Also, the large surface areas and interconnected porosity of the PAN nanofiber mats provide an improved interfacial interaction with the epoxy matrix and the glass fibers as shown in Figure 5.20.

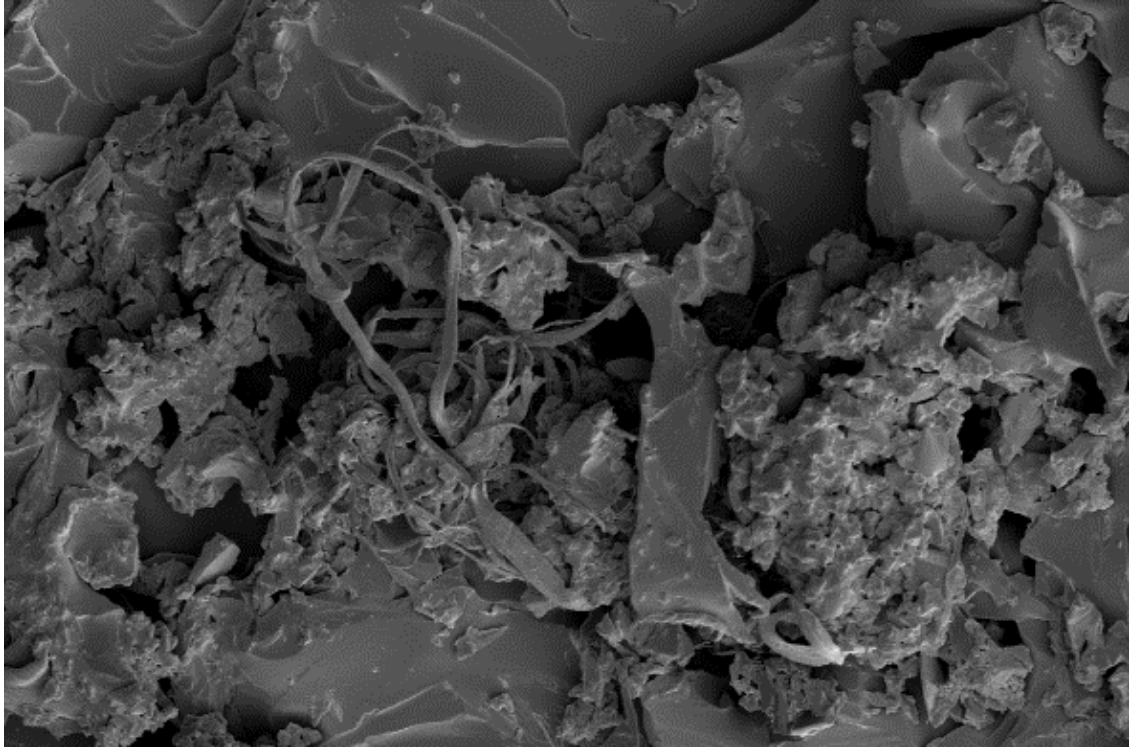


Figure 5.19: SEM image of 0.5% PAN reinforced GRPCs failed three point bending test sample showing good adhesion between nanofibers and matrix

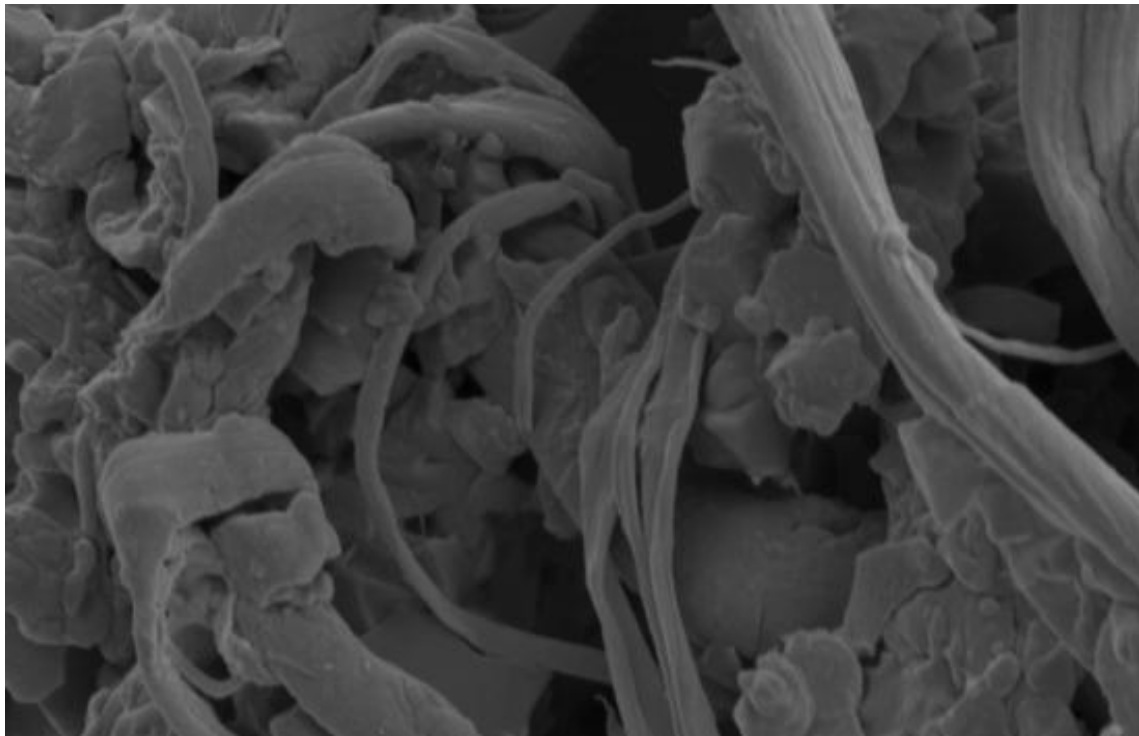


Figure 5.20: SEM image of 0.2% PAN reinforced GRPCs failed three point bending test sample showing the large surface areas and interconnected porosity of the PAN nanofibers which improved interfacial interaction with the epoxy matrix and the glass fibers

5.2.3 Impact Results

Poor fracture toughness and impact resistance have been the major concern surrounding the long-term reliability of thermosetting matrices such as epoxy resins. However, with the interlayer toughening reinforcement of polymer nanofibers, there could be much improvement of the impact resistance of the composites with no decrease in their in-plane mechanical properties. This is as a result of the entangled nanofiber layer which is characterized by a combination of interlocked in-plane and out-of-plane nanofibers that contribute to the improvement of the interlaminar fracture resistance. The raw data was processed from each impact specimen tested for all the various glass/PAN fiber multiscale reinforced composite volume fractions, and the impact resistance was determined. The results for the various glass/PAN fiber multiscale reinforced composite volume fractions shown in Figure 5.21. The error bars in the Figure show the standard deviation in results.

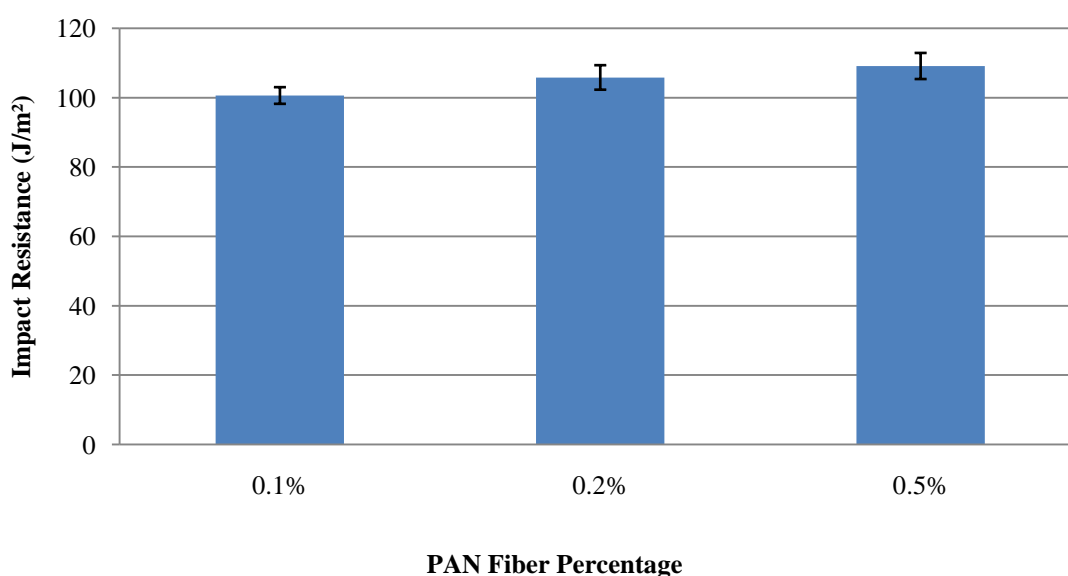


Figure 5.21: Impact resistance of varying PAN nanofiber volume fraction GRPC

The effect of PAN additions on the impact resistance of the 32% volume fraction GRPCs is shown in Figure 5.21. For all PAN fiber volume fractions, the composites achieved a higher impact resistance when compared to the 32% volume fraction GRPCs. From this it was evident that the addition of PAN fibers had improved the impact resistance of the epoxy matrix, where the PAN fibers were able to absorb and distribute the maximum impact energy during loading to the stronger and higher moduli glass fibers. The initial increase in impact resistance from the neat glass to the 0.1% fiber volume PAN/GRPC was negligible. This was as a result of the lack of amount of fibers which lead to large matrix rich zones between fibers resulting in the lack of reinforcement. The impact resistance continued to improve with increased fiber reinforcement. The relative increase in resistance was linear as the fiber volume fraction increased, 5% and 10% fiber volume fractions, respectively. This could be attributed to the broader span of the distribution network of the interlaminar PAN nanofiber mats

which resulted in decreased distances between fibers and thus less weak matrix rich zones as shown in Figure 5.22.



Figure 5.22: Distribution network of a PAN nanofiber mat which resulted in decreased distances between fibers

These improvements can also be explained by the energy absorption behaviour of the interply layers whereby failure occurred gradually as opposed to without nanofibers, where the damage process of the specimens was more rapid. In the former case, the layers broke independently one after the other which was confirmed by visual and acoustic observations of the damage process.

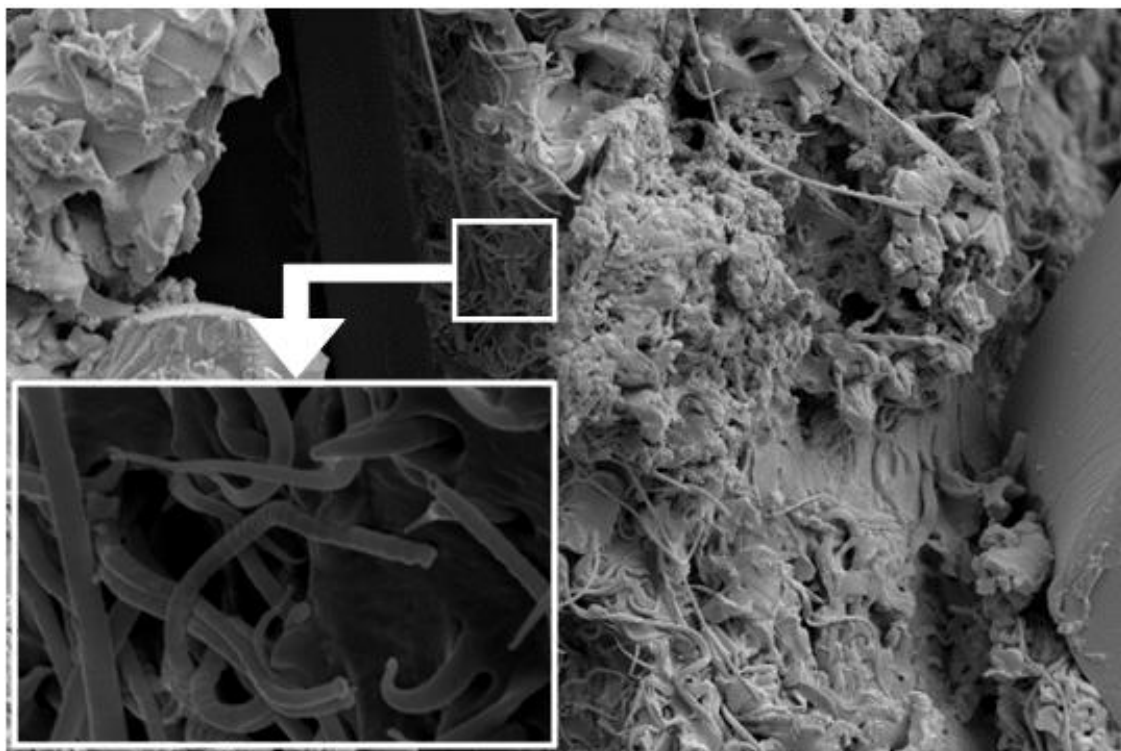


Figure 5.23: SEM image of the failure surface of a 0.5% PAN/GRPC impact sample showing the nano fibrous layer after impact failure whereby crack propagation was restricted

Figure 5.23 shows the failed fracture surface of a 0.5% PAN volume fraction GRPC sample where it can be seen how the nanofibrous layer affected crack propagation during impact failure. When the cracks reached the nanofibrous band of the composite, the number of micro crack lines increased dramatically resulting in dispersed load transfer causing the improved toughness. At the moment of impact when the sample was hit, parallel to the reinforcing plane of the glass and PAN layers, the PAN layers absorbed and then instantaneously spread the applied load through the nanofibrous network to the adjacent glass layers and throughout the entire shear plane, whilst deforming plastically. Sihn *et al.* [120] showed similar results with electrospun polycarbonate nanofiber reinforced carbon fiber/epoxy composites whereby the constraint due to the interply layers appeared to play a vital role on the microcracking damage resistance. It was shown that the higher impact energy induced a damaged area that, in the case of the interleaved laminate, was about one-third of the damage area of the plain laminate. Consequently, the Authors concluded that, in the case of impact, nanofiber interleaving increased the impact damage resistance three times with minimal increase in the thickness or weight.

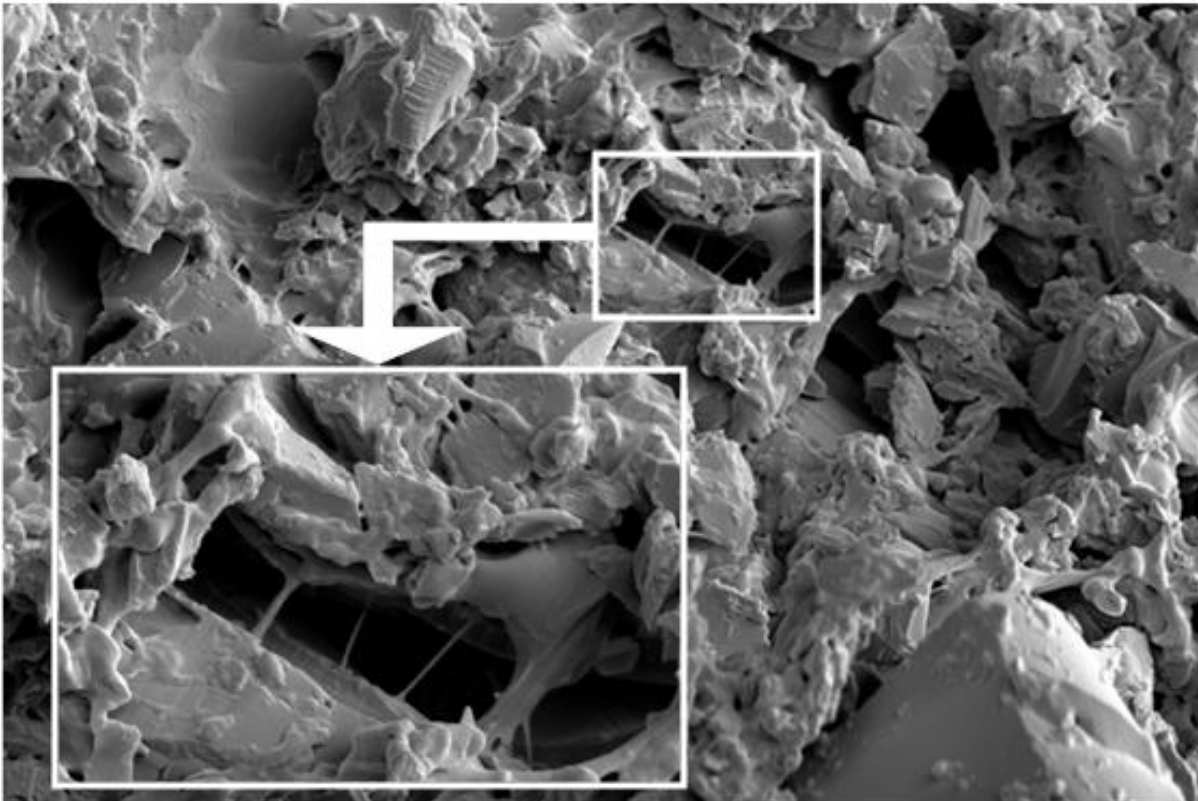


Figure 5.24: SEM image of the failure surface of a 0.5% PAN/GRPC impact sample showing nanofiber bridging

In comparing the GRPC fracture method which was dominated by resin cracking and fiber breakage, the fracture of the PAN reinforced composite showed initial resin deformation occurring nearby the nanofiber layer and then the crack propagation was slowed down by nanofiber bridging as shown in Figure 5.24.

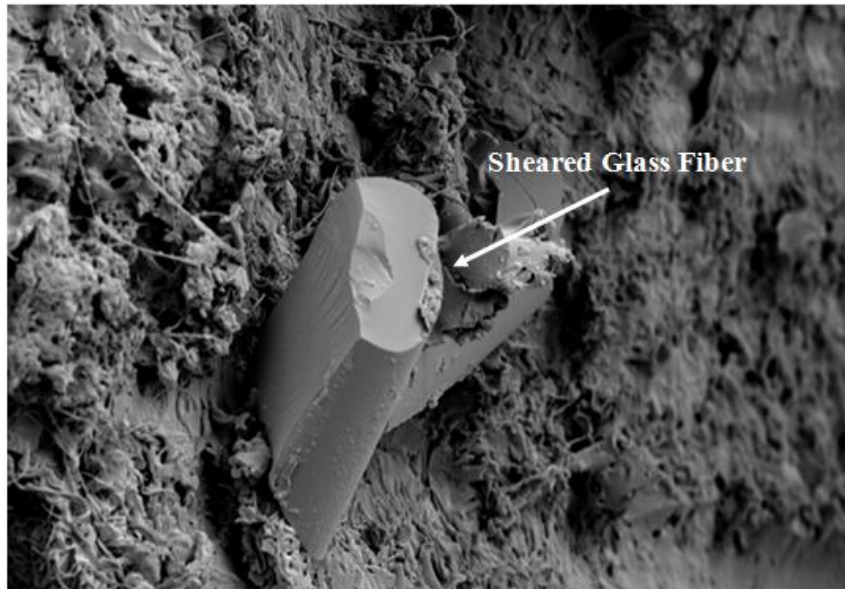


Figure 5.25: SEM image of the failure surface of a 0.5% PAN/GRPC impact sample showing the debris of glass fiber after failure

Figure 5.25 shows that there was good adhesion present between the nanofibers and the matrix; shown by the remnants of epoxy which was still adhered to the glass fibers after the impact sample's failure. The fracture around the nanofibers showed that the load was absorbed by the nanofiber and distributed throughout the matrix resulting in the prevention of crack propagation and the transfer of loads to the glass fibers which in this case failed by shearing.

5.3 ECNF doped PAN Reinforced GFR Hybrid Composite

The ECNFs produced via the electrospinning process and subsequent heat treatments possesses high strength and high modulus properties. The ECNFs were also shown to possess an extremely high degree of macromolecular orientation and a significantly reduced amount of structural imperfections as compared with conventional macro carbon fibers; in addition, the diameters of nanofibers were magnitudes smaller which prevented the formation of major sheath/core structures during stabilisation and carbonisation which has been shown to reduce mechanical properties. It was of great interest to incorporate these superior fibers into the epoxy GRPCs. However, their application for reinforcement was largely dependent upon the interfacial region between the nanofibers and the epoxy matrix which ultimately determined the failure mode of the composites as was shown with the PAN nanofiber reinforced GRPC. When the interfacial bonding strength was high, then matrix failure was shown to be the main mode of failure. When the interfacial bonding strength was low, then the fiber-matrix interfacial bonding was shown to be the weakest link under loading causing fiber pull out. Therefore, for the GRPC properties to improve, the reinforcement effect of the ECNFs needed to show effective load transfer from the epoxy matrix to the ECNFs through the PAN fibers.

In order to achieve this and circumvent the issues of poor dispersion and lack of fiber alignment of CNFs within composite materials, electrospinning of the ECNFs within the outer PAN shell was performed. Improved nanofiber alignment was achieved by the self-aligning mechanism of ECNFs within the PAN fibers caused by the whipping effect of the electrospinning process. Improved nanofiber dispersion was achieved by the collection of random, non-woven PAN fibers resulting in good dispersion and homogeneity. Also, electrospinning of the ECNFs within the PAN nanofibers, resulted in isolation and debundling of the ECNFs within the PAN fibers which provided for improved dispersion and alignment of ECNFs within the overall composite. Figure 5.26 shows the good alignment of ECNFs along the PAN nanofiber length as well as the diameters and surface quality of the ECNF embedded PAN nanofibers.

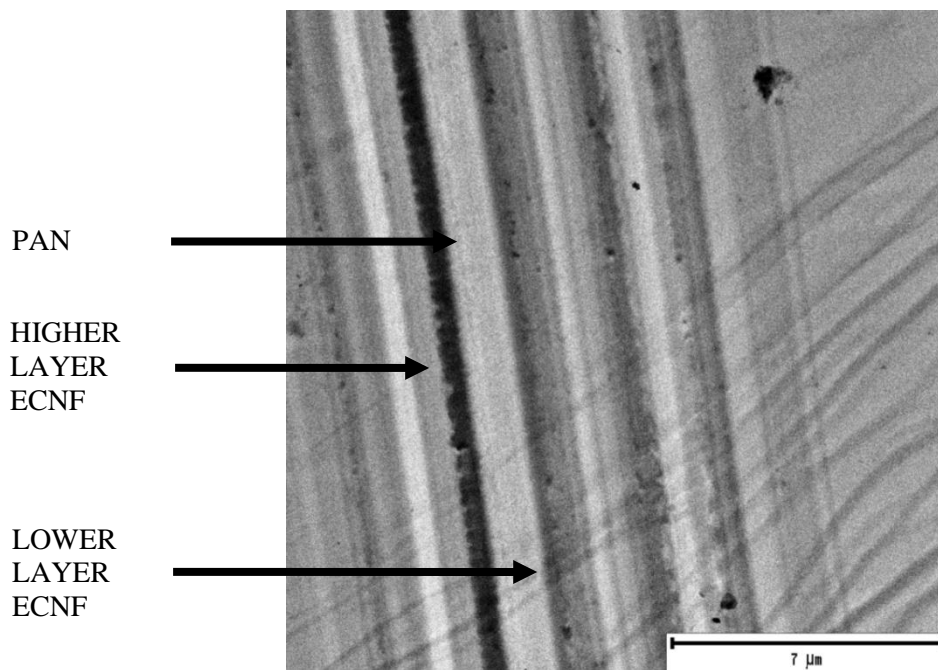


Figure 5.26: SEM image of fibrous mat showing alignment of ECNFs along the PAN nanofiber length

The higher volume fraction of ECNFs present in the epoxy would also result in higher strength and modulus of the resulting composite; however, the dispersion and alignment of ECNFs within the epoxy matrix are generally difficult to achieve since ECNFs are easy to bundle together and agglomerate due to van der Waal's force interactions. It was thus expected that a nanocomposite matrix containing higher concentration of ECNFs would adversely affect the impregnation of continuous fiber reinforcement by blocking the micro-flow channel in fiber bundle and thereby the mechanical properties. Thus an optimum amount of ECNFs within the composite needed to be identified.

For the purposes of this experiment, the two volume fractions of 0.5% and 1% were chosen based on the following arguments; it was observed during testing that the viscosity of the DMF solution did not noticeably vary from the addition of 0.5% volume fraction ECNF to the DMF solution; however the

viscosity of the DMF was increased dramatically from the addition of the 1.0% volume fraction of ECNFs, and became unworkable above 1.0% fiber volume fraction. Pilehrood *et al.* observed similar results with the additions of 0.25% and 0.75% volume fraction of CNTs to a 10% volume fraction PAN/DMF solution [113]. They found that the 0.25% CNT addition had no noticeable effect on the PAN/DMF solutions viscosity; however the 0.75% addition showed a dramatic rise in viscosity approximately 200 times that of the PAN/DMF viscosity. Dimchev *et al.* studied the effect of carbon nanofibers on the tensile and compression properties of hollow particles filled composites [132]. The result of this study showed that with the addition of 0.25% volume fraction carbon nanofibers resulted in improvements in both tensile modulus and strength compared to similar syntactic foam compositions without nanofibers, and volume fractions above 1% resulted in decreased mechanical properties.

The mechanical tests (tensile, flexural and impact) of the 0.5% and 1.0% ECNF doped PAN fiber multiscale hybrid reinforced epoxy composites were then performed in order to optimize the PAN/ECNF loading for the improvement of mechanical properties of the optimum, 32% volume fraction GRPC. Subsequently, the results of the mechanical characterisation are presented in this section.

5.3.1 *Tensile Results*

The inherent crystalline quality and the straightness of the embedded ECNFs were significant factors influencing the tensile reinforcement capabilities of the ECNFs within the PAN nanofibers. However control of this was found to be difficult. As mentioned before, the whipping effect of the electrospinning causes randomly oriented and isotropic structures in the form of nonwoven nanofibers mats. Therefore, these mats were generated with a lack of control over the forces driving fiber orientation and crystallization, resulting in varying qualities of fibers produced.

The effect of ECNF additions on the tensile strengths of the PAN/GRPCs is shown in Figure 5.27. For all fiber volume fractions, the composites achieved higher tensile strengths when compared with the neat PAN/GRPCs. From this it was evident that the ECNF reinforced PAN fibers had improved the tensile strength of the neat PAN/GRPCs. There was an increasing trend of tensile strength with increased ECNF loadings. The 0.5% ECNF reinforced PAN/GRPC showed linear tensile strength improvements over the GRPC with an increase of tensile strength of 2%, 8% and 15%, for each PAN loading respectively. Also, the respective increase in tensile strength from the addition of 0.5% ECNF over the PAN/GRPC was 28%, 25% and 15%, respectively. The 1.0% ECNF reinforced PAN/GRPC showed greater tensile strength improvements above the 0.5% ECNF reinforced PAN/GRPC with an increase of tensile strength of 15%, 10% and 17%, for each PAN loading respectively. The maximum improvement of tensile strength was shown with the 1.0% ECNF embedded 0.5% PAN/GRPC with an overall increase of 36% above the neat Glass samples. He *et al.* [123] showed similar results with tensile strength at break being improved much compared to that of pure PMIA nanofiber mats, for

instance, the tensile strength was increased by 86% with the addition of 0.6% volume fraction MWNTs.

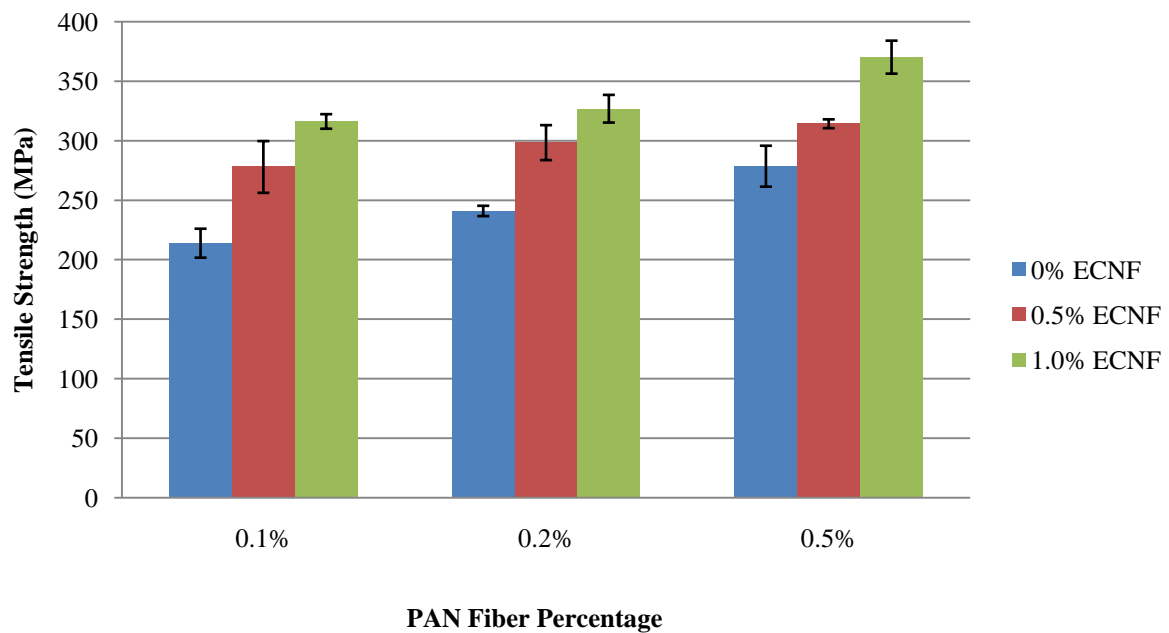


Figure 5.27: Tensile strengths of varying ECNF reinforced PAN nanofiber volume fraction GRPC

The effect of ECNF additions on the tensile moduli of the PAN/GRPCs is shown in Figure 5.28. The incorporation of 0.5% ECNFs in to the PAN/GRPC, showed reduced tensile moduli, 14%, 8% and 12% reduction respectively, when compared with the neat PAN/GRPCs. From this it was evident that the 0.5% ECNF reinforced PAN/GRPCs had decreased the tensile moduli of the neat PAN/GRPCs. Also, the moduli of all three 0.5% ECNF reinforced PAN/GRPC were similar in magnitude at around $10GPa$, regardless of the amount of PAN added. This shows that at 0.5% ECNF loadings, the modulus is governed by the amount of ECNFs in the overall composite and thus the PAN had very little effect on the overall modulus. This then confirms the result found for the PAN/GRPC results shown in Figure 5.16.

The 1.0% ECNF reinforced PAN/GRPCs showed increased tensile moduli over the 0.5% ECNF reinforced PAN/GRPCs with an increase of tensile modulus of 12%, 45% and 30%, for each PAN loading respectively. The incorporation of 1.0% ECNFs in to the 0.2% PAN nanofiber volume fractions, showed the greatest increase in tensile modulus of 45% when compared with the neat PAN/GRPCs and an increase of 16% when compared with the neat GRPC. The 1.0% ECNF reinforced 0.5% PAN/GRPC's tensile modulus was then reduced from the 1.0% ECNF reinforced 0.2% PAN/GRPC.

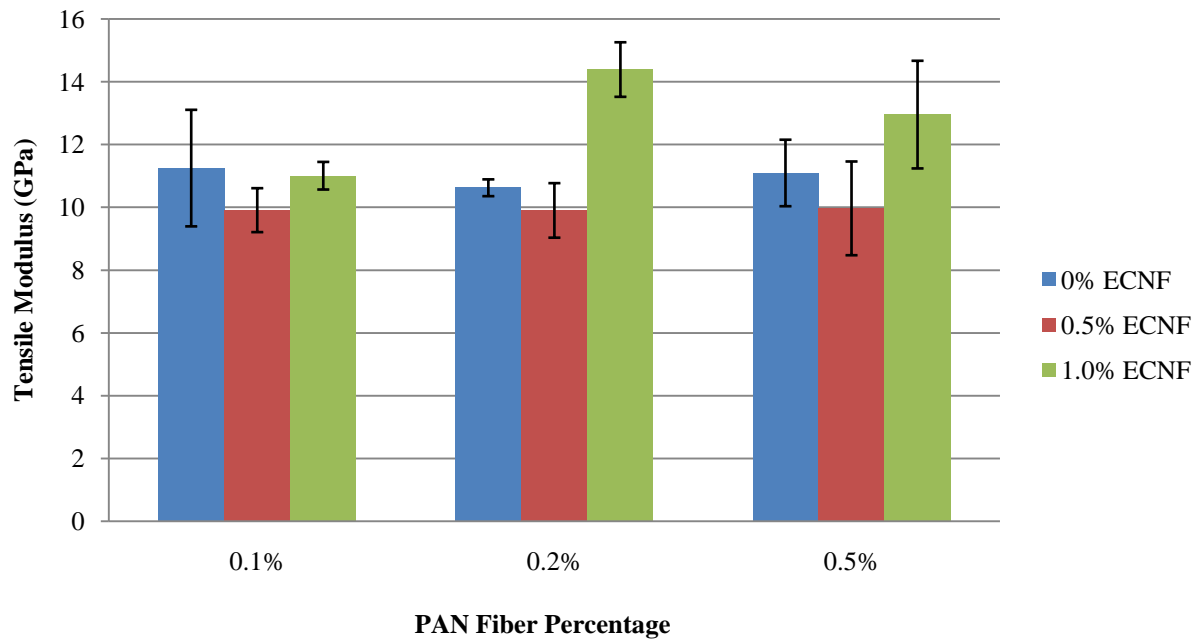


Figure 5.28: Tensile moduli of varying ECNF reinforced PAN nanofiber volume fraction GRPC

To further understand the reinforcement and failure mechanisms of ECNFs in hybrid multiscale GFRP composites, the fracture surfaces of tensile tested specimens, as shown in Figure 5.29, were examined by SEM. The representative fracture surfaces of GFRP composites with 0.5% ECNFs and 1.0% ECNFs, as well as the control sample can be found in Appendix A.

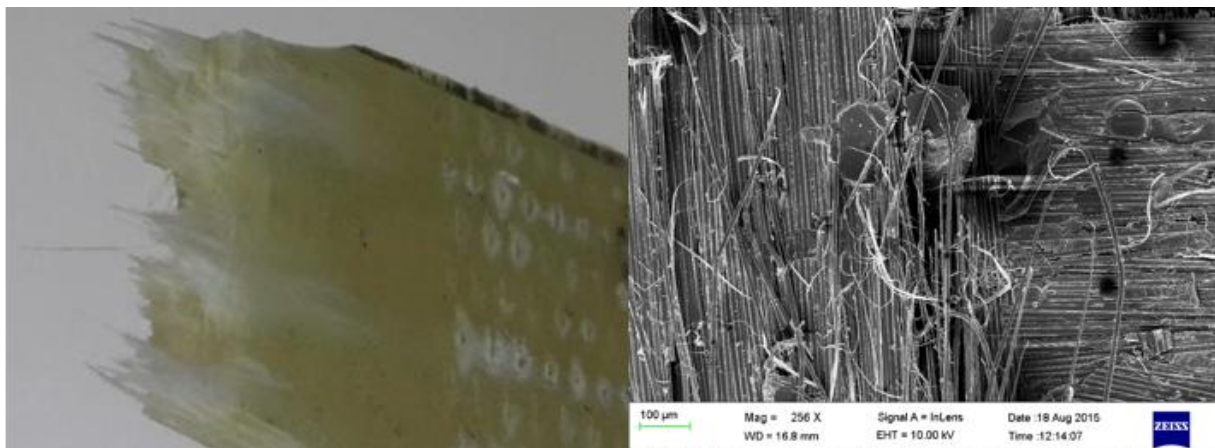


Figure 5.29: Fracture surface of a 1.0% ECNF reinforced PAN/GRPC sample

A two-stage cracking behaviour of the individual composite fibers under tension, including crazing of the polymer matrix and ECNF pull out, was observed as shown in Figure 5.30. Ko *et al.* [91] also showed similar rupture behaviours with CNT/PAN nanofibers using both single-wall carbon nanotubes and multiwall carbon nanotubes.

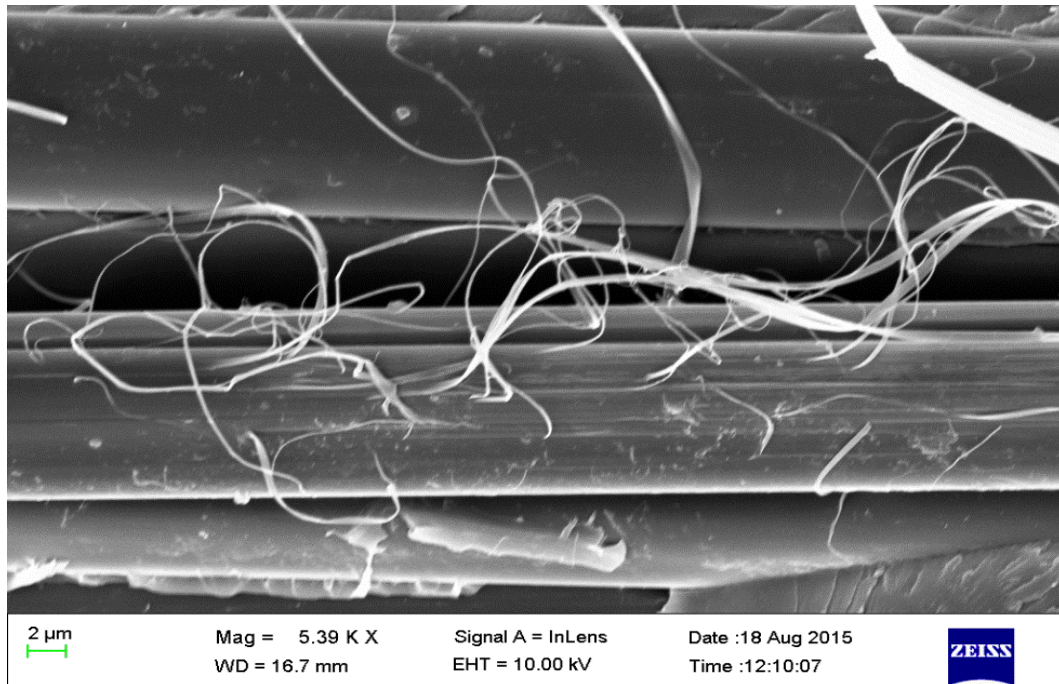


Figure 5.30: SEM images showing the cracking behaviour of the individual composite fibers under tension

Ko *et al.* experimented with loadings as high as 10% volume fraction, reinforcing PAN composite fibers synthesized by electrospinning. They suggested that the CNTs had reinforced the PAN fibers by obstructing crazing extension, reducing stress concentrations, and successfully dissipating the energy via fiber pull out. Such crazing was also observed as shown in Figure 5.31.

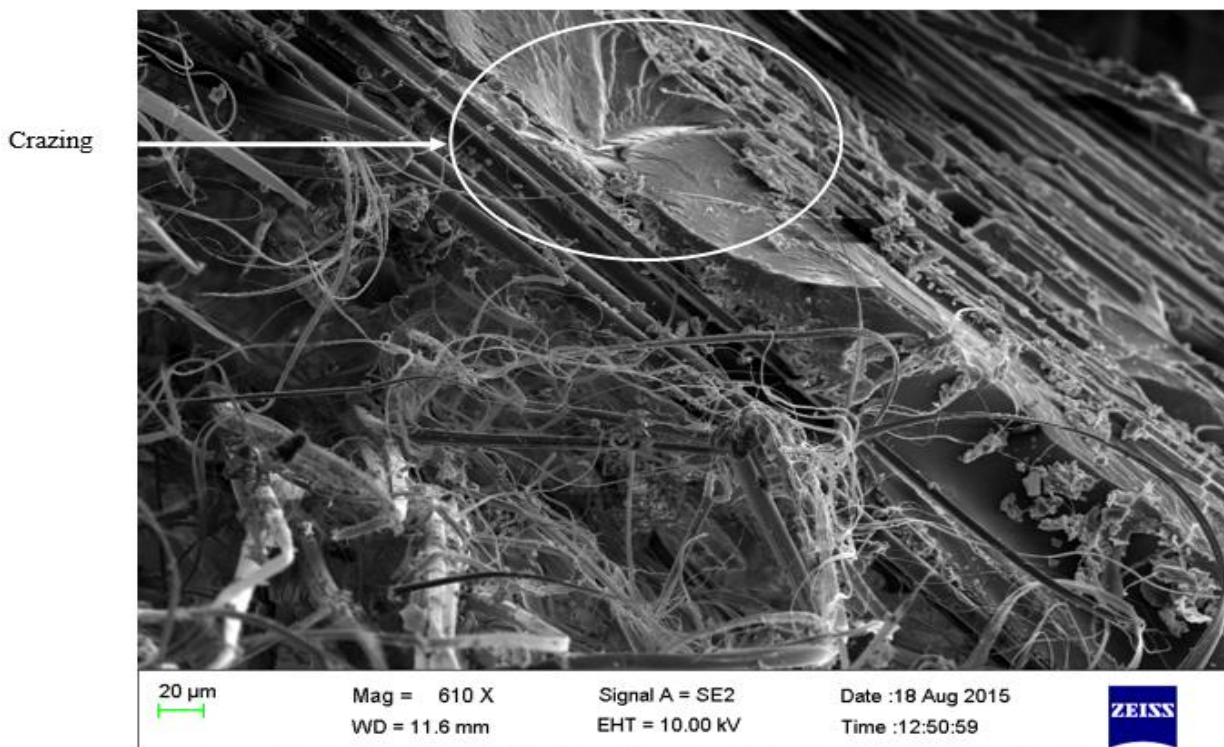


Figure 5.31: SEM images showing the polymeric crazing effect under tension

As mentioned before, the inherent crystalline quality, alignment and the straightness of the embedded ECNFs are significant factors influencing the tensile reinforcement capabilities of the ECNFs within the PAN nanofibers. Figure 5.26 shows that the orientation of the ECNFs within the PAN nanofibers was very good, which is indicative of high strength reinforcement. Ge *et al.* [89] suggested that not only surface tension and jet elongation but also slow relaxation of CNTs within PAN nanofibers was a vital factor in the alignment of CNTs. This was shown by the extensive fine absorption structure of the composite fibers which indicated that charge-transfer complexes formed between the CNTs and negatively charged (C=N) functional groups in the PAN during electrospinning. This was shown to lead to a strong interfacial bonding between the CNTs and the surrounding polymer chains. Therefore, as a result of this highly anisotropic orientation and the formation of complexes, according to Ge *et al.* [89], the composite nanofiber sheets possessed improved, mechanical properties, thermal stability, and dimensional stability.

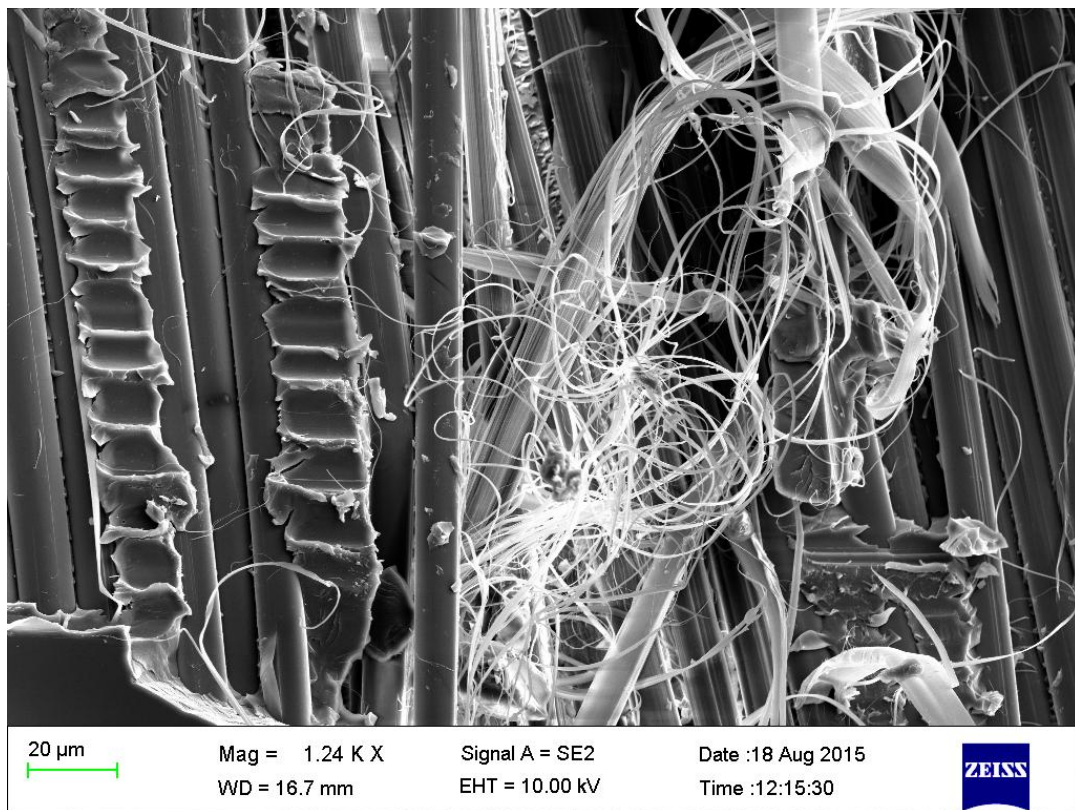


Figure 5.32: Fracture surface of a GFRP composite sample with 0.5% ECNFs added

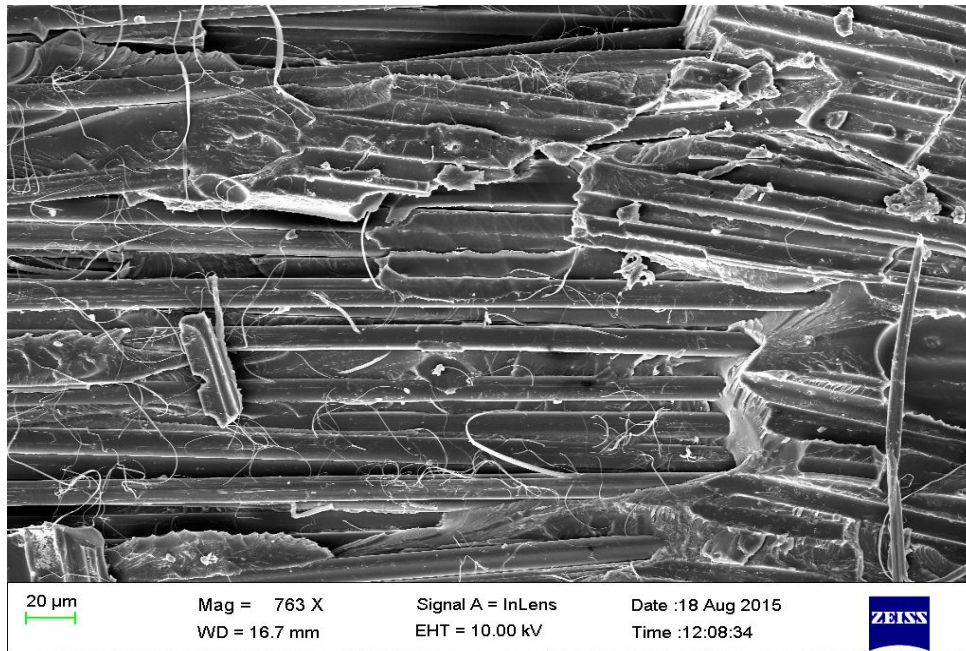


Figure 5.33: Fracture surface of a GFRP composite sample with 0.5% ECNFs added

Figure 5.32 and Figure 5.33 show SEM images of the fracture surfaces of 0.5% ECNF and Figure 5.34 and Figure 5.35 show SEM images of the fracture surfaces of 1.0% ECNF reinforced PAN/Glass fiber hybrid composite, respectively. Figure 5.32 and Figure 5.33 clearly show that fiber glass pull out was the a dominating failure mechanism, however the load transfer to the glass fibers is still clear as shown by the after failure structure of the glass fibers. The inclusion of 1.0% ECNF, as shown in Figure 5.34 and Figure 5.35, shows much better load transfer than the 0.5% ECNF. Fiber pull out is not as evident but the failure mechanism is still much improved, caused by the increased strength of the PAN nanofibers.

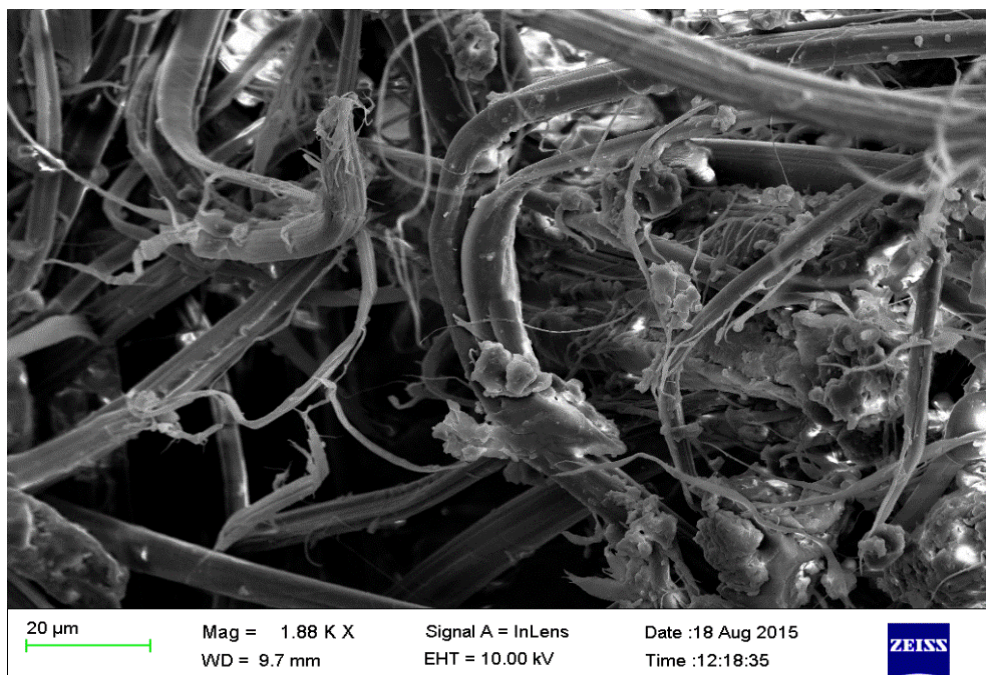


Figure 5.34: Fracture surfaces of GFRP composites with 1.0% ECNFs added

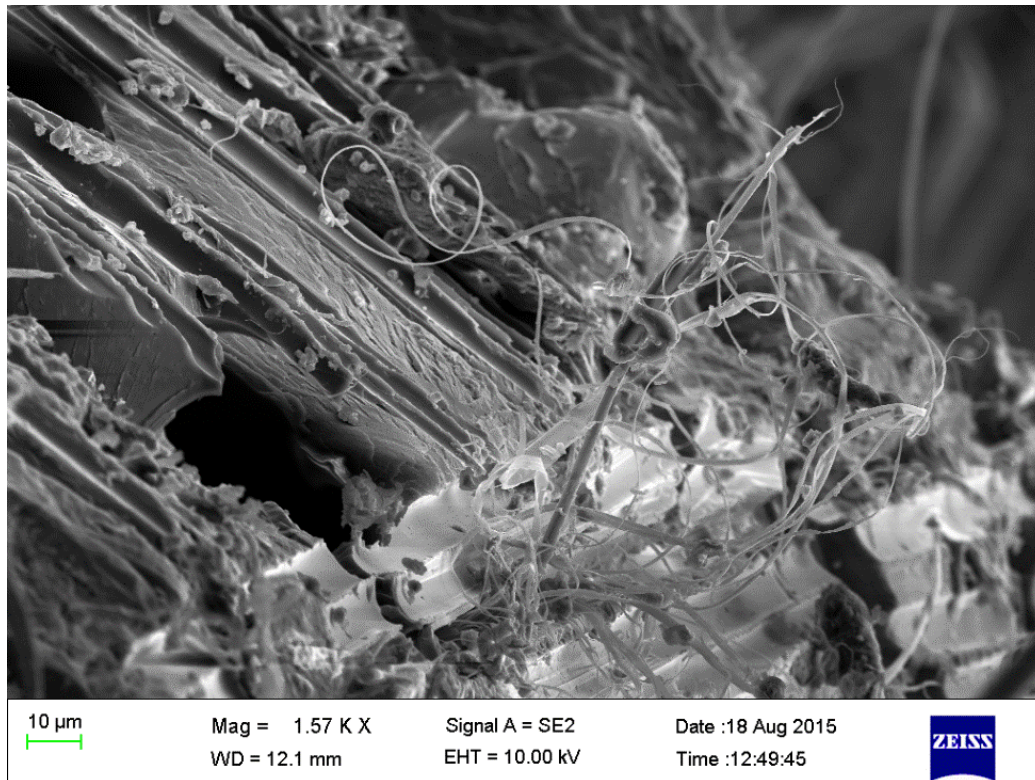


Figure 5.35: Fracture surfaces of GFRP composites with 0.5% ECNFs added

One would expect the tensile modulus of the composite material to increase with the inclusion of ECNFs because of the higher aspect ratio, smaller particulate size and higher rigidity of the hybrid ECNF/PAN fibers. Yet, it would appear that the PAN characteristics shown in Figure 5.16 are more dominant with addition of the lower 0.5% weight fraction ECNF which could be as a result of a weaker PAN/ECNF interface. This anomaly can be described further as the strengthening of the PAN chains without the formation of stress concentrators, allowing improved stretching capabilities during tensile failure. It is believed that the inclusion of the higher 1.0% weight fraction ECNFs would limit the PAN fibers ability to stretch as the distances between ECNFs within the PAN fibers would be shortened, thus resulting in higher strengths coupled with increased stiffness and modulus as would be expected.

5.3.2 Flexural Results

Generally, the shear stress is transferred from layer to layer through matrix rich zones during the three-point flexural failure of laminated composites. Therefore, the major failure mechanism is associated with the interfacial bonding strength and as a result the fracture of the matrix leading to failure occurs. It is thus imperative to improve the mechanical properties of GRPC laminated composites, by improving the interfacial bonding strength between fiber and matrix. This was then achieved with the addition of nano-scaled diameter ECNFs which have massive specific surface areas much larger than those of the glass fibers. This meant that the interfacial bonding strength between ECNF embedded PAN/glass fiber mats and epoxy resin was much stronger than that between conventional glass fiber fabrics and epoxy resin.

The results, ultimate flexural strength and flexural modulus, for the various glass/ECNF-PAN fiber multiscale reinforced composite volume fractions shown in Figure 5.36 and Figure 5.37. The error bars in these Figures show the standard deviation in results which is a direct correlation to the consistency of the obtained results.

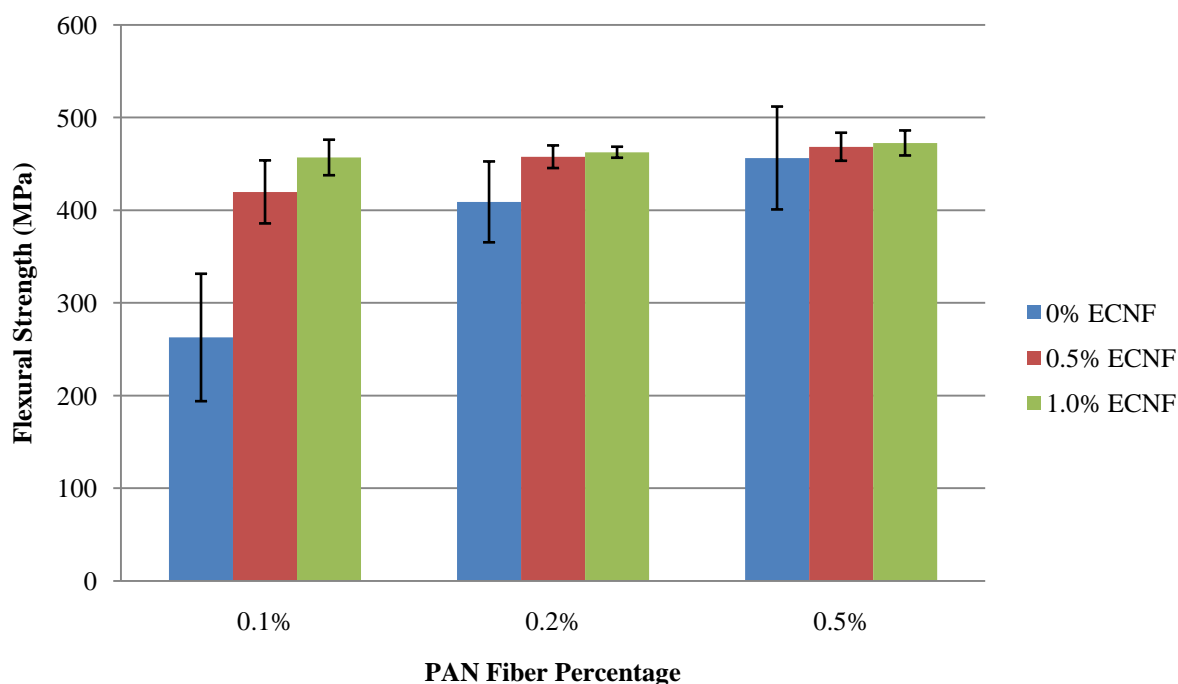


Figure 5.36: Flexural strengths of varying ECNF reinforced PAN nanofiber volume fraction GRPC

The effect of ECNF additions on the flexural strengths of the PAN/GRPCs is shown in Figure 5.36. For all fiber volume fractions, the composites achieved higher flexural strengths when compared with the neat PAN/GRPCs. From this it was evident that the ECNF reinforced PAN fibers had improved the flexural strength of the neat PAN/GRPCs. There was an increasing trend of flexural strength with increased ECNF loadings. The 0.5% ECNF reinforced PAN/GRPC showed linear flexural strength improvements over the PAN/GRPC with an increase of flexural strength of 55%, 10% and 8%, for

each PAN loading respectively. Also, the respective increase in flexural strength from the addition of 0.5% ECNF over the GRPC was 58%, 73% and 80%, respectively. The 1.0% ECNF reinforced PAN/GRPC showed greater flexural strength improvements above the 0.5% ECNF reinforced PAN/GRPC with an increase of flexural strength of 8%, 3% and 4%, for each PAN loading respectively. The maximum improvement of flexural strength was shown with the 1.0% ECNF embedded 0.5% PAN/GRPC with an overall increase of 84% above the neat glass fiber samples.

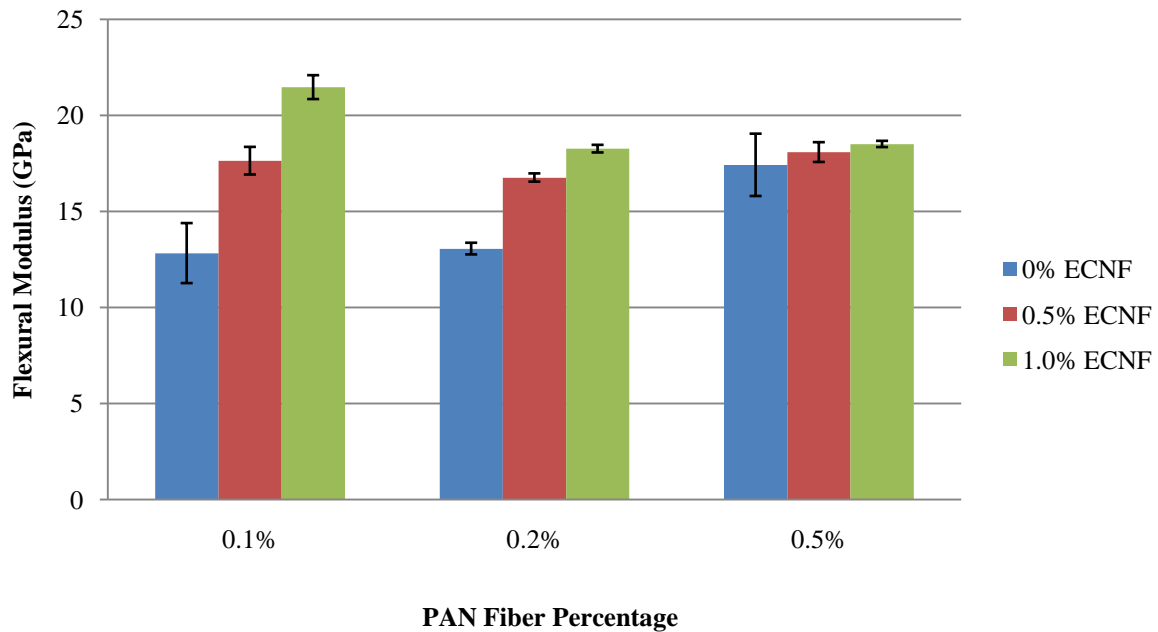


Figure 5.37: Flexural moduli of varying ECNF reinforced PAN nanofiber volume fraction GRPC

The effect of ECNF additions on the flexural moduli of the PAN/GRPCs is shown in Figure 5.37. The incorporation of 0.5% ECNFs in to the PAN/GRPC, showed increased flexural moduli, 37%, 28% and 3% increase respectively, when compared with the neat PAN/GRPCs. Also, as with the tensile modulus, the moduli of all three 0.5% ECNF reinforced PAN/GRPC were similar in magnitude, regardless of the amount of PAN added. This shows that at 0.5% ECNF loadings, the modulus is governed by the amount of ECNFs in the overall composite and thus the PAN had very little effect on the overall modulus.

The 1.0% ECNF reinforced PAN/GRPCs showed increased flexural moduli over the 0.5% ECNF reinforced PAN/GRPCs with an increase of flexural modulus of 21%, 8% and 6%, for each PAN loading respectively. The incorporation of 1.0% ECNFs in to the 0.1% PAN nanofiber volume fractions, showed the greatest increase in flexural modulus of 68% when compared with the neat PAN/GRPCs and an increase of 104% when compared with the neat GRPC. The 1.0% ECNF reinforced 0.2% and 0.5% PAN/GRPC's flexural moduli were then reduced from the 1.0% ECNF reinforced 0.1% PAN/GRPC by roughly 20% each.

To further understand the reinforcement mechanisms of ECNF embedded PAN nanofibers in hybrid multiscale GFRP composites, the fracture surfaces of the three-point bending specimens were examined by SEM. During bending failure of GRPC samples, the epoxy matrix detached from the surface of the glass fibers due to weak interfacial bonding strength, and the failure surfaces of glass fibers were relatively smooth without remnants of epoxy resin attached to the glass fibers. In comparison, the samples with the addition of pan nanofibers containing the ECNFs could be distinguished from significantly different interfacial microstructures and the fracture of the epoxy matrix, as shown in Figure 5.38.

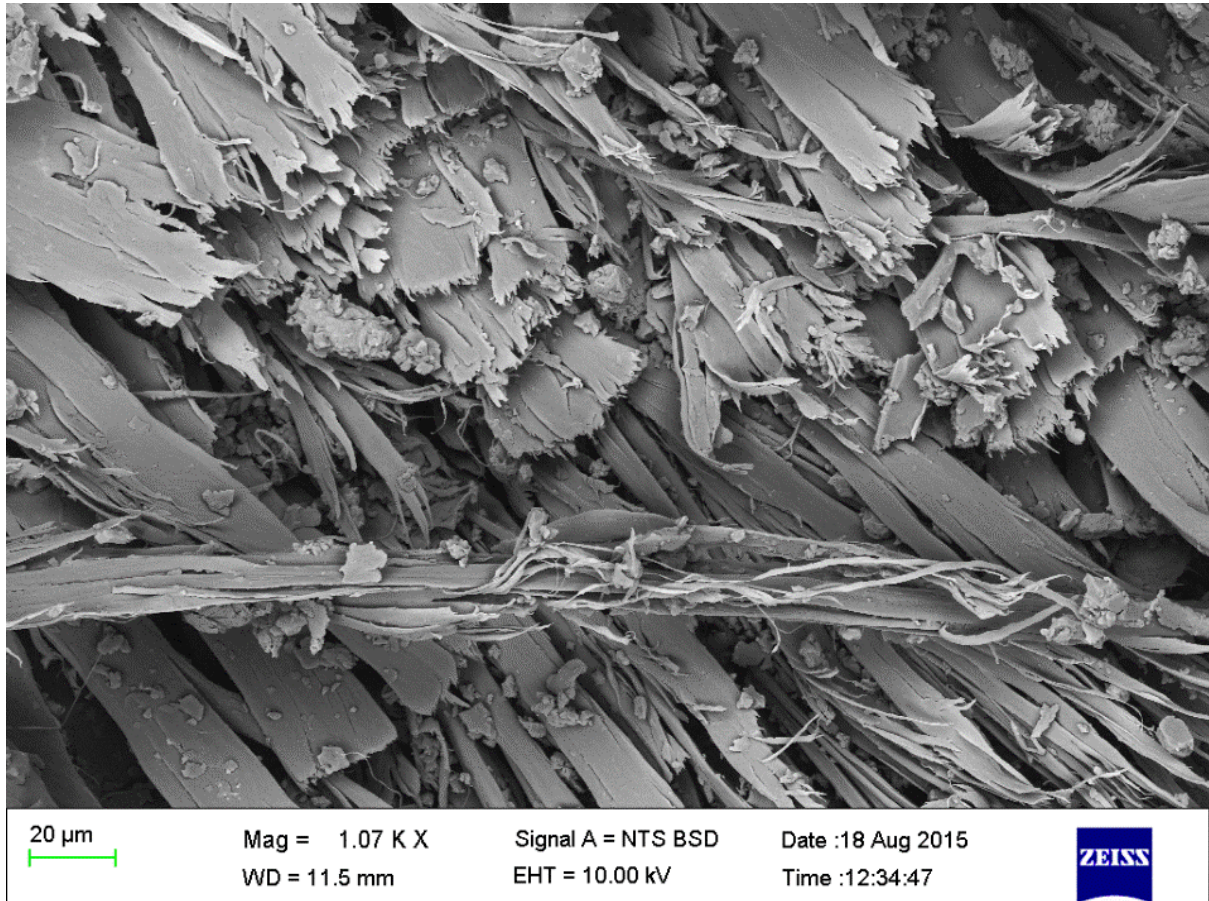


Figure 5.38: SEM image of the 0.5% ECNF sample showing the mechanism of failure

These SEM micrographs showed that the glass fibers were surrounded by and/or adhered to the epoxy matrix, indicating that the interfacial bonding strength between the glass fibers and the epoxy matrix was improved by the addition of PAN nanofiber mats containing ECNFs. In addition, Figure 5.39 shows the ridged fracture feature, which could explain the formation of tougher interfacial regions between the epoxy matrix and glass fibers.

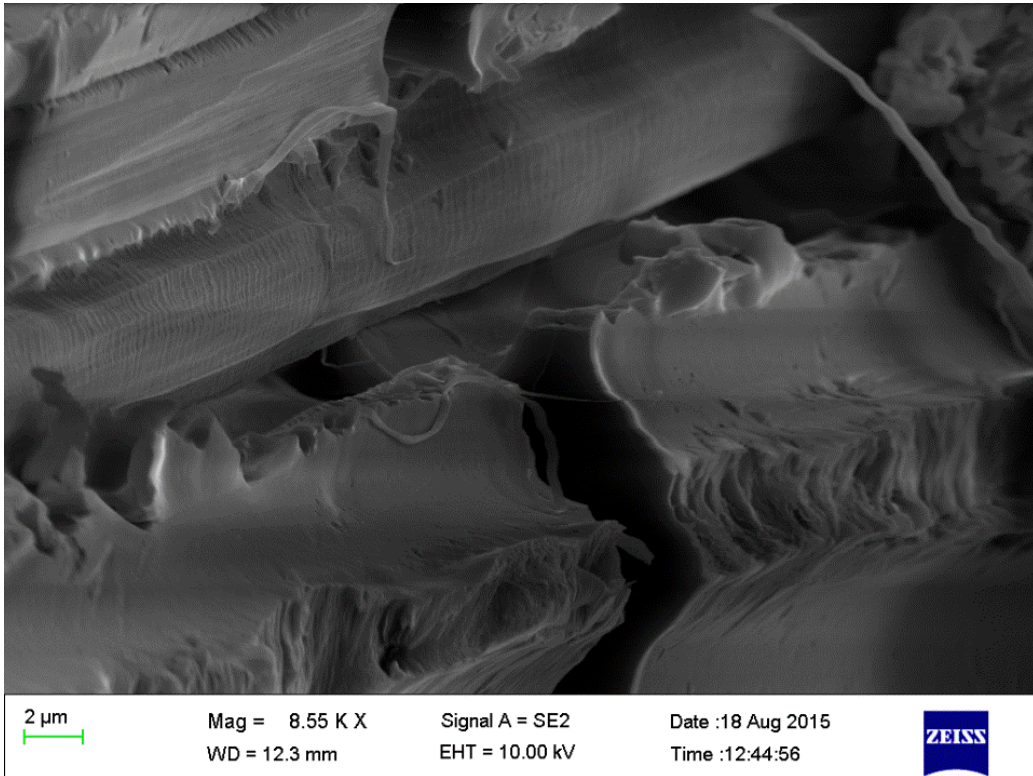


Figure 5.39: SEM image of failed 1.0% ECF sample showing the pitted fracture feature

The presence of closely arranged broken glass fibers as shown in Figure 5.40 then further confirmed that the interfacial bonding strength between the epoxy resin and glass fibers was improved.

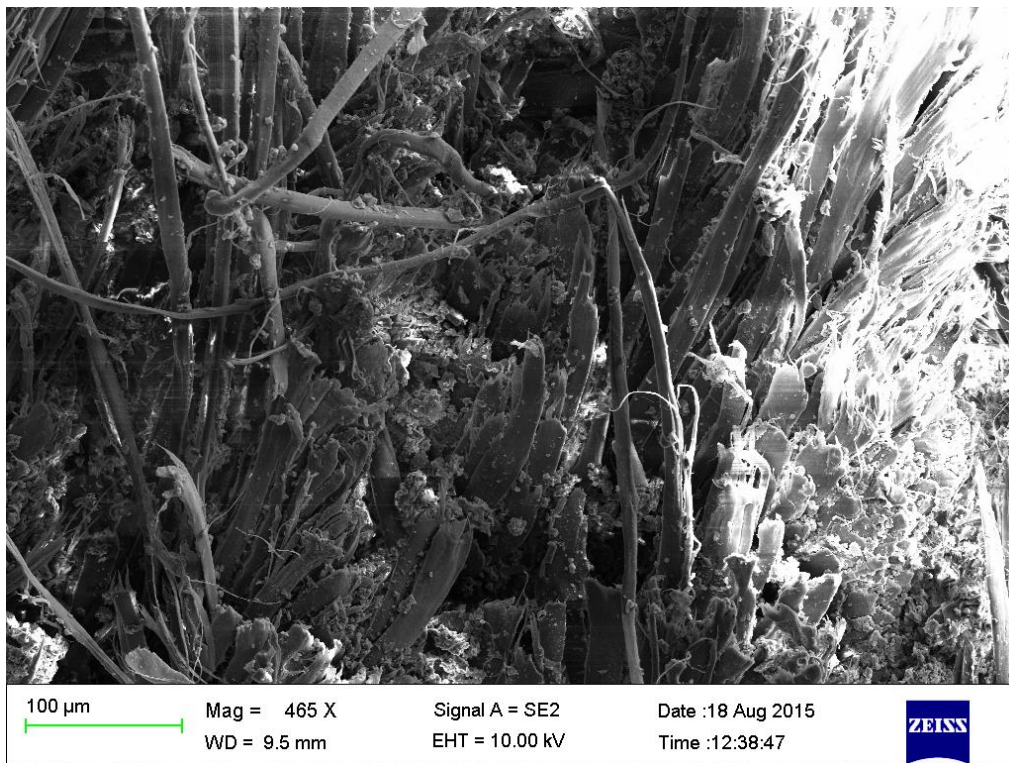


Figure 5.40: SEM image of the 1.0% ECF sample showing the presence of closely arranged broken glass fibers

These results have shown that the ECNF embedded PAN fibrous mats were able to deflect micro-cracks, and thus improve the resistance to crack growth, ensuring that delamination would be more difficult to occur. Also, the ECNFs could also detach, or break away, from the PAN nanofibers within the epoxy matrix when the load was applied. This would then increase the matrix deformation and dissipate the strain energy, further preventing the failure of composites and leading to the improved mechanical properties.

5.3.3 Impact Results

In general, the incorporation of ECNF/PAN mats into the epoxy resin considerably improved the impact resistance of the resulting hybrid multiscale ECNF-PAN/GRPC, since the ECNF mats attached onto the glass fiber mats can function as nano-reinforcement to the interlaminar regions. In particular, the presence of ECNFs could effectively mitigate the propagation of micro-cracks in the matrix rich interlaminar zones. If a micro-crack initiated in this region due to a stress concentration site, the ECNF-PAN nanofibers remained intact across the crack plane and supported the applied load by the bridging mechanism. The impact absorption energy resulted in the deformation of the epoxy matrix, delamination of GRPCs, and breakage and/or pull out of fibers, which were also related to the inter phase between fibers and matrix.

The raw data was processed from each impact specimen tested for all the various glass/PAN fiber multiscale reinforced composite volume fractions, and the impact resistance was determined. The results for the various glass/PAN fiber multiscale reinforced composite volume fractions shown in Figure 5.41. The error bars in the figure show the standard deviation in results.

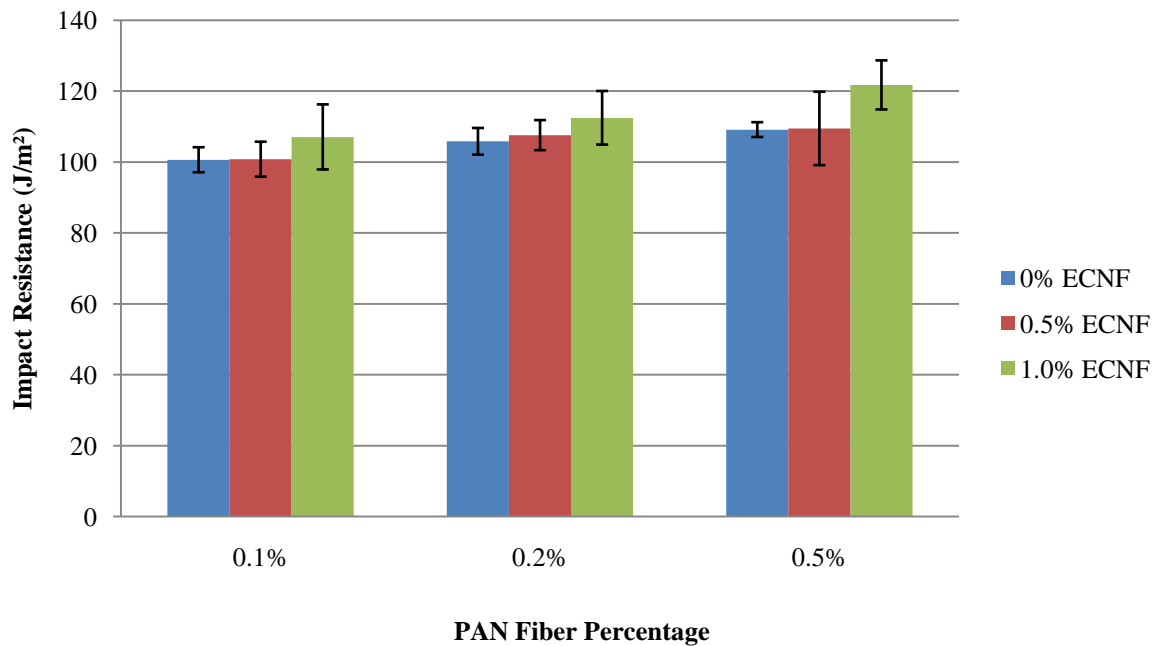


Figure 5.41: Impact resistance of varying ECNF reinforced PAN nanofiber volume fraction GRPC

The effect of ECNF additions on the impact resistance of the PAN/GRPCs is shown in Figure 5.41. For all fiber volume fractions, the composites achieved a slightly higher impact resistance compared with the neat PAN/GRPCs. The incorporation of 0.5% ECNFs into the PAN/GRPC, showed increased impact resistance of, 2%, 3% and 1%, when compared with the 0.1%, 0.2% and 0.5% PAN/GRPCs respectively. Therefore, the addition of 0.5% ECNFs into PAN/GRPC has negligible improvements on the impact resistance which can be explained by the lack of amount of ECNFs which were too far spread in the PAN interplay network.

The 1.0% ECNF reinforced PAN/GRPC showed greater impact resistance improvements above the 0.5% ECNF reinforced PAN/GRPC with an increase in resistance of 7%, 5% and 10%, for each PAN loading respectively. From this it was evident that the ECNF reinforced PAN fibers had improved the impact resistance of the neat PAN/GRPCs. The 1.0% ECNF reinforced 0.5% PAN/GRPC showed the greatest impact resistance improvement with an increase of impact resistance of 22%. This result can be explained by the reduction of mobility of the epoxy chains that were being increased due to the addition of ECNFs having a much greater specific surface area to the epoxy resins and newly formation of mechanical interlocking with epoxy matrix, resulting in an improvement in the toughness of ECNF/PAN nanocomposites.

To further understand the reinforcement mechanisms of ECNF embedded PAN nanofibers in hybrid multiscale GFRP composites, the fracture surfaces of the impact samples were examined by SEM. During impact failure of GRPC samples, the epoxy matrix detached from the surface of the glass fibers and the relatively smooth surface of the epoxy, with oriented fracture lines initiated from sites of crack growth, was observed on the sample fracture surfaces. In comparison, the samples with the addition of pan nanofibers containing the ECNFs showed rough fracture surface features with short, jagged and multi-plane fracture lines which indicated that the crack fronts were deflected and kinked during growth, as shown in Figure 5.42.

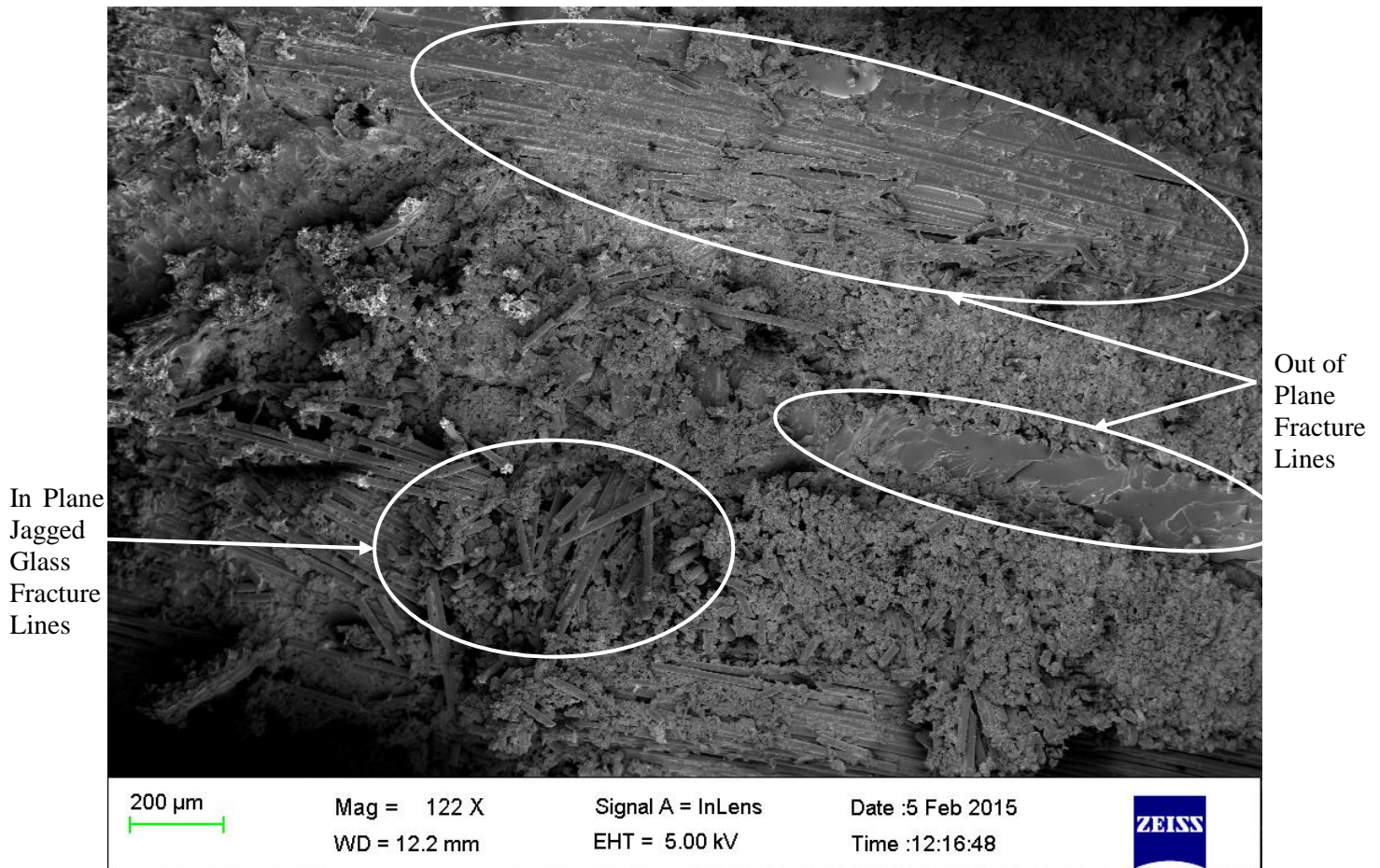


Figure 5.42: Fracture surface of the 1.0% ECNF embedded PAN nanofiber reinforced GRPC showing short, jagged and multi-plane fracture lines

Therefore, the main function of the imbedded ECNFs within the PAN nanofibers was to improve the effect of deflecting the propagating cracks and force the crack growth to deviate from the existing fracture plane. Therefore, additional strain energy was required in order to continuously force the growth of cracks, since the creation of additional fracture surface area would consume energy. Increasing the mass fraction of ECNFs from 0.5% to 1.0% resulted in a higher degree of deflection, which further improved the overall mechanical properties of the hybrid multiscale composites.

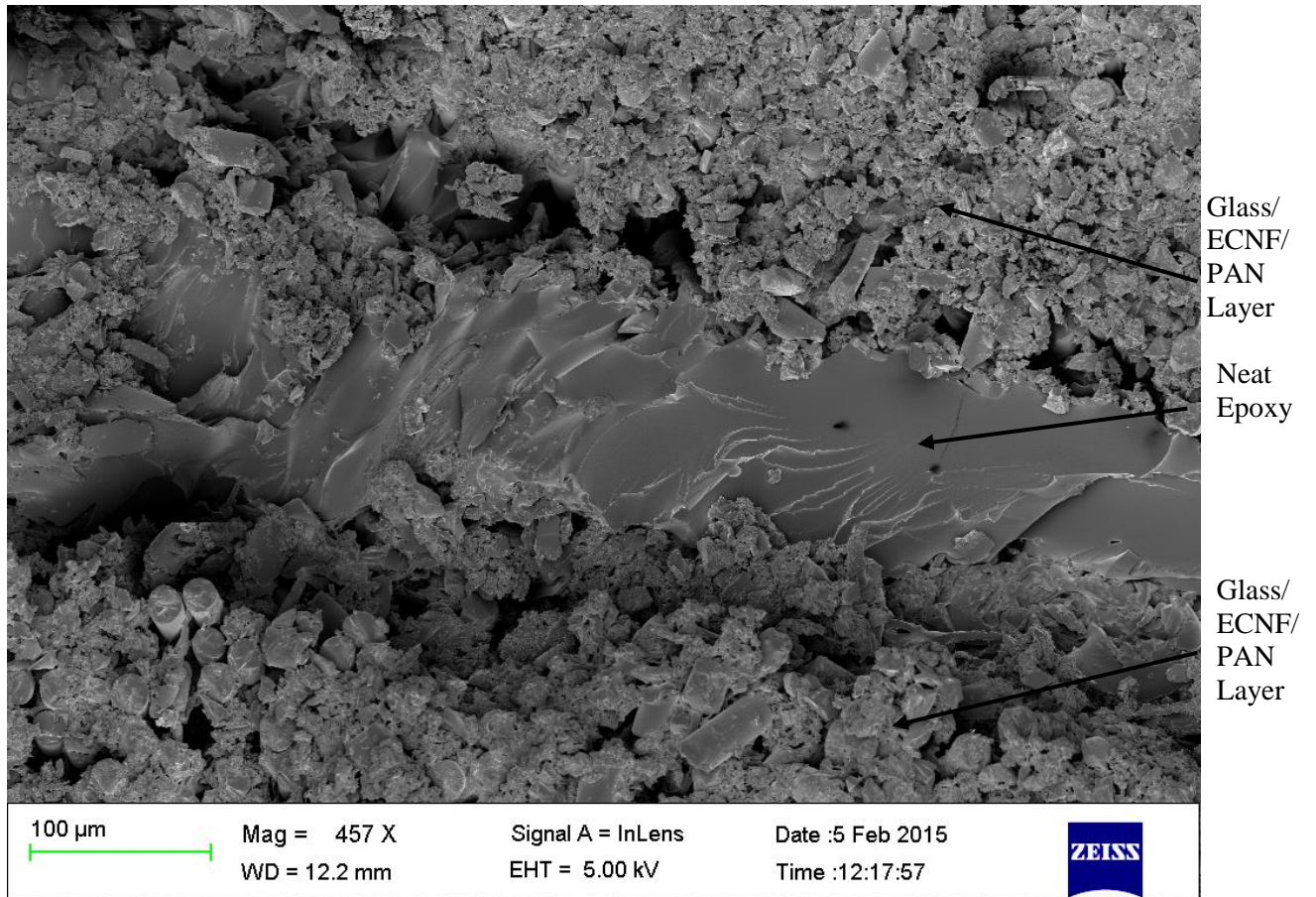


Figure 5.43: Fracture surface of a 1.0% ECNF embedded PAN nanofiber reinforced GRPC sample

Figure 5.43 shows that the ECNFs embedded PAN nanofibers were uniformly dispersed within the epoxy matrix and showed an improved interfacial region between the glass fibers and epoxy matrix and a reduced matrix rich zone between layers. Through inspection of the fracture surfaces of the ECNF embedded PAN nanofiber reinforced Glass fabrics/mats, it was evident that the same conclusions could be drawn as those from the flexural properties. Which were that the ECNF/PAN mats attached on the surfaces of the woven glass mats could increase the interfacial bonding strength and improve mechanical properties of the resulting hybrid multiscale ECNF/PAN reinforced GRPCs.

6 CONCLUSIONS

In this study, hybrid multiscale epoxy composites were developed from woven glass fabrics and PAN nanofibers embedded with short ECNFs (with diameters of $\sim 200nm$) produced via electrospinning. Unlike VGCFs or CNTs which are prepared through bottom-up methods, ECNFs were produced through a top-down approach; hence, ECNFs are much more cost-effective than VGCFs or CNTs. Impact absorption energy, tensile strength, and flexural strength of the hybrid multiscale reinforced GFRP composites were investigated. The control sample was the conventional GFRP composite prepared from the neat epoxy resin. With the increase of ECNFs amounts up to 1.0%, the impact absorption energy, tensile strength, and flexural strength also increased. The following remarks were concluded from the experimental results:

- (1) A functional electrospinning setup was designed and built at the University of the Witwatersrand which was capable of fabricating electrospun PAN nanofibers with diameters as low as $200nm$.
- (2) Smooth carbon nanofibers were produced from electrospun PAN nanofibers at a carbonisation temperature of $800^{\circ}C$ which showed improved thermal degradation and good graphitic ordering of the Carbon atoms which led to stronger bonding and lower free energy.
- (3) Two volume fraction multidirectional hybrid multiscale epoxy composites consisting of both PAN based ECNFs embedded in PAN nanofibers and woven glass fiber mats, 0.5% and 1% respectively, were investigated.
- (4) The incorporation of ECNFs embedded in the PAN nanofibers resulted in improvements on impact absorption energy, tensile strength, and flexural properties (strength and modulus) of the GFPC. Compared to the PAN reinforced GRPC, the incorporation of 1.0% ECNFs resulted in the improvements of impact absorption energy by roughly 9%, tensile strength by 37% and flexural strength by 29%, respectively. Interfacial debonding of matrix from the fiber was shown to be the dominant mechanism for shear failure of composites without ECNFs. PAN/ECNFs networks acted as microcrack arresters enhancing the composites toughness through the bridging mechanism in matrix rich zones. More energy absorption of the laminate specimens subjected to shear failure was attributed to the fracture and fiber pull out of more ECNFs from the epoxy matrix.
- (5) The VARTM process was utilised to cast the composite test samples. Since the processing parameters, such as mould filling pressure, temperature and fiber volume fraction were approximately kept the same, the only significant difference in mechanical properties values for the composites to the impregnation and interfacial bonding occurring between ECNFs/epoxy nanocomposite matrix and glass fiber during the processing.

This study suggests that, the developed hybrid multiscale ECNF/PAN epoxy composite could replace conventional GRPC as low-cost and high-performance structural composites with improved out of

plane as well as in plane mechanical properties. The strengthening/toughening strategy formulated in this study indicates the feasibility of using the nano-scale reinforcements to further improve the mechanical properties of currently structured high-performance composites in the coming years. In addition, the present study will significantly stimulate the long-term development of high-strength high-toughness bulk structural nanocomposites for broad applications. In order to achieve this long term goal, additional work to this research is required which are recommended as follows;

1. Research into the improvements of fiber collecting techniques and technologies such that rapid collections of aligned fibers on a much larger scale are achievable.
2. Further experimentation with fiber alignment and its effects on the structural properties of composite materials with aligned fibrous mats as opposed to non-woven mats.
3. Further insight into the interfacial bonds between ECNF, PAN and epoxy should be gained via computational modelling to better understand the bonding characteristics of the hybrid composite.
4. Further experimentation should be performed with additional primary fiber reinforcements and various matrices to confirm the results found from this investigation.
5. The effects of chemical functionalisation of the ECNFs should be investigated with particular focus on the interfacial bonding between PAN and ECNFs.

7 BIBLIOGRAPHY

- [1] N. Prasad, "Development and characterization of metal matrix composite using red mud an industrial waste for wear resistant applications," PhD Thesis, Department of Mechanical Engineering National Institute of Technology Rourkela, 2006.
- [2] K. Devendra and T. Rangaswamy, "Strength Characterization of E-glass Fiber Reinforced Epoxy Composites with Filler Materials," *Journal of Minerals and Materials Characterization and Engineering*, no. 1, pp. 353-357, 2013.
- [3] G. Kickelbick, "Hybrid materials: synthesis, characterization and applications", Wiley-VCH Verlag GmbH & Co KGaA, 2007.
- [4] Q. Chen, et al., "Fabrication and mechanical properties of hybrid multi-scale epoxy composites reinforced with conventional carbon fiber fabrics surface-attached with electrospun carbon nanofiber mats," *Composites: Part B*, no. 44, pp. 1-7, 2013.
- [5] Q. Chen, et al., "Hybrid multi-scale epoxy composite made of conventional carbon fiber fabrics with interlaminar regions containing electrospun carbon nanofiber mats," *Composites: Part A*, no. 42, pp. 2036-2042, 2011.
- [6] Q. Chen, et al., "Nano-epoxy resins containing electrospun carbon nanofibers and the resulting hybrid multi-scale composites," *Composites: Part B*, no. 58, p. 43–53, 2014.
- [7] Y. Shan and K. Liao, "Environmental fatigue behavior and life prediction of unidirectional glass–carbon/epoxy hybrid composites," *International Journal of Fatigue*, no. 24, p. 847–859, 2002.
- [8] M. Thwe and K. Liao, "Characterization of bamboo-glass fiber reinforced polymer matrix hybrid composite," *Journal of Material Science Letters*, no. 19, p. 1873–1876, 2000.
- [9] M. Miwa and N. Horiba, "Effects of fiber length on tensile strength of carbon/glass fiber hybrid composites," *Journal of Material Science*, no. 29, pp. 973-977, 1994.
- [10] A. Baji, Y. W. Mai, S. C. Wong, M. Abtahi, and P. Chen, "Electrospinning of polymer nanofibers: Effects on oriented morphology, structures and tensile properties," *Composites Science and Technology*, volume 70, p. 703–718, 2010.
- [11] S. Gu, Q. Wu, and J. Ren, "Preparation and surface structures of carbon nanofibers produced

- from electrospun PAN precursors," *New Carbon Materials*, volume 23, no. 2, pp. 171-176, Mar. 2008.
- [12] I. Chun, et al., "Carbon nanofibers from polyacrylonitrile and mesophase pitch," *J Adv Mater*, no. 31, pp. 36-41, 1999.
- [13] Y. Dzenis and Y. Wen, "Continuous carbon nanofibers for nanofiber composites," in *Materials Research Society Symposium*, 2002, pp. 173-178.
- [14] Y. Wang, S. Serrano, and J. Santiago-Aviles, "Conductivity measurement of electrospun PAN-based carbon nanofiber," *Journal of Materials Science Letters*, volume 21, no. 13, p. 1055-1057, 2002.
- [15] P. Jose et al., "Advances in Polymer Composites: Macro- and Microcomposites – State of the Art, New Challenges, and Opportunities," *Polymer Composites*, volume 1, no. 1, 2012.
- [16] V. Mittal, "Polymer Nanocomposites: Synthesis, Microstructure, and Properties", *Optimization of Polymer Nanocomposite Properties*, Wiley-VCH Verlag GmbH & Co. KGaA, 2010, ch. 6, pp. 123-135.
- [17] US Congress Office of Technology Assessment, "Advanced Materials by Design", US Government Printing Office, 1988.
- [18] P. C. Painter and M. M. Coleman, "Fundamentals of polymer science: an introductory text", Lancaster, United States of America: Technomic, 1997.
- [19] D. Geoffrey, "Materials for Automobile Bodies", 2nd ed. Oxford, UK: Butterworth-Heinemann, 2012.
- [20] A. M. James, "Design of an advanced composites aileron for commercial aircraft," *Composites*, volume 7, no. 2, pp. 73-80, Apr. 1976.
- [21] M. K. Seo, K. E. Choi, S. H. Park, Y. T. Hong, and S. J. Park, "Preparation and Characterization of Poly(amide imide)-based Carbon Nanofibers/Epoxy Nanocomposites," *Carbon Letters*, volume 10, pp. 329-334, 2009.
- [22] T. Johnson. (2014) About.com. [Online]. <http://composite.about.com/od/Resins/a/Epoxy-Resin.htm>
- [23] N. Notman. (2012, Nov.) rsc.org. [Online]. <http://www.rsc.org/chemistryworld/2012/11/bpa-bisphenol>

- [24] Chemicalbook.com. (2008) [Online].
http://www.chemicalbook.com/ProductChemicalPropertiesCB8183772_EN.htm
- [25] D. Cripps. (1999) netcomposites.com. [Online]. <http://www.netcomposites.com/guide/glass-fiberfiber/32>
- [26] M. I. Kiron. (2011, Aug.) textilelearner.blogspot.com. [Online].
http://textilelearner.blogspot.com/2011/08/glass-fiber-types-of-glass-fiber_3834.html
- [27] S. Rapra. (2008) rapra.net. [Online]. <http://www.rapra.net/composites/material-selection/reinforcement-types.asp>
- [28] W. F. Smith, "Foundations of Materials Science and Engineering", New York, United States of America: McGraw Hill, 1993.
- [29] Y. Zhou, F. Pervin, V. Rangari, and S. Jeelani, "Fabrication and evaluation of carbon nanofiber filled carbon/epoxy composite," *Mater Sci Eng A*, volume 426, no. 2, pp. 221-228, 2006.
- [30] M. Kim, Y. Park, O. Okoli, and C. Zhang, "Processing, characterization, and modeling of carbon nanotube-reinforced multiscale composites," *Compos Sci Technol*, volume 69, no. 2, p. 335–342, 2009.
- [31] Y. Zhou, M. Hosur, S. Jeelani, and P. Mallick, "Fabrication and characterization of carbon fiber reinforced clay/epoxy composite," *J Mater Sci*, volume 47, pp. 5002-5012, 2012.
- [32] J. Qiu, C. Zhang, B. Wang, and R. Liang, "Carbon nanotube integrated multifunctional multiscale composites," *Nanotechnology*, volume 18, no. 27, pp. 1-11, 2007.
- [33] E. J. Rigas, T. J. Mulkern, S. M. Walsh, and S. P. Nguyen, "Effects of Processing Conditions on Vacuum Assisted Resin Transfer Molding Process (VARTM)," ARMY RESEARCH LABORATORY, 2001.
- [34] S. Singh, P. Kumar, and S. K. Jain, "An experimental and numerical investigation of mechanical properties of glass fiber reinforced epoxy composites," *Advanced Materials Letters*, volume 4, no. 7, p. 567, Jul. 2013.
- [35] P. Deogonda and V. N. Chalwa, "Mechanical Property of Glass Fiber Reinforcement Epoxy Composites," *International Journal of Scientific Engineering and Research*, volume 1, no. 4, pp. 2347-3878, Dec. 2013.

- [36] S. D. McCullen, et al., "Morphological, Electrical, and Mechanical Characterization of Electrospun Nanofiber Mats Containing Multiwalled Carbon Nanotubes," *Macromolecules*, volume 40, no. 4, pp. 997-1003, 2007.
- [37] S. N. Arshad, M. Naraghi, and I. Chasiotis, "Strong Carbon Nanofibers from electrospun polyacrylonitrile," *Carbon*, volume 49, pp. 1710-1719, 2011.
- [38] T. V. Chambers and R. Hughes, U.S. Patent UNKNOWN, 1889.
- [39] M. L. Toebes, "The influence of oxidation on the texture and the number of oxygen-containing surface groups of carbon nanofibers," *Carbon*, volume 42, no. 2, pp. 307-315, 2004.
- [40] R. Bacon, "Growth, Structure, and Properties of Graphite Whiskers," *Journal of Applied Physics*, pp. 283-290, 1960.
- [41] A. Oberlin, M. Endo, and T. Koyama, "Filamentous growth of carbon through benzene decomposition," *J. Cryst. Growth*, pp. 332-335, 1976.
- [42] S. Iijima, "Helical microtubules of graphitic carbon," *Nature*, volume 354, pp. 354-356, 1991.
- [43] Z. Zhou, et al., "Development of carbon nanofibers from aligned electrospun polyacrylonitrile nanofiber bundles and characterization of their microstructural, electrical, and mechanical properties," *Polymer*, no. 50, pp. 2999-3006, 2009.
- [44] E. Zussman, et al., "Mechanical and structural characterization of electrospun pan-derived carbon nanofibers," *Carbon*, no. 43, pp. 2175-2185, 2005.
- [45] E. Fitzer, W. Frohs, and M. Heine, "Optimization of stabilization and carbonization treatment of PAN fibers and structural characterization of resulting carbon fibers," *Carbon*, volume 24, no. 4, pp. 387-395, 1986.
- [46] H. Chae, Y. Choi, M. Minus, and S. Kumar, "Carbon nanotube reinforced small diameter polyacrylonitrile based carbonfiber," *Compos Sci Technol*, volume 69, pp. 406-413, 2009.
- [47] H. Chae, M. Minus, A. Rasheed, and S. Kumar, "Stabilization and carbonization of gel spun polyacrylonitrile/single wall carbonnanotube composite fibers," *Polymer*, volume 48, pp. 3781-3789, 2007.
- [48] R. H. Baughman, A. A. Zakhidov, and W. A. de Heer, "Carbon Nanotubes--the Route Toward Applications," *Science*, volume 297, no. 5582, pp. 787-792, 2002.

- [49] K. Laua, C. Gub, and D. Huic, "A critical review on nanotube and nanotube/nanoclay related polymer composite materials," *Composites Part B: Engineering*, volume 37, no. 6, pp. 425-436, 2006.
- [50] M. Katarzyna, K. Sawicka, and P. Gouma, "Electrospun composite nanofibers for functional applications," *Journal of Nanoparticle Research*, volume 8, p. 769–781, 2006.
- [51] T. Ozkan, M. Naraghi, and I. Chasiotis, "Mechanical properties of vapor grown carbon nanofibers," *Carbon*, volume 48, pp. 239-244, 2010.
- [52] F. Fisher, R. Bradshaw, and L. Brinson, "Fiber waviness in nanotube-reinforced polymer composites—I: modulus predictions using effective nanotube properties," *Composite Science Technology*, volume 63, pp. 1689-1703, 2003.
- [53] L. Liu, Y. M. Liang, G. Y. Xu, H. S. Zhang, and Z. M. Huang, "Mode I Interlaminar Fracture of Composite Laminates Incorporating with Ultrathin Fibrous Sheets," *Journal of Reinforced Plastics and Composites*, volume 27, pp. 1147-1162, Apr. 2008.
- [54] P. Quynh, U. Sharma, and A. G. Mikos, "Electrospinning of Polymeric Nanofibers for Tissue Engineering Applications: A Review," *Tissue Engineering*, volume 12, no. 5, pp. 1197-1211, Jun. 2006.
- [55] Z. Kurban, et al., "Turbostratic graphite nanofibers from electrospun solutions of PAN in dimethylsulphoxide," *European Polymer Journal*, volume 46, pp. 1194-1202, 2010.
- [56] A. Formhals, "Process and apparatus for preparing artificial threads," U.S. Patent 1 975 504, 1934.
- [57] S. Ramakrishna, K. Fujihara, W. E. Teo, T. Lim, and Z. Ma, "An introduction to electrospinning and nanofibers," *World Scientific*, volume 90, 2005.
- [58] J. Taylor, "Electrically driven jets," *Proc. R. Soc.*, volume 313, no. 1515, p. 453–475, 1969.
- [59] C. Shin and G. G. Chase, "Nanofibers from recycle waste expanded polystyrene using natural solvent," *Polym. Bull*, volume 55, no. 3, pp. 209-215, 2005.
- [60] M. V. Kakade, et al., "Electric field induced orientation of polymer chains in macroscopically aligned electrospun polymer nanofibers," *J. Am. Chem. Soc.*, volume 129, no. 10, p. 2777–2782, 2007.
- [61] S. Warner, et al., "Electrostatic Spinning and Properties of Ultrafine Fibers," MIT, Annual

Report, 2001.

- [62] A. L. Yarin, S. Koombhongse, and D. H. Reneker, "Bending instability in electrospinning of nanofibers," *Journal of Applied Physics*, volume 89, no. 5, pp. 3018-3026, 2001.
- [63] S. Gu, J. Ren, and G. Vancso, "Process optimization and empirical modeling for electrospun polyacrylonitrile (PAN) nanofiber precursor of carbon nanofibers," *European Polymer Journal*, volume 41, pp. 2559-2568, 2005.
- [64] P. Heikkilä and A. Harlin, "Electrospinning of polyacrylonitrile (PAN) solution: Effect of conductive additive and filler on the process," *eXPRESS Polymer Letters*, volume 3, no. 7, pp. 437-445, 2009.
- [65] X. Fong, et al., "Structure and process relationship of electrospun bioabsorbable nanofiber membranes," *Polymer*, volume 43, no. 16, pp. 4403-4412, 2002.
- [66] Y. A. Dzenis and D. H. Reneker, "Delamination Resistant Composites Prepared by Small Diameter Fiber Reinforcement at Ply Interfaces," in *European Conference of Composite Materials*, Naples, 1998, pp. 517-524.
- [67] Y. A. Dzenis and D. H. Reneker, "Delamination Resistant Composites Prepared by Small Diameter Fiber Reinforcement at Ply Interfaces," U.S. Patent 6265333, Jul. 24, 2001.
- [68] M. M. Vancso and G. J. Bergshoef, "Transparent Nanocomposites with Ultrathin, Electrospun Nylon-4,6 Fiber Reinforcement," *Advanced Materials*, volume 11, no. 16, pp. 1362-1365, Nov. 1999.
- [69] X. F. Wu, "Fracture of advanced polymer composites with nanofiber reinforced interfaces," Ph.D. thesis, University of Nebraska-Lincoln, 2003.
- [70] E. Ozden, Y. Menciloglu, and M. Papila, "Engineering chemistry of electrospun nanofibers and interfaces in nanocomposites for superior mechanical properties," *ACS Appl Mater Interf*, volume 2, no. 1, p. 1788-1793, 2010.
- [71] H. Fong, "Electrospun nylon 6 nanofiber reinforced Bis-GMA/TEGDMA dental restorative composite resins," *Polymer*, volume 45, pp. 2427-2432, 2004.
- [72] S. Lin, et al., "Electrospun nanofiber reinforced and toughened composites through in situ nano-interface formation," *Compos Sci Technol*, volume 68, pp. 3322-3329, 2008.
- [73] Aussawasathien, E. Sancaktar, and Darunee, "Nanocomposites of Epoxy with Electrospun

- Carbon Nanofibers: Mechanical Behavior," *The Journal of Adhesion*, volume 85, p. 160–179, 2009.
- [74] S. N. Arshad, "High strength carbon nanofibers derived from electrospun polyacrylonitrile," Master of Science, University of Illinois at Urbana-Champaign, Urbana, Illinois, 2010.
- [75] J. Kim and D. H. Reneker, "Mechanical properties of composites using ultrafine electrospun fibers," *Polym Compos*, volume 20, pp. 124-131, 1999.
- [76] Z. M. Huang, Y. Z. Zhanb, M. Kotaki, and S. Ramakrishna, "A review on polymer nanofibers by electrospinning and their applications in nanocomposites," *Composites Science and Technology*, volume 63, pp. 2223-2253, 2003.
- [77] K. Song, et al., "Structural Polymer-Based Carbon Nanotube Composite Fibers: Understanding the Processing–Structure–Performance Relationship," *Materials*, volume 6, pp. 2543-2577, 2013.
- [78] A. Plaseieda, A. Fatemib, and M. R. Colemanc, "Influence of Carbon Nanofiber Content and Surface Treatment on Mechanical Properties of Vinyl Ester," *Polymers & Polymer Composites*, volume 16, no. 7, pp. 405-414, 2008.
- [79] M. H. G. Wichmann, "Glass-fiber-reinforced composites with enhanced mechanical and electrical properties – Benefits and limitations of a nanoparticle modified matrix," *Engineering Fracture Mechanics*, volume 73, p. 2346–2359, 2006.
- [80] F. H. Schulte and K. Gojny, "Functionalisation effect on the thermo-mechanical behaviour of multi-wall carbon nanotube/epoxy-composites," *Composites Science and Technology*, volume 64, p. 2303–2308, 2004.
- [81] D. Puglia, L. Valentini, and J. M. Kenn, "Analysis of the cure reaction of carbon nanotubes/epoxy resin composites through thermal analysis and Raman spectroscopy," *Journal of Applied Polymer Science*, volume 88, no. 2, p. 452–458, 2003.
- [82] S. G. Prolongo, et al., "Effects of dispersion techniques of carbon nanofibers on the thermo-physical properties of epoxy nanocomposites," *Composites Science and Technology*, no. 68, p. 2723, 2008.
- [83] J. Zhu, et al., "Improving the Dispersion and Integration of Single-Walled Carbon Nanotubes in Epoxy Composites through Functionalization," *Nano Letters*, volume 3, no. 8, pp. 1107-1113, 2003.

- [84] T. Wan, S. Liao, K. Wang, P. Yan and M. Clifford, "Multi-scale hybrid polyamide 6 composites reinforced with nano-scale clay and micro-scale short glass fiber," *Composites: Part A*, volume 50 , p. 31–38, Mar. 2013.
- [85] E. T. Thostenson, W. Z. Li, D. Z. Wang, Z. F. Ren and T. W. Chou, "Carbon nanotube/carbon fiber hybrid multiscale composites," *Journal of Applied Physics*, volume 91, no. 9, 200.
- [86] Y. Xu and S. V Hoa, "Mechanical properties of carbon fiber reinforced epoxy/clay nanocomposites," *Composite Science Technology* , volume 68, p. 854–861, 2008.
- [87] E. T. Thostenson, L. Chunyu, and T. W. Chou, "Nanocomposites in context," *Composite Science Technology*, no. 65, p. 491–516, 2005.
- [88] W. Salalha, et al., "CNFs embedded in oriented polymer nanofibers by electrospinning," *Langmuir*, no. 19, p. 7012–7020, 2003.
- [89] J. J. Ge, et al., "Assembly of well-aligned multiwalled carbon nanotubes in confined polyacrylonitrile environments: electrospun composite nanofiber sheets," *J. Am. Chem. Soc.*, no. 126, pp. 15754-15761, 2004.
- [90] R. Sen, et al., "Preparation of single-walled carbon nanotube reinforced polystyrene and polyurethane nanofibers and membranes by electrospinning," *Nano Lett.*, no. 4, p. 459–464, 2004.
- [91] F. Ko, et al., "Electrospinning of continuous carbon nanotube-filled nanofiber yarns," *Adv. Mater.*, no. 15, p. 1161–1165, 2003.
- [92] H. Ye, H. Lam, N. Titchenal, Y. Gogotsi, and F. Ko, "Reinforcement and rupture behavior of carbon nanotubes–polymer nanofibers," *Applied Physics Letters*, no. 85, p. 1775–1777, 2004.
- [93] ASTM, "ASTM Standard D638," in *Standard Test Method for Tensile Properties of Plastics*. ASTM International, 2010.
- [94] ASTM, "ASTM Standard D256," in *Determining the Izod Pendulum Impact Resistance of Plastics*. ASTM International, 2010.
- [95] Semrock. (2006) semrock.com. [Online].
http://www.semrock.com/Data/Sites/1/semrockimages/technote_images/raman_layout_withb_s.jpg

- [96] D. Darling. (2013, Jan.) www.daviddarling.info. [Online].
http://www.daviddarling.info/encyclopedia/R/Raman_effect.html
- [97] M. Pacheco, J. Pacheco, and R. Valdivia, *Synthesis of Carbon Nanofibers by a Glow-Arc Discharge*. 2010.
- [98] Y. Wang, S. Serrano, and J. J. Santiago-Aviles, "Raman characterization of carbon nanofibers prepared using electrospinning," *Synthetic Metals*, volume 138, pp. 423-427, 2003.
- [99] F. Pashaloo, S. Bazgir, M. Tamizifar, M. Faghihisani, and S. Zakerifar, "Preparation and Characterization of Carbon Nanofibers via Electrospun PAN Nanofibers," *Textile Science and Technology Journal*, volume 3, no. 2, 2008.
- [100] K. I. Winey and R. A. Vaia, "Polymer Nanocomposites," *MRS Bulletin*, volume 32, pp. 314-322, 2007.
- [101] G. Sui, W. H. Zhong, X. Ren, X. Q. Wang, and X. P. Yang, "Structure, mechanical properties and friction behavior of UHMWPE/HDPE/carbon nanofibers," *Materials Chemistry and Physics*, volume 115, no. 1, p. 404–412, May 2009.
- [102] A. W. Redfern and J. P. Coats, "Thermogravimetric analysis. A review," *Analyst*, volume 88, pp. 906-924, 1963.
- [103] J. Muthu and C. Dendere, "Functionalized multiwall carbon nanotubes strengthened GRP hybridcomposites: Improved properties with optimum fiber content," *Composites: Part B*, no. 67, pp. 84-94, Jun. 2014.
- [104] Gurit. (2009) www.amtcomposites.co.za. [Online].
<http://www.amtcomposites.co.za/sites/default/files/media/data-sheets/ampreg%2021%20v7.pdf>
- [105] H. S. Kim, K. Kim, H. J. Jin, and I. Chin, "Morphological characterization of electrospun nano-fibrous membranes of biodegradable poly(L-lactide) and poly(lactideco- glycolide)," *Macromol Symp*, volume 224, p. 145–154, 2005.
- [106] H. Liu and Y. Hsieh, "Ultrafine fibrous cellulose membranes from electrospinning of cellulose acetate," *J Polym Sci Part B: Polym Phys*, volume 40, p. 2119–2129, 2002.
- [107] B. Sundaray, et al., "Electrospinning of continuous aligned polymer fibers," *Appl Phys Lett*, volume 84, pp. 1222-1224, 2004.

- [108] A. Theron, E. Zussman, and A. Yarin, "Electrostatic field-assisted alignment of electrospun nanofibers," *Nanotechnology*, volume 12, pp. 384-390, 2001.
- [109] S. D. McCullen, "Development, Characterization, and Function of Electrospun Nanocomposites for Tissue Engineering," Master of Science, North Carolina State University, Raleigh, North Carolina, 2006.
- [110] S. Zhnag, "Mechanical and Physical Properties of Electrospun Nanofibers," Master of Science, North Carolina State University, Raleigh, North Carolina, 2009.
- [111] V. Boppa, "Characterization of Structure and Tensile Properties of Electrospun Web," Master of Science, North Carolina State University, Raleigh, North Carolina, 2009.
- [112] F. Ko, "Carbonization conditions for electrospun nanofiber of polyacrylonitrile copolymer," *Indian Journal of Fiber & Textile Research*, volume 33, pp. 345-353, 2008.
- [113] M. K. Pilehrood, P. Heikkilä, and A. Harlin, "Preparation of Carbon Nanotube Embedded in Polyacrylonitrile (PAN)," *AUTEX Research Journal*, volume Volume 12, no. 1, pp. 1-6, Mar. 2012.
- [114] A. A. Al-Jeebory, A. I. Al-Mosawi, and S. A. Abdullah, "Effect of percentage of fibers reinforcement on thermal and mechanical properties for polymeric composite material," *The Iraqi Journal for mechanical and materials Engineering*, no. Special, 2009.
- [115] D. Ratna, T. K. Chongdar, and B. C. Chakraborty, "Mechanical Characterization of New Glass Fiber Reinforced Epoxy Composites," *Polymer Composites*, volume 25, no. 2, pp. 165-171, Apr. 2004.
- [116] M. Naraghi, S. N. Arshad, and I. Chasiotis, "Molecular Orientation and Mechanical Property Size Effects in Electrospun Polyacrylonitrile Nanofibers," *Polymer*, volume 52, p. 1612, 2011.
- [117] L. S. Chen, et al., "Development of a transparent PMMA composite reinforced with nanofibers," *Polym. Compos*, volume 30, no. 3, p. 239–247, Mar. 2009.
- [118] A. Arinstein and E. Zussman, "Electrospun polymer nanofibers: Mechanical and thermodynamic perspectives," *J. Polym. Sci. Part B Polym. Phys.*, no. 49, p. 691–707, 2011.
- [119] E. Ozden, Y. Z. Menciloglu, and M. Papila, "Electrospun Polymer/MWCNTs Nanofiber Reinforced Composites "Improvement of Interfacial Bonding by Surface Modified

- Nanofibers," in *MRS Proceedings*, Cambridge, 2009, p. 1224.
- [120] S. Sihm, R. Y. Kim, W. Huh, K. H. Lee, and A. K. Roy, "Improvement of damage resistance in laminated composites with electrospun nano-interlayers," *Composites Science and Technology*, volume 68, p. 673–683, 2008.
- [121] J. Chen, M. A. Hamon, and H. Hu, "Solution properties of single-walled carbon nanotubes," *Science*, volume 282, p. 95, 1998.
- [122] A. C. Robertson and J. Ferrari, "Interpretation of Raman spectra of disordered and amorphous carbon," *Physical Review B*, volume 61, no. 20, pp. 14095-14107, May 2000.
- [123] B. He, J. Li, and Z. Pan, "Morphology and mechanical properties of MWNT/PMIA nanofibers by electrospinning," *Textile Research Journal*, volume 82, no. 13, p. 1390–1395, Mar. 2012.
- [124] P. Harris, *Carbon Nanotube Science*. Cambridge, United Kingdom: Cambridge University Press, 2009.
- [125] Y. Im and J. Sun, "Preparation of Functionalized Nanofibers and Their Applications", A. Kumar, Ed. 2010.
- [126] S. D. Robertson, "Graphite Formation from Low Temperature Pyrolysis of Methane over some Transition Metal Surfaces," *Nature*, volume 221, p. 1044, Mar. 1969.
- [127] J. Summerscales (2006), *Composites Design and Manufacture*, Advanced Composites Manufacturing Centre (Plymouth University teaching support materials). [Online] <https://www.fose1.plymouth.ac.uk/sme/MATS347/MATS347A16%20nano.htm>
- [128] G. Rathnakar and H. K. Shivanan, "Experimental Evaluation of Strength and Stiffness of Fiber Reinforced Composites under Flexural Loading", *International Journal of Engineering and Innovative Technology*, volume 2, issue 7, p 219-222, Jan.2013.
- [129] R. Neppalli, M. Bajgai, C. Marega, H. Y. Kim, A. Marigo and V. Causin, "Poly(ϵ -caprolactone) filled with electrospun nylon fibers: A model for a facile composite fabrication", *European Polymer Journal*, volume 46, p 968-976, Jan. 2010.
- [130] K. Molnár, E. Kostavora and L. Mészáros, "The effect of needleless electrospun nanofibrous interleaves on mechanical properties of carbon fabrics/epoxy laminates", *eXPRESS Polymer Letters*, volume 8, No.1, p 62–72, Jun. 2013.

- [131] M. Tian, et al. "Bis-GMA/TEGDMA Dental Composites Reinforced with Electrospun Nylon 6 Nanocomposite Nanofibers Containing Highly Aligned Fibrillar Silicate Single Crystals." *Polymer* 48.9, p 2720–2728, 2007.
- [132] M. Dimchev, R. Caeti and N. Gupta, "Effect of carbon nanofibers on tensile and compressive characteristics of hollow particle filled composites", *Materials & Design*, Composite Materials and Mechanics Laboratory, Department of Mechanical and Aerospace Engineering, Polytechnic Institute of New York University, p 1332 -1337, 2010.

APPENDIX A (Raw Testing Data and Samples)

A.1 Tensile and Flexural Testing Results

The Shimadzu universal testing machine was used to obtain the load and extension data for each sample, both tensile and flexural samples, which was recorded by the data acquisition software automatically. This data was saved as comma separated value (CSV.) files and is provided for in electronic format, on a compact disc to be submitted with this thesis, due to the numerous amounts of data.

The raw data was processed from each tensile and flexural specimen tested for the various glass fiber, PAN fiber and ECNF embedded PAN fiber volume fractions. The tensile strength, flexural strength and flexural strain were determined together with the Young's modulus and flexural modulus. The Young's modulus is represented as the gradient of the stress-strain curve, only in the linear (elastic) region. The tensile and flexural stress-strain curves, for all 5 specimens tested, of all the samples are presented below.

Table A.1: Tensile specimen observations for neat epoxy

Specimen number	Dimensions		Tensile Strength [MPa]	Tensile Modulus [MPa]	Flexural Strength [MPa]	Flexural Modulus [MPa]
	Width Tensile [mm]	Width Flexural [mm]				
1	12.7	12.3	46.2	2715.0	78.2	2303.9
2	12.6	14.0	39.2	1550.0	74.6	2365.9
3	12.0	15.1	26.8	1044.0	66.9	1956.3
4	12.1	14.5	20.1	740.2	75.4	2199.3
5	12.5	14.7	29.7	1158.0	67.6	2395.8
Mean	12.4	14.1	32.4	1441.4	72.6	2244.2
Standard Deviation	0.30	1.15	10.3	768.7	4.9	177.6

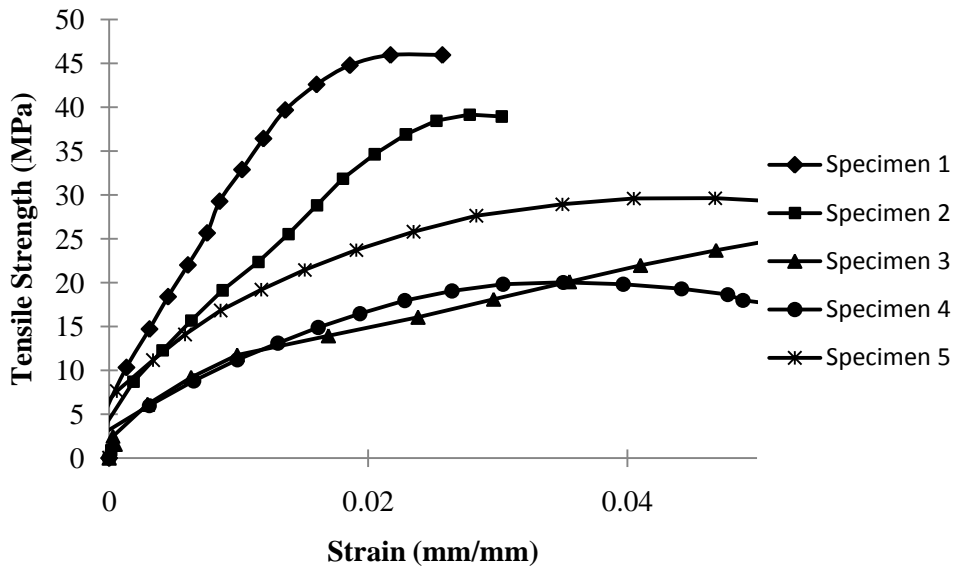


Figure A.1: Tensile strengths of neat epoxy samples

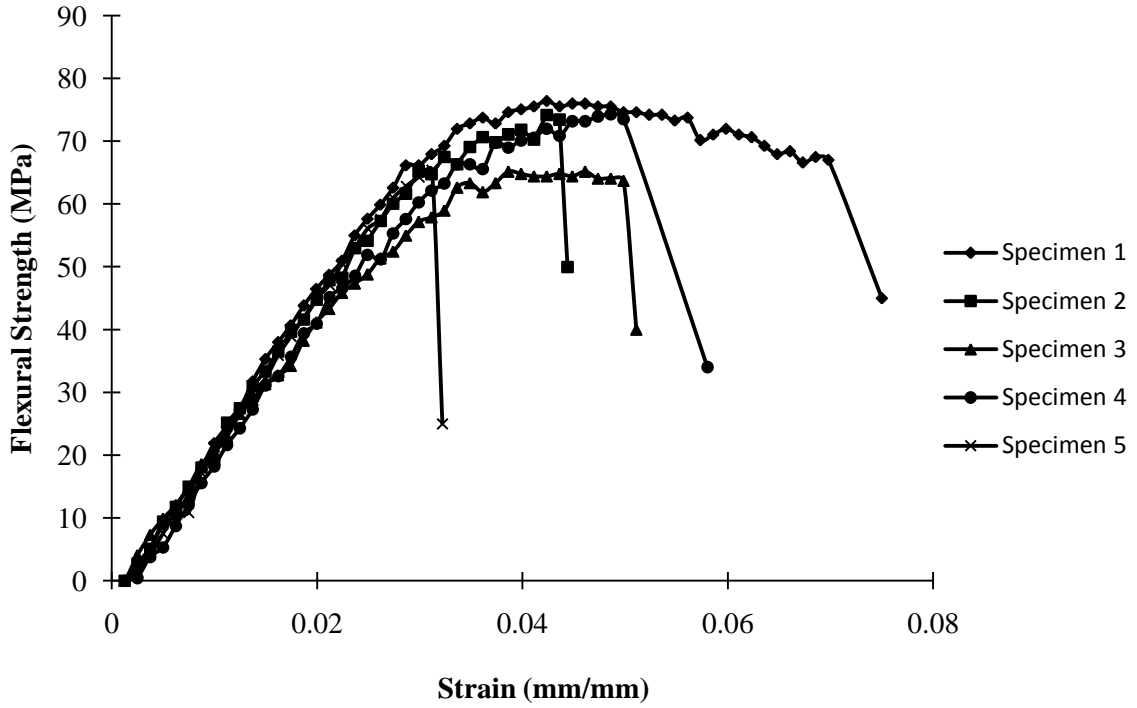


Figure A.2: Flexural strengths of neat epoxy samples

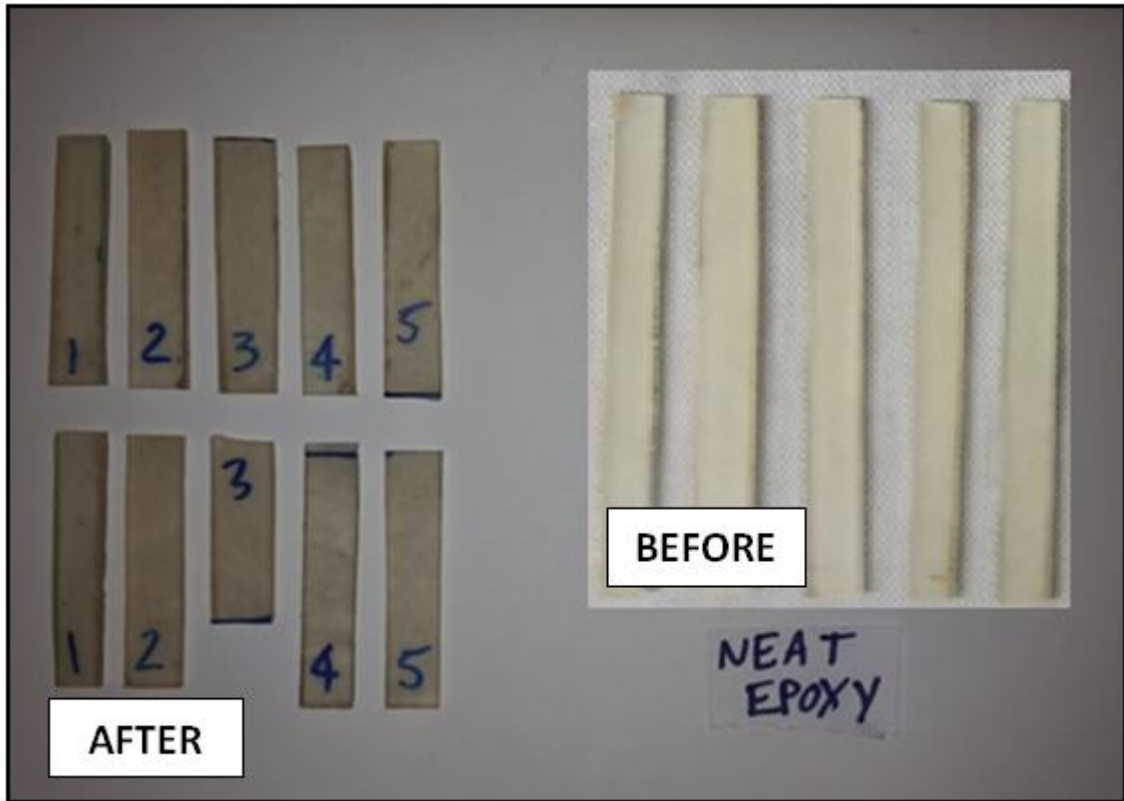


Figure A.3: Neat epoxy flexural samples

Table A.2: Tensile specimen observations for 16% GRPC

Specimen number	Dimensions		Tensile Strength [MPa]	Tensile Modulus [MPa]	Flexural Strength [MPa]	Flexural Modulus [MPa]
	Width Tensile [mm]	Width Flexural [mm]				
1	12.9	14.1	191.8	9671.0	167.2	6824.5
2	12.8	13	153.5	6381.0	157.7	6520.8
3	12.7	13.7	220.4	6196.0	166.1	6222.6
4	12.8	11.5	195.3	6101.0	181.1	6858.4
5	13.1	13.7	190.6	5993.0	139.6	6029.1
Mean	12.86	13.2	190.3	6868.4	162.394	6491.08
Standard Deviation	0.15	1.02	23.9	1573.17	15.24	364.85

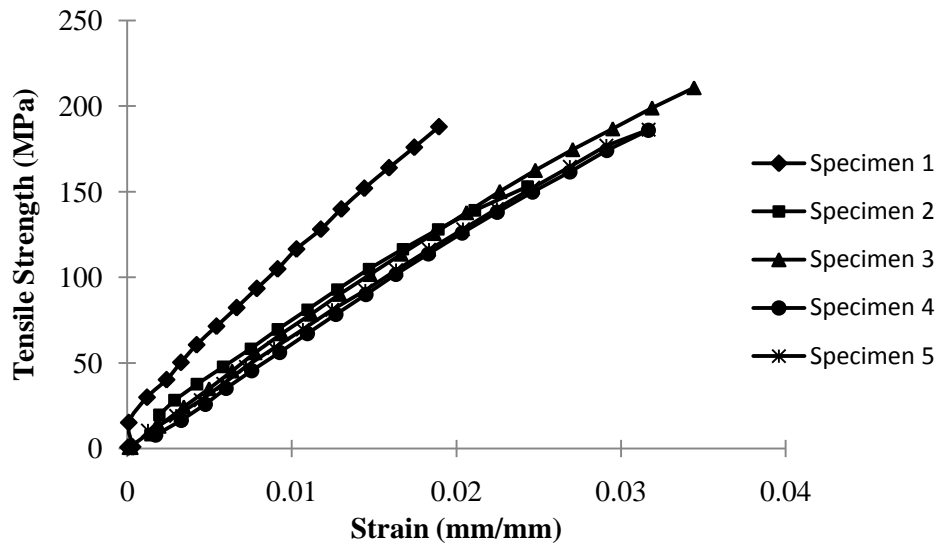


Figure A.4: Tensile strengths of 16% volume fraction glass fiber samples

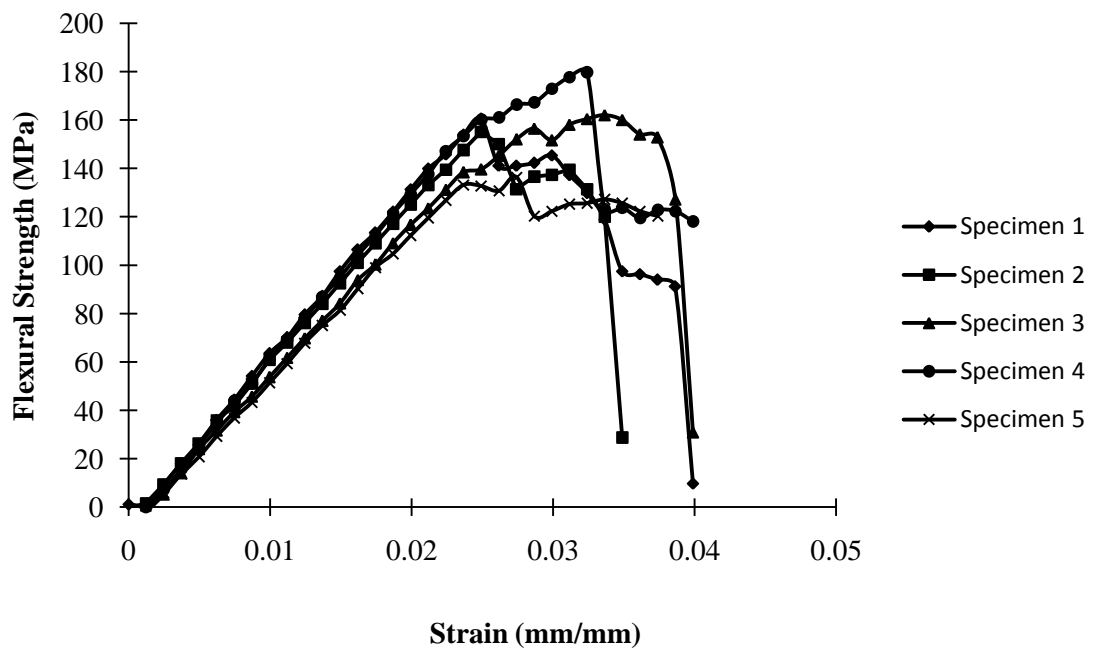


Figure A.5: Flexural strengths of 16% volume fraction glass fiber samples



Figure A.6: 16% GRPC flexural samples

Table A.3: Tensile specimen observations for 24% GRPC

Specimen number	Dimensions		Tensile Strength [MPa]	Tensile Modulus [MPa]	Flexural Strength [MPa]	Flexural Modulus [MPa]
	Width Tensile [mm]	Width Flexural [mm]				
1	12.7	13.5	208.51	11351	246.38	8264.4
2	12.7	14.8	206.82	7983	239.6	8236.7
3	12.6	16	231.31	8910	252.2	8712.7
4	12.8	14.9	205.59	11621	104.8	3293.1
5	12.9	13.6	234.69	9229	170.19	8778.8
Mean	12.74	14.56	217.38	9818.8	202.63	7457.14
Standard Deviation	0.11	1.03	14.34	1592.12	63.95	2341.03

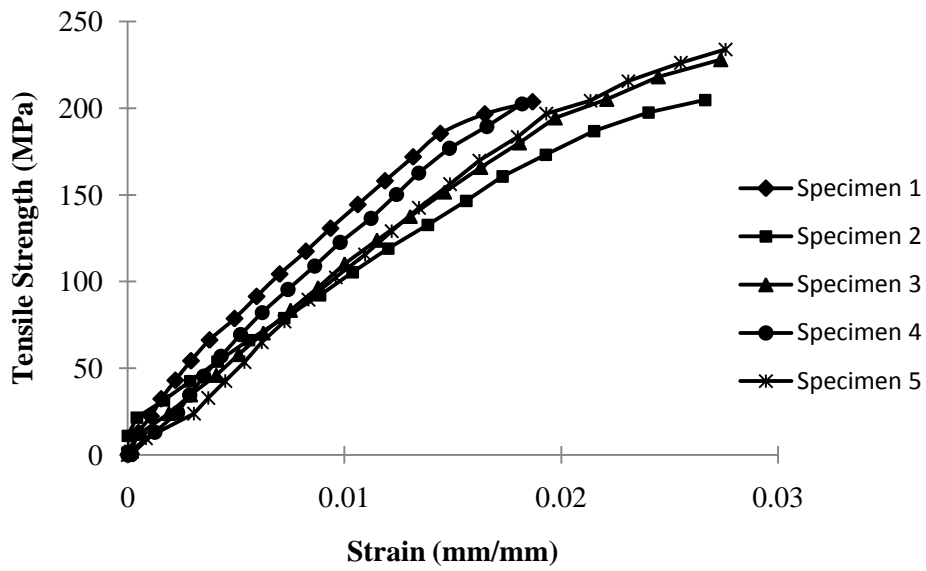


Figure A.7: Tensile strengths of 24% volume fraction glass fiber samples

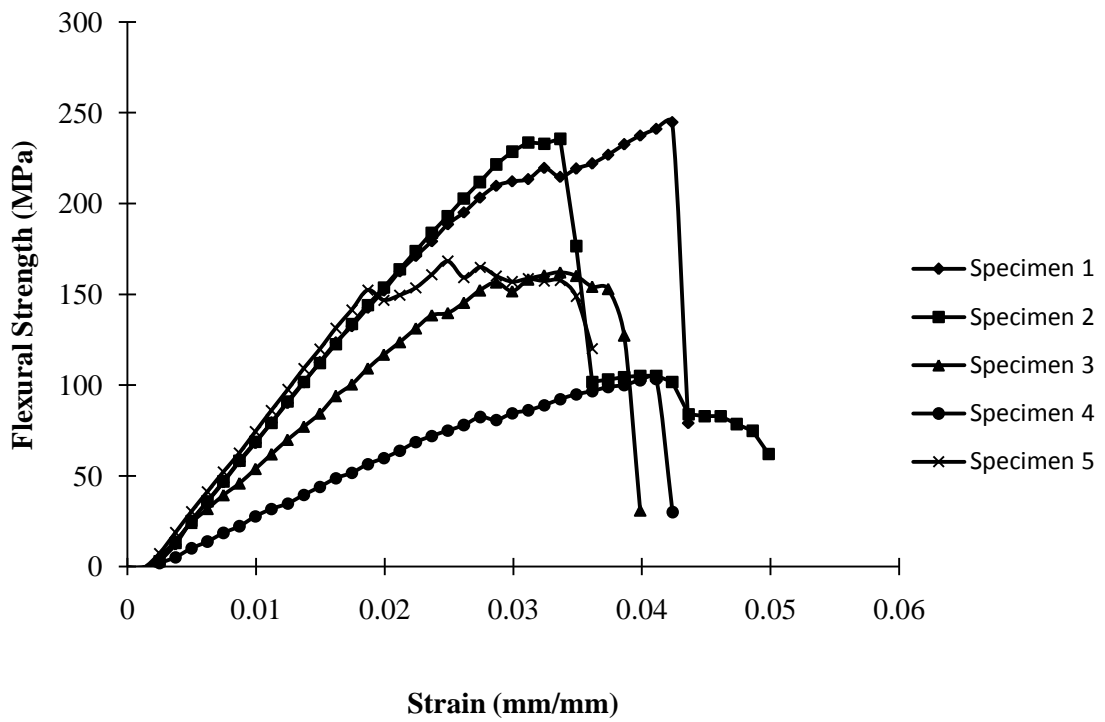


Figure A.8: Flexural strengths of 24% volume fraction glass fiber samples

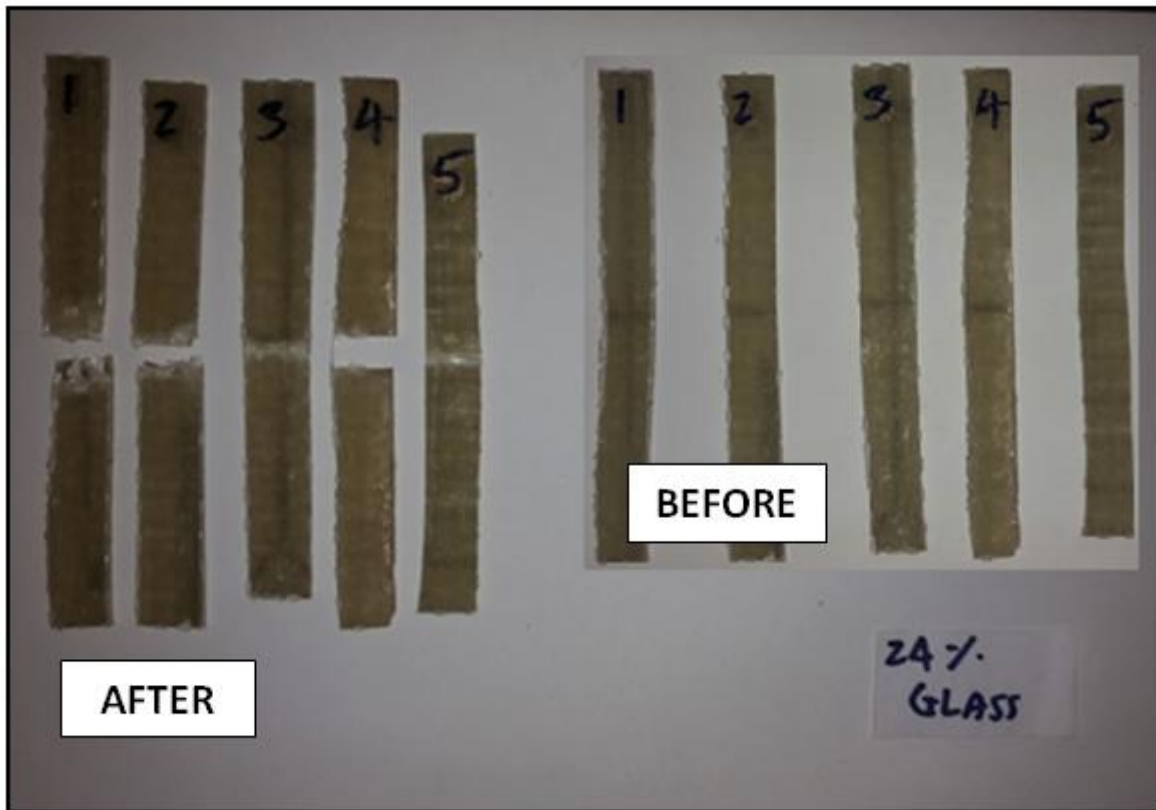


Figure A.9: 24% GRPC flexural samples

Table A.4: Tensile specimen observations for 32% GRPC

Specimen number	Dimensions		Tensile Strength [MPa]	Tensile Modulus [MPa]	Flexural Strength [MPa]	Flexural Modulus [MPa]
	Width Tensile [mm]	Width Flexural [mm]				
1	12.7	13.6	296.46	14280	247.8	9739.9
2	12.4	12.2	291.54	14809	280.74	10840
3	12.7	11.5	258.35	8341	271.54	9896
4	12.6	12.6	281.11	10788	231.7	9271
5	12.6	12	250.23	13319	204.33	10396
Mean	12.6	0.01	275.53	12307.4	247.22	8049.98
Standard Deviation	0.12	0.78	20.37	2702.47	30.80	4538.40

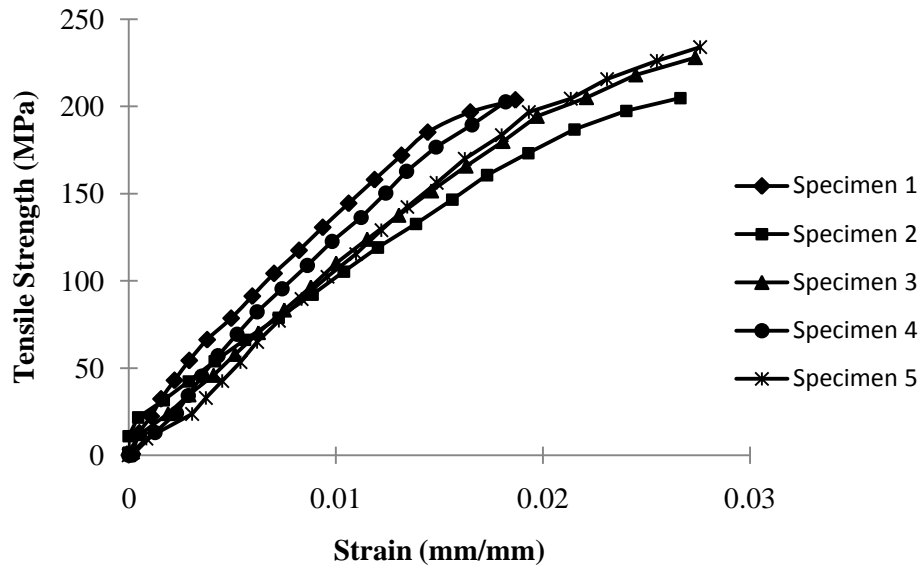


Figure A.10: Tensile strengths of 32% volume fraction glass fiber samples

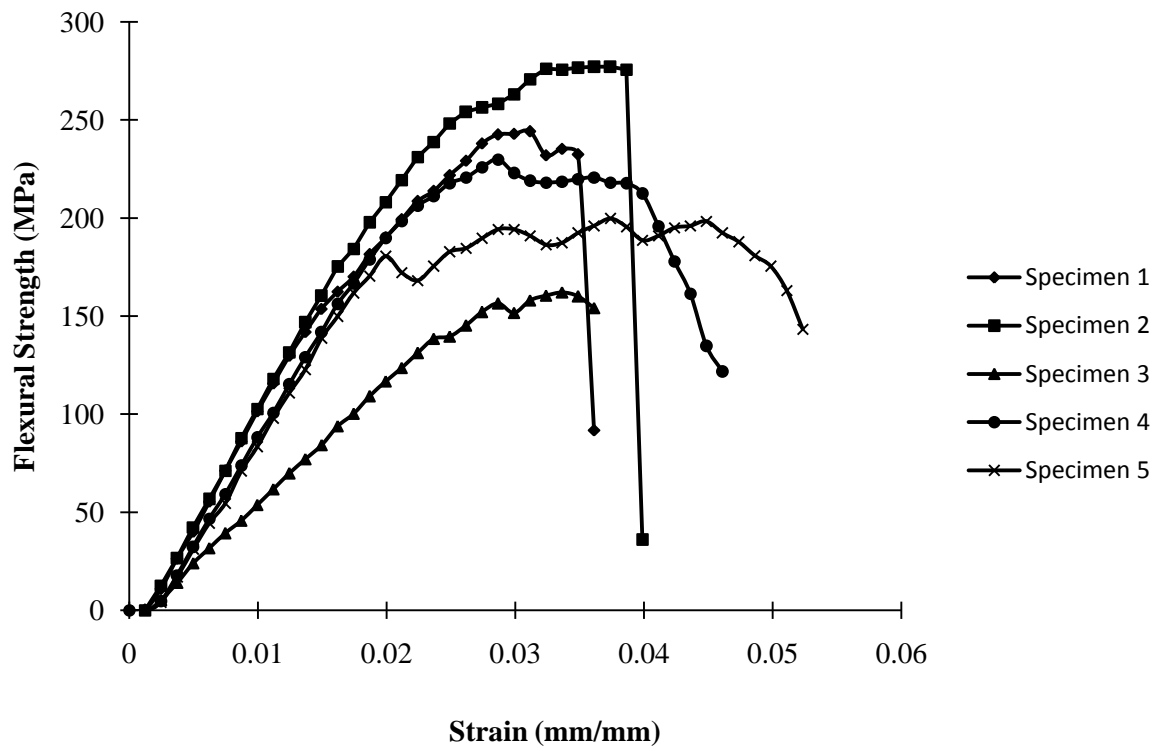


Figure A.11: Flexural strengths of 32% volume fraction glass fiber samples



Figure A.12: 32% GRPC flexural samples

Table A.5: Tensile specimen observations for 0.1% PAN/GRPC

Specimen number	Dimensions		Tensile Strength [MPa]	Tensile Modulus [MPa]	Flexural Strength [MPa]	Flexural Modulus [MPa]
	Width Tensile [mm]	Width Flexural [mm]				
1	13	12.2	236.54	11008	165.4	9858.6
2	12.8	13.4	199.93	17730	471.74	15008
3	11.7	10.3	180.07	9143	149.35	10754
4	12.9	11	217	9153	332.75	17176
5	12.9	12.7	236.33	9188	194.5	11317
Mean	12.66	12.5	213.974	11244.4	262.748	12822.72
Standard Deviation	0.541	0.64	24.31	3712.73	137.45	3124.87

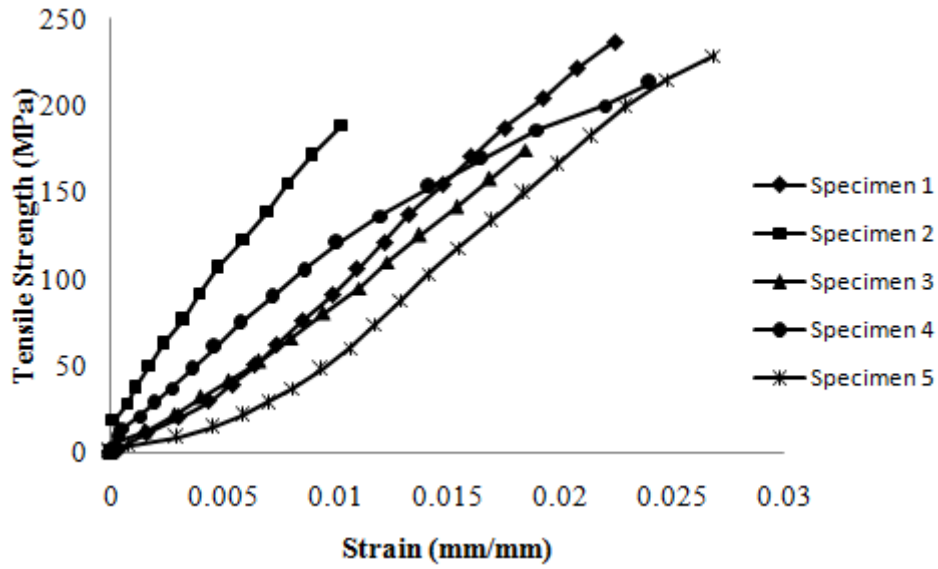


Figure A.13: Tensile strengths of 0.1% volume fraction PAN/GRPC samples

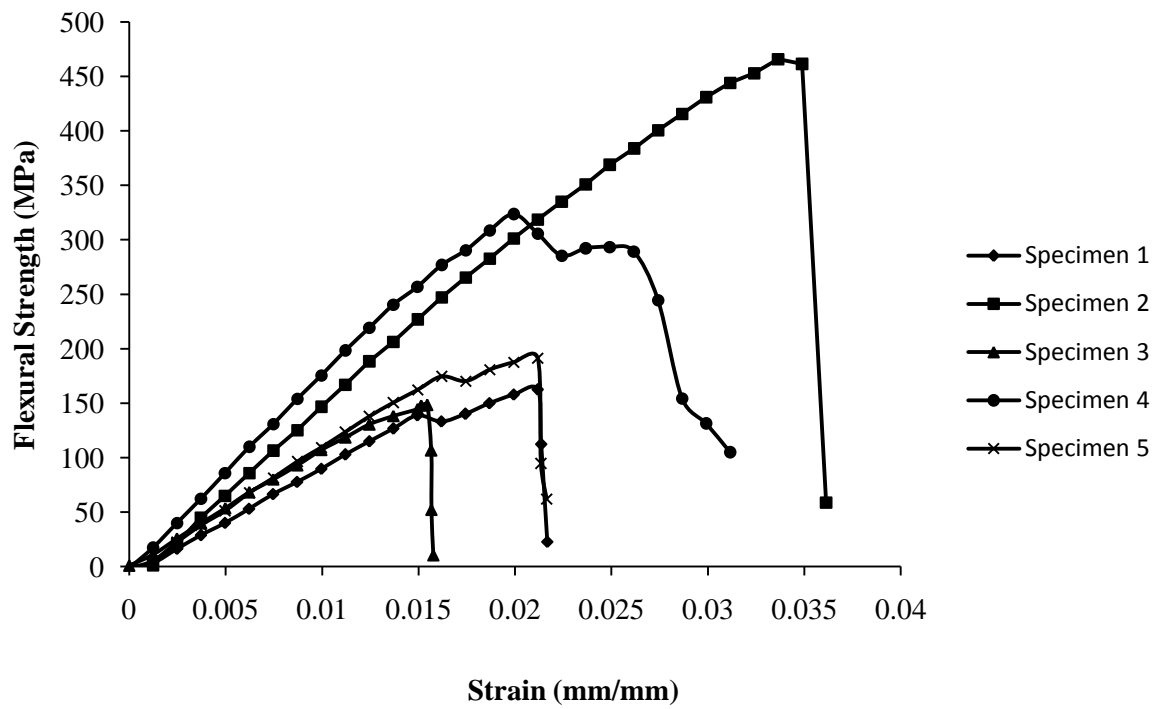


Figure A.14: Flexural strengths of 0.1% volume fraction PAN/GRPC samples

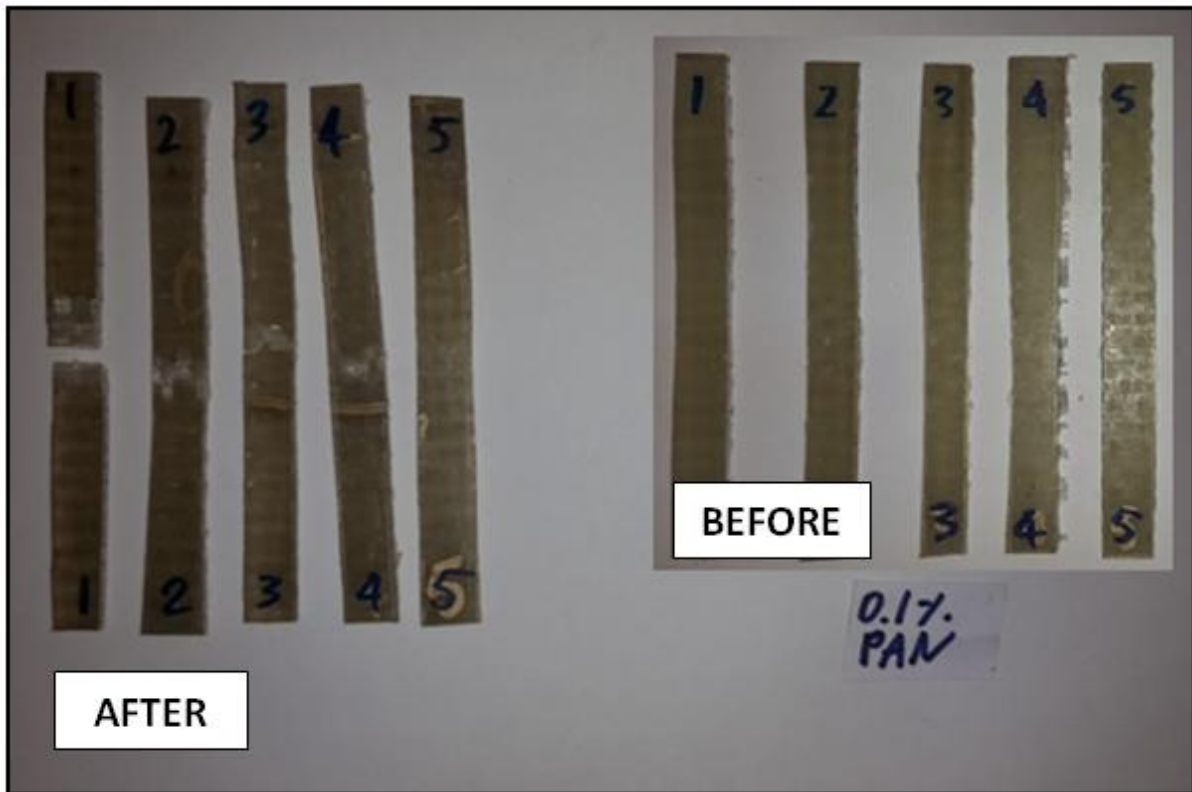


Figure A.15: 0.1% PAN/GRPC flexural samples

Table A.6: Tensile specimen observations for 0.2% PAN/GRPC

Specimen number	Dimensions		Tensile Strength [MPa]	Tensile Modulus [MPa]	Flexural Strength [MPa]	Flexural Modulus [MPa]
	Width Tensile [mm]	Width Flexural [mm]				
1	12.7	13	247.91	10504	393.3	12413
2	13	12.3	248.15	11259	414.4	12721
3	12.7	12.4	243.29	10341	414.54	13336
4	12.5	12.6	238.77	11044	413.64	13763
5	13	13.5	227.15	9939	421.5	13362
Mean	12.78	12.76	241.05	10617.4	411.47	13119
Standard Deviation	0.21	0.49	8.67	534.58	10.64	542.61

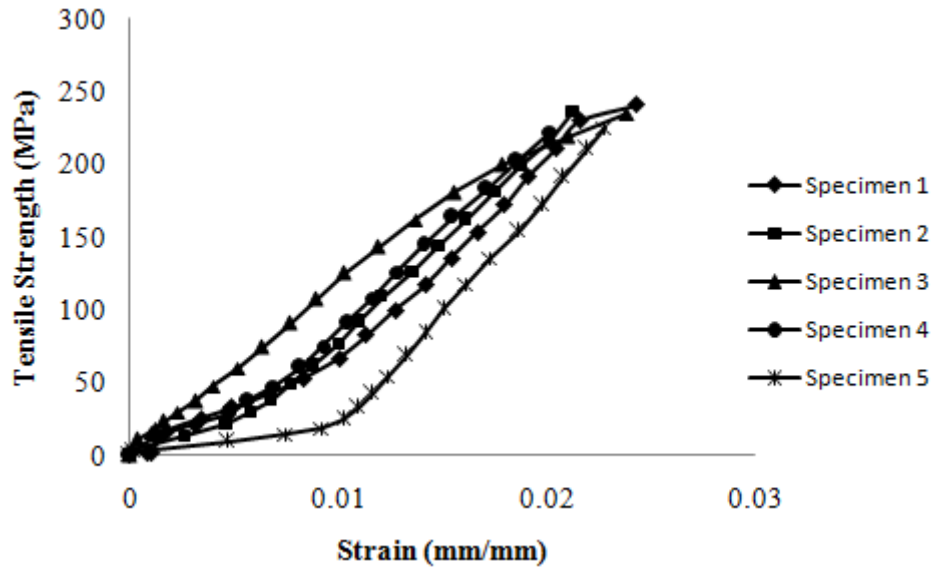


Figure A.16: Tensile strengths of 0.2% volume fraction PAN/GRPC samples

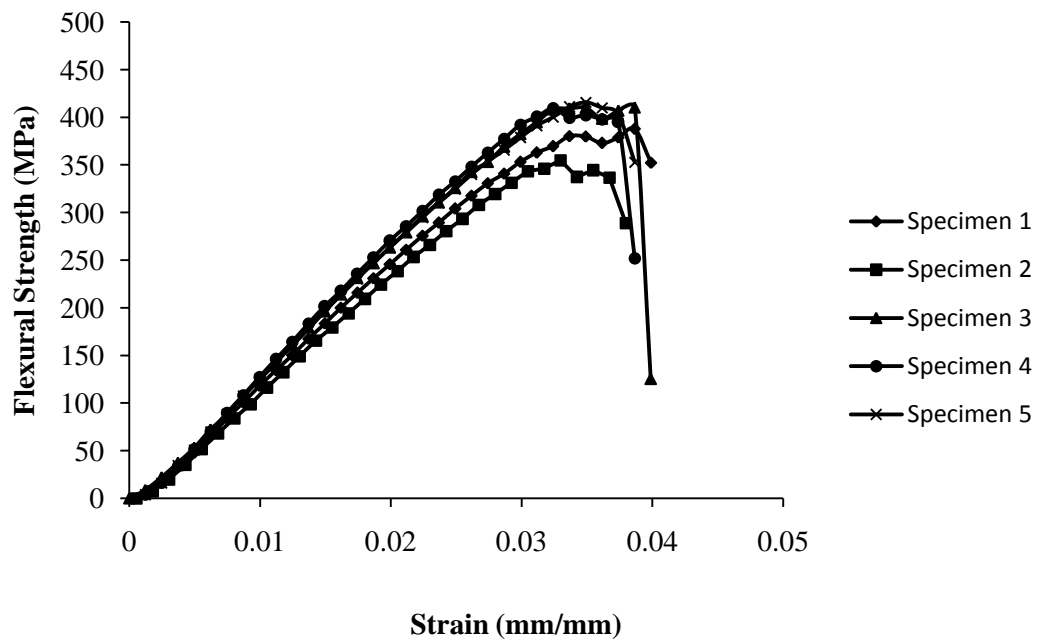


Figure A.17: Flexural strengths of 0.2% volume fraction PAN/GRPC samples



Figure A.18: 0.2% PAN/GRPC flexural samples

Table A.7: Tensile specimen observations for 0.5% PAN/GRPC

Specimen number	Dimensions		Tensile Strength [MPa]	Tensile Modulus [MPa]	Flexural Strength [MPa]	Flexural Modulus [MPa]
	Width Tensile [mm]	Width Flexural [mm]				
1	12.6	13	267.38	8395	281.72	12857
2	12.4	11.5	276.06	12757	542.1	20086
3	12.6	12.1	326.27	10396	445.4	18646
4	12.5	14.2	244.83	12805	449.9	20377
5	12.6	13.2			562.5	20555
Mean	12.54	12.8	278.63	11088.25	456.32	18504.2
Standard Deviation	0.089	1.04	34.37	2118.55	110.99	3245.23

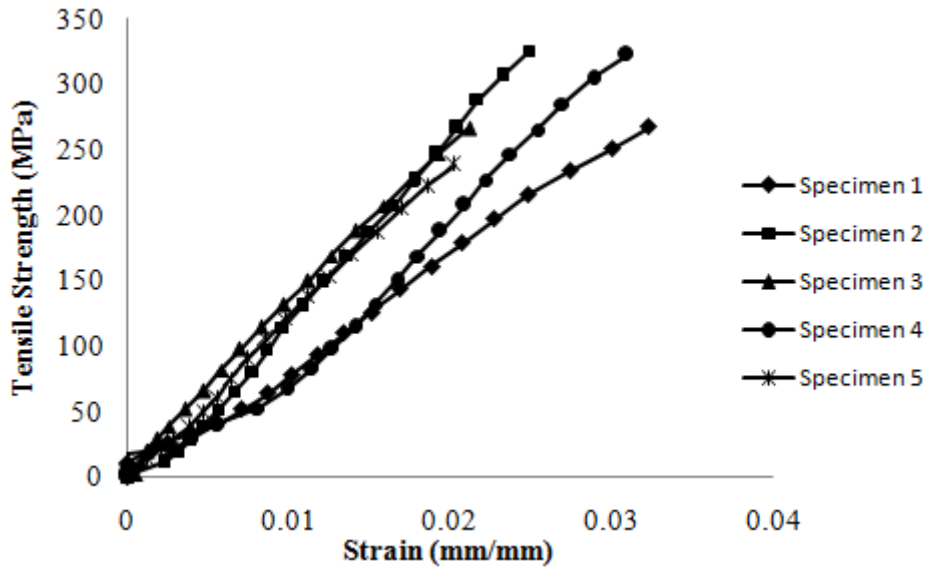


Figure A.19: Tensile strengths of 0.5% volume fraction PAN/GRPC samples

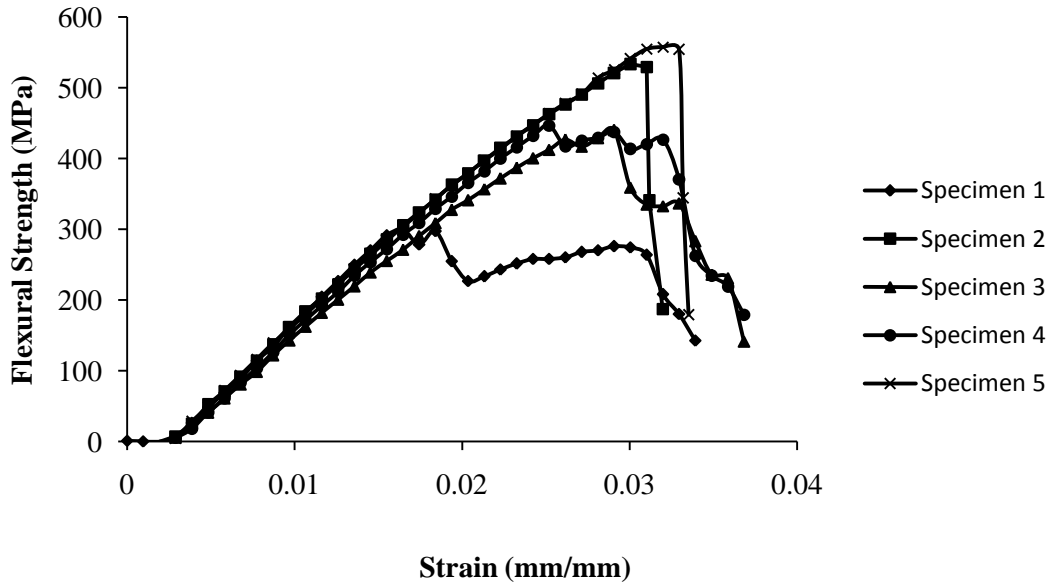


Figure A.20: Flexural strengths of 0.5% volume fraction PAN/GRPC samples



Figure A.21: 0.5% PAN/GRPC flexural samples

Table A.8: Tensile specimen observations for 0.5% ECNF embedded 0.1% PAN/GRPC

Specimen number	Dimensions		Tensile Strength [MPa]	Tensile Modulus [MPa]	Flexural Strength [MPa]	Flexural Modulus [MPa]
	Width Tensile [mm]	Width Flexural [mm]				
1	13.2	12.2	226.67	9675	465.3	15782
2	12.7	13.4	334.52	8354	475.1	16710
3	12.8	10.3	250.14	9536	447	18195
4	12.7	11	270.65	9764	465.6	17072
5	13.4	12.7	308	12191	447.9	17096
Mean	12.96	11.92	277.99	9904	460.18	16971
Standard Deviation	0.32	1.25	43.47	1400.02	12.27	866.86

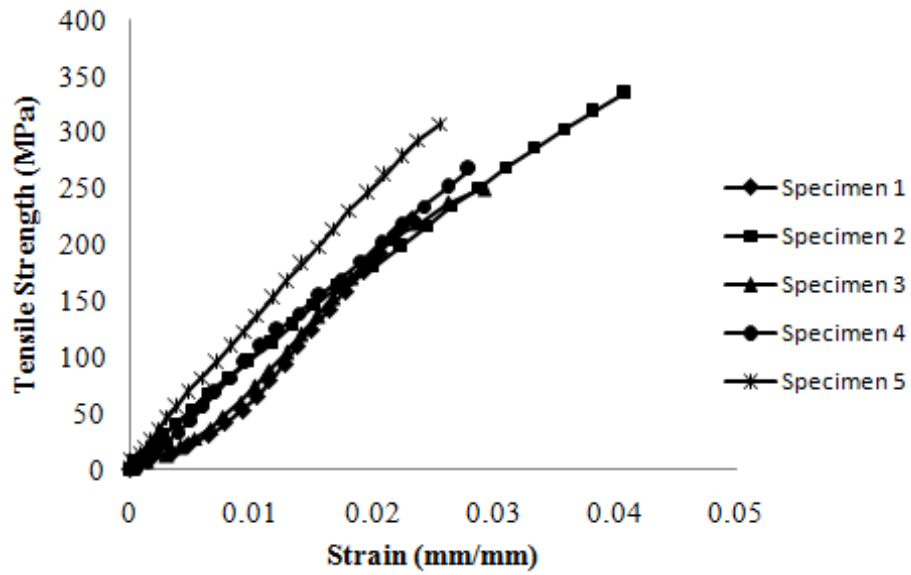


Figure A.22: Tensile strengths of 0.1% volume fraction PAN/GRPC samples reinforced with 0.5% ECNF

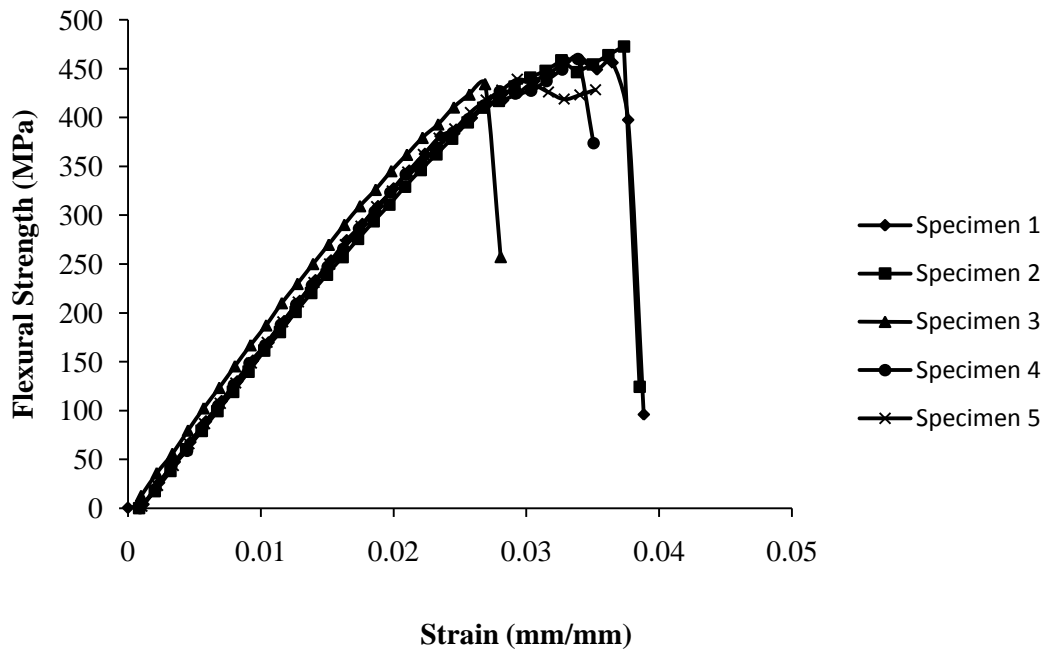


Figure A.23: Flexural strengths of 0.1% volume fraction PAN/GRPC samples reinforced with 0.5% ECNF

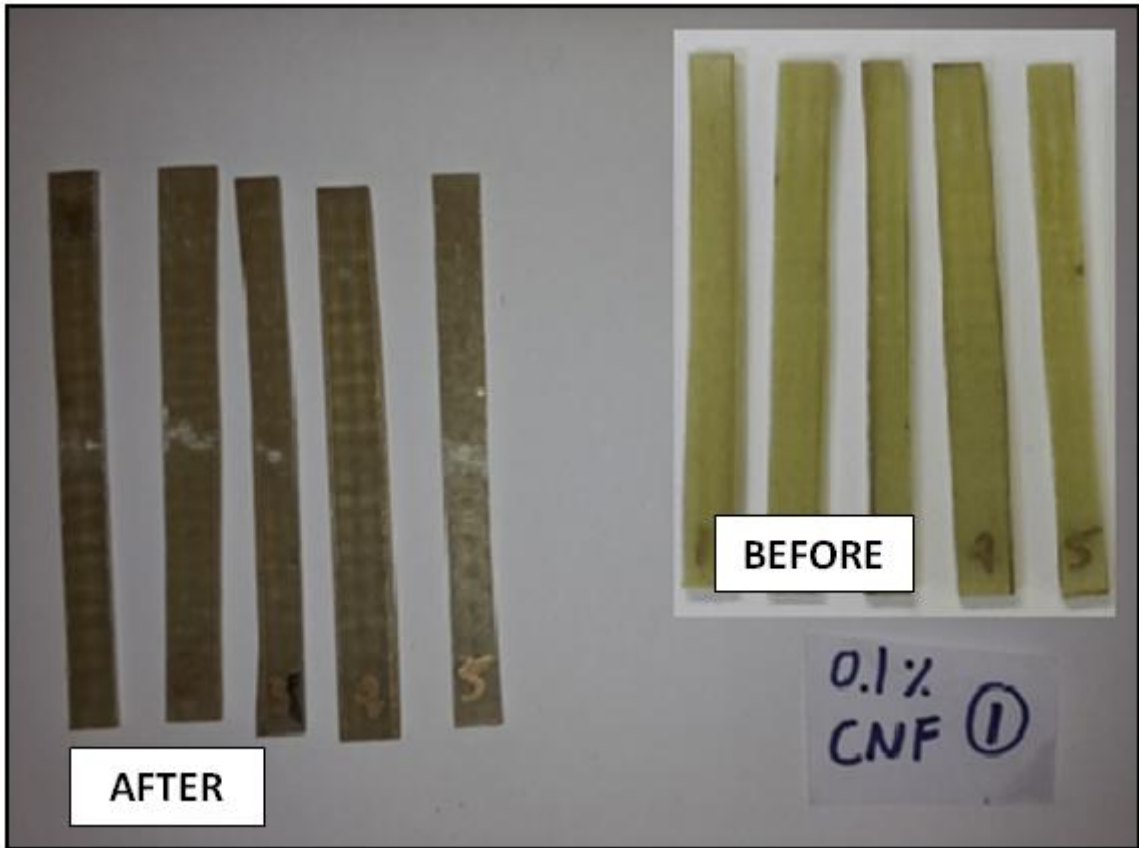


Figure A.24: 0.5% ECNF embedded 0.1% PAN/GRPC flexural samples

Table A.9: Tensile specimen observations for 0.5% ECNF embedded 0.2% PAN/GRPC

Specimen number	Dimensions		Tensile Strength [MPa]	Tensile Modulus [MPa]	Flexural Strength [MPa]	Flexural Modulus [MPa]
	Width Tensile [mm]	Width Flexural [mm]				
1	12.9	11.3	294.98	14407	463	16886
2	13	12.9	260.65	13711	443.9	16352
3	12.7	11.7	323.87	14788	451.5	17431
4	13	12.7	281.49	12115	490.7	17006
5	13.5	11.3	331.24	16895	475.6	16538
Mean	13.02	11.98	298.44	14383.2	464.94	16842.6
Standard Deviation	0.29	0.76	29.36	1737.10	18.73	420.79

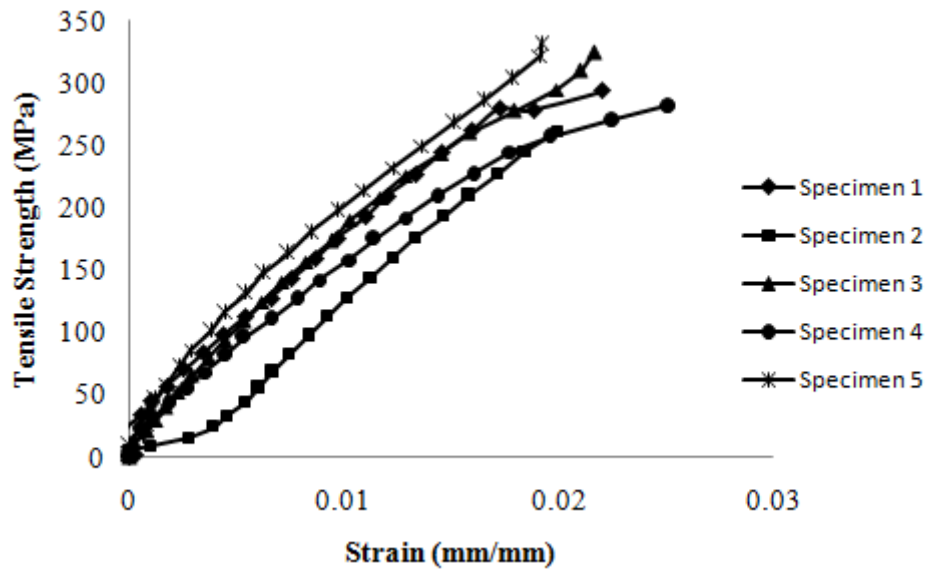


Figure A.25: Tensile strengths of 0.2% volume fraction PAN/GRPC samples reinforced with 0.5% ECNF

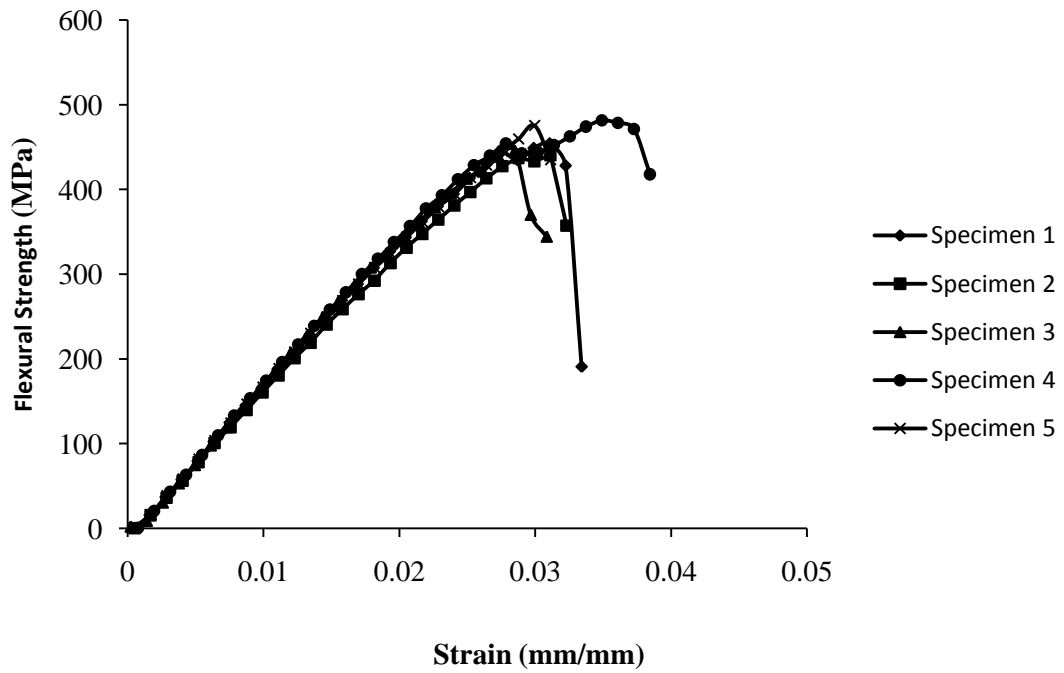


Figure A.26: Flexural strengths of 0.2% volume fraction PAN/GRPC samples reinforced with 0.5% ECNF

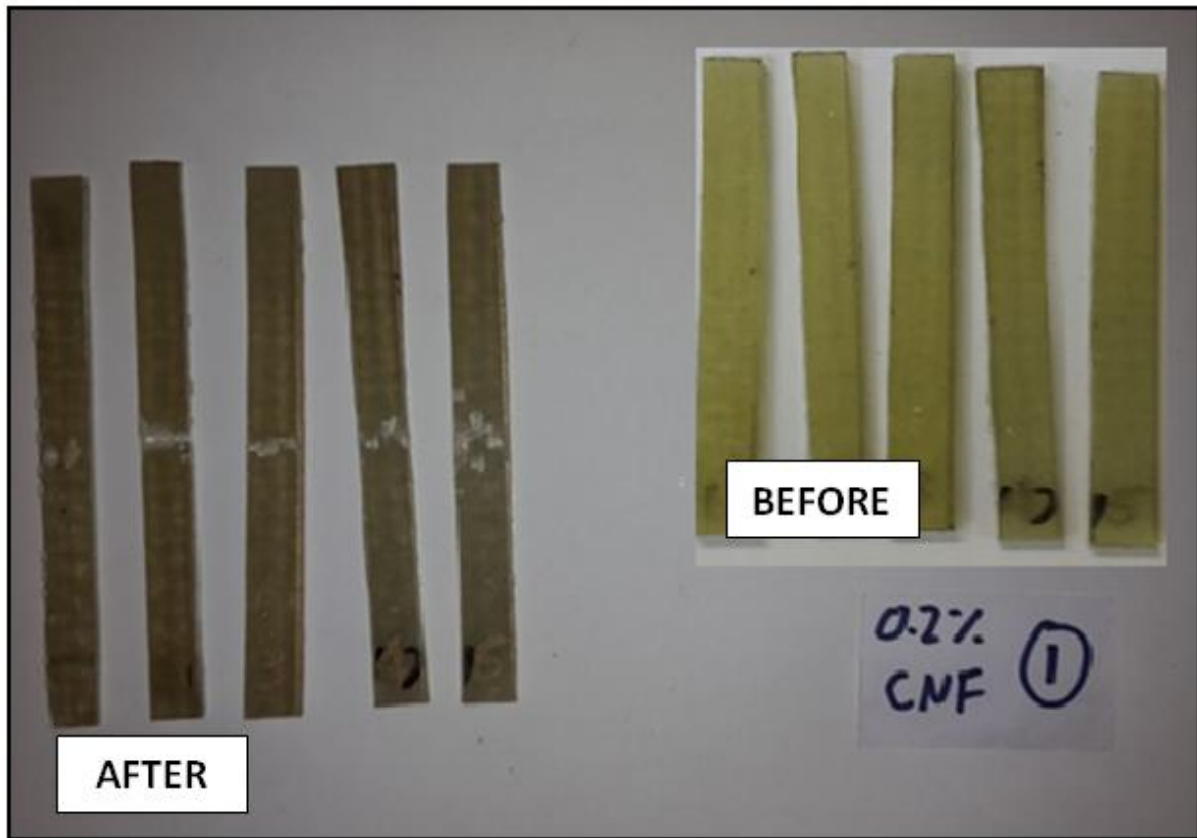


Figure A.27: 0.5% ECNF embedded 0.2% PAN/GRPC flexural samples

Table A.10: Tensile specimen observations for 0.5% ECNF embedded 0.5% PAN/GRPC

Specimen number	Dimensions		Tensile Strength [MPa]	Tensile Modulus [MPa]	Flexural Strength [MPa]	Flexural Modulus [MPa]
	Width Tensile [mm]	Width Flexural [mm]				
1	13.1	11.8	307.7	15147	437.7	18765
2	13	12.4	325.12	8206	451.3	15734
3	12.7	11.9	311.84	8060	480.1	17725
4	13.1	11.8	308.34	9867	476.4	17479
5	13.2	11.5	318.45	8526	512.9	18008
Mean	13.02	11.88	314.29	9961.2	471.68	17542.2
Standard Deviation	0.19	0.32	7.40	2985.65	28.99	1120.17

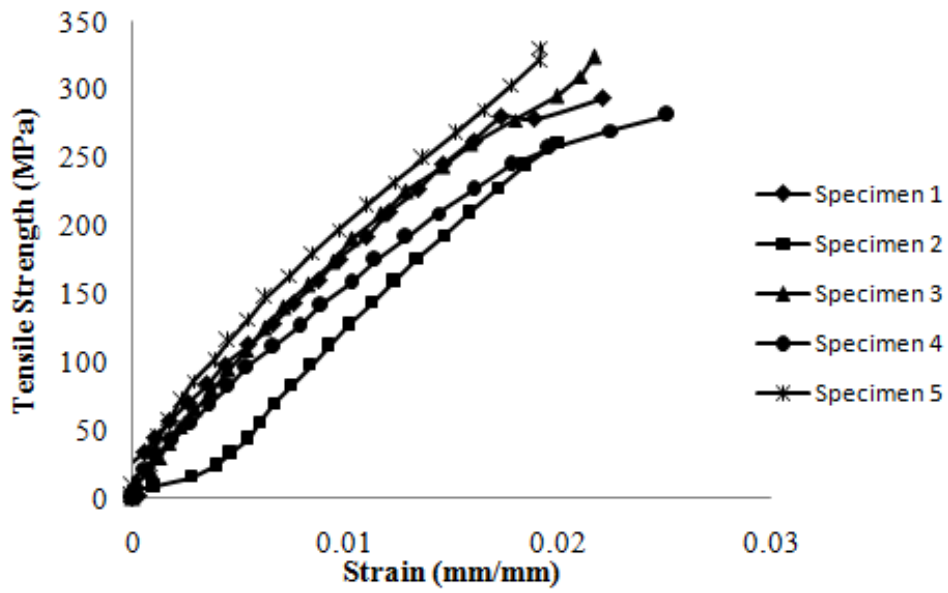


Figure A.28: Tensile strengths of 0.5% volume fraction PAN/GRPC samples reinforced with 0.5% ECNF

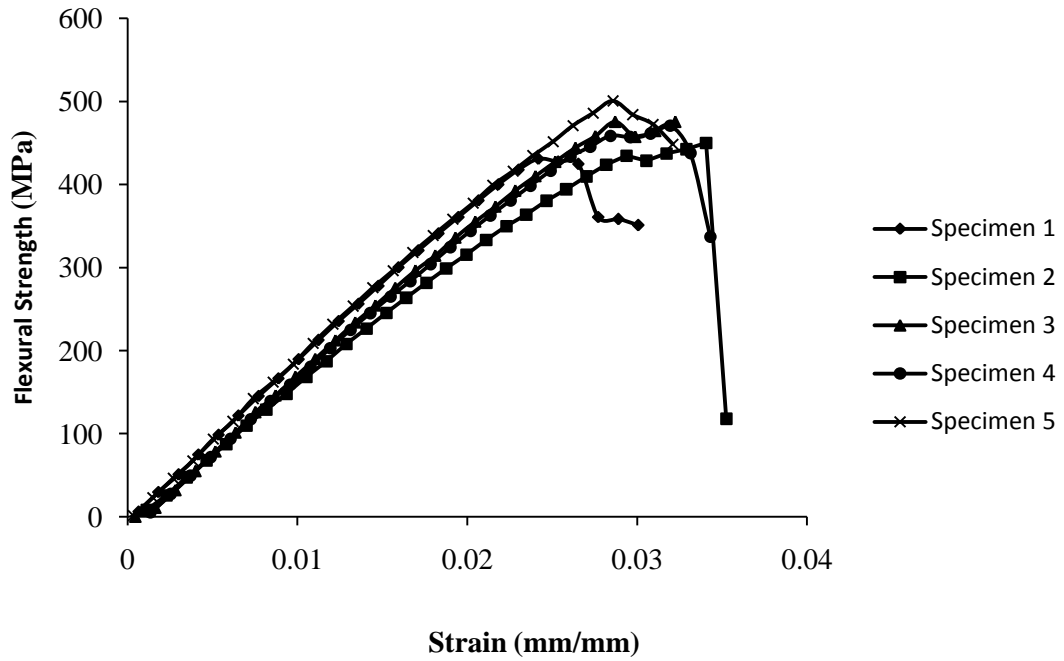


Figure A.29: Flexural strengths of 0.5% volume fraction PAN/GRPC samples reinforced with 0.5% ECNF

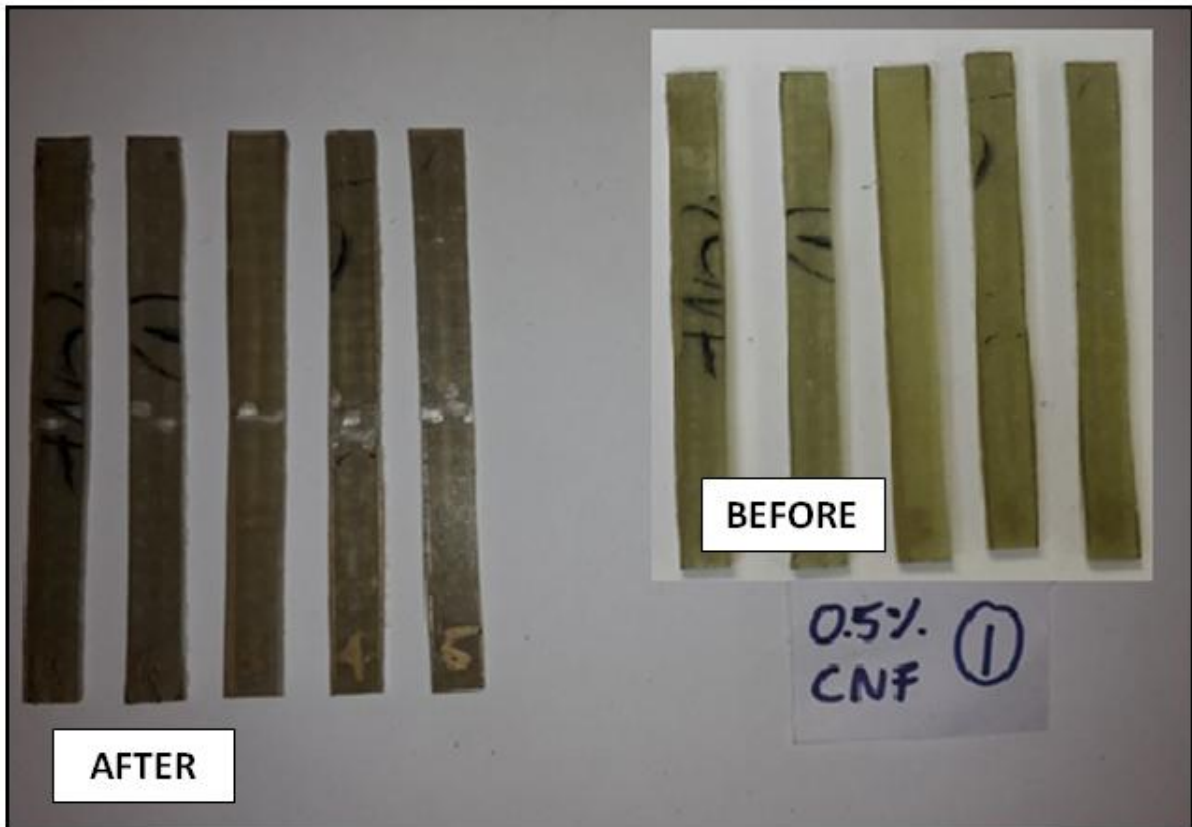


Figure A.30: 0.5% ECNF embedded 0.5% PAN/GRPC flexural samples

Table A.11: Tensile specimen observations for 1.0% ECNF embedded 0.1% PAN/GRPC

Specimen number	Dimensions		Tensile Strength [MPa]	Tensile Modulus [MPa]	Flexural Strength [MPa]	Flexural Modulus [MPa]
	Width Tensile [mm]	Width Flexural [mm]				
1	13	13.4	318.2	10393	475.6	19803
2	13.4	13	305.27	11536	403.5	20992
3	13	11	332.64	11949	488	22768
4	13.1	11.1	308.75	10125	415.34	22314
5	13.3	11.6			494.14	22524
Mean	13.16	12.02	316.21	11000.75	455.31	21680.2
Standard Deviation	0.18	1.10	12.23	879.76	42.63	1254.44

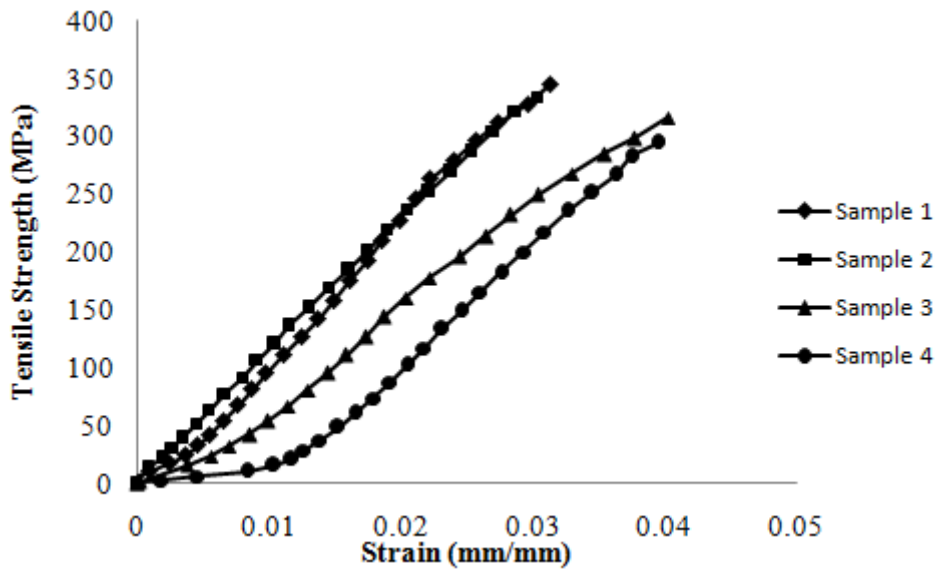


Figure A.31: Tensile strengths of 0.1% volume fraction PAN/GRPC samples reinforced with 1.0% ECNF

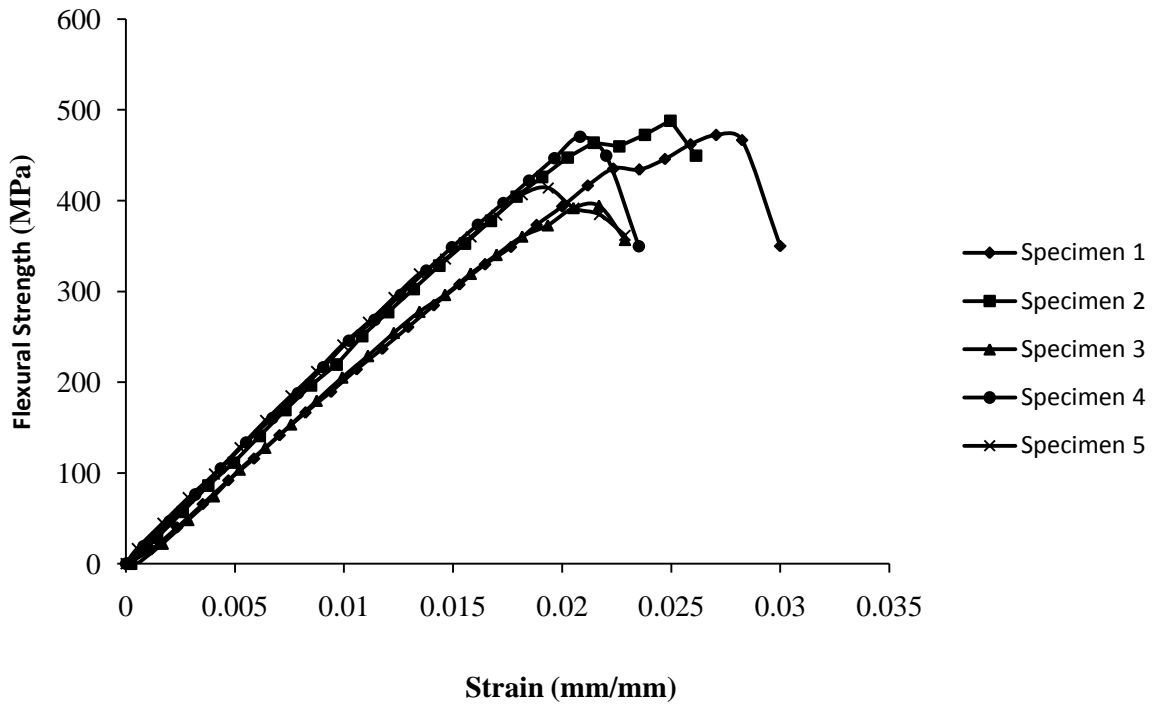


Figure A.32: Flexural strengths of 0.1% volume fraction PAN/GRPC samples reinforced with 1.0% ECNF

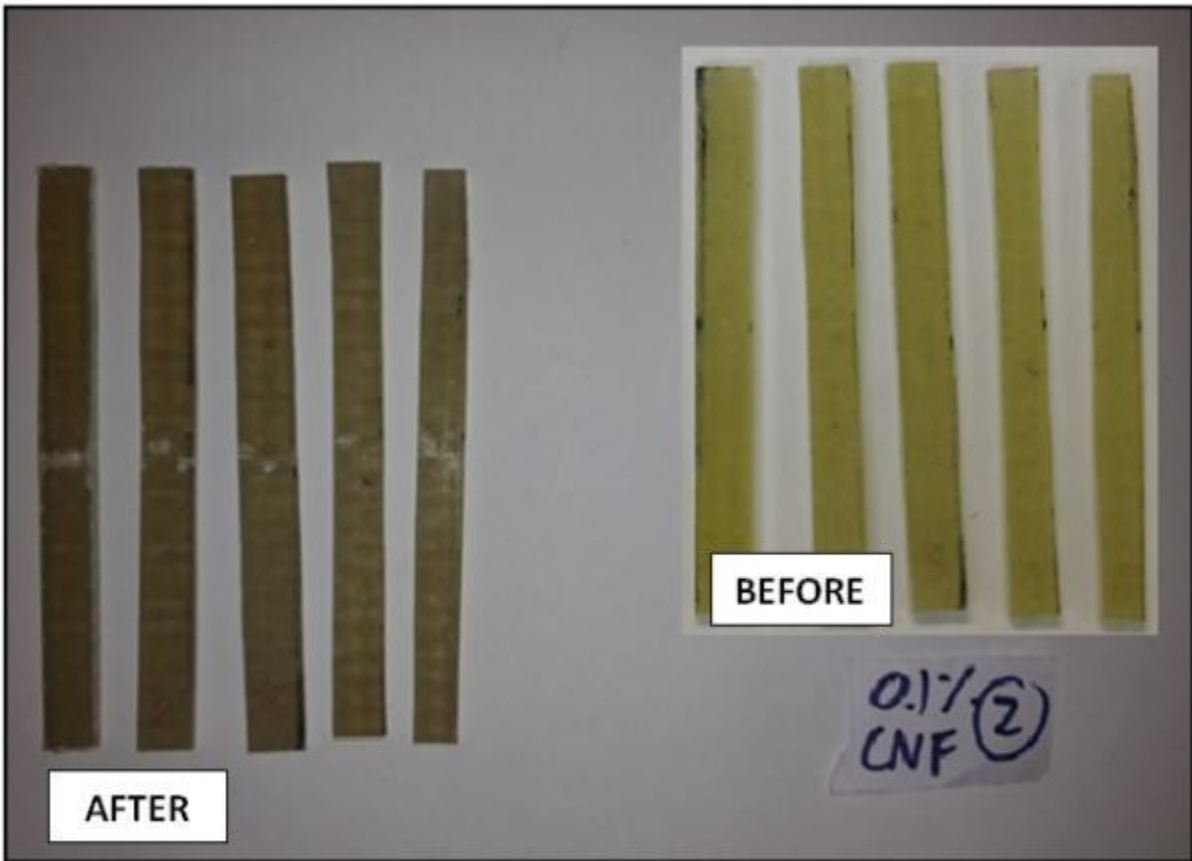


Figure A.33: 0.5% ECNF embedded 0.1% PAN/GRPC flexural samples

Table A.12: Tensile specimen observations for 1.0% ECNF embedded 0.2% PAN/GRPC

Specimen number	Dimensions		Tensile Strength [MPa]	Tensile Modulus [MPa]	Flexural Strength [MPa]	Flexural Modulus [MPa]
	Width Tensile [mm]	Width Flexural [mm]				
1	13.5	12.5	354.52	11610	457.6	18257
2	13.4	11.1	333.94	11175	450.3	18576
3	12.7	12	319.83	8465	473.6	17682
4	13.2	12.9	299.35	8333	476.8	18675
5	12.9	12.1			454.4	18112
Mean	13.14	12.12	326.91	9895.75	462.54	18260.4
Standard Deviation	0.33	0.67	23.24	1738.23	11.89	396.25

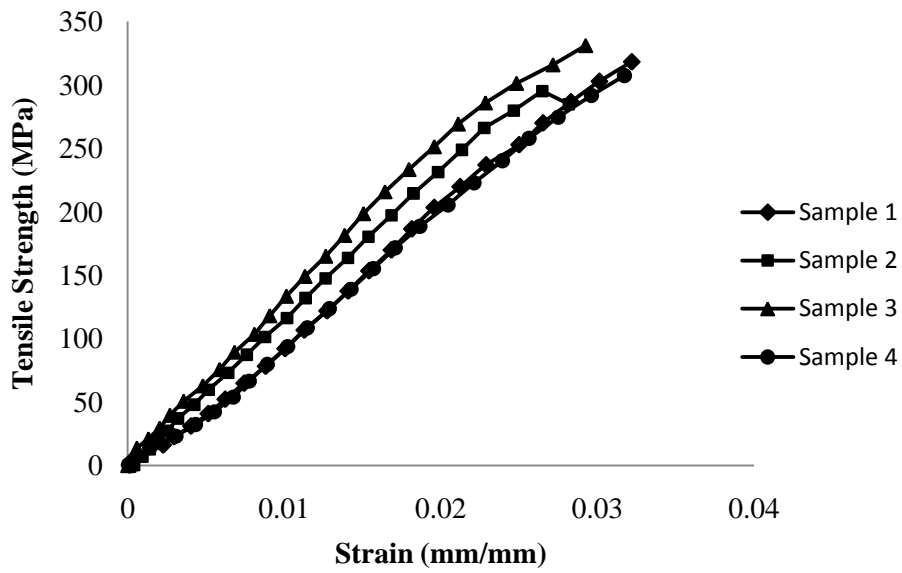


Figure A.34: Tensile strengths of 0.2% volume fraction PAN/GRPC samples reinforced with 1.0% ECNF

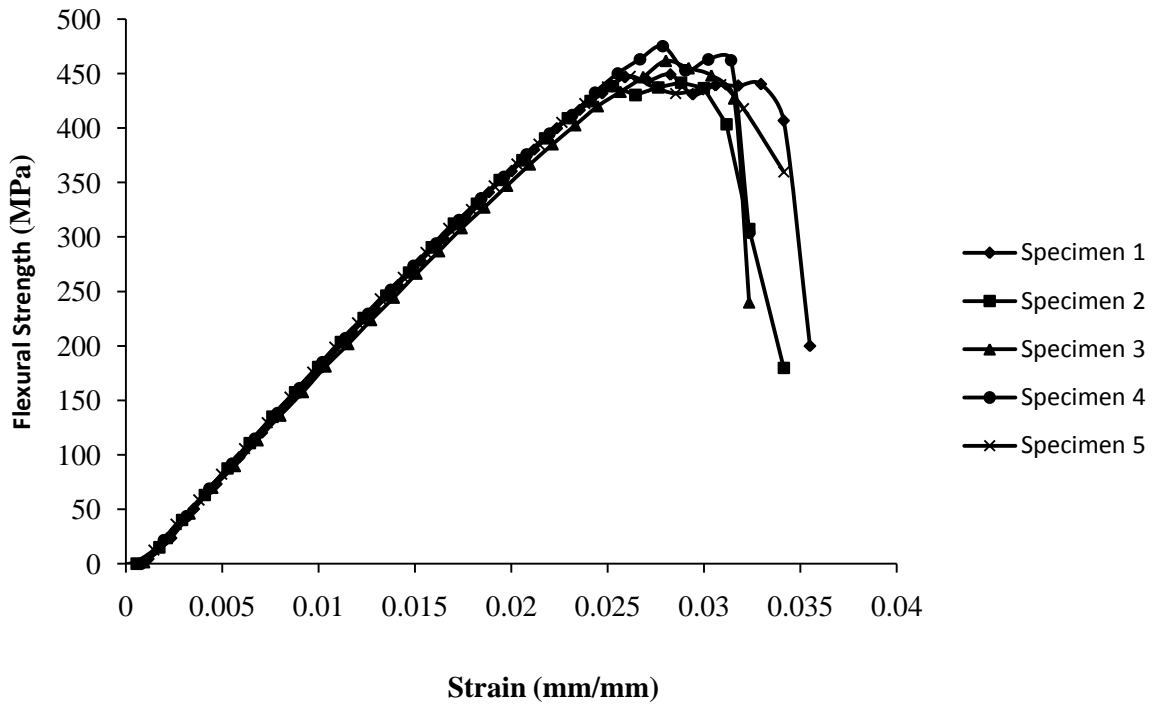


Figure A.35: Flexural strengths of 0.2% volume fraction PAN/GRPC samples reinforced with 1.0% ECNF

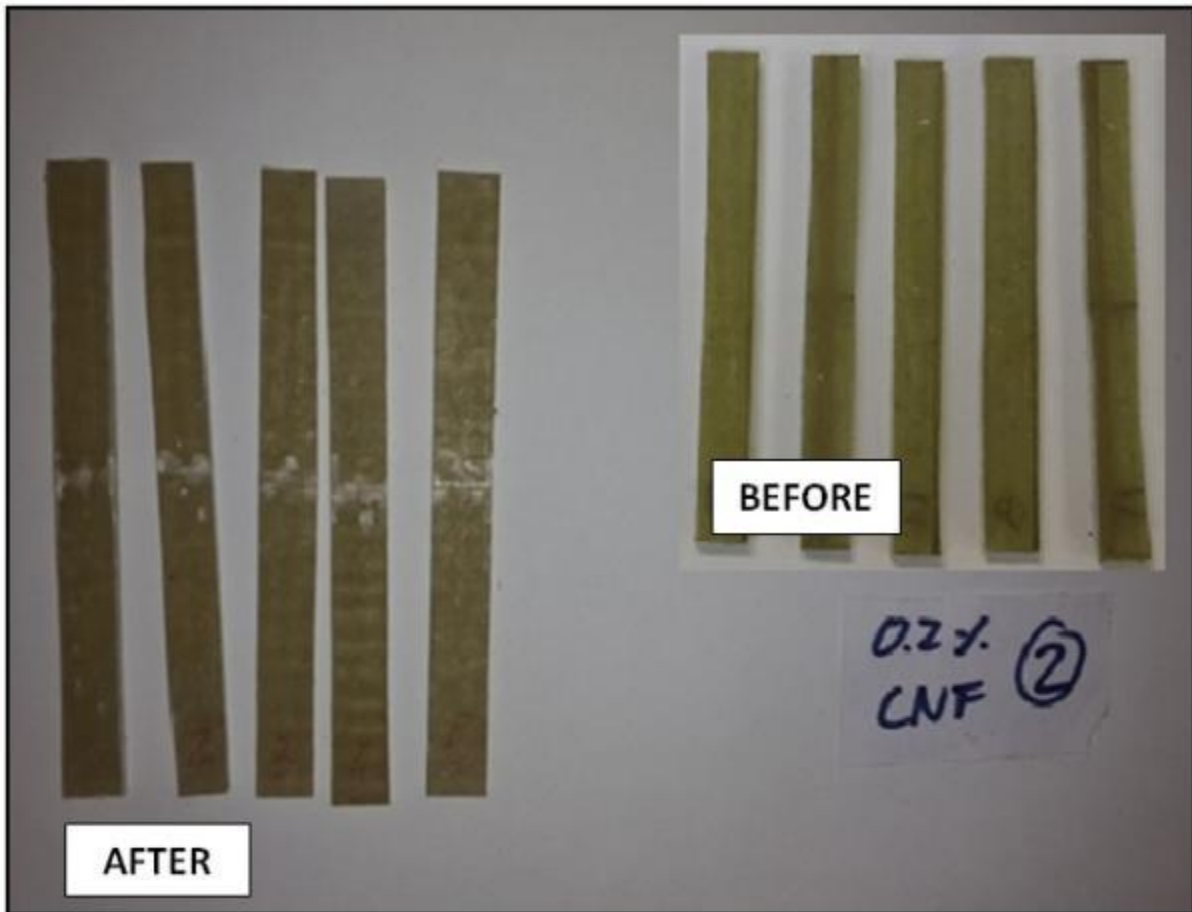


Figure A.36: 1% ECNF embedded 0.2% PAN/GRPC flexural samples

Table A.13: Tensile specimen observations for 1.0% ECNF embedded 0.5% PAN/GRPC

Specimen number	Dimensions		Tensile Strength [MPa]	Tensile Modulus [MPa]	Flexural Strength [MPa]	Flexural Modulus [MPa]
	Width Tensile [mm]	Width Flexural [mm]				
1	12.8	13	400.77	10496	449.9	18224
2	13.1	12	346.85	9808	480.75	18377
3	13.2	12.2	386.6	14370	471.4	18100
4	13.3	13.5	346.64	17118	469.8	17626
5	13	11.8			519.7	19331
Mean	13.08	12.5	370.21	12948	478.31	18331.6
Standard Deviation	0.19	0.72	27.71	3429.42	25.7215	625.28

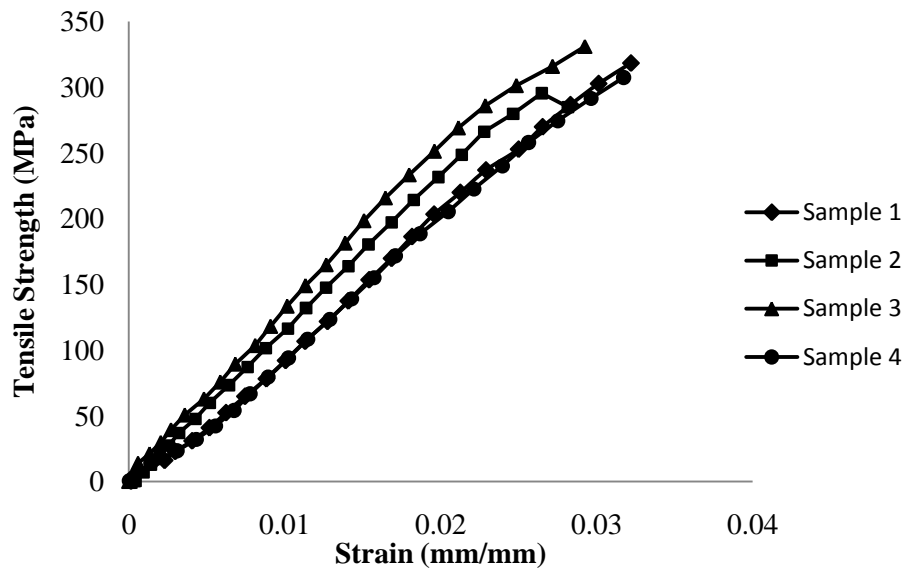


Figure A.37: Tensile strengths of 0.5% volume fraction PAN/GRPC samples reinforced with 1.0% ECNF

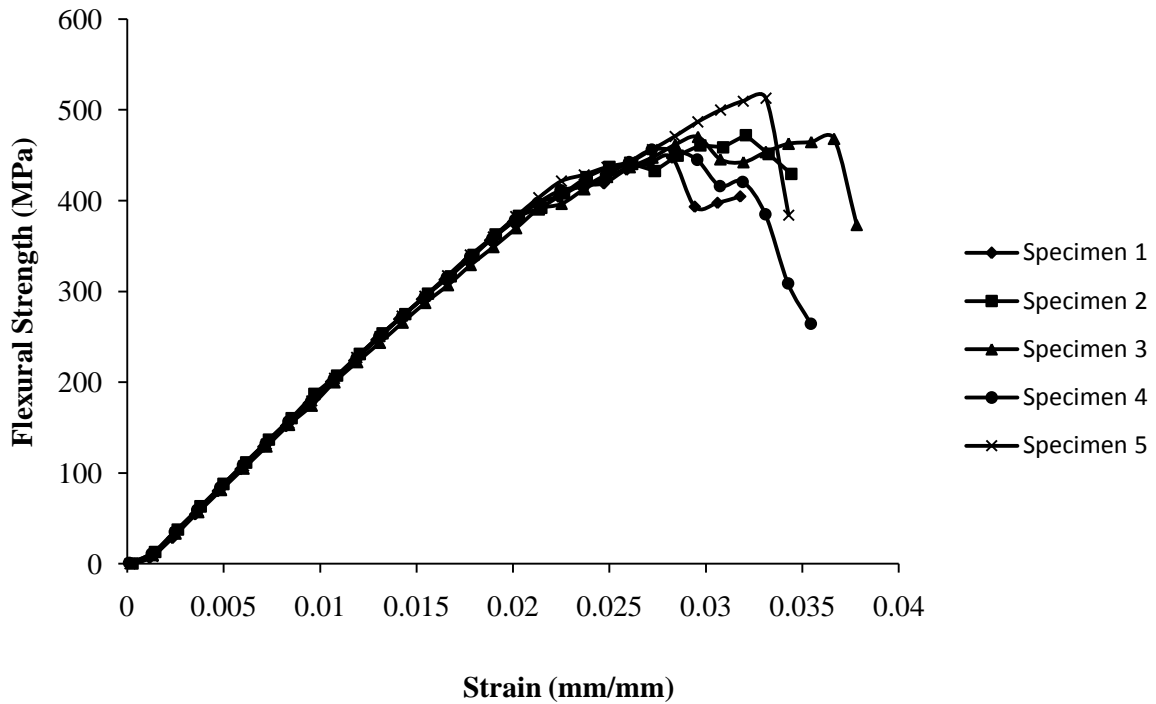


Figure A.38: Flexural strengths of 0.5% volume fraction PAN/GRPC samples reinforced with 1.0% ECNF

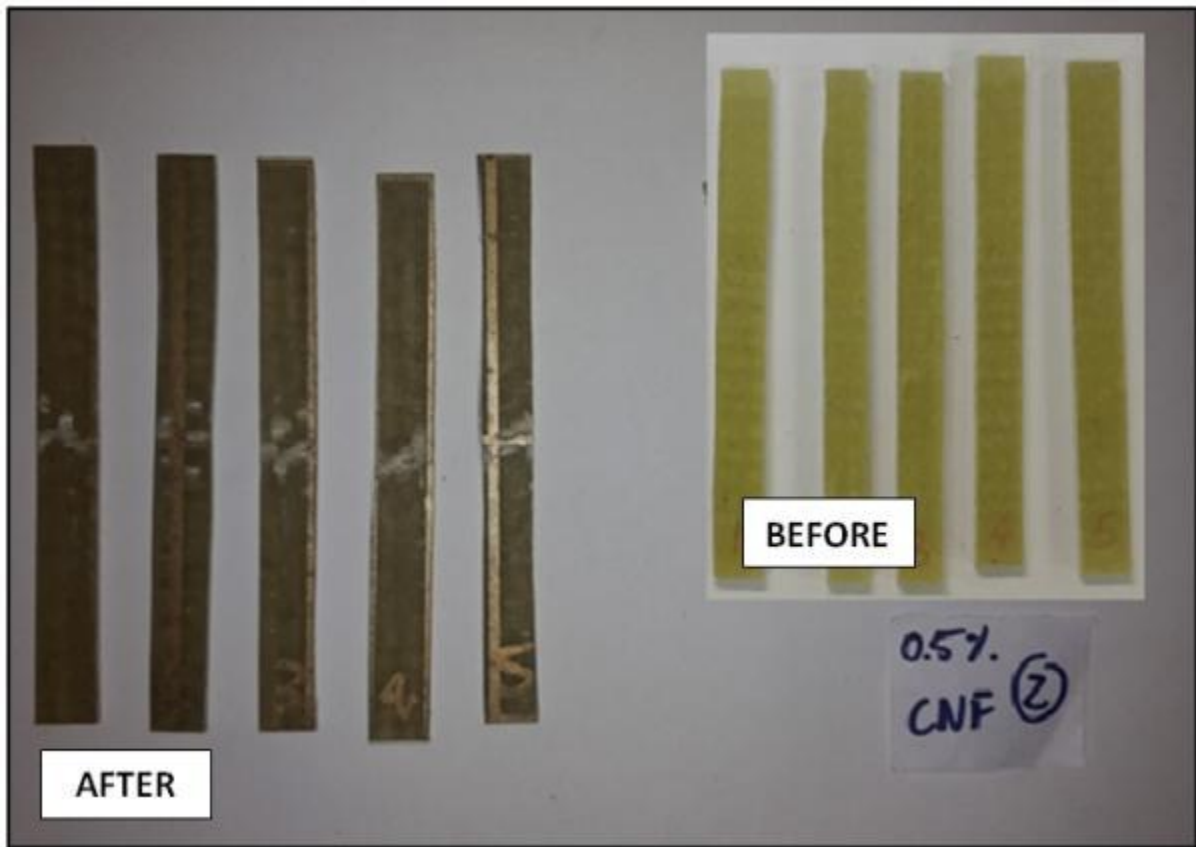


Figure A.39: 1% ECNF embedded 0.5% PAN/GRPC flexural samples

A.2 Impact Testing

The Avery impact testing machine was used to test the impact test specimens and unlike the other test methods the data was all recorded manually. Firstly, Table 9.14 below shows the measured readings that were taken during the calibration test prior to specimen testing so as to determine the gauge correction factor for the machine.

Table A.14: Measured readings during calibration test

Test run	Reading [J]
1	0.125
2	0.110
3	0.105
4	0.110
5	0.115
6	0.110
7	0.115
8	0.100

9	0.110
10	0.115

The two sets of data that needed to be manually recorded for the impact testing was the width and thickness of each test specimen, measured at three points along its gauge length as per the ASTM standards, and the excess energy readings provided for by the Avery machine. The data was recorded as shown in Table A.15 for all of the test specimens. Note that the width and thickness shown here is the average of the three readings along the gauge length of the samples.

Table A.15: Impact specimen observations for all Glass fiber volume fractions of the composite

Volume Fraction Glass Fiber [%]	Sample No.	Dimensions		Energy Absorption (J/mm ²)
		Width [mm]	Thickness [mm]	
0	1	12	3.46	2.45
0	2	10.9	3.58	1.34
0	3	11.8	3.41	2.49
0	4	11.9	3.61	1.23
0	5	12	3.57	2.45
16	1	11.1	3.61	64.91
16	2	12.8	3.56	65.48
16	3	12.5	3.42	70.58
16	4	10.4	3.75	65.04
16	5	11.7	3.44	61.58
24	1	12	3.72	102.94
24	2	12.1	3.50	102.09
24	3	11.5	3.68	86.95
24	4	12.2	3.53	101.25
24	5	12	3.83	83.33
32	1	10.6	3.82	94.33
32	2	11.6	3.46	98.88
32	3	11	3.34	97.59
32	4	11.6	3.47	106.49
32	5	10.8	3.77	95.31

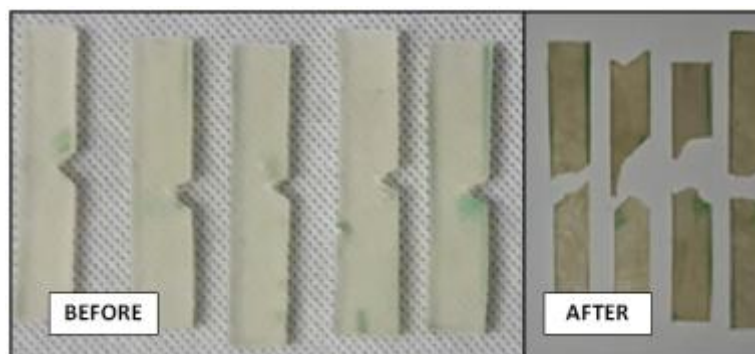


Figure A.40: Neat impact samples

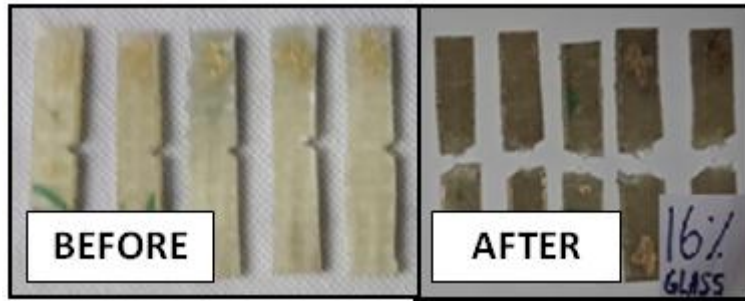


Figure A.41: 16% volume fraction GRPC samples

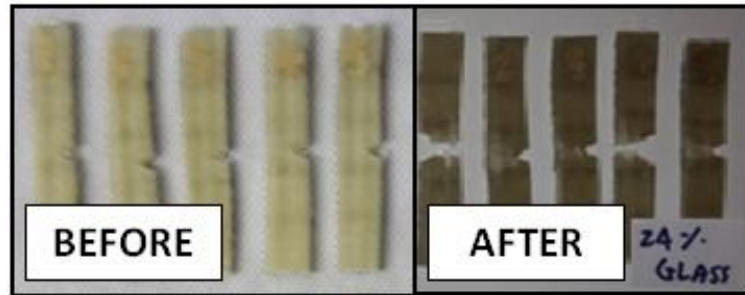


Figure A.42: 24% volume fraction GRPC samples

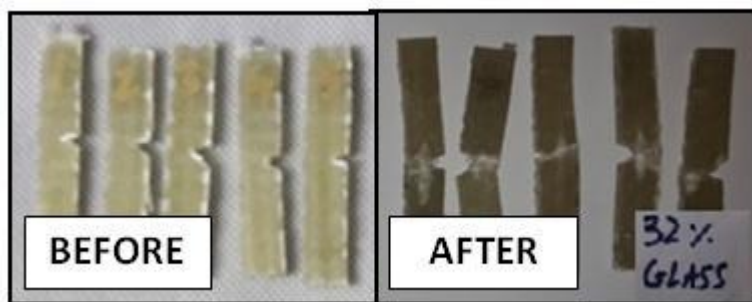


Figure A.43: 32% volume fraction GRPC samples

Table A.16: Impact specimen observations for all PAN volume fractions of the composite

Volume Fraction PAN Fiber [%]	Sample No.	Dimensions		Energy Absorption (J/mm ²)
		Width [mm]	Thickness [mm]	
0.1	1	10.6	3.46	99.88
0.1	2	10.9	3.58	98.48
0.1	3	10	3.41	100
0.1	4	10	3.61	92.64
0.1	5	10.5	3.57	112.04
0.2	1	11.2	3.61	108.98
0.2	2	10	3.56	95.58
0.2	3	10.3	3.42	101.37
0.2	4	10.6	3.75	115.14
0.2	5	11.3	3.44	108.01
0.5	1	10.6	3.72	115.14

0.5	2	10	3.50	111.76
0.5	3	9.9	3.68	105.46
0.5	4	11.5	3.53	106.13
0.5	5	11.4	3.83	107.06

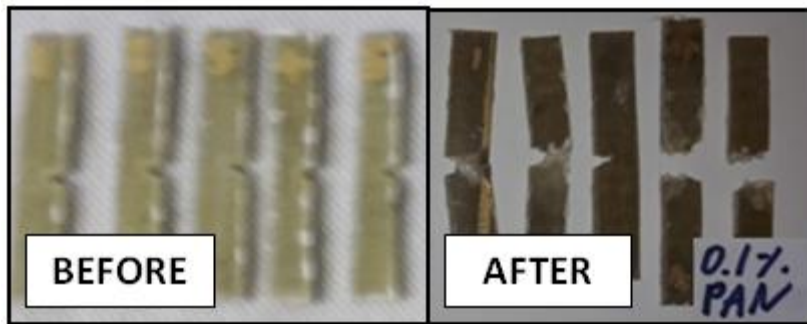


Figure A.44: 0.1% PAN reinforced GFPC samples

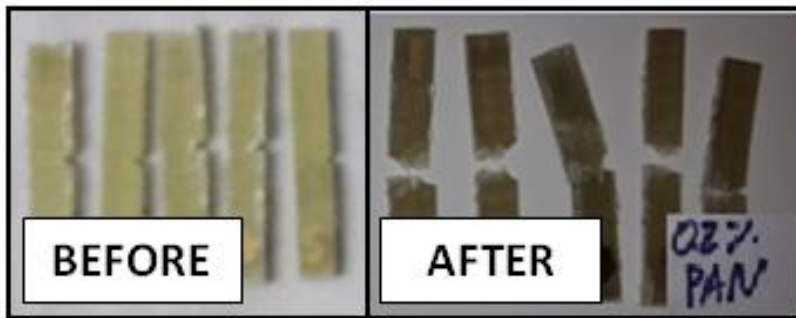


Figure A.45: 0.2% PAN reinforced GFPC samples

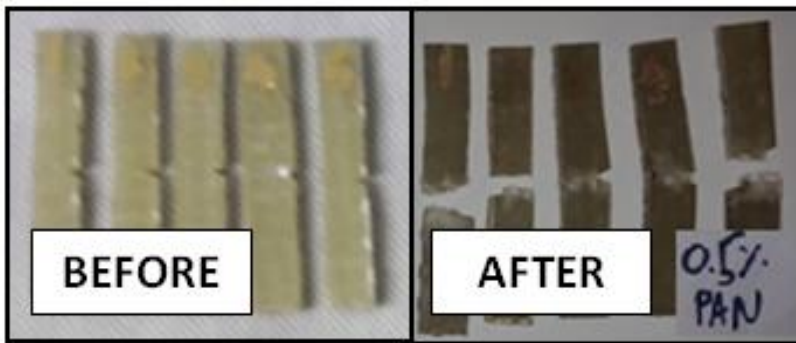


Figure A.46: 0.5% PAN reinforced GFPC samples

Table A.17: Impact specimen observations for all 0.5% ECNF volume fractions of the composite

Volume Fraction ECNF [%]	Volume Fraction PAN Fiber [%]	Sample No.	Dimensions		Energy Absorption (J/mm ²)
			Width [mm]	Thickness [mm]	
0.5	0.1	1	10	3.46	106.67
0.5	0.1	2	8.7	3.58	99.61

0.5	0.1	3	10.2	3.41	114.37
0.5	0.1	4	9.5	3.61	91.22
0.5	0.1	5	8.7	3.57	91.95
0.5	0.2	1	9.2	3.61	99.63
0.5	0.2	2	9.5	3.56	110.52
0.5	0.2	3	8.2	3.42	113.82
0.5	0.2	4	9.4	3.75	97.51
0.5	0.2	5	9.6	3.44	116.31
0.5	0.5	1	9.5	3.72	145.61
0.5	0.5	2	8.7	3.50	103.44
0.5	0.5	3	9.2	3.68	94.20
0.5	0.5	4	9.5	3.53	98.24
0.5	0.5	5	10.4	3.83	105.76
1	0.1	1	9.9	3.82	124.57
1	0.1	2	9.8	3.46	85.03
1	0.1	3	10.1	3.34	95.70
1	0.1	4	9.9	3.47	102.69
1	0.1	5	11	3.77	127.27
1	0.2	1	10	3.43	96.66
1	0.2	2	9.1	3.51	135.53
1	0.2	3	9.4	3.48	115.24
1	0.2	4	10.2	3.63	101.30
1	0.2	5	9.1	3.51	113.55
1	0.5	1	10.9	3.66	126.14
1	0.5	2	9	3.57	118.51
1	0.5	3	9.7	3.48	99.65
1	0.5	4	10.4	3.76	128.20
1	0.5	5	10.1	3.42	136.13

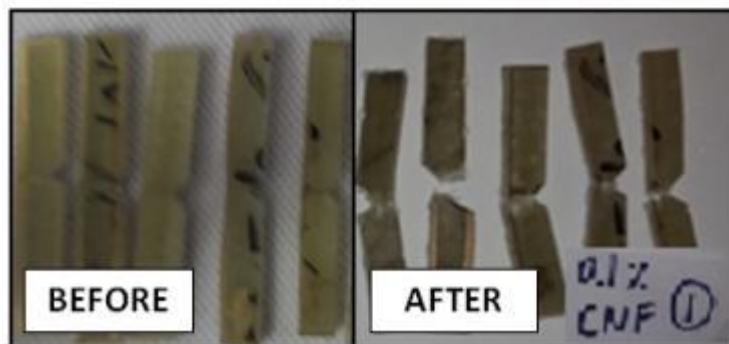


Figure A.47: 0.5% ECNF reinforced 0.1% PAN/GFPC samples

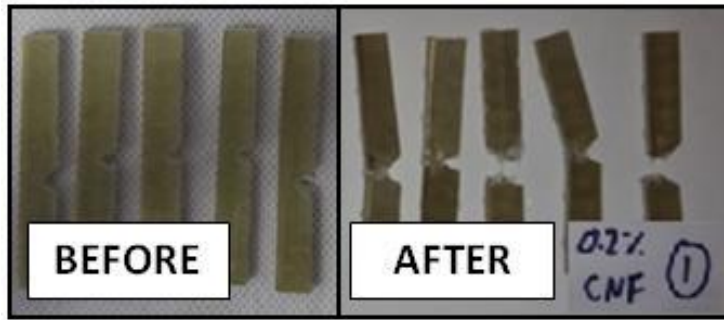


Figure A.48: 0.5% ECNF reinforced 0.2% PAN/GFPC samples

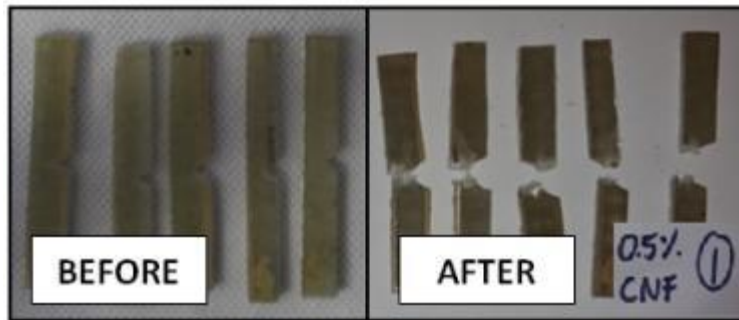


Figure A.49: 0.5% ECNF reinforced 0.5% PAN/GFPC samples

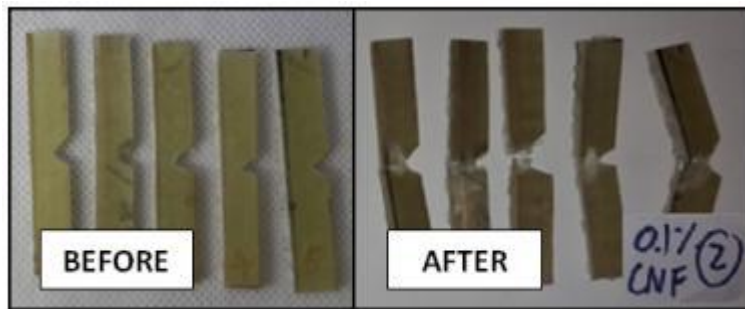


Figure A.50: 1.0% ECNF reinforced 0.1% PAN/GFPC samples

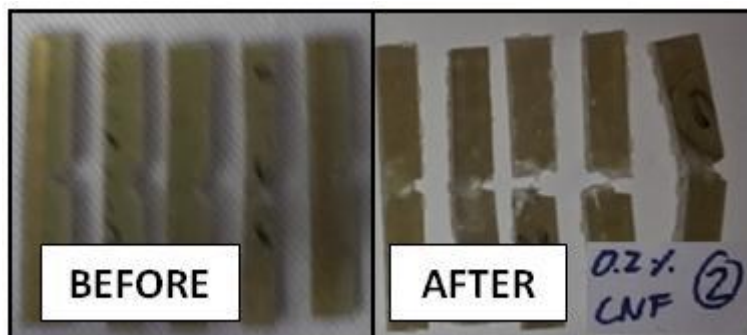


Figure A.51: 1.0% ECNF reinforced 0.2% PAN/GFPC samples

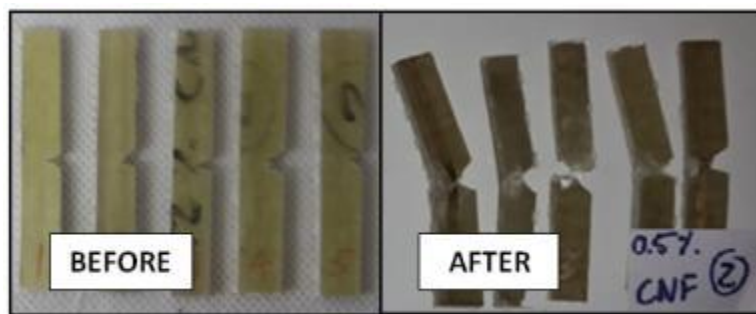


Figure A.52: 1.0% ECNF reinforced 0.2% PAN/GFPC samples

APPENDIX B (Sample Calculations)

B.1 Tensile Data

Using a random neat epoxy sample as the test sample, the following sample calculations demonstrate how the ultimate tensile strength as well as the elastic modulus for each specimen was calculated. Section 3.2.1 provides the formulae used in the calculations below. The following data was recovered from the CSV file saved for this particular tensile sample:

Table B.1: Tensile Data

Data	Symbol	Value	Unit
Force at failure	F_{max}	1120.8	N
Width	w	13.82	mm
Thickness	t	3.54	mm
Extension	Δl	3.598431	mm
Gauge Length	l	50	mm

The average area was determined from equation 1 below:

$$\begin{aligned} A &= w \times t \\ &= (13.82)(3.54) \\ &= 48.9228 mm^2 \end{aligned}$$

The ultimate tensile strength was then determined from equation 2 below:

$$\begin{aligned} \sigma_{uts} &= \frac{F_{max}}{A} \\ &= \frac{1120.8}{48.9228} \\ &= 22.91 MPa \end{aligned}$$

The tensile strain was then determined from equation 3 below:

$$\begin{aligned} \varepsilon &= \frac{\Delta l}{l} \\ &= \frac{3.598431}{50} \\ &= 0.72 mm/mm \end{aligned}$$

These formulae above apply to each and every data point saved in the CSV file. All the calculated data points are then plotted to yield a tensile stress-strain graph such as the one shown in Figure B.1 below.

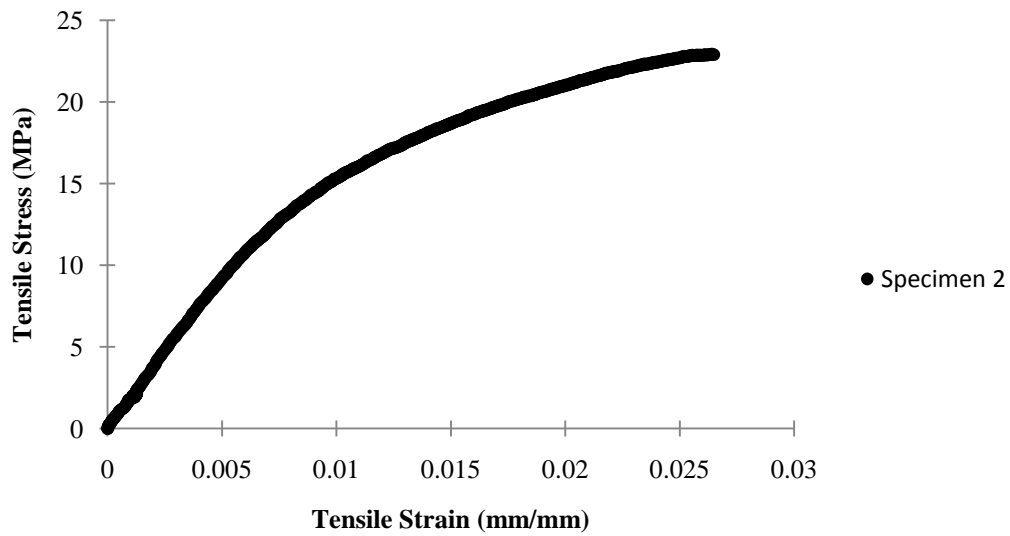


Figure B.1: Tensile stress-strain curve for neat epoxy specimen

The tensile elastic modulus, or Young’s modulus, is determined from the slope of the most linear portion of the stress-strain curve where the material still behaves elastically. It was determined that in most cases the linear region of the stress-strain curves were found to fall between the tensile strain range of $0.001 < \epsilon < 0.005$. Therefore, using Figure B.1 above and Equation 3.7, the elastic modulus was calculated as follows:

$$\begin{aligned}
 E &= \frac{\Delta\sigma}{\Delta\epsilon} \\
 &= \frac{\sigma_2 - \sigma_1}{\epsilon_2 - \epsilon_1} \\
 &= \frac{9.267663 - 1.806928}{0.005043 - 0.00102} \\
 &= 1854.7 \text{ MPa} \\
 &= 1.85 \text{ GPa}
 \end{aligned}$$

The ultimate tensile strength and elastic modulus for all sample batches were determined using the same method. The average ultimate tensile strength and elastic modulus from the each batch of specimens was then calculated by determining the mean of the combined individual specimens. The standard deviation and the coefficient of variance were calculated for each batch.

B.2 Flexural Data

The following sample calculations demonstrate how the maximum flexural strength as well as the flexural modulus for each specimen was calculated. Section 3.2.1 provides the formulae used in the calculations below.

Table B.2: Flexural data

Data	Symbol	Value	Unit
Force at failure	F_{max}	59.5	N
Width	w	10	mm
Thickness	t	4	mm
Extension	Δl	7.93	mm
Gauge Length	l	63	mm

Thus for a maximum applied load of 59.5 N, the ultimate flexural strength of the specimen was calculated using the equation below, given by:

$$\begin{aligned}\sigma_f &= \frac{3F_{max}L}{2bh^2} \\ &= \frac{3(59.5)(63)}{2(10)(4)^2} \\ &= 35.14MPa\end{aligned}$$

Thus for the corresponding maximum force, the vertical deflection of the specimen as measured by the internal encoder of the Shimadzu testing machine was 7.93mm. The flexural strain in the specimen was then calculated using the equation below, given by:

$$\begin{aligned}\varepsilon_f &= \frac{6hD}{L^2} \\ &= \frac{6(4)(7.93)}{(63)^2} \\ &= 0.04795mm/mm\end{aligned}$$

These formulae above apply to each and every data point saved in the CSV file. All the calculated data points are then plotted to yield a flexural stress-strain graph such as the one shown in Figure B.2 below.

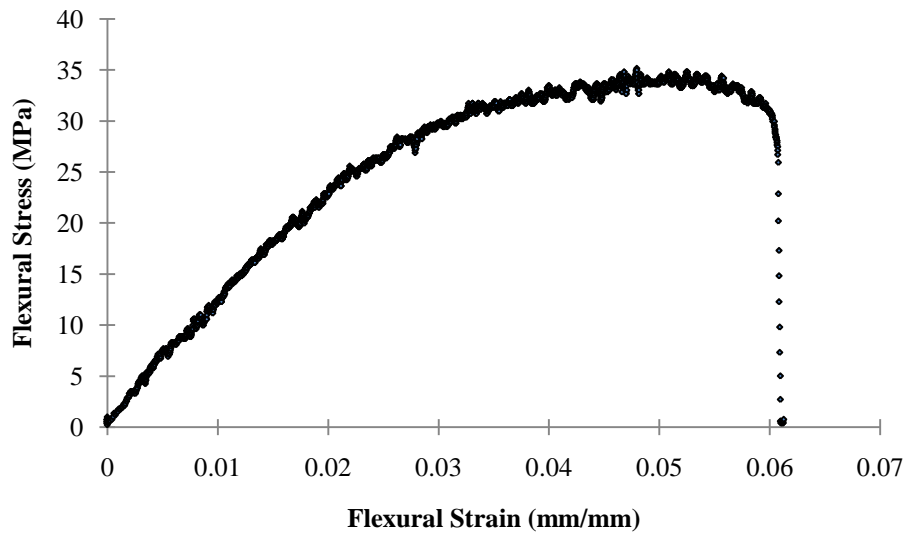


Figure B.2: Flexural stress-strain curve for neat epoxy specimen

The flexural elastic modulus was determined from the slope of the most linear portion of the flexural stress-strain curve where the material still behaves elastically. It was determined that in most cases the linear region of the stress-strain curves were found to fall between the flexural strain range of $0 < \epsilon < 0.02$. Thus by plotting the data points that lie only within this range, and then fitting a linear curve to the data, the flexural modulus of the specimen can be closely approximated by the slope of the fitted line. Therefore, Figure B.3 below shows only the linear elastic region of the curve where the flexural elastic modulus was found to be $1.2 GPa$.

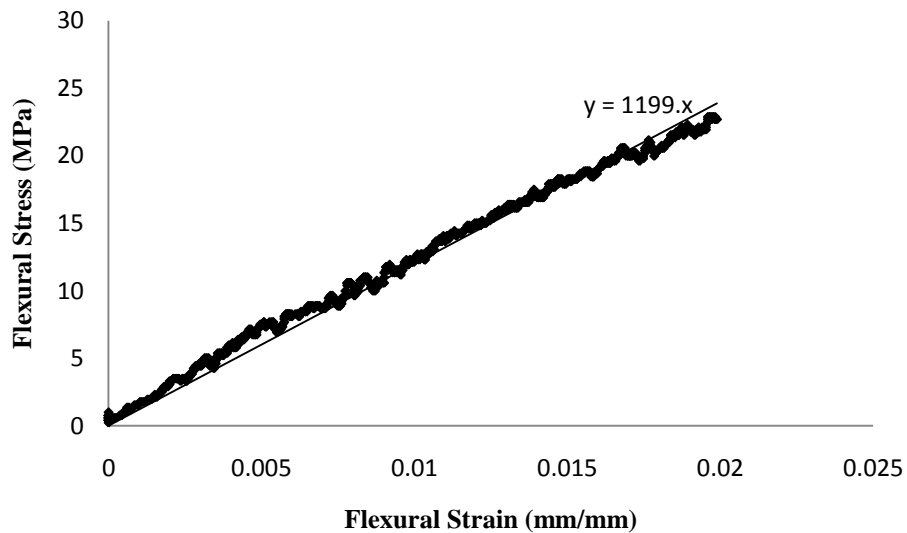


Figure B.3: Graphical illustration of flexural modulus for specimen neat epoxy sample

The ultimate flexural strength and flexural elastic modulus for all sample batches were determined using the same method. The average ultimate flexural strength and flexural elastic modulus from all

the specimens in each batch was then calculated by determining the mean of the combined individual specimens.

B.3 Impact Data

The following sample calculations demonstrate how the impact toughness for each specimen was calculated. Section 3.2.2 provides the formulae used in the calculations below.

The initial step was to determine the calibration correction factor for the particular volume fraction test. This was done by calculating the mean of the 10 calibration runs performed prior to testing. The result for the calibration correction factor was calculated to be 0.1115J as shown in Table B.3 below.

Table B.3: Results for calibration correction factor

Test run	Reading [J]
1	0.125
2	0.110
3	0.105
4	0.110
5	0.115
6	0.110
7	0.115
8	0.100
9	0.110
10	0.115
	0.112
	Mean

The dimensions of the specimen used were 13mm x 3.50mm. The impact toughness was then given by the equation below as:

$$\begin{aligned}
 K_t &= \frac{\Delta e_1}{A_1} \\
 &= \frac{(0.55 - 0.11)}{(1.3 \times 0.35)} \\
 &= 0.967J / mm^2
 \end{aligned}$$